NEW LABORATORY TEST PROCEDURE FOR THE ENHANCED CALIBRATION OF CONSTITUTIVE MODELS

A Thesis
Presented to
The Academic Faculty

by

Ahmed Bayoumi

In Partial Fulfillment
of the Requirements of the Degree
Doctor of Philosophy in Civil and Environmental Engineering

Georgia Institute of Technology

May, 2006

NEW LABORATORY TEST PROCEDURE FOR THE ENHANCED

CALIBRATION OF CONSTITUTIVE MODELS

Approved by:

J. Carlos Santamarina, Chairman
Professor, CEE
Georgia Institute of Technology

J. David Frost
Professor, CEE
Georgia Institute of Technology

Paul W. Mayne
Professor, CEE
Georgia Institute of Technology

Glenn J. Rix
Professor, CEE
Georgia Institute of Technology

Yi-Chang James Tsai
Adjunct Associate Professor, CEE
Georgia Institute of Technology

Date Approved: April 3, 06

To my parents and my wife

ACKNOWLEDGMENTS

The well-earned reputation of the Geotechnical Engineering program at Georgia Institute of Technology that is founded on high quality and diversity of research turned my Ph.D. term into an extraordinary academic experience. I am thankful to Georgia Tech and to the Geosystems group for giving me this opportunity.

Indeed, I was privileged to join the Particulate Media Research Laboratory managed by Professor J. Carlos Santamarina, who is keen on research novelty and pioneering while encompassing a wide range of research interests. Such qualities facilitate a dynamic knowledge exchange and allow a wider academic exposure in a stress-free environment. Not only did he guide my research but also encouraged me to have a deeper insight into challenging problems. Without his scientific and moral support the completion of my research in a year and a half would have been extremely difficult if not impossible.

I would like to extend my thanks to the members of the Particulate Media Group for their thoughtful comments on my research and most importantly for their sincerity.

I have a deep gratitude to the faculty of the College of Engineering at Ain Shams University in Egypt for providing me with the fundamentals in engineering. Their contribution to my education is truly appreciated.

Finally, I am profoundly grateful to my parents for their continuous encouragement and for the unforgettable sacrifices they made for me. My wife Toulin deserves my deepest appreciation for her outmatched patience and for her magnificent moral backup until I earned my degree. I am sincerely indebted to God for all His blessings throughout my entire life.

TABLE OF CONTENTS

ACKNOWLEDGMENTS iv

LIST OF TABLES vii

LIST OF FIGURES viii

SUMMARY xiii

CHAPTER I. INTRODUCTION 1

1.1 Scope 1
1.2 Organization 3

CHAPTER II. NUMERICAL MODELING OF TRIAXIAL COMPRESSION TESTS .. 5

2.1 Constitutive Models in Geomechanics: An Overview 5
2.2 The Modified Cam-Clay Model 6
2.3 Simulations Using Finite Element Program (ABAQUS) 17
2.4 Finite Element Method vs. Direct Use of Constitutive Equations 29
2.5 Limitations of the Modified Cam-Clay Model - Developments 33
2.6 Conclusions 35

CHAPTER III. MODEL CALIBRATION AS AN INVERSE PROBLEM 36

3.1 Introduction to Inverse Problem Solving 36
3.2 Optimization and Search Algorithms 38
3.3 Inverse Problems in Geotechnical Engineering 41
3.4 Design of an experiment 41
3.5 A Study on Error Surfaces 42

3.6 Summary and Conclusions 63

CHAPTER IV. MEASUREMENT AND MODELLING ERRORS - IMPLICATIONS 64

4.1 Measurement Errors 65

4.2 Modeling Errors 82

4.3 Summary and Conclusions 94

CHAPTER V. A NEW GEOTECHNICAL TEST - DESIGN 97

5.1 Lessons from Conventional Tests 97

5.2 Preliminary Testing - Experimental 98

5.3 Three Dimensional Simulation of Flexural Test 102

5.4 Closing Observations 111

CHAPTER VI. MODEL CALIBRATION BASED ON AN INFORMATION-RICH TEST 112

6.1 Devices and Procedures 112

6.2 Material and Specimen Preparation 116

6.3 Measurements 117

6.4 Numerical Modeling of the Flexural Test 132

6.5 Studies in Inversion 133

6.6 Test Mechanism and Stress Field 151

6.7 Discussion and Conclusions 159

CHAPTER VII. CONCLUSIONS AND RECOMMENDATIONS 160

APPENDIX A 163

REFERENCES 191

LIST OF TABLES

Table Page

2.1 Critical-state parameters for selected soils 16

2.2 Cam-Clay parameters of Pueblo sand and Weald clay used in FEM simulations 19

2.3 Comparison between FEM simulations and constitutive equations (1-element) at critical state 30

2.4 Some Cam-Clay model modifications 34

3.1 Investigated range of Cam-Clay parameters for Pueblo Sand 43

3.2 Investigated range of Cam-Clay parameters for Weald Clay 43

3.3 Stress paths for triaxial simulations 45

3.4 Error (%) in individual measurements with parameters variations for Pueblo sand 50

3.5 Error (%) in individual measurements with parameters variations for Weald clay 51

3.6 Contribution of Cam-Clay parameters to individual errors 62

4.1 Loading phases. Number of increments 64

4.2 Single parameter study. Sets of parameter and errors (L2-Norm) 78

4.3 Progressive search: sets of parameters and associated errors (L2-Norm) 81

4.4 Numerically reported triaxial measurements at each *i*-th increment 86

5.1 Preliminary loading patterns 101

5.2 Kernel (no tension zone) check of flexural test - elastic 105

5.3 Cam-Clay parameters for Weald Clay 106

5.4 Flexural test simulation - MCCM 108

6.1 Properties of Ottawa 20-30 sand 116

6.2 Inverted critical state parameters from flexural tests on Ottawa 20-30 sand 149

LIST OF FIGURES

Figure Page

1.1 Guiding philosophy for this study 2

2.1 Critical State: (a) 3D space; (b) q-p' projection; (c) e-p' projection; (d) Specific volume-lnp` plane 7

2.2 Triaxial test simulation for idealized boundary conditions (a) Geometry, boundary conditions, and loading. (b) Finite element mesh 18

2.3 Consolidated-drained test (CID) - NC Pueblo Sand 21

2.4 Consolidated-drained test (CID) - NC Weald clay 22

2.5 Consolidated-undrained test (CIU) - NC Pueblo sand 23

2.6 Consolidated-undrained test (CIU) - NC Weald clay 24

2.7 Consolidated-drained test (CID) - OC Pueblo sand 26

2.8 Consolidated-drained test (CID) - OC Weald clay 27

2.9 Consolidated-undrained test (CIU) - OC Pueblo sand 28

2.10 Consolidated-undrained test (CIU) - OC Weald clay 29

2.11 Finite element vs. 1-element simulations for consolidated-drained CID test - NC Pueblo Sand 31

2.12 Finite element vs. 1-element simulations for consolidated-drained CIU test - NC Pueblo Sand 32

2.13 Finite element vs. 1-element simulations for consolidated-drained CID test - OC Pueblo Sand 33

3.1 Definition of error 38

3.2 Graphical representation of the steepest descent method 40

3.3 Triaxial test simulation. (a) Geometry, boundary conditions, and loading. (b) Finite element mesh 44

3.4 Error surfaces for Pueblo sand 47

3.5 Error surfaces for Weald clay 48

3.6 Effect of G on measurements of CID triaxial test for Weald clay 53

3.7 Effect of M on measurements of CID triaxial test for Weald clay 54

3.8 Effect of λ on measurements of CID triaxial test for Weald clay 55

3.9 Effect of κ on measurements of CID triaxial test for Weald clay 56

3.10 Total L2-norm - NC Weald clay - CID triaxial test 57

3.11 L2-norm of the mean effective stress p`- NC Weald clay - CID triaxial test 58

3.12 L2-norm of the deviatoric stress q - NC Weald clay - CID triaxial test 59

3.13 L2-norm of the axial normal strain ε_z - NC Weald clay - CID triaxial test 60

3.14 L2-norm of the void ratio e - NC Weald clay - CID triaxial test 61

4.1 Original data and simulated data with 5% noise. Idealized CID triaxial simulations of Weald clay 66

4.2 Inversion by successive forward simulation for CID triaxial test - Algorithm 67

4.3 Matching trials using G only for CID triaxial test on Weald clay 68

4.4 Matching trials using M only for CID triaxial test on Weald clay 69

4.5 Matching trials using λ only for CID triaxial test on Weald clay 70

4.6 Matching trials using κ only for CID triaxial test on Weald clay 71

4.7 L2-norm of the mean effective stress p` - CID triaxial test on Weald clay 72

4.8 L2-norm of the deviatoric stress q - CID triaxial test on Weald clay 73

4.9 L2-norm of the axial normal strain ε_z - CID triaxial test on Weald clay 74

4.10 L2-norm of the void ratio e - CID triaxial test on Weald clay 75

4.11 Total L2-norm - CID triaxial test on Weald clay 76

4.12 Matching trials using combinations of Cam-Clay parameters - CID triaxial test - Weald clay 80

4.13 Triaxial test simulation for frictional boundaries (a) Geometry, boundary conditions, and loading. (b) Finite element mesh 85

4.14 Consolidated-drained test (CID) - normally consolidated Pueblo sand 87

4.15 Consolidated-drained test (CID) - over consolidated Pueblo sand 88

4.16 Consolidated-undrained test (CIU) - normally consolidated Pueblo sand 89

4.17 Consolidated-undrained test (CIU) - over consolidated Pueblo sand 90

4.18 Normal stresses and strains for CIU test on normally consolidated Pueblo sand at the end of the deviatoric loading (ε_z = 10%, confining stress = 100 kPa) 92

4.19 Examples of fitting test data with different constitutive models 94

5.1 Preliminary study - setup for specimen preparation and boundary conditions 99

5.2 Preliminary tests. (a) Flexure. (b) Torsion. (c) Shear 100

5.3 Flexural test. (a) Geometry, mesh, boundary conditions, and loading. (b) Circular cross section 103

5.4 Flexural test - MCCM - eccentricity e_k = 0.2. (a) Mean effective stress p'. (b) Axial strain. (c) Radial strain. (d) Hoop strain 109

5.5 Flexural test - Specimen mid height. (a) Stress path in p'-q plane. (b) Stress ratio η = q/p' vs. eccentricity e/r 110

6.1 Lateral-deformation controlled flexural test - Front view 113

6.2 Lateral-deformation controlled flexural test - Side view. (a) Procedure schematic. (b) Peripherals 114

6.3 Load cell calibration curve 115

6.4 End caps: a thin layer of sand is glued. (a) Bottom cap: vacuum hose protected by filter paper at the center of the bottom cap. (b) Top cap 115

6.5 Flexural test measurements - D_r = 69 and R = 1.1. (a) Horizontal force and vacuum. (b) Global vertical displacement Δ_{hl}. (c) Tilt angle ψ 119

6.6 Flexural test measurements - D_r = 66 and R = 1.5. (a) Horizontal force and vacuum. (b) Global vertical displacement Δ_{hl}. (c) Tilt angle ψ 120

6.7 Flexural test measurements - D_r = 64 and R = 2. (a) Horizontal force and vacuum. (b) Global vertical displacement Δ_{hl}. (c) Tilt angle ψ 121

6.8 Flexural test measurements - D_r = 93 and R = 1.1. (a) Horizontal force and vacuum. (b) Global vertical displacement Δ_{hl}. (c) Tilt angle ψ 122

6.9 Flexural test measurements - D_r = 90 and R = 1.5. (a) Horizontal force and vacuum. (b) Global vertical displacement Δ_{hl}. (c) Tilt angle ψ 123

6.10 Flexural test measurements - D_r = 86 and R = 1.9. (a) Horizontal force and vacuum. (b) Global vertical displacement Δ_{hl}. (c) Tilt angle ψ 124

6.11 Global measurements of flexural test. (a) Applied normalized horizontal force. (b) Global tilt angle 125

6.12 Measured horizontal displacement for the midline. Ottawa 20-30 sand at Dr = 69 and stress ratio R = 1.1 126

6.13 Measured horizontal displacement for the midline. Ottawa 20-30 sand at Dr = 66 and stress ratio R = 1.5 127

6.14 Measured horizontal displacement for the midline. Ottawa 20-30 sand at Dr = 64 and stress ratio R = 2 128

6.15 Measured horizontal displacement for the midline. Ottawa 20-30 sand at Dr = 93 and stress ratio R = 1.1 129

6.16 Measured horizontal displacement for the midline. Ottawa 20-30 sand at Dr = 90 and stress ratio R = 1.5 130

6.17 Measured horizontal displacement for the midline. Ottawa 20-30 sand at Dr = 86 and stress ratio R = 1.9 131

6.18 Flexural test: model dimensions, mesh, loading, and constraints and boundary conditions 133

6.19 Back-calculation of constitutive model parameters -Algorithm 134

6.20 Localization manifesting itself in the oscillation of normalized horizontal force. Ottawa 20-30 sand at D_r = 90 and stress ratio R = 1.5 137

6.21 Finite element trials to fit the normalized horizontal load for Ottawa 20-30 sand, at D_r = 90 and stress ratio R = 1.5 137

6.22 Finite element fit to normalized horizontal force 138

6.23 Global tilt angle: finite element prediction vs. experimental measurements 139

6.24 Midline horizontal displacement for Ottawa 20-30 sand at Dr = 69 and stress ratio R = 1.1 141

6.25 Midline horizontal displacement for Ottawa 20-30 sand at Dr = 66 and stress ratio R = 1.5 142

6.26 Midline horizontal displacement for Ottawa 20-30 sand at Dr = 64 and stress ratio R = 2.0 143

6.27 Midline horizontal displacement for Ottawa 20-30 sand at Dr = 93 and stress ratio R = 1.1 144

6.28 Midline horizontal displacement for Ottawa 20-30 sand at Dr = 90 and stress ratio R = 1.5 145

6.29 Midline horizontal displacement for Ottawa 20-30 sand at Dr = 86 and stress ratio R = 1.9 146

6.30 Vertical displacement of soil right below top cap δ_{vl}. Finite element prediction vs. experimental measurements 148

6.31 Out-of-plane displacement field - transverse profile. Ottawa 20-30 sand at Dr = 64 and stress ratio R = 2.0 150

6.32 Numerical prediction of normal vertical stress distribution for Ottawa 20-30 sand (Dr = 69, stress ratio R = 1.1). (a) Top of the specimen right below top cap. (b) Mid height. (c) Bottom of the specimen right above the bottom cap..... 154

6.33 Stress paths for Ottawa 20-30 sand (Dr = 69; stress ratio R = 1.1). (a) Top of the specimen. (b) Mid height. (c) Bottom of the specimen 155

6.34 Numerical prediction of normal vertical stress distribution for Ottawa 20-30 sand (Dr = 64, stress ratio R = 2). (a) Top of the specimen right below top cap. (b) Mid height. (c) Bottom of the specimen right above the bottom cap..... 156

6.35 Stress path for Ottawa 20-30 sand (Dr = 64; stress ratio R = 2.0). (a) Top of the specimen. (b) Mid height. (c) Bottom of the specimen 157

6.36 Hoop stress contour for Ottawa 20-30 sand (Dr = 64; stress ratio R = 2.0) at applied horizontal stress Δ_{hl} = 0.4 mm..... 158

SUMMARY

Constitutive model parameters are identified during model calibration through a trial-and-error process driven to fit test data. In this research, the calibration of constitutive models is formally handled as an inverse problem.

The first phase of this research explores error propagation. Data errors, experimental biases (e.g. improper boundary conditions), and model errors affect the inversion of model parameters and ensuing numerical predictions. Drained and undrained tests are simulated to study the effect of these three classes of errors. Emphasis is placed on the analysis of error surfaces computed by successive forward simulations.

The second phase of this research centers on test procedures. Conventional soil tests were developed to create uniform stress and strain fields; consequently, they provide limited amount of information, the inversion is ill-posed, and results enhance uncertainty and error propagation. This research examines soil testing using new, non-conventional loading and boundary conditions to create rich, diverse, non-uniform strain and stress fields. In particular, the flexural excitation of cylindrical soil specimens is shown to provide rich data leading to a more informative test than conventional geotechnical tests. The new test is numerically optimized. Then a set of unique experimental studies is conducted.

CHAPTER I

INTRODUCTION

1.1 SCOPE

A wide range of soil tests has been developed and used in geomechanics to address research questions and engineering needs. Current engineering design methods favor conventional soil tests. The success and the wide acceptance of these soil tests are based on their simplicity and practicality. Yet, more than one geotechnical test is required to extract all the parameters needed for design.

Field and laboratory geotechnical tests provide engineering design parameters within the framework of a selected constitutive model. Extracting soil parameters from a test is an inverse problem. The inversion process requires enough independent information to unequivocally identify the constitutive model parameters. Conventional soil tests have been purposely designed with simple symmetric boundary conditions to provide homogenous strain and stress fields; furthermore, current testing routines provide global measurements rather than local measurements. Such a test is information limited. Thus, despite the availability of high-precision and diverse transducers, most conventional soil tests cannot provide an extensive base of independent information to adequately support the inversion.

The purpose of this research is to identify enhanced testing approaches in view of constitutive model calibration. This implies the design of a new geotechnical test that is capable of providing "rich" information and the development of a robust inversion approach to back-calculate material parameters for a selected constitutive model. The philosophy behind this study is schematically depicted in Figure 1.1.

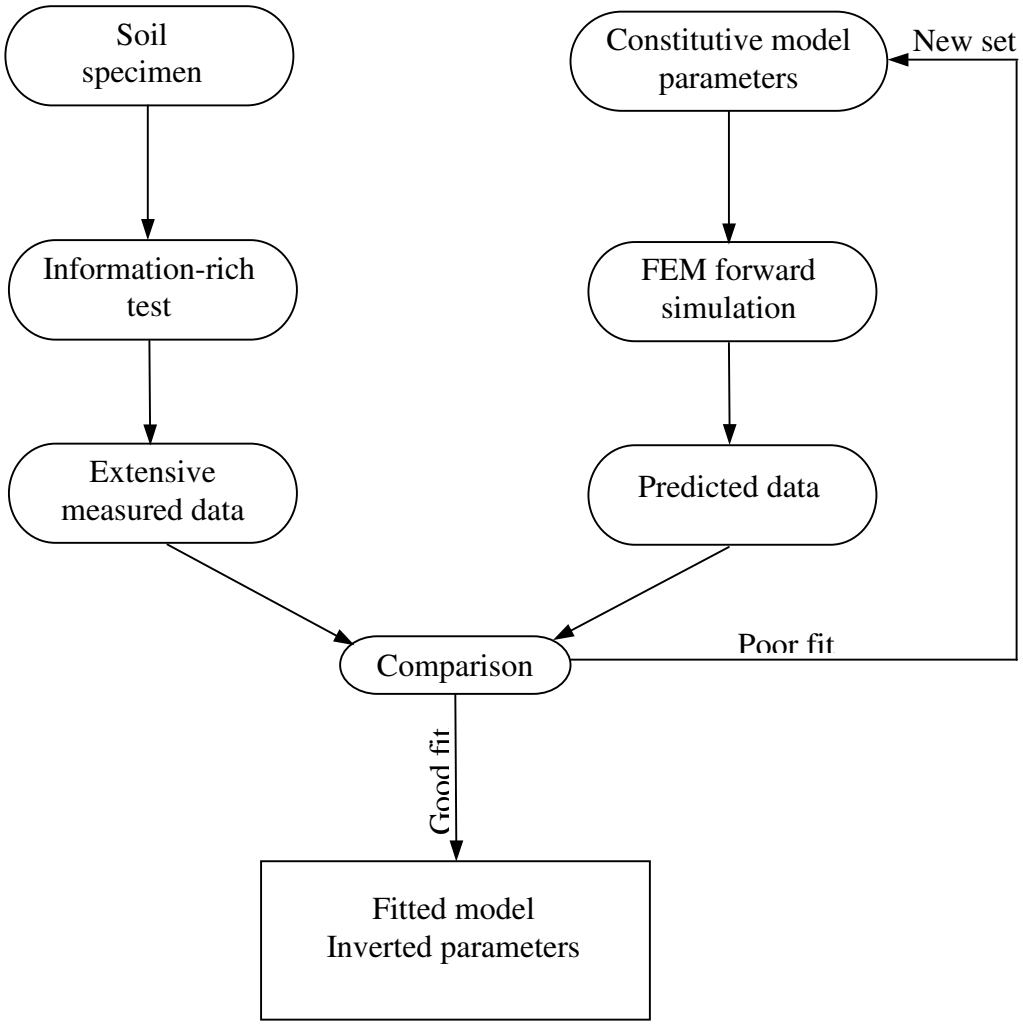

Figure 1.1 Guiding philosophy for this study.

1.2 ORGANIZATION

Chapter 2 presents a review of the Modified Cam-Clay model and a compilation of model parameters for different soils. Then triaxial tests with idealized frictionless platens are numerically simulated to model contractive and dilative soils. Finite element results are confirmed for a single element via the direct use of Cam-Clay constitutive equations. These results show the potential and inherent limitations that simple yet robust constitutive models have in simulating soil behavior.

Chapter 3 introduced the concept of model calibration as an inverse problem. Error functions are defined and optimization and search algorithms are briefly reviewed. The discussion centers on the role that various types of experimental data play in inversion.

Chapter 4 explores the effect of improper test simulations on back-calculated constitutive model parameters. The sources of error that are considered include boundary conditions, measurement errors and the selected constitutive model errors.

Chapter 5 utilizes numerical modeling to explore new tests. Simulations of several soils and boundary conditions show the advantages and limitations of various test procedures.

Chapter 6 presents experimental results and numerical inversion of a new flexural test. The test setup, testing procedure and inversion results are discussed in detail.

Finally, Chapter 7 summarizes the major conclusions of this study and suggests potential improvements for the proposed test as well as avenues for further research.

CHAPTER II

NUMERICAL MODELING OF TRIAXIAL COMPRESSION TESTS

This chapter reviews in detail the Modified Cam-Clay model, its main characteristics, model parameters, and its numerical implementation. The direct use of Cam-Clay equations is compared against finite element simulations of idealized triaxial compression tests. More recent modifications and extensions of the Modified Cam-Clay model and the suitability of the Modified Cam-Clay model for capturing soil response in idealized triaxial finite element simulations are discussed at the end of this chapter.

2.1 CONSTITUTIVE MODELS IN GEOMECHANICS

Soils can be numerically modeled as assemblies of discrete particles, or as an elastic-viscous-plastic continuum (Oda, 1993). Both approaches face challenges in the complex nature of particulate media, such as inherently non-linear, non-elastic, and non-homogenous characteristics. Furthermore, unlike solid media, particulate media are uniquely influenced by a variety of factors including drainage conditions, in-situ stress conditions, stress paths, chemical changes, saturation level, anisotropy, aging, softening and degradation, crushing and failure, cyclic loading, time-dependency and liquefaction. There is no single unified constitutive model that successfully incorporates all these factors. Therefore, models are applicable only for the conditions considered in their design (Desai, 2005).

Simple constitutive models usually employ parameters that have a clear physical meaning. More intricate constitutive models utilize additional parameters, and their inversion becomes curve-fitting as they bare no physical significance. Lade (2005) provides a thorough discussion on the role of each parameter in three constitutive models: the Elastic Perfectly Plastic, the Modified Cam-Clay model, and the Single Hardening model.

Conventional soil tests were developed to produce uniform stress and strain fields. This facilitates easier interpretation within the framework of constitutive modeling. However, most conventional soil tests, such as triaxial test, suffer from the effect of non-ideal boundary conditions which cause non-uniform stress and strain fields (Liyanapathirana et al., 2005).

2.2 THE MODIFIED CAM-CLAY MODEL

2.2.1 Introduction - Fundamentals

The Cam-Clay Model CCM is an elasto-plastic constitutive model. CCM captures soil behavior from an initial state of stress until it reaches its critical state. The critical state is attained when the material is sheared at constant volume. Regardless of the initial conditions, critical states fall on a single curve in the void ratio e, mean effective stress p`, and deviatoric stress q space; this is the critical state line (Figure 2.1 - Murthy et al., 1988).

The isotropic consolidation line ICL and the critical state line CSL are shown in Figure 2.1.c and d. The elastic behavior, yield surface, plastic potential, and hardening rule in the Modified Cam-Clay Model MCCM are summarized next (Burland, 1967; Wood, 1990).

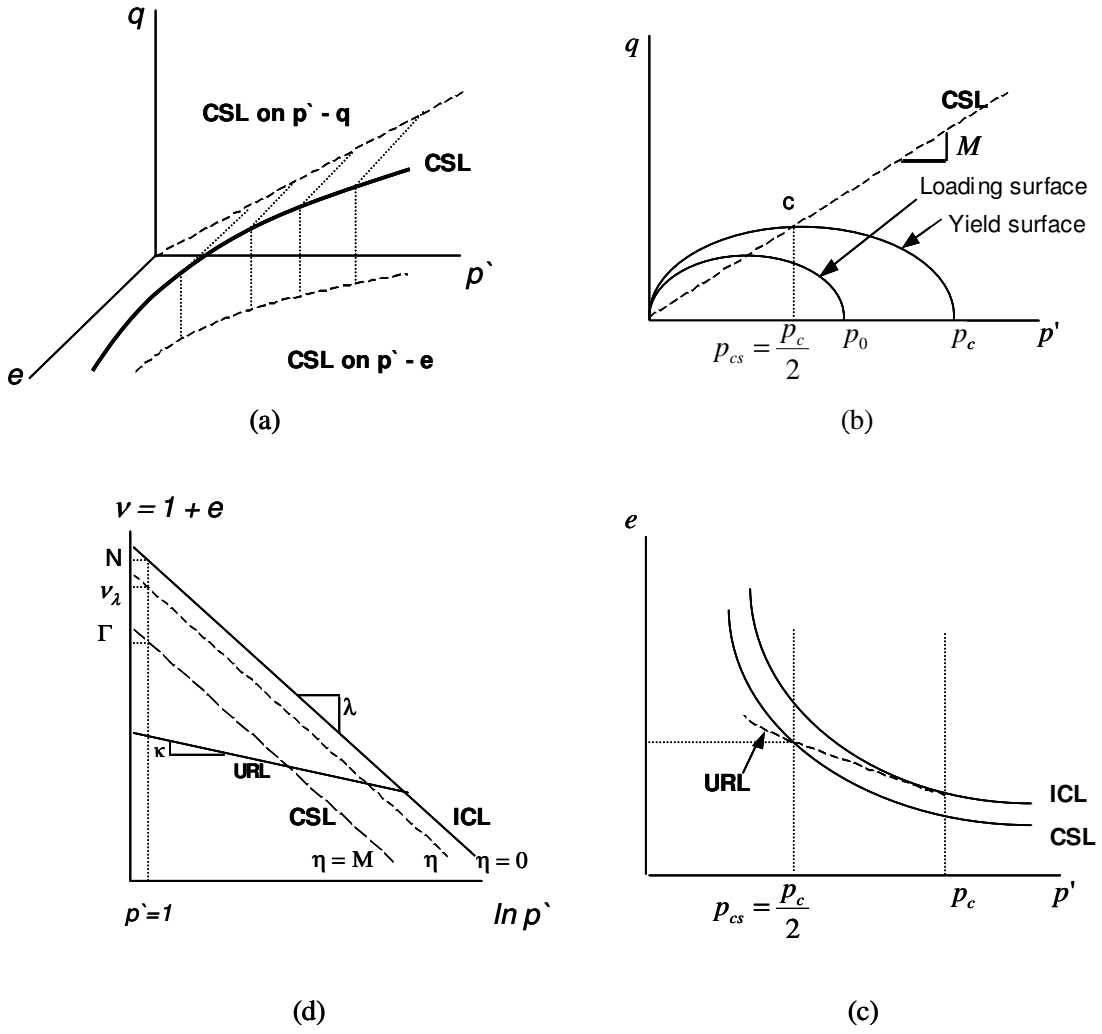

Figure 2.1 Critical State: (a) 3D space; (b) q-p' projection; (c) e-p' projection; (d) Specific volume-ln p` plane (From Santamarina et. al, 1998, and Wood, 1990). Notation: Mean effective stress p`, deviatoric stress q, void ratio e, axial strain ε_z, isotropic consolidation line ICL, and critical state line CSL.

1. Elastic Behavior. The elastic behavior is fully decoupled, i.e. volumetric response is dependent only of the change in the mean effective stress and the shear response is only dependent on the deviatoric stress:

$$\begin{bmatrix} \delta\varepsilon_p^e \\ \delta\varepsilon_q^e \end{bmatrix} = \begin{bmatrix} \kappa/\nu p' & 0 \\ 0 & 1/3G \end{bmatrix} \begin{bmatrix} \delta p' \\ \delta q \end{bmatrix} \tag{2.1}$$

where $p^{'}$ is the current mean effective stress, κ is the slope of the unloading-reloading line URL in ln p`-e plane, ν is the initial specific volume (ν = 1 + e), and G is the shear modulus.

2. Yield Surface. The yield surface (p`-q plane) of MCCM is assumed to be elliptical:

$$f = q^2 - M^2[p^{'}(p_0^{'} - p^{'})] = 0 \tag{2.2}$$

where $M = q_{cs} / p_{cs}^{`}$, is the slope of the CSL in p`-q plane, q_{cs} is the deviator stress at critical state, $p_{cs}^{`}$ is the mean effective stress at critical state, and $p_0^{'}$ is the initial size of the yield surface which is the largest mean effective stress the soil has ever experienced (i.e. the pre-consolidation stress for over consolidated soils).

3. Hardening Rule. The plastic volumetric strain, $\delta\varepsilon_p^p$, is related to the change in yield surface size, $\delta p_0^{'} / p_0^{'}$, via the hardening rule.

$$\delta\varepsilon_p^p = \left[\frac{(\lambda - \kappa)}{\nu}\right] \frac{\delta p_0^{'}}{p_0^{'}} \tag{2.3}$$

where λ is the slope of the critical state line or isotropic consolidation line in ln p`-e plane, and $k$ is the slope of the unloading reloading branch in ln p`-e plane.

4. Plastic Potential and Flow Rule. The Modified Cam-Clay model assumes associated plastic flow. Thus, the plastic potential, g , is or coincides with the yield surface, $g = f$ (Equation 2.2), and the flow rule is given as

$$\frac{\delta\varepsilon_p^p}{\delta\varepsilon_q^p} = \frac{\partial g / \partial p'}{\partial g / \partial q} = \frac{M^2\left(2p' - p_0'\right)}{2q} = \frac{M^2 - \eta^2}{2\eta} \tag{2.4}$$

where η is the slope of the stress ratio (q/p`) and $\delta\varepsilon_q^p$ is the plastic change in shear strain. The plastic change in volumetric and shear strains can be expressed as follows:

$$\begin{bmatrix} \delta\varepsilon_p^p \\ \delta\varepsilon_q^p \end{bmatrix} = \frac{(\lambda - \kappa)}{vp'\left(M^2 + \eta^2\right)} \begin{bmatrix} \left(M^2 - \eta^2\right) & 2\eta \\ 2\eta & 4\eta^2 / \left(M^2 - \eta^2\right) \end{bmatrix} \begin{bmatrix} \delta p' \\ \delta q \end{bmatrix} \tag{2.5}$$

Plastic strains occur only when the stress state (p`, q, e) is located out of the initial yield surface. It is obvious that the plastic behavior is coupled, i.e., a change in either the mean effective stress or the deviatoric stress or both result in shear and volumetric strains. Equation 2.5 is based on the associated flow rule.

The projection of the CSL on p`-e plane is a straight line if plotted on a semi-log graph ln p`-e or ln p`-ν (Figure 2.1.d). The ICL, η-Line, CSL, and URL in the ln p`-e can be expressed as:

$$v = N - \lambda \ln p' \qquad \text{ICL} \tag{2.6}$$

$$\nu = \nu_{\lambda} - \lambda \ln p' \qquad \eta\text{-line} \qquad (2.7)$$

$$\nu = \Gamma - \lambda \ln p' \qquad \text{CSL} \qquad (2.8)$$

$$\nu = \nu_{\kappa} - \kappa \ln p' \qquad \text{URL} \qquad (2.9)$$

where N, ν_λ, and Γ are the specific volumes at an arbitrary reference stress, typically at a stress p` = 1.0 kPa. The location of the CSL with respect to the ICL can be expressed by:

$$\Gamma = N - (\lambda - \kappa)\ln 2 \qquad (2.10)$$

2.2.2 Key Features

The success of the critical state model resides in its ability to capture the behavior of soils using a relatively simple formulation. The key features of Cam-Clay models can be summarized as follows (Gens and Potts, 1988):

- Critical state that is independent of initial conditions (Figure 2.1).
- The assumption of isotropic hardening leads to succession of critical state points on the CSL (Figure 2.1).
- Volumetric response is dependent on stress history.
- The critical state surface limits the presence of stress state and specific volume only inside the defined critical state surface.
- The ability of determining consolidation and swelling behavior of soils using the slopes λ and κ at a given pre-consolidation stress (Figure 2.1).

2.2.3 Model Parameters

This section summarizes the role of the parameters of the Modified Cam-Clay model.

1. Pre-consolidation Stress - p_0`. The size of the yield surface is necessary to determine whether the soil at a given state of stress and void ratio is located within the elastic zone or the plastic zone. Equally important, the size of the yield surface "records" the loading history. The size of the yield surface is the current mean effective stress for normally consolidated soils and the pre-consolidation stress for over consolidated soils.

2. Initial Void Ratio e_0 or Initial Specific Volume v_0. The initial void ratio or the initial specific volume $v_0 = 1 + e_0$ is necessary for the complete definition of the initial state of the soil before loading. The elastic volumetric behavior is dependent on the initial void ratio and the bulk modulus K which can be computed from κ at a given mean effective stress p`, as:

$$K(\text{Bulk modulus}) = \frac{p'(1+e_0)}{\kappa} \tag{2.11}$$

3. Shear Modulus or Poisson's Ratio. The shear modulus G is used to obtain the elastic shear strain within the elastic zone, and it is related to the bulk modulus K and the Poisson's ratio μ as:

$$G = \frac{3}{2} K \frac{1-2\mu}{1+\mu} \tag{2.12}$$

when computed as indicated, equations 2.11 and 2.12, the elastic shear response is dependent on the effective stress during loading. The elastic dependency of shear modulus on Poisson's ratio would lead to non-conservative strains for highly over consolidated soils (Zytynski et al., 1978). This effect is rather limited for static problems because the energy dissipation by plastic strains appreciably exceeds the energy dissipation by the constant Poisson's ratio model (Yu, 1998). On the other hand, a constant shear modulus results in a physically unrealistic stress-strain behavior (Zytynski et al., 1978). The variable shear modulus captures the non-linear elastic behavior prior to plastic deformations while a constant shear modulus results in a linear elastic response. The suggested elastic relationship in the literature generally oversimplifies the real behavior of soils for states inside the yield locus (Gens and Potts, 1988).

4. *Slope of Unloading-Reloading-Line URL.* The logarithmic bulk modulus, κ, in ν-ln p` controls the elastic volumetric strain during unloading and reloading. It also affects the elastic shear strains if a combination of (p`, q) exists such that the soil is not at its critical state. The parameter κ appears in the plastic strains formulas too; however, it is used to offset the elastic strains from the total strain.

5. *Slope of Critical State Line CSL.* The CSL and ICL line are parallel. The slope λ in ν-ln p` controls the size of the new yield surface due to lading. Accordingly, λ determines the corresponding specific volume ν or void ratio e during plastic loading.

6. Effective Stress Ratio at Critical State. The shear strength of the soil is captured in M, which is a function of the friction angle ϕ'. Defining M = $q_{cs} / p_{cs}^{`}$, then:

$$M = \frac{6\sin\phi'}{3-\sin\phi'} \text{ or} \qquad \sin\phi' = \frac{3M}{6+M} \text{ in triaxial compression} \tag{2.13}$$

$$M = \frac{-6\sin\phi'}{3+\sin\phi'} \text{ or} \qquad \sin\phi' = \frac{3M}{6-M} \text{ in triaxial extension} \tag{2.14}$$

2.2.4 Assumptions vs. Limitations

The original yield surface in the CCM is naturally reached from Taylor's dilatancy (Schofield, 2006; Taylor, 1948). Later on, the elliptical yield surface in MCCM was selected to eliminate the unrealistic shear strains during isotropic consolidation in the original CCM (Roscoe and Burland, 1968). Despite that the assumed normality of the MCCM is convenient for clayey soils, this assumption results in very large dilation rates and volumetric expansion at failure for sandy soils (Lade, 2005). MCCM does not model cemented soil behavior satisfactorily (Lade, 2005). The yield surface in both original CCM and MCCM is symmetric about the mean stress axis, i.e. isotropy is assumed. Still, the MCCM provides a simple, versatile and robust tool that encompasses consolidation, yielding, and failure in a single framework (Murthy et al., 1988).

2.2.5 Determination of Parameters

Triaxial Test. Typically, three triaxial compression tests and one isotropic compression test are used to determine M, λ, and κ parameters (Lade, 2005).

Oedometer Test. Given the parallelism between the 1-D consolidation line (1-DCL) and CSL in e–ln p` the critical state parameters may be related to 1-DCL as follows (Wood, 1990):

$$\lambda \cong \frac{C_C}{2.3} \tag{2.15}$$

$$\kappa \cong \frac{C_S}{2.3} \tag{2.16}$$

where C_C is the compression index and C_S is the swell index.

Index Tests - Fine-Grained Soils. Consistency indices are correlated with the compression index C_c and Cam-Clay parameters κ and λ as follows:

$$\lambda \cong 0.6\frac{I_p}{100} \quad \text{(Schofield and Wroth, 1968, and Wood, 1990)} \tag{2.17}$$

$$\sin\phi' = 0.35 - 0.1\ln\frac{I_p}{100} \quad \text{(Wood, 1990)} \tag{2.18}$$

$$\lambda \cong 0.92\left(\frac{PL}{100} - 0.09\right) \quad \text{(Schofield and Wroth, 1968)} \tag{2.19}$$

$$C_c = \frac{I_p G_s}{200} \quad \text{(Atkinson, 1993)} \tag{2.20}$$

$$\lambda = \frac{I_p G_s}{460} \quad \text{(Skempton and Northey, 1952)} \tag{2.21}$$

$$\Gamma = 1.25 + \lambda \ln 10000 \quad \text{(Atkinson, 1993)} \tag{2.22}$$

$$\frac{\kappa}{\lambda} = 0.2 - 0.5 \text{ (for plastic clays)} \quad \text{(Atkinson, 1993)} \tag{2.23}$$

where I_p = LL-PL is the plasticity index, PL is the plastic limit, LL is liquid limit, and G_s is the specific gravity.

Correlations for Coarse-Grained Soils. Cho et al. (2005) investigated the effect of particle shape and size as index properties on macroscale soil properties. Cho et al. (2005) reported a decrease in three of the critical state parameters (Γ, λ and ϕ) with increasing roundness, sphericity and overall regularity of the sand particles. Particle roundness, R, showed stronger correlation to critical state friction angle, ϕ, and intercept, Γ, than sphericity (Cho et al., 2005). The correlations with Cam-Clay parameters can be summarized as follows:

$$\phi' = 42 - 17R \tag{2.24}$$

$$\Gamma = 1.2 - 0.4R \tag{2.25}$$

$$e_{cs100} = 1.1 - 0.42\rho \tag{2.26}$$

$$\lambda = 0.5(\Gamma - e_{cs100}) \tag{2.27}$$

where R is particle roundness, ρ is particle angularity, and e_{cs100} is the critical state void ratio at a mean principal stress p' = 100 kPa (for details see Cho et al., 2005).

2.2.6 Typical Values

Table 2.1 summarizes the values of critical state parameters for a wide range of soils. Some values are re-calculated from values published to accommodate differences in reference stress, units, or designated compression plane (e-log p` vs. e-ln p`). M and ϕ parameters are related through Equations 2.13 and 2.14.

Table 2.1 Critical-state parameters for selected soils.

	λ	$\Gamma^{\#}$	M	κ	G (MPa)	e_0	p_0` (kPa)	ϕ'_{TC} (deg.)	Notes
Weathered Bangkok Clay[10]	0.40		0.90	0.10		3.82	35		
Soft Clay[1]	0.250	2.500	0.898	0.050	0.500	1.64*		26*	
Kaolin Clay[1]	0.250	3.440	0.900	0.050	0.075 p`	2.58*		23*	
Kaolin Clay[2]	0.260	3.265	1.020	0.050		1.065	690	26 *	
Kaolin Clay[3]	0.187		0.95	0.05					
Kaolin Clay[4]	0.19	3.14	1.00	0.05			1	25	
Leda Clay[10]	0.223		1.20	0.03		2.338	169		
Natural Calcarenite[8]	0.216		1.45	0.0136		2.5	2400		$\nu = 0.13$
Gault Clay[1]	0.219	2.960	1.000	0.035	2.250	2.09*		25*	
Norrköping Clay[9]	0.20		1.20	0.02		2.50	120		$\nu = 0.36$
Boston Blue Clay[4]	0.184	2.120*	1.348*	0.034	0.525K	1.12	100	33*	
Clay (NC)[5]	0.174	2.175*	1.000	0.026		1.072	69	25*	
London Clay[2]	0.161	2.448	0.888	0.062		0.700	690	23*	Γ @ 1 psi
London Clay[7]	0.161	2.759	0.888	0.062		1.759	1		Γ @ 1 kPa
London Clay[11]	0.16	2.45	0.89	0.0624			1	23	
Wiener Tegel V[2]	0.122	2.130	1.010	0.026		0.558	690	26*	Γ @ 1 psi
Weald Clay[1]	0.088	2.058	0.882	0.031	3.0	0.628*	207	23	Γ @ 1 kPa
Weald Clay[2]	0.093	1.880	0.950	0.035		0.48*	690	24	Γ @ 1 psi
Weald Clay[7]	0.093	2.060	0.900	0.025		1.06*	1	23 *	Γ @ 1 kPa
Glacial Till[11]	0.09	1.81	1.18	0.0144			1	29	
Silty Clay[6]	0.143	2.120*	1.027*	0.028	1.70	1.200*		26	
Silty Clay[6]	0.080	1.763*	1.200*	0.026	4.150	0.800*		30	
Clayey Silt[6]	0.064	1.820*	1.027*	0.021	2.70	0.850*		26	
Natural Clayshale[10]	0.06		1.45		29*	0.668	3800		
Sandy Clayey Silt[6]	0.060	1.722*	1.287*	0.020	5.350	0.750*		32	
Corinth Canal Marl[8]	0.039		1.38	0.008		0.725	3800		$\nu = 0.25$
Silty Sand (Pueblo)[5]	0.014	1.332*	1.240	0.0024	20.0	0.340	69	31*	
Ticino Sand[7]	0.024	1.986	1.290	0.008		0.986*	1	32*	
Erksak Sand 330/0.7[7]	0.014	1.8167	1.200	0.005		0.817*	1	30*	Γ @ 1kPa
Ottawa Sand[7]	0.017	1.864	1.190	0.005	69-138[12]	0.864*	1	30*	Γ @ 1kPa

[1] Wood, 1990; [2] Schofield and Wroth, 1968; [3] Murthy et al., 1991; [4] Whittle and DeGroot, 1994; [5] Desai and Siriwardane, 1984; [6] Bose and Som, 1998; [7] H.S. Yu, 1998; [8] Liyanapathirana et al., 2005; [9] Sheng et al., 1997; [10] Liu and Carter, 2002; [11] Atkinson, 1993; [12] Lambe and Whitman, 1969.

Notation: Slope of critical state line in ν-ln p` Plane $\lambda$, effective stress ratio at failure M, slope of unload-reload-line in $\nu$-ln p` plane κ, shear modulus G, Initial void ratio e_0, pre-consolidation stress p_0`, critical friction angle from triaxial compression test $\phi'_{TC}$, calculated value from other properties *, The reported $\Gamma$ is not necessarily at the shown $p_0$' [#], bulk modulus K, mean effective stress p`, , Poisson's ratio ν.

2.3 SIMULATIONS USING FINITE ELEMENT PROGRAM (ABAQUS)

In this section the results of triaxial compression simulations of normally consolidated and over consolidated soils are presented for both consolidated-drained and consolidated-undrained cases

2.3.1 Model Components

Triaxial simulations shown in this section are for ideal boundary conditions: i.e., frictionless top and bottom platens. This assumption creates a homogenous stress field within the soil specimen. Thus, stresses and stains are identical everywhere in the soil specimen. Consequently, one point could represent the stress state in the specimen.

The cylindrical specimen is modeled as an axi-symmetric slice (Figure 2.2). The slice is discretized into 192 eight-node quadrilateral elements (633 nodes). The simulation is implemented in ABAQUS.

The soil is isotropically consolidated and then failed by applying a uniform vertical displacement on the soil specimen. Undrained loading is simulated by allowing soil consolidation for a very short time (0.00001 sec). Over consolidation is simulated by consolidating the soil specimen to a preselected pre-consolidation stress, followed by isotropic unloading to the “initial stress”.

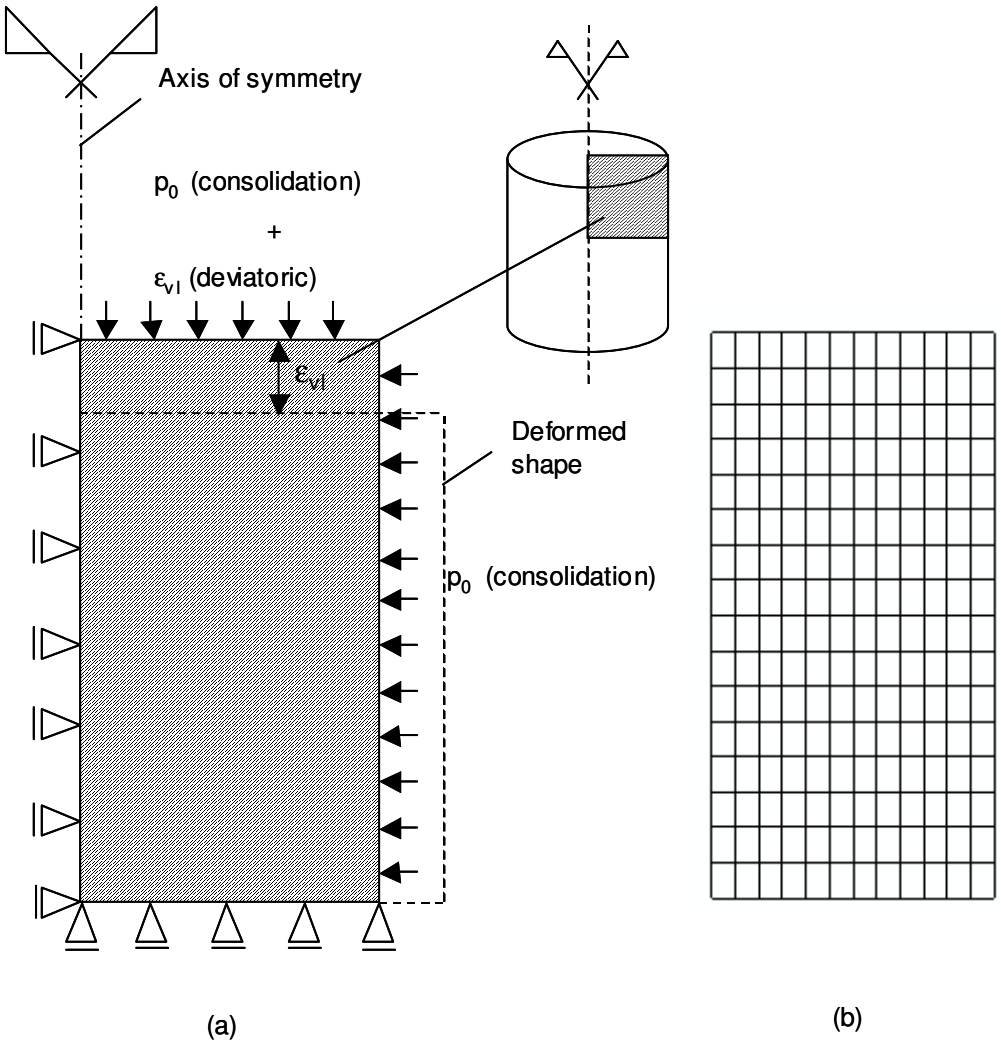

Figure 2.2 Triaxial test simulation for idealized boundary conditions (a) Geometry, boundary conditions, and loading. (b) Finite element mesh. Notation: confining stress p_0', and vertical applied displacement δ_{vl}.

All simulations end with deviatoric unloading. For drained unloading the p`-e slope should be equal to $\kappa$ (swell/unloading index $C_r$ in log p`-e plane). For undrained unloading this slope is zero because of the constant volume condition. The simulations are run for Pueblo sand and Weald clay. The Cam-Clay parameters of Pueblo sand and Weald clay are shown in Table 2.2.

Table 2.2 Cam-Clay parameters of Pueblo sand and Weald clay used in FEM simulations.

	λ	M	κ	G (kPa)	e_0 @ p'_0	p'_0 (kPa)
Weald Clay	0.088	0.882	0.031	3000	0.628	207
Pueblo Sand	0.014	1.240	0.0024	20000	0.340	69

2.3.2 Notation and Sign Convention

The Cambridge stress definitions are adopted in this study.

$$p' = \frac{\sigma_v' + 2\sigma_r'}{3} \tag{2.28}$$

$$q = \sigma_v' - \sigma_r' \tag{2.29}$$

where σ_v' is the vertical effective stress, and σ_r' is the radial effective stress. The corresponding volumetric and shear strains in a triaxial space are defined as follows:

$$\varepsilon_v = \varepsilon_z + 2\varepsilon_r \tag{2.30}$$

$$\varepsilon_q = \frac{2}{3}(\varepsilon_z - \varepsilon_r) \tag{2.31}$$

where ε_z is the vertical strain, and ε_r is the radial strain. Contractive volumetric strain is positive and dilation is negative. Axial strain is considered positive for axial specimen shortening. The critical state line CSL and the isotropic consolidation line ICL are presented in the p`−q−e space as dashed lines (Equations 2.8 and 2.10).

2.3.3 Normally Consolidated (Contractive) Soil

The results of isotropically consolidated-drained CID and isotropically consolidated–undrained CIU triaxial finite element simulations for normally consolidated NC soils are shown in Figures 2.3 through 2.6. Each simulation is

performed at three confining stresses. For all cases the soil is loaded to its critical state before unloading. The results agree with the main characteristics of normally consolidated soils: the magnitude of the deviatoric stress at failure is directly proportional to the confining stress and stress-hardening response. The e-p` curve for the isotropic consolidation phase coincides with ICL. The end of the e-p` curve of the deviatoric phase is located on the CSL. The transition from ICL to CSL during the deviatoric phase is associated with an increase in mean effective stress and a decrease in void ratio for drained simulations (Figures 2.3 and 2.4) and occurs at constant void ratio for undrained simulations (Figures 2.5 and 2.6).

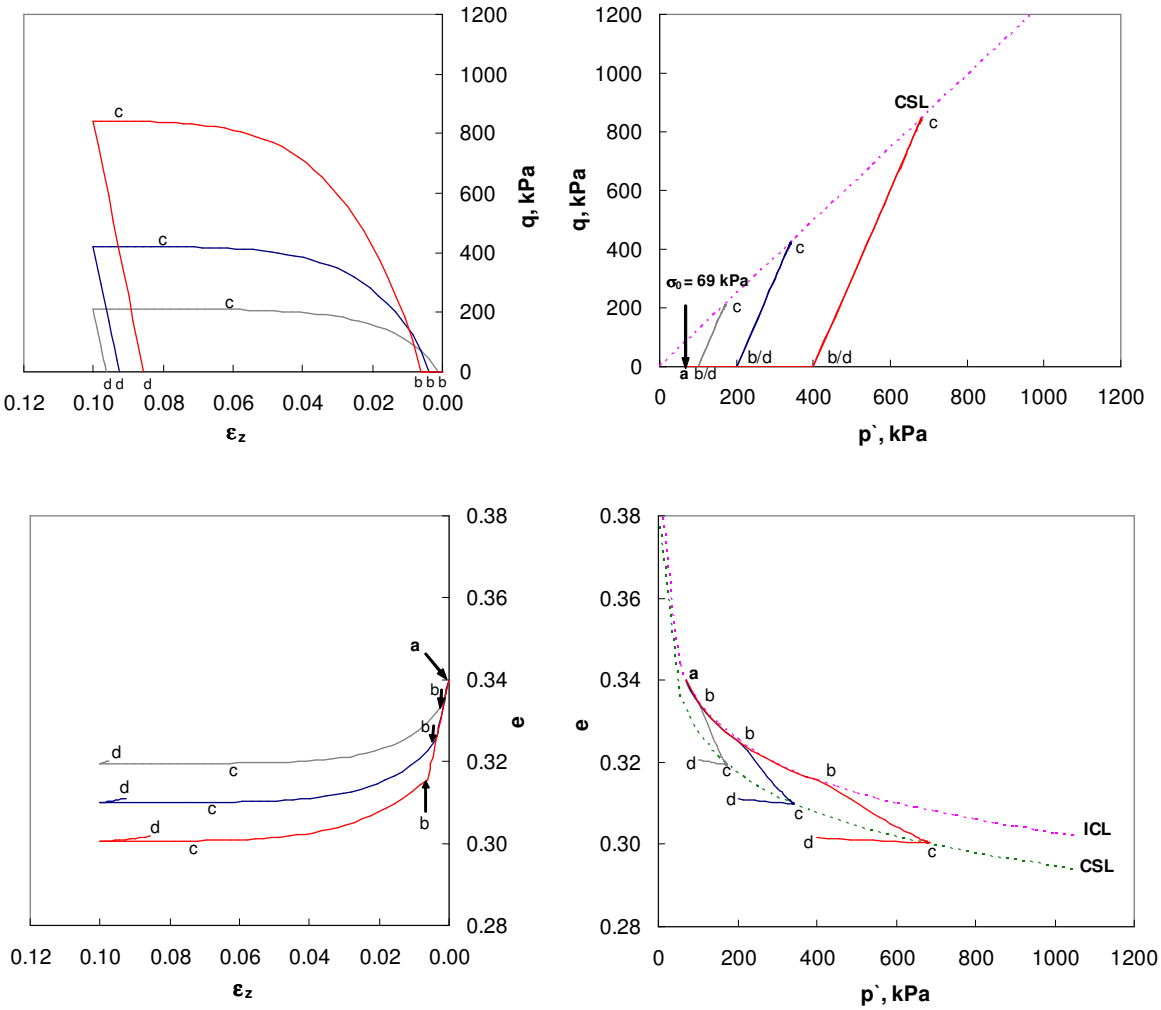

Figure 2.3 Consolidated-drained test (CID) - NC Pueblo Sand. Notation: Mean effective stress p', deviatoric stress q, void ratio e, axial strain ε_z, isotropic consolidation line ICL, and critical state line CSL. Limit ε_z = 10%.

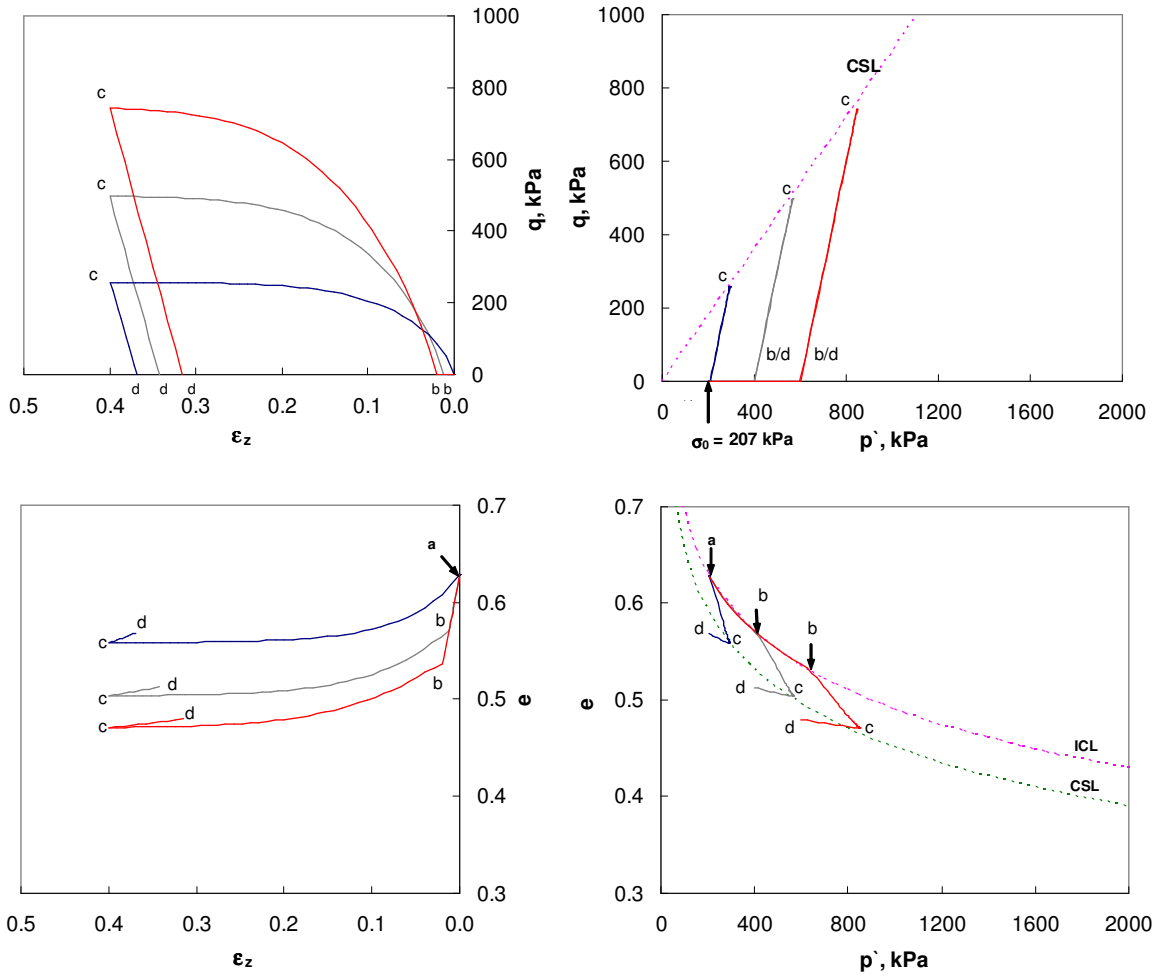

Figure 2.4 Consolidated-drained test (CID) - NC Weald clay. Notation: Mean effective stress p', deviatoric stress q, void ratio e, axial strain ε_z, isotropic consolidation line ICL, and critical state line CSL. Limit $\varepsilon_z = 40\%$.

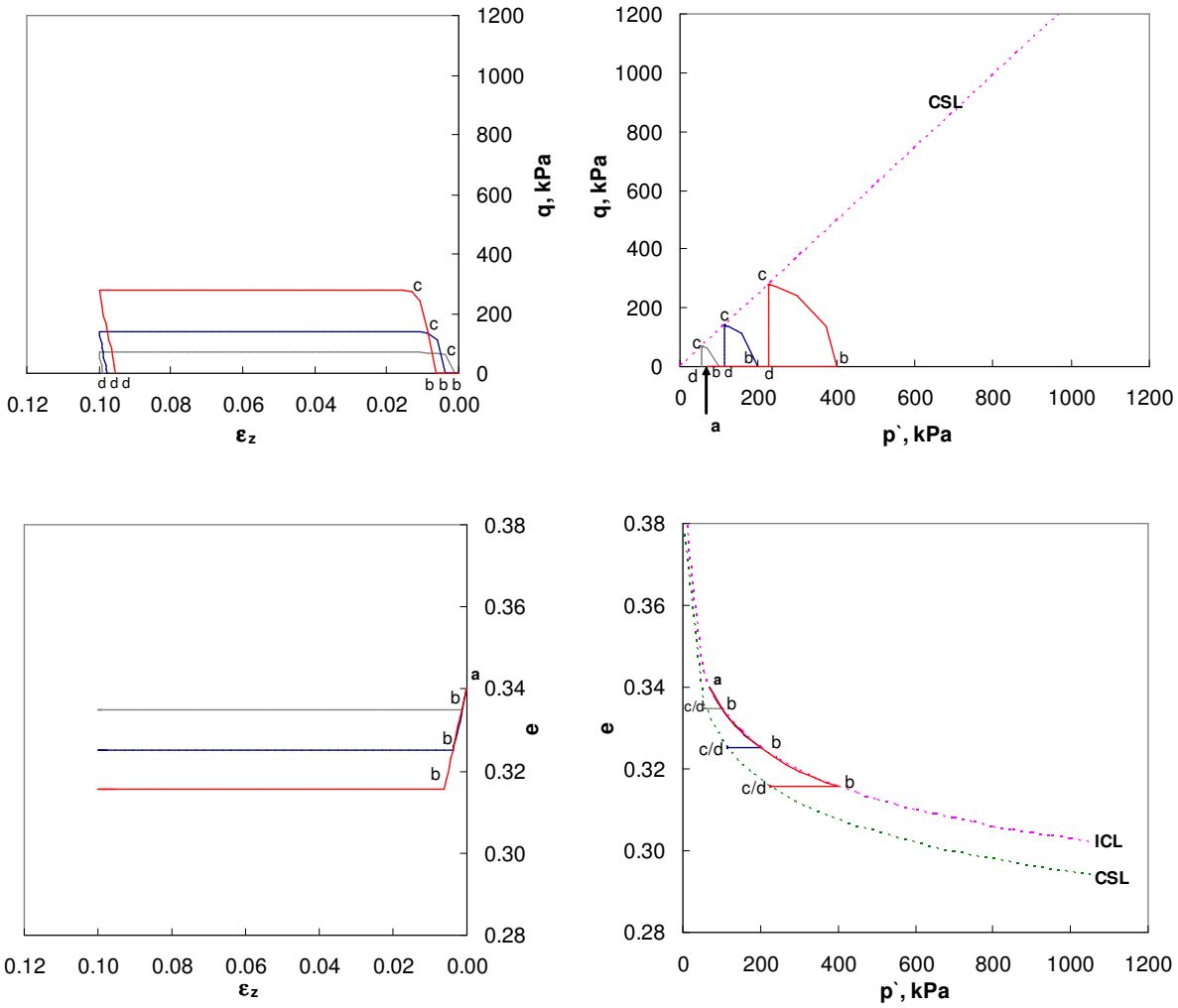

Figure 2.5 Consolidated-undrained test (CIU) - NC Pueblo sand. Notation: Mean effective stress p', deviatoric stress q, void ratio e, axial strain ε_z, isotropic consolidation line ICL, and critical state line CSL. Limit ε_z = 10%.

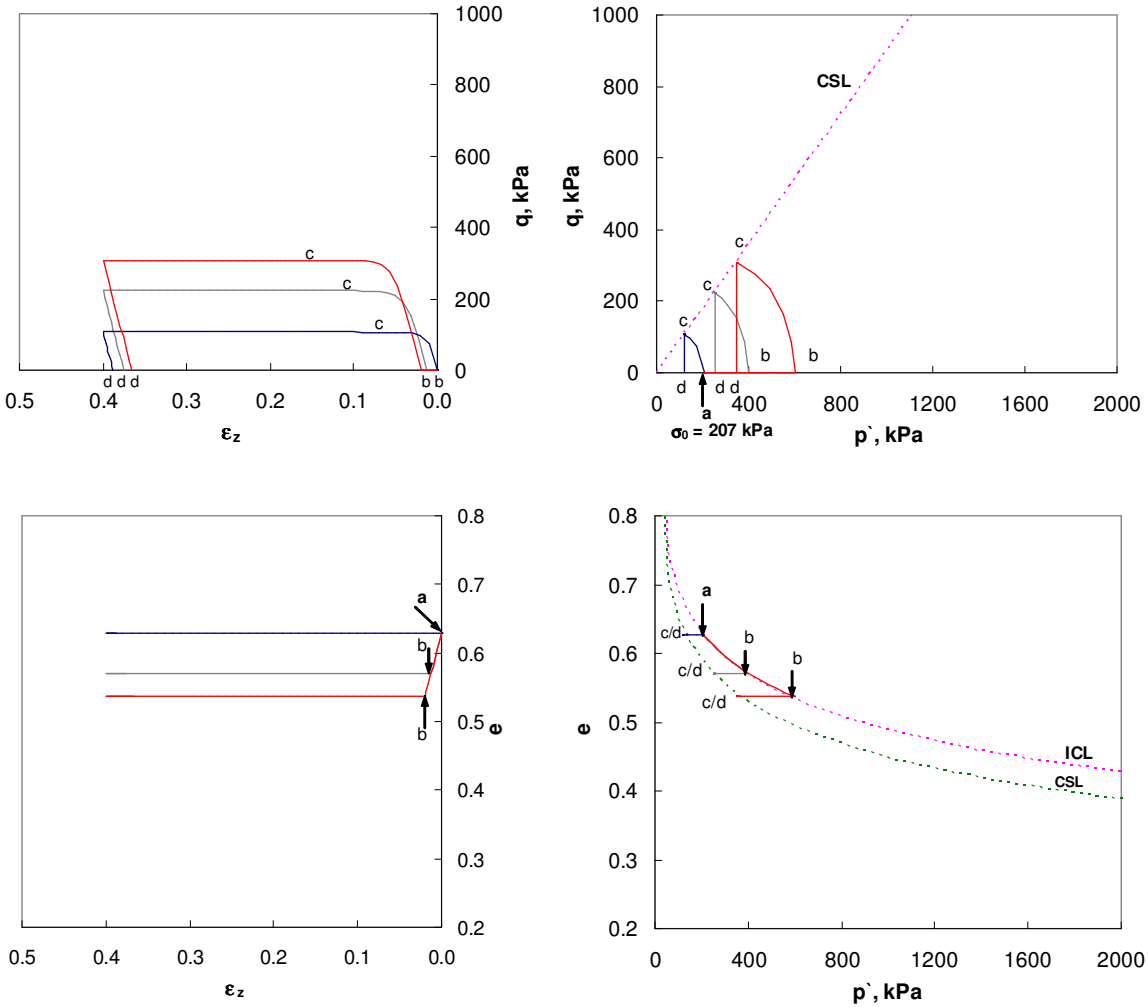

Figure 2.6 Consolidated-undrained test (CIU) - NC Weald clay. Notation: Mean effective stress p', deviatoric stress q, void ratio e, axial strain ε_z, isotropic consolidation line ICL, and critical state line CSL. Limit $\varepsilon_z = 40\%$.

2.3.4 Over Consolidated (Dilative) Soil

Results for isotropically consolidated-drained CID and isotropically consolidated–undrained CIU triaxial finite element simulations for over consolidated OC soils are shown in Figures 2.7 through 2.10. Both Pueblo sand and Weald clay are over consolidated to various stresses. For all cases, the isotropic consolidation path coincides with the ICL and the deviatoric loading brings the soil to its critical state CSL before unloading. The results are in good agreement with the typical over consolidated (dilative) trends: occurrence of peak deviatoric stress at failure for heavily consolidated soils under drained conditions that is followed by asymptotic approach to the critical state (Figures 2.7 and 2.8), and dependency of critical deviatoric stress in undrained simulations on the over consolidation ratio (Figures 2.9 and 2.10). The drained critical deviatoric stress (Figures 2.7 and 2.8) is equal to that of the normally consolidated soil at the same confining stress (Figures 2.3 and 2.4). The e-p` curve for the isotropic loading phase coincides with ICL.

The drained simulations of over consolidated soils have two distinct trends during deviatoric loading. For small OCR values, the increase in mean effective stress is associated with volume decrease until the critical state is reached. For large OCR values, volume decreases until peak deviator stress is reached (points c' in $q-\varepsilon_z$ plot) then volume increases with strain softening to the same critical deviator stress.

The undrained simulations (Figures 2.9 and 2.10) reflect the dependency of deviatoric shear stress on OCR. Deviatoric loading for large OCR values is associated with negative pore pressure, while positive pore pressure is created in low OCR specimens (e.g. OCR = 1.25). Therefore, for large OCR values the mean effective stress increases during deviatoric loading and the opposite is true for small OCR values.

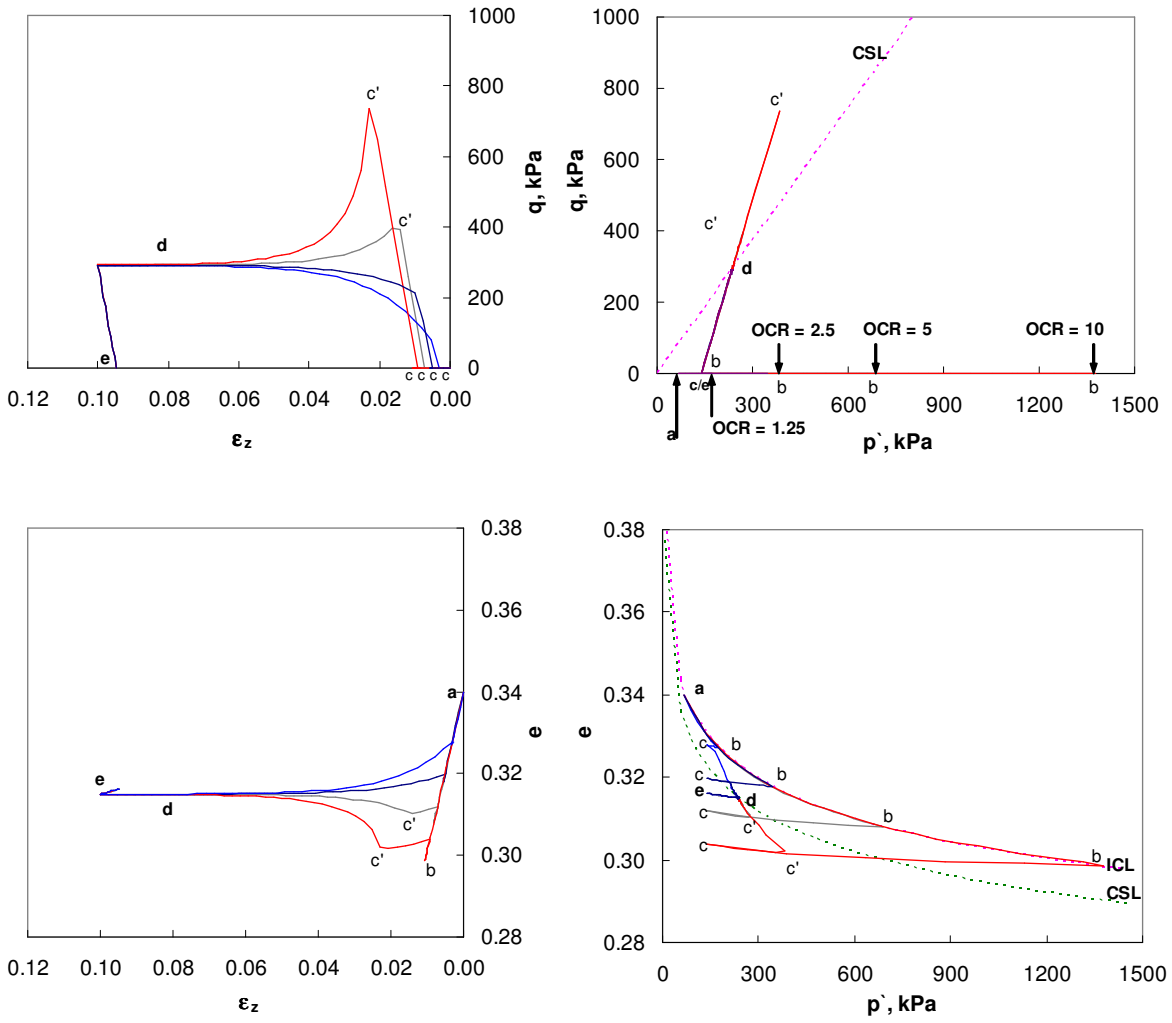

Figure 2.7 Consolidated-drained test (CID) - OC Pueblo sand. Notation: Mean effective stress p', deviatoric stress q, void ratio e, axial strain ε_z, isotropic consolidation line ICL, and critical state line CSL. Limit ε_z = 10%.

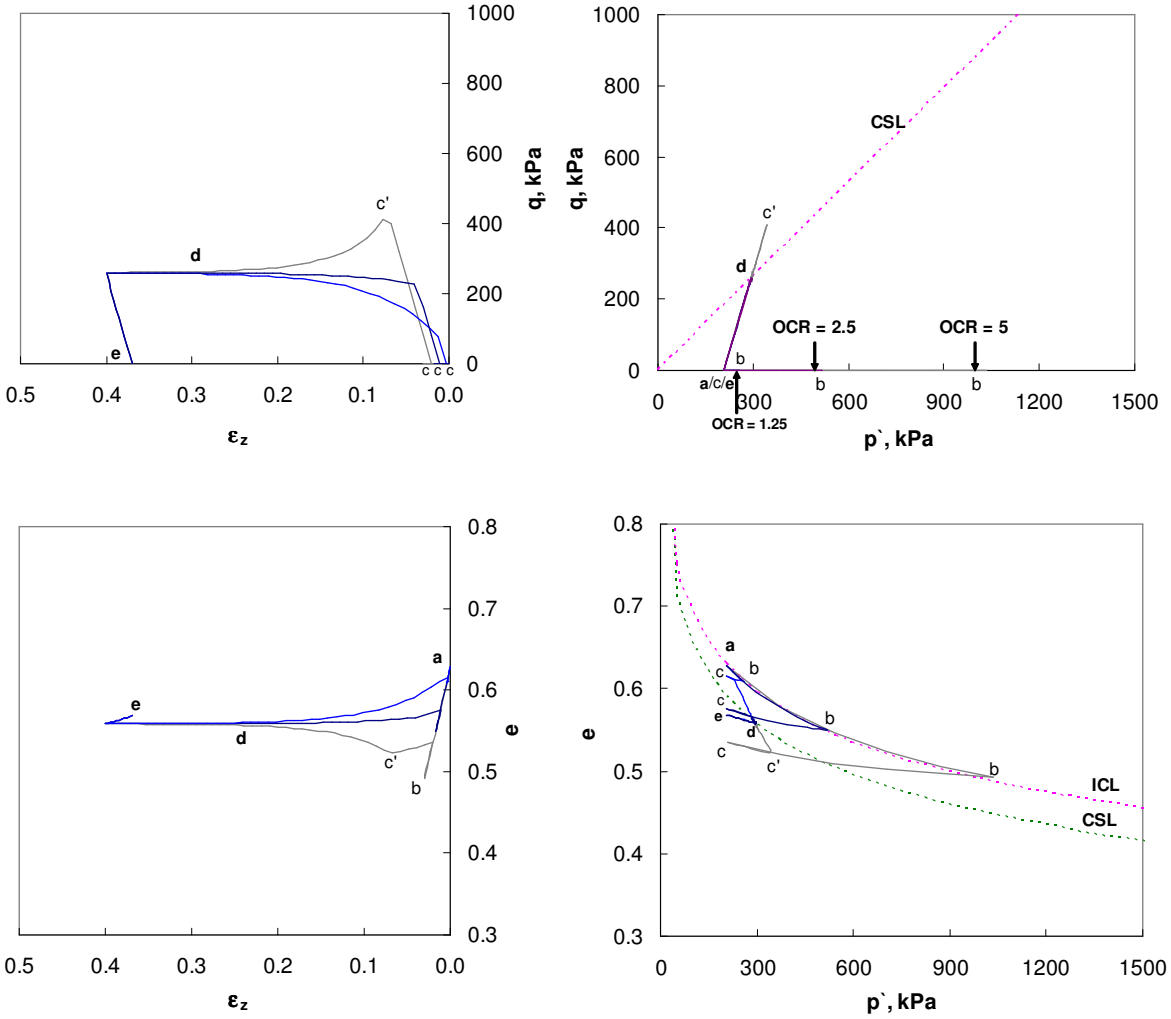

Figure 2.8 Consolidated-drained test (CID) - OC Weald clay. Notation: mean effective stress p', deviatoric stress q, void ratio e, axial strain ε_z, isotropic consolidation line ICL, and critical state line CSL. Limit $\varepsilon_z = 40\%$.

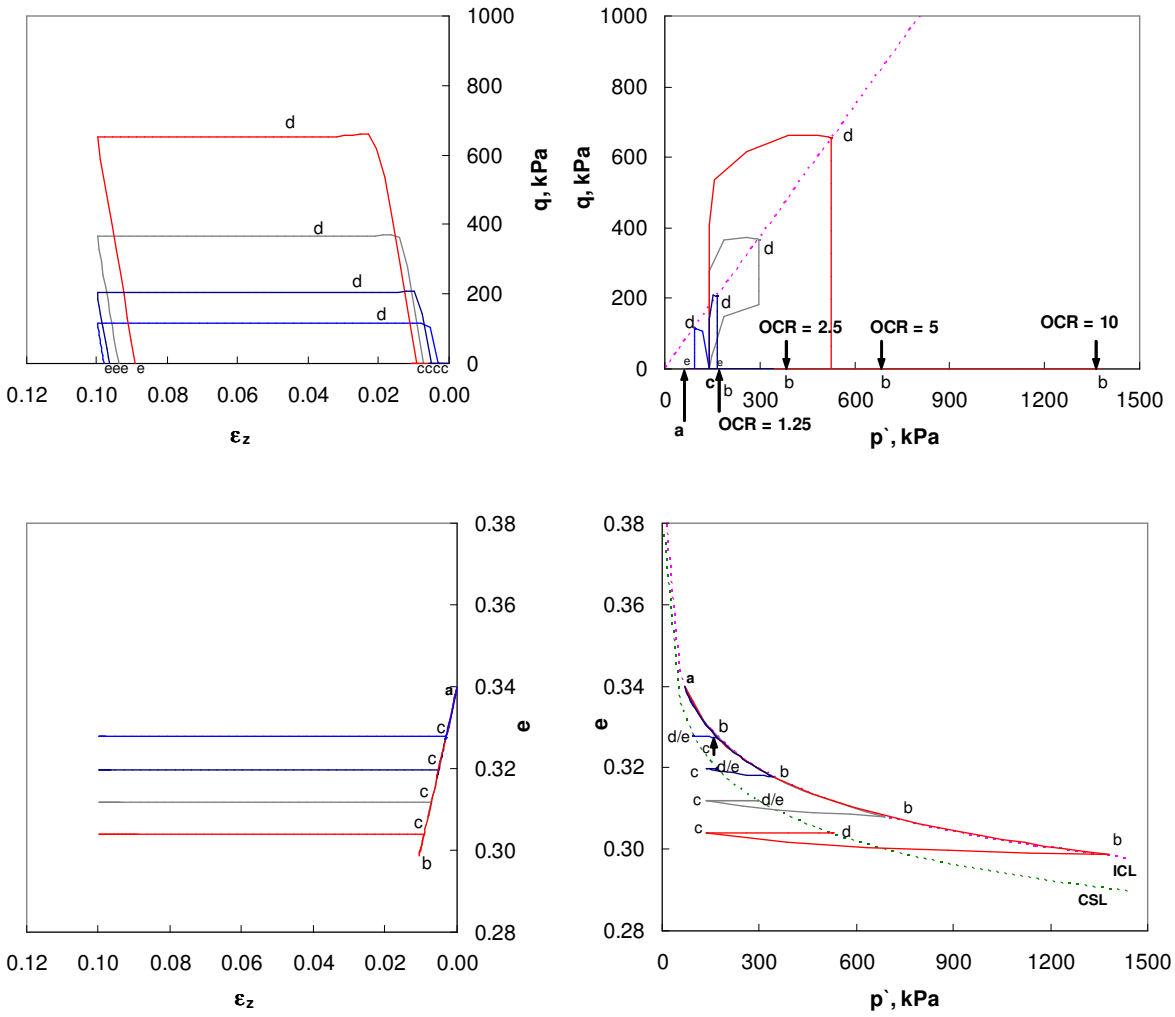

Figure 2.9 Consolidated-undrained test (CIU) - OC Pueblo sand. Notation: Mean effective stress p', deviatoric stress q, void ratio e, axial strain ε_z, isotropic consolidation line ICL, and critical state line CSL. Limit ε_z = 10%.

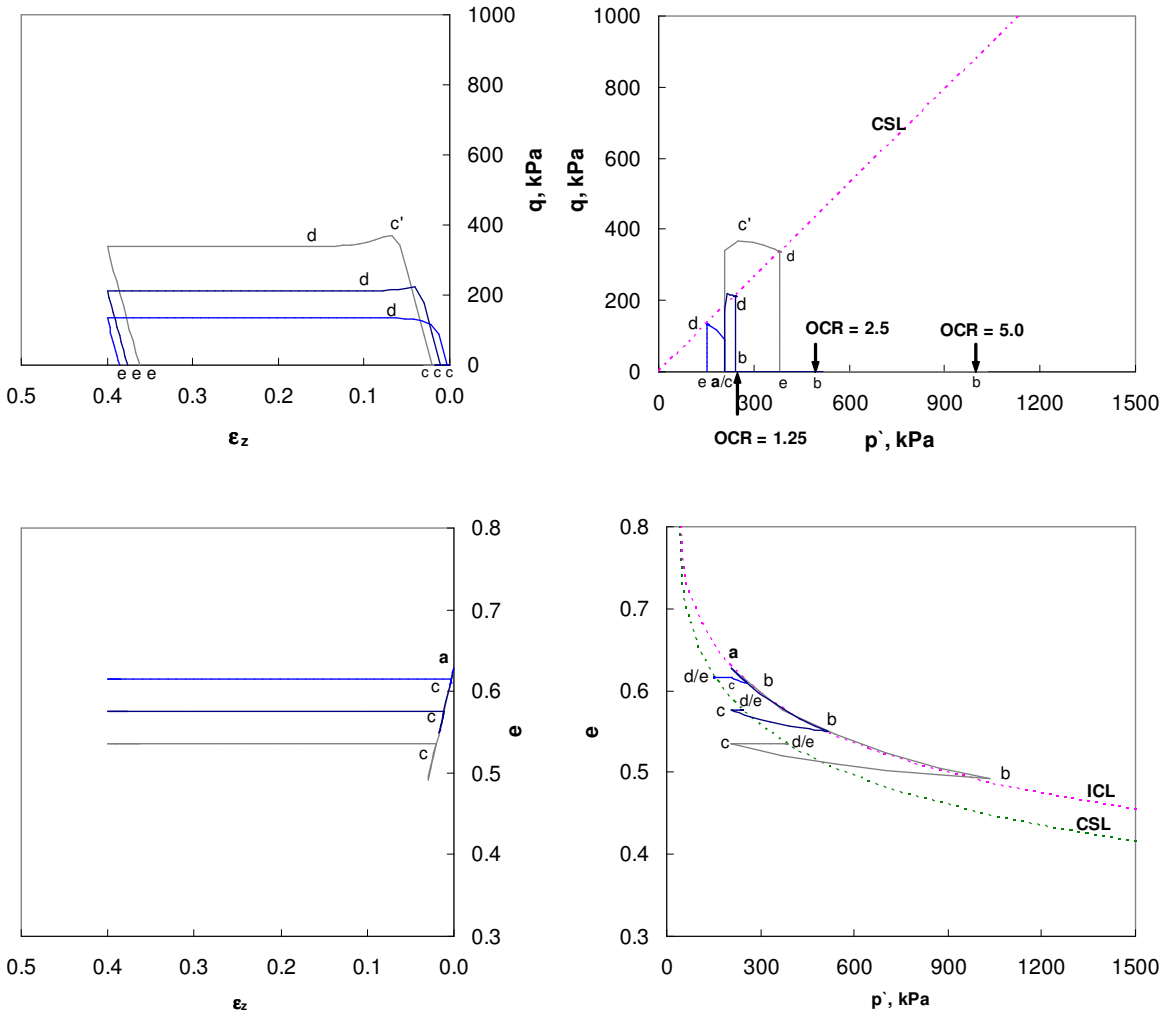

Figure 2.10 Consolidated-undrained test (CIU) - OC Weald clay. Notation: Mean effective stress p', deviatoric stress q, void ratio e, axial strain ε_z, isotropic consolidation line ICL, and critical state line CSL. Limit $\varepsilon_z = 40\%$.

2.4 FINITE ELEMENT METHOD VS. DIRECT USE OF CONSTITUTIVE EQUATIONS

One-element simulations of ideal triaxial tests are conducted using the constitutive equations of the MCC model. This assumes that boundary conditions are non-frictional in the idealized triaxial simulations. Equations 2.1 through 2.7 are

implemented in MathCAD (MathSoft, 2001) to simulate both contractive and dilative soil response under drained and undrained conditions. The isotropic consolidation line (ICL) and critical state line (CSL) are computed using Equations 2.6 and 2.8, respectively. Pueblo sand parameters are used for demonstration purposes. Appendix A includes the mathgram and the results plotted in of p`-q-e projections. Auxiliary plots, equations and points of transition in loading state are added for clarity.

For verification purposes the results of the finite element method are compared to the results of direct use of constitutive equations of Cam-Clay. Table 2.3 summarizes this comparison for the four types of simulations NC-CID, NC-CIU, OC-CID, and OC-CIU at critical state. The results show very good agreement. Discretization and numerical error may give rise to some of the very small differences shown in the table. Results for Pueblo sand are graphically compared shown in the 4D space in Figures 2.11, 2.12 and 2.13.

Table 2.3 Comparison between FEM simulations and constitutive equations (1-element) at critical state.

	NC-CID (p_0 = 100 kPa)			**NC-CIU** (p_0 = 100 kPa)			**OC-CID** (p_c = 690 kPa, OCR = 5)			**OC-CIU** (p_c = 690 kPa, OCR = 5)		
	$p`_{cs}$	q_{cs}	e_{cs}	$p`_{cs}$	q_{cs}	e_{cs}	$p`_{cs}$	q_{cs}	e_{cs}	$p`_{cs}$	q_{cs}	e_{cs}
Finite Element	170	211	0.319	56.3	69.8	0.335	235	292	0.315	296	366	0.312
Constitutive Equations	170	210	0.319	55.6	69.5	0.335	235	291	0.315	295	366	0.312

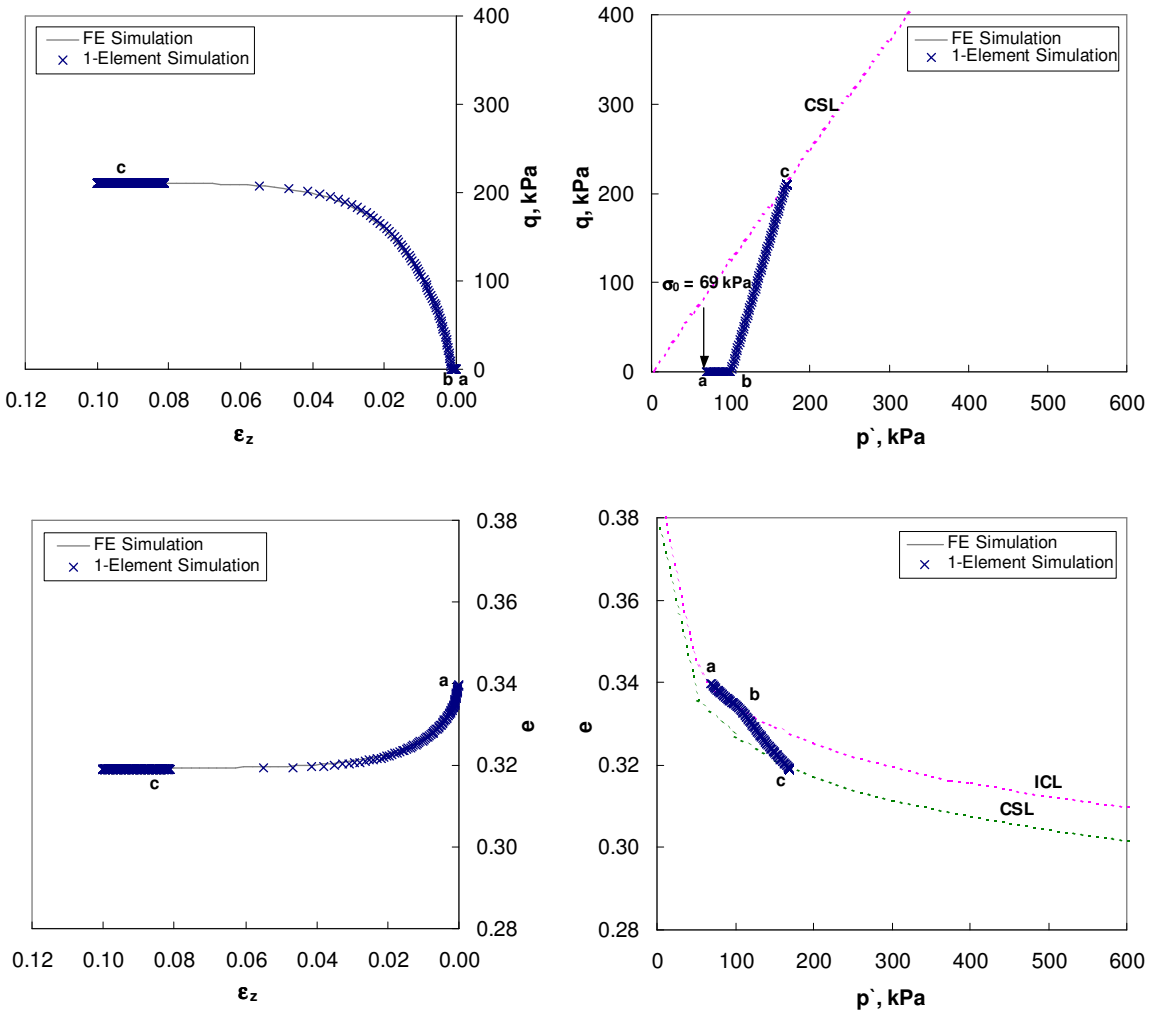

Figure 2.11 Finite element vs. 1-element simulations for consolidated-drained CID test - NC Pueblo Sand. Notation: Mean effective stress p', deviatoric stress q, void ratio e, axial strain ε_z, isotropic consolidation line ICL, and critical state line CSL. Limit ε_z = 10%.

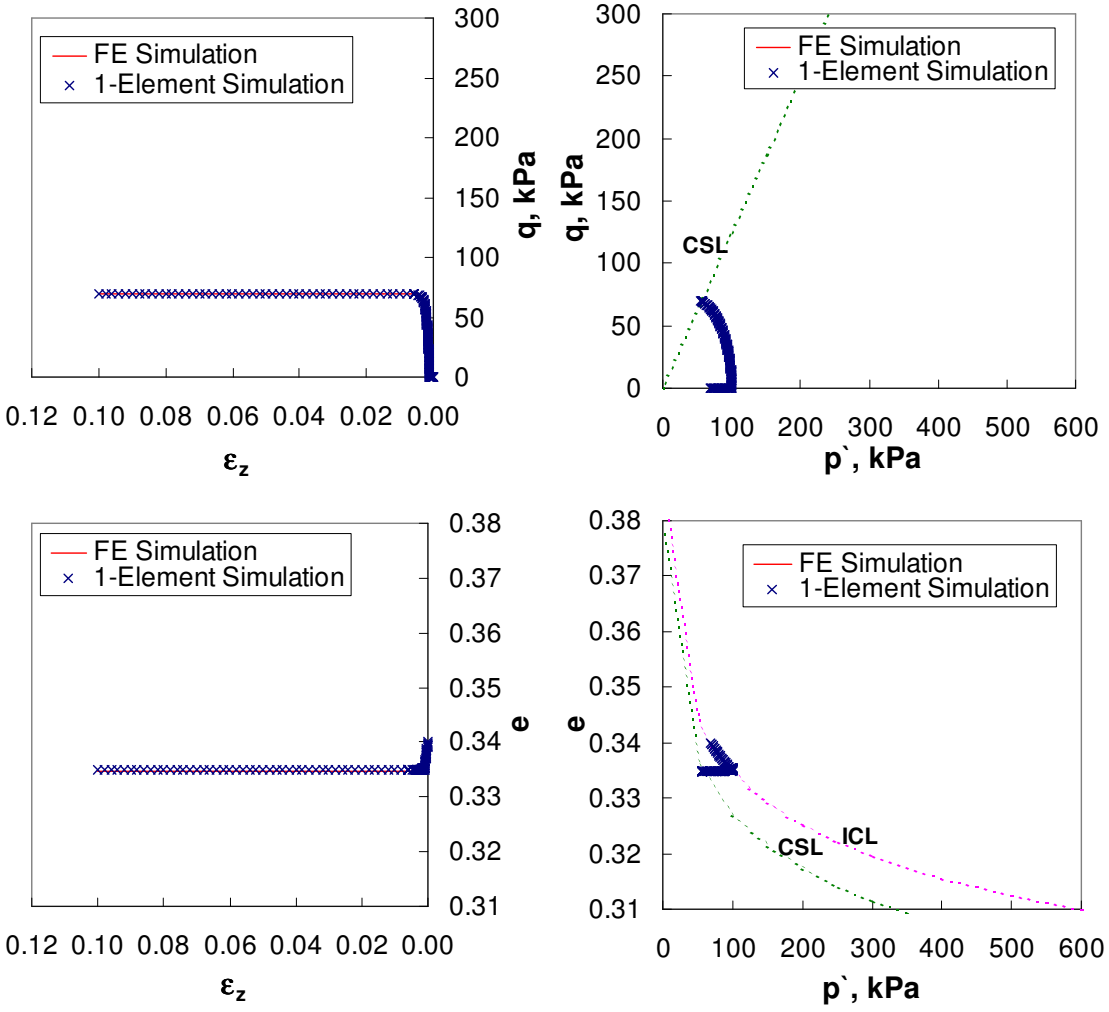

Figure 2.12 Finite element vs. 1-element simulations for consolidated-drained CIU test - NC Pueblo Sand. Notation: Mean effective stress p', deviatoric stress q, void ratio e, axial strain ε_z, isotropic consolidation line ICL, and critical state line CSL. Limit ε_z = 10%.

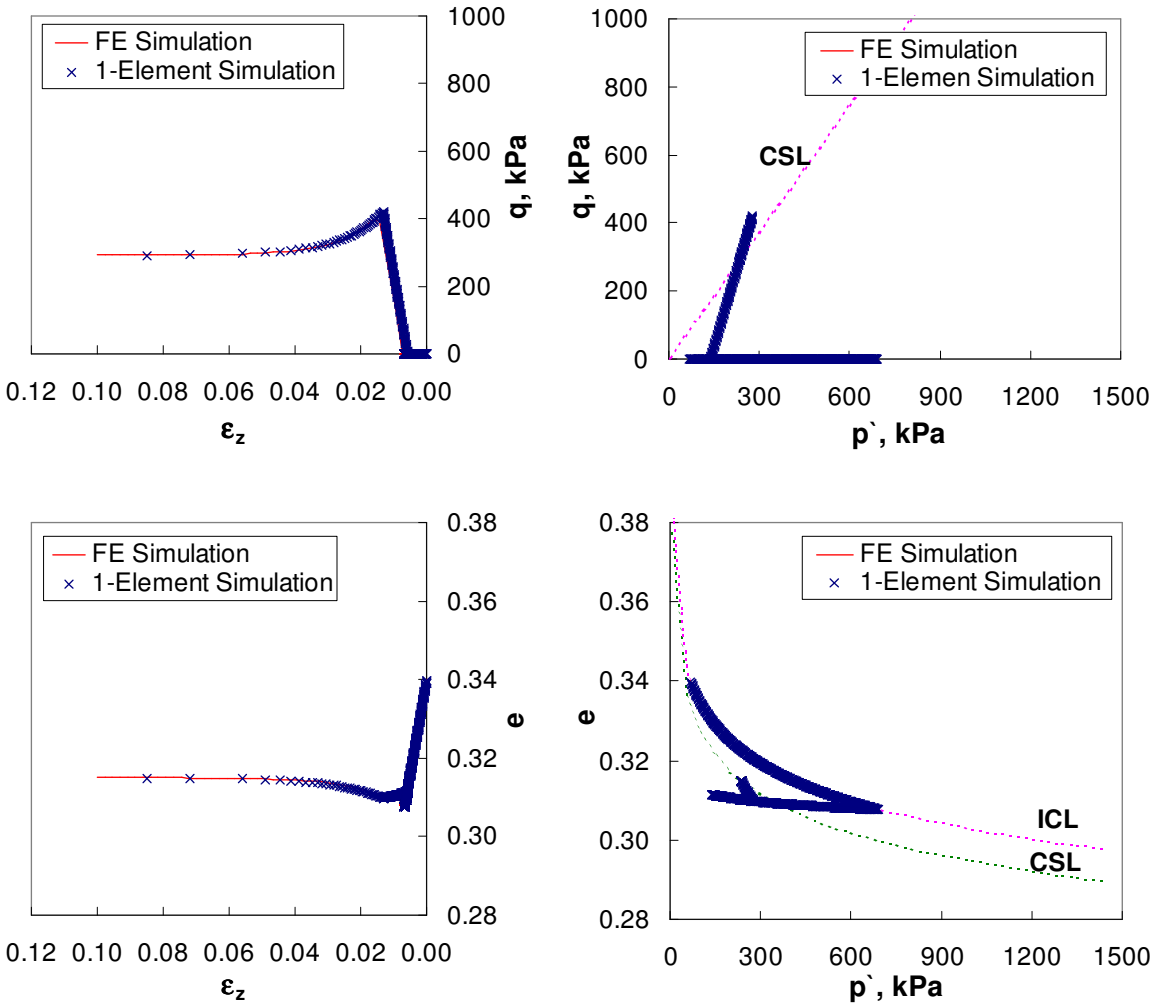

Figure 2.13 Finite element vs. 1-element simulations for consolidated-drained CID test - OC Pueblo Sand. Notation: Mean effective stress p', deviatoric stress q, void ratio e, axial strain ε_z, isotropic consolidation line ICL, and critical state line CSL. Limit ε_z = 10%.

2.5 LIMITATIONS OF THE MODIFIED CAM-CLAY MODEL - DEVELOPMENTS

The main limitations in the original and modified Cam-Clay models include: the failure stresses are over-estimated for dilative specimens, the associated flow rule over-estimates dilatancy for granular soils, the model does not account for the

anisotropic behavior and viscous effects in soils (Gens and Potts, 1988, Lade, 2002, Lade, 2005, Wood and Graham, 1990).

There have been many attempts to account for the factors not considered in the MCCM model or to modify its features to better predict soil behavior. However, all these changes have brought added complexity to the model. Table 2.4 summarizes some of these modifications and the researchers involved.

Table 2.4. Some Cam-Clay model modifications.

Model	Change/Contribution	Yield Surface	Author
Original Cam-Clay (OCCM)	Introduced critical state concept to constitutive modeling	Bullet-shaped	Schofield and Wroth (1968)
Modified Cam-Clay (MCCM)	Eliminate singularity created by bullet-shaped yield surface of OCCM	Elliptical cap	Roscoe and Burland (1968)
Nor-Sand	Undrained cyclic loading	Bullet-shaped	Jefferies (1993)
MIT-E3	Anisotropy Non-associated flow rule	Rotated, elliptical cap	Whittle (1993) Ganendra and Potts (1995)
Anisotropic Plasticity	Anisotropy	Distorted ellipse	Defalias et al. (2003)
	Physico-chemical behavior of fine-grained soils, double layer integration in MCCM	Elliptical cap	Murthy et al. (1988 and 1991) Robinet et al. (1999)
	Time dependency - Elasto-viscoplastic	Elliptical cap	Yin and Graham (1999)

2.6 CONCLUSIONS

The Modified Cam Clay model is a simple and robust model for soil behavior. With very few parameters, the Modified Cam Clay model is capable of modeling soil tests with acceptable success through relatively simple forward simulations. More advanced Cam-Clay model versions provide more versatility, however the large number of parameters hinder the inversion process and uniqueness. The results of the finite element simulations closely match the analytical solution using the constitutive equations of the Modified Cam-Clay model, i.e., the 1-element simulation.

CHAPTER III

MODEL CALIBRATION AS AN INVERSE PROBLEM

Model calibration using experimental data is an inverse problem. This chapter discusses the selection of error, error function and inversion techniques needed for model calibration.

3.1 INTRODUCTION TO INVERSE PROBLEM SOLVING

A mathematical model always deviates from the true physical reality. This deviation is referred to as 'error'. Several error functions or norms are used to assess the distance between the model and reality.

Assume a function f to approximate measured values $f_i^{<m>}$ (Figure 3.1). The error between predicted $f_i^{<p>}$ and measured $f_i^{<m>}$ values for the ith measurement can be expressed in several forms:

$$e_i = f_i^{<m>} - f_i^{<p>} \tag{3.1}$$

$$e_i = logf_i^{<m>} - logf_i^{<p>} \tag{3.2}$$

$$e_i = \frac{f_i^{<m>} - f_i^{<p>}}{f_i^{<p>}} \tag{3.3}$$

The most common norms are the sum of absolute errors L_1, the sum of squared errors L_2, and the maximum error L_∞.

$$L_1 = \sum_{i=1}^{N} |e_i| \qquad \text{Sum of absolute errors} \qquad (3.4)$$

$$L_2 = \sqrt{\sum_{i=1}^{N} |e_i|^2} \qquad \text{Sum of squared errors} \qquad (3.5)$$

$$L_\infty = \max\left(|e_1|,...|e_i|,...,|e_N|\right) \qquad \text{Maximum error} \qquad (3.6)$$

Once an error and a norm are selected, inverse problem solving attempts to find the parameters in f by minimizing the norm, so that the selected function or model justifies the data best.

The selection of error and error norm affects the inversion. The sum of absolute errors L_1 suggests equal error weights for all readings. Therefore L_1 is the least sensitive norm to large errors. On the other hand, the maximum error L_∞ only considers the measurement with maximum error; hence, L_∞ is very sensitive to large errors and even one outlier could be detrimental to the quality of the solution (Santamarina and Fratta, 1998). The maximum error L_∞ is insensitive to the spatial distribution of the data. On the other hand, the L_2 norm is most adequate for common linear-Gaussian problems (Santamarina and Fratta, 1998). The least-square inversion method implies deriving the solution to minimize L_2.

The success of an inversion is highly dependent on the quality of data and on the adequacy of the presumed model. Ill conditioning and non-uniqueness are exacerbated when the number of unknowns (i.e., model parameters) is high. The principle of Ockham's razor reads: "Plurality must not be posited without necessity" (Jefferys and

Berger, 1992). In the context of model calibration, this principle encourages us to favor simple models.

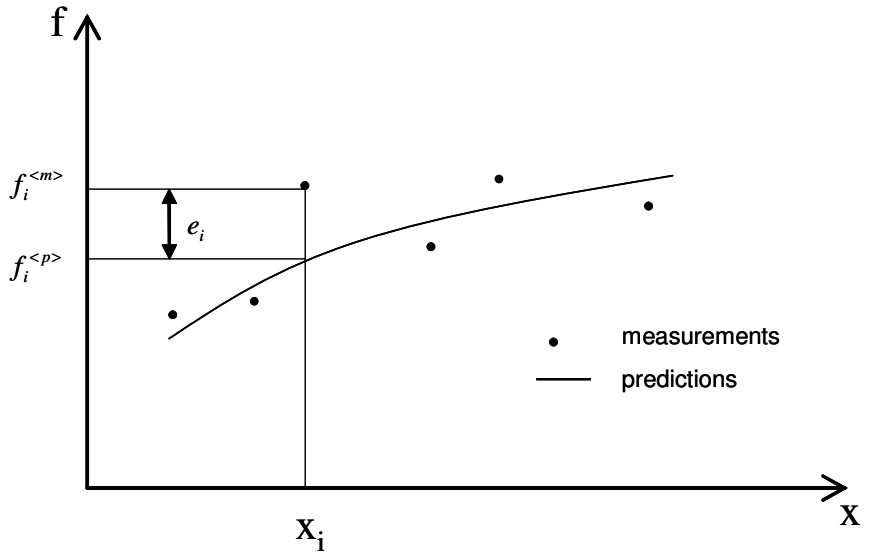

Figure 3.1 Definition of error.

3.2 OPTIMIZATION AND SEARCH ALGORITHMS

The error norm defines a surface in the N+1 space of the N unknown model parameters. The goal is to identify the values of the N model parameters that minimize the error. The steepest descent technique (Cauchy's method) is the simplest of the gradient methods. It involves two components for each dimension: the gradient direction toward the minimum and the gradient or the steepness. The search starts at an arbitrary point x_n. A jump is made in the direction of the steepest descent. Therefore, every update step is perpendicular to the previous step. A graphical representation of the steepest descent method is shown in Figure 3.2. The method may face slow convergence (small variable changes), divergence (excessive variable change), oscillation close to the minimum, and entrapment in local minima.

The Gauss-Newton method is a special case of the more general Newton-Raphson method (Bates and Watts, 1988). The Gauss-Newton method is an iterative procedure, which requires an initial guess for the unknowns. The objective is to minimize the least squares criterion or the objective function (Levenberg, 1944; Marquardt, 1963). Subsequent guess of unknowns targets minimize the residual. This method does not guarantee convergence. However, quick convergence is achieved if the initial guess is close to a local minimum.

Levenberg (1944) introduced an extension of Newton's methods to incorporate damping and weighing factors that increase the principal diagonal of the minimized residuals matrix. The damping factor (ω) is a positive quantity that defines the relative importance of the residuals and increments in the minimization process. The weighing factors (a, b, and c) express the relative importance of damping the different increments (Levenberg, 1944). The method may be termed the method of damped least squares.

The Levenberg-Marquardt method is a combined approach that encompasses the best features of both the Levenberg method and the steepest descent method (Marquardt, 1963). The Levenberg-Marquardt is considered a popular alternative to Newton's methods (Gill et. al, 1981). The steepest-descent method consistently seeks the direction of the minimum, but as the solution progresses, convergence occurs more slowly. Therefore, the steepest descent can be combined with the Levenberg method so that the steepest descent begins the search and proceeds towards a 'trust region'

within which the Levenberg method takes over to guide the search towards the optimum solution. In the Levenberg-Marquardt algorithm the direction and step size are determined simultaneously (Marquardt, 1963).

Monte Carlo simulation is centered around the concept of finding a statistical estimate of a function by randomly varying a variable or several variables (Sobol, 1974). The maximum likelihood approach centers on maximizing the probably density function (PDF) of the parameters used to estimate a quantity or a set of quantities (Ledesma et al., 1996a). These are the most likely parameters. Finally, the Bayesian approach maximizes the probability density function of the unknown parameters using some measured or existing data (Ledesma et al., 1996a; Ledesma et al., 1996b).

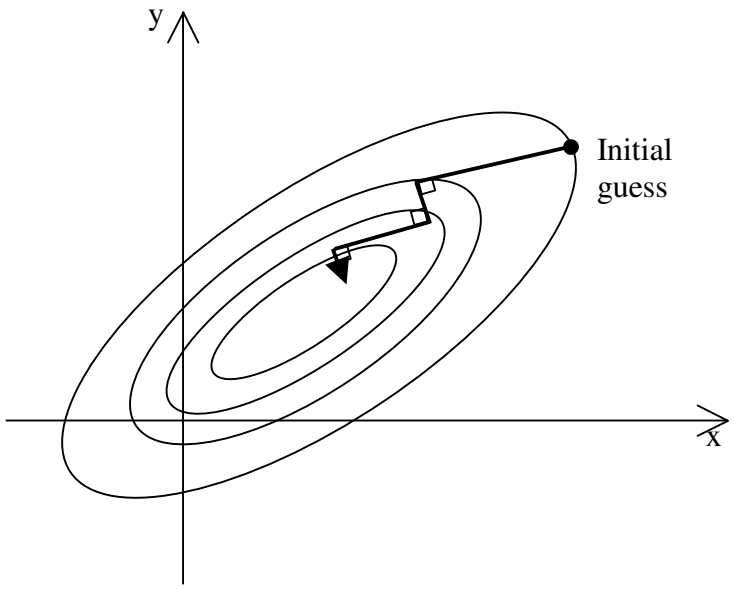

Figure 3.2 Graphical representation of the steepest descent method (from Tarantola, 1987).

3.3 INVERSE PROBLEMS IN GEOTECHNICAL ENGINEERING

Geotechnical testing, characterization, design and construction can be improved within the framework of inverse problems by coupling inverse techniques with measurements and forward numerical simulation. Examples include underground excavation (maximum likelihood approach, Ledesma et al., 1996a, Ledesma et al., 1996b, and Bayesian approach, Honjo et al., 1994), and slope stability (least-square approach Feng et al., 2004). The three approaches have proven suitable for geotechnical applications (Ledesma et al., 1996a; Ledesma et al., 1996b).

3.4 DESIGN OF AN EXPERIMENT

Most of the current, conventional tests in geomechanics provide global information, gathered by imposing uniform boundary conditions and using very few sensors. The design of an experiment must explicitly recognize the needed model information to reduce the cost of data collection and processing (Curtis, 2004). The field of statistical experimental design (SDE) provides a proper mathematical framework to analyze optimal test sequences with minimal redundancy.

6.1.1 Design of an Experiment Guided by Inverse Problem Solving

The design of an experiment is in many instances guided by the ease with which measurements can be made (Curtis, 2004). However, such casual approaches do not necessarily lead to a set of data that is suitable for readily solving the inverse problem. Several factors and precautions must be considered for proper experiment design. The

following summarizes a framework for a robust solution of inverse problems (Santamarina and Fratta, 1998, see also Curtis, 2004):

1. Proper understanding of the physics of the experiment
2. Proper experimental design: including high quality data acquisition and adequate coverage of measurements
3. High-quality data (including complementary measurements)
4. Pre-processing of data to filter out blunders and erroneous measurements
5. A proper physical model that closely captures the relationship between the measurements and model parameters
6. Alternative inversion techniques
7. Analysis and evaluation of final solution

3.5 A STUDY OF ERROR SURFACES

The error norm defines an N+1 dimensional error surface in terms of the N model parameters. The study of error surfaces is facilitated by cutting 2D slices and provides important information for experimental design and about the invertability of model parameters.

In this section 2D slices of the error surfaces for Pueblo sand and Weald clay are presented for typical triaxial values (i.e., mean effective stress p`, deviatoric stress q, void ratio e, axial strain ε_z, and pore pressure u). The error is numerically generated by perturbing each of the Cam-Clay model parameters (λ, κ, M, e_0, G) from the correct values. The objectives of this study are to investigate the possible occurrence of non-

convexity in error surfaces to determine the most error-contributing material parameters, and to explore invertability for various soil conditions (normally consolidated vs. over consolidated) and triaxial test conditions (consolidated-drained vs. consolidated-undrained).

3.5.1 Ranges of Material Parameters

A wide range of material parameters is explored to assess convergence conditions. Tables 3.1 and 3.2 show the parameter space explored for Pueblo Sand and Weald Clay, respectively.

Table 3.1 Investigated range of Cam-Clay parameters for Pueblo Sand.

λ	0.005	0.075	0.01	**0.014***	0.02	0.025	0.03
κ	0.001	0.0015	0.002	**0.0024***	0.004	0.007	0.01
M	1.0	1.1	1.2	**1.24***	1.3	1.35	1.4
e_0	0.25	0.27	0.3	**0.34*#**	0.4	0.5	0.6
G (MPa)	2	5	10	**20**	40	60	100

* correct material parameters
# initial void ratio at a confining stress of 69 kPa

Table 3.2 Investigated range of Cam-Clay parameters for Weald Clay.

λ	0.04	0.06	0.07	**0.088***	0.1	0.2	0.4
κ	0.005	0.01	0.02	**0.031***	0.04	0.05	0.08
M	0.7	0.75	0.8	**0.882***	1.0	1.1	1.2
e_0	0.3	0.4	0.5	**0.628*#**	0.7	0.8	0.9
G (MPa)	0.3	0.6	1	**3**	5	15	30

* correct material parameters
# initial void ratio at a confining stress of 207 kPa

3.5.2 Implementation

A frictionless boundary triaxial test is simulated in this study. An axi-symmetric slice of the cylindrical specimen suffices. A mesh comprised of 192 eight-node quadrilateral elements and 633 nodes is modeled using finite elements (ABAQUS, 2005). Geometry, boundary conditions, loading and mesh are shown in Figure 3.3.

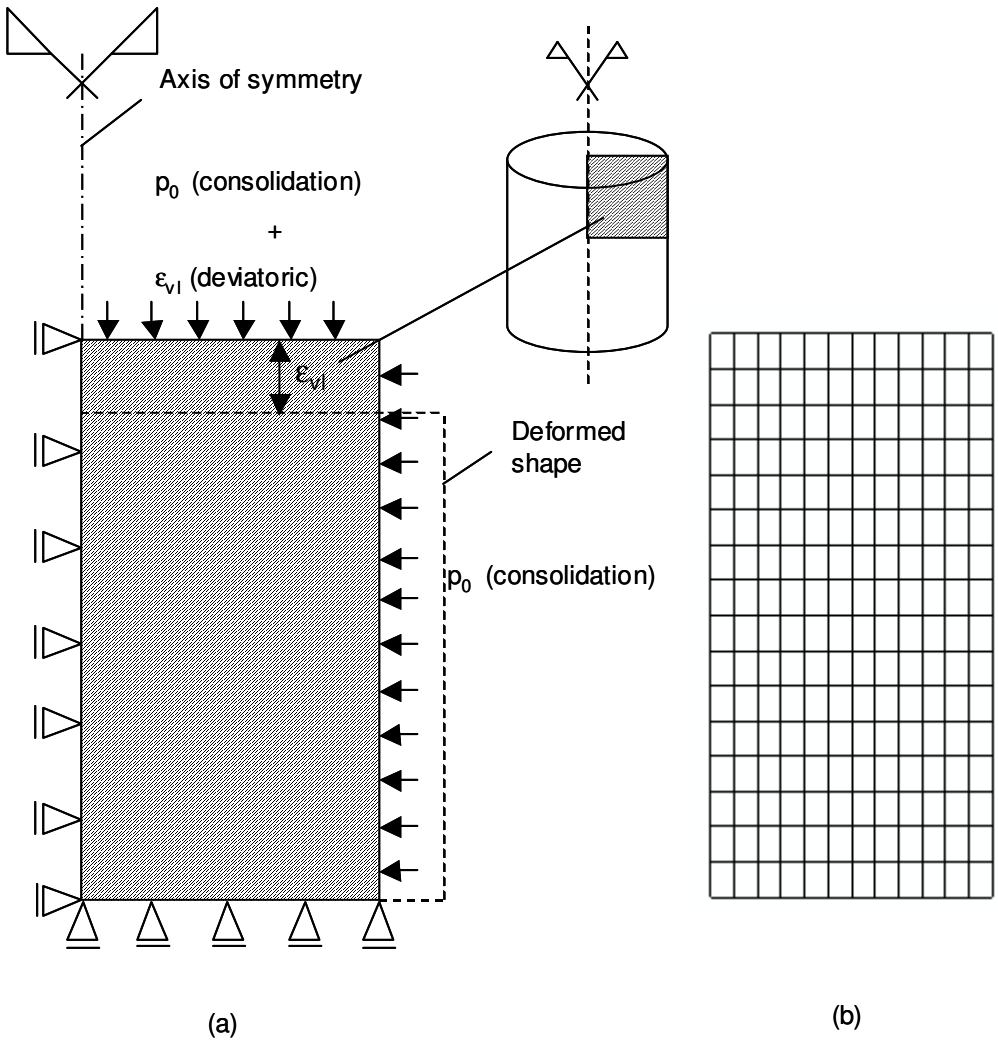

Figure 3.3 Triaxial test simulation. (a) Geometry, boundary conditions, and loading. (b) Finite element mesh. Notation: Confining stress p_0, and vertical applied displacement δ_{vl}.

3.5.3 Stress Paths for Drained and Undrained Triaxial Compression Tests

The deviatoric phase is applied under strain-controlled conditions at constant confining stress. The different cases and stress paths for Pueblo sand and Weald clay are summarized in Table 3.3.

Table 3.3 Stress paths for triaxial simulations

Pueblo Sand

Stage / Cases	1	2	3	4
	Iso-consolidation	Iso-unloading	Deviatoric (ε_z)	Unloading
NC - CID	100 kPa	-	10%	100 kPa
NC - CIU	200 kPa	-	10%	200 kPa
OC – CID (OCR=2.5)	345 kPa	138 kPa	10%	138 kPa
OC – CIU (OCR=2.5)	345 kPa	138 kPa	10%	138 kPa

Weald Clay

Stage / Cases	1	2	3	4
	Iso-consolidation	Iso-unloading	Deviatoric (ε_z)	Unloading
NC - CID	400 kPa	-	40%	400 kPa
NC - CIU	400 kPa	-	40%	400 kPa
OC – CID (OCR=2.0)	400 kPa	200 kPa	40%	200 kPa
OC – CIU (OCR=2.0)	400 kPa	200 kPa	40%	200 kPa

In this study, measurements refer to data or values gathered during a test, while parameters refer to constitutive model constants. The correct measurements, mc, are generated first using the correct model parameters. The erroneous measurements, m, are calculated by perturbing model parameters one at the time while all others remain at their "correct value". The normalized error for any measurement, m, at the i^{th} test increment is

$$e_i = \frac{m_i - mc_i}{mc_i} \tag{3.7}$$

The normalized error is non-dimensional which allows using a single total error by adding errors in all measurements. Therefore, the total L2-norm is the sum of L2 for all of the measurements: p', q, e, and ε_z for drained tests or p', q, e, ε_z, and u for undrained tests. In mathematical terms, if there are k measured parameters at n test increments, the total L2-norm:

$$L2\,(total) = \sum_{j}^{j=k}\left[\sum_{i}^{i=n}\left(\frac{m_i - mc_i}{mc_i}\right)^2\right]_j \tag{3.8}$$

The total L2-norm for the idealized triaxial simulation can be expressed as follows:

$$L2(total) = \sqrt{\sum_{i}^{n}\left(\frac{p_i^g - p_i^c}{p_i^c}\right)^2 + \sum_{i}^{n}\left(\frac{q_i^g - q_i^c}{q_i^c}\right)^2 + \sum_{i}^{n}\left(\frac{e_i^g - e_i^c}{e_i^c}\right)^2 + \sum_{i}^{n}\left(\frac{\varepsilon_{zi}^g - \varepsilon_{zi}^c}{\varepsilon_{zi}^c}\right)^2 + \sum_{i}^{n}\left(\frac{u_i^g - u_i^c}{u_i^c}\right)^2} \tag{3.9}$$

where superscripts c and g denote correct and predicted measurements, respectively. Note that the magnitude of the total L2-norm is dependent on the number of increments, number of measurements, and mesh density (for non-idealized boundary conditions).

The total error (L2-norm) for Pueblo sand and Weald clay is depicted in Figures 3.4 and 3.5, respectively. All critical state parameters are plotted in arithmetic scale except for the G parameter which is in logarithmic scale. Error curves are plotted for normally consolidated and over consolidated cases, and drained and undrained conditions. The following observations can be made:

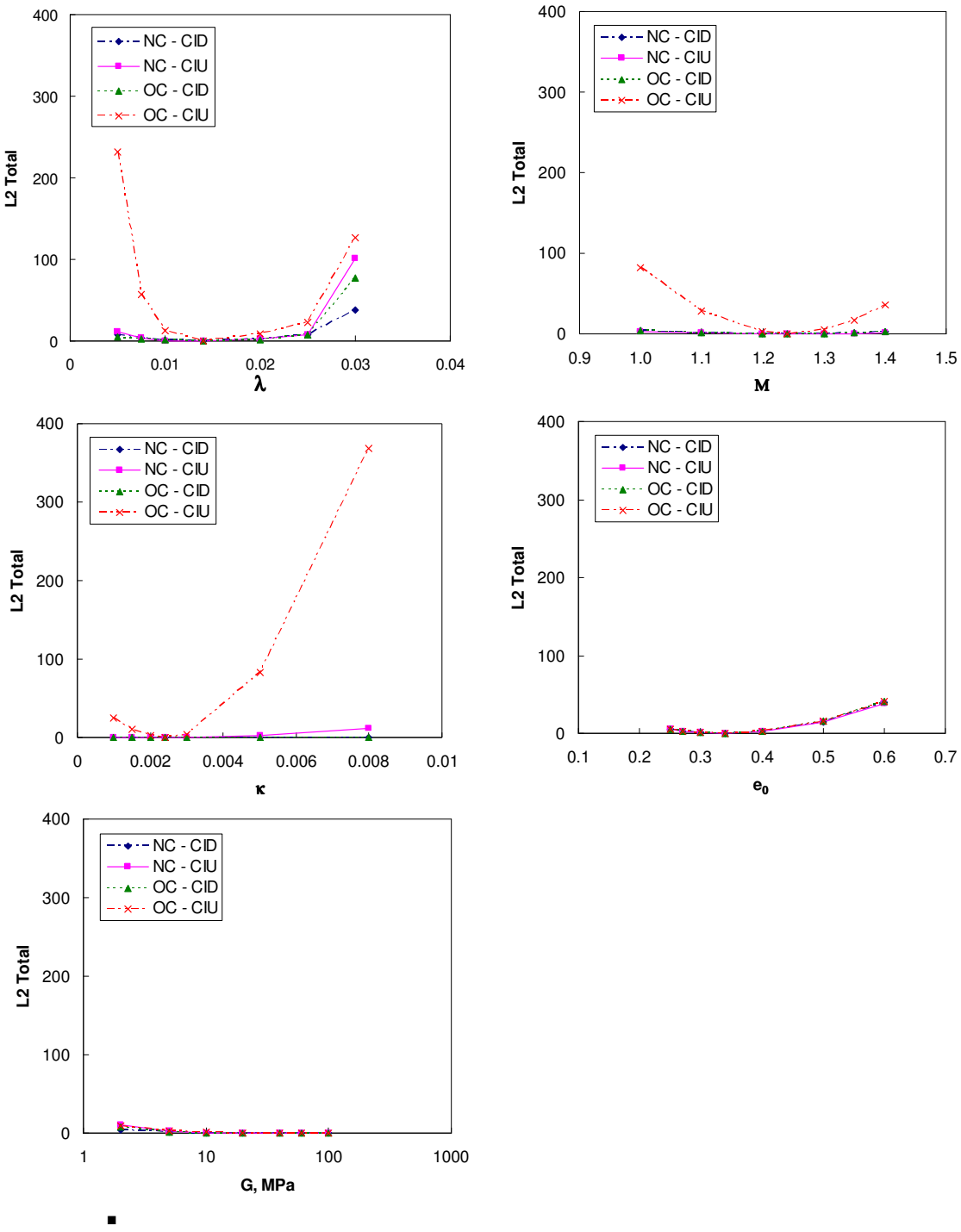

Figure 3.4 Error surfaces for Pueblo sand. Notation: Total error L2 total, consolidated-drained test CID, consolidated-undrained test CIU, normally consolidated NC, and over consolidated OC.

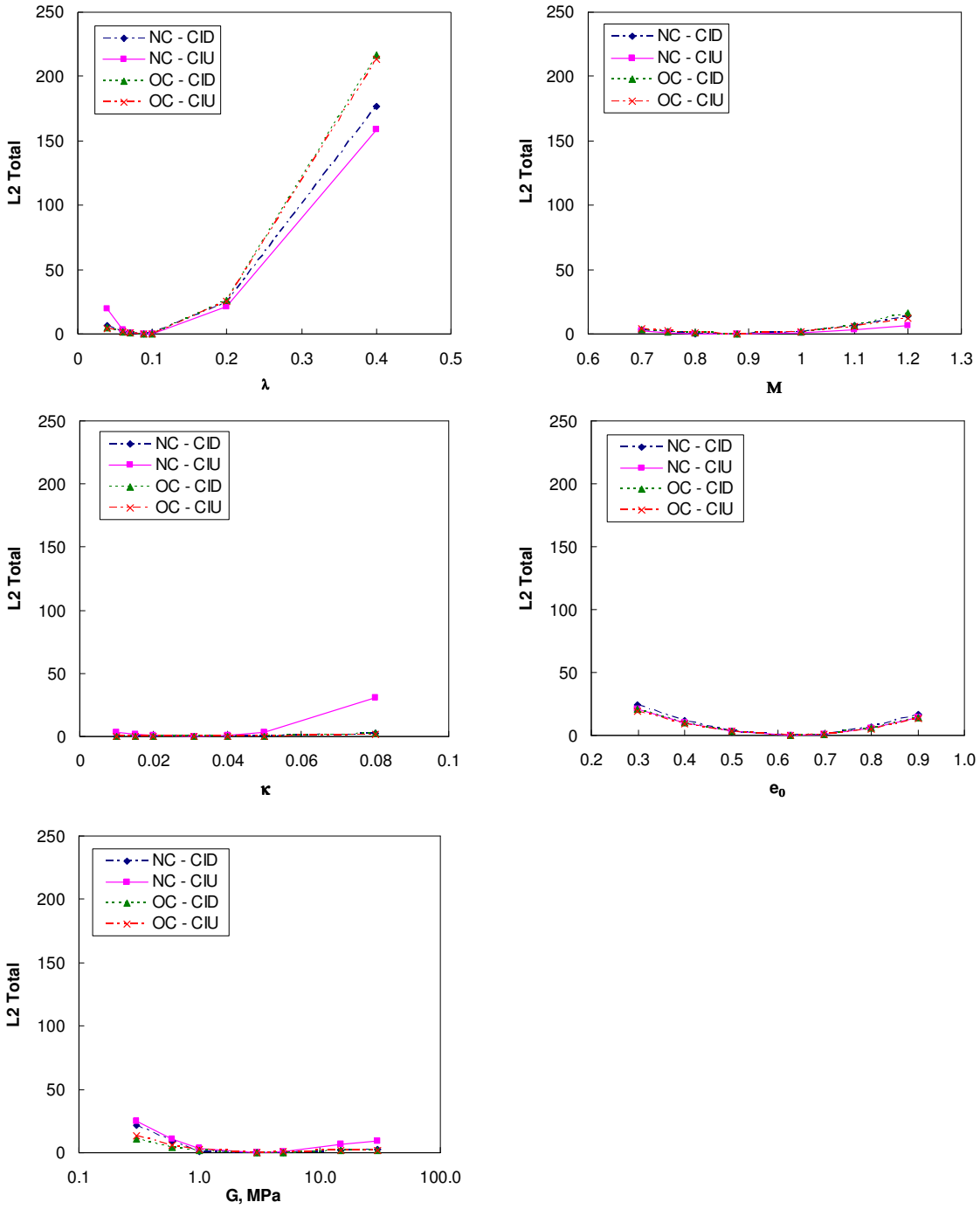

Figure 3.5 Error surfaces for Weald clay. Notation: Total error L2 total, consolidated-drained test CID, consolidated-undrained test CIU, normally consolidated NC, and over consolidated OC.

- Within the selected range of parameters, the error surfaces are concave for total error and individual measurement errors (not shown). Concavity supports standard gradient-based search approaches and the identification of unique solutions.
- The contribution by each measurement to the total error varies.
- The sampling interval in each loading phase affects the weight each loading phase receives in matching.
- The total error curves follow similar trends in all four simulations (NC-CID, NC-CIU, OC-CID, and OC-CIU). Figures 3.4 and 3.5 show that invertability of constitutive model parameters is not affected by the type of test (drained vs. undrained) or stress history (normally consolidated vs. over consolidated)
- The parameter λ has the most significant effect on the total error (This realization is more pronounced for Weald clay). On the other hand, the parameter κ has a relatively limited contribution to the total error.
- The total error is a crude measure of error and it is not satisfactory to properly identify the model parameters. A deeper insight into errors of individual measurements is needed.

The relative contribution of the error component in each measurement to the total error (Equation 3.9) is computed for all Cam-Clay parameters. The individual error percentage of test measurements (p', q, e, ε_z, and u) for Pueblo sand and Weald clay

are shown in Tables 3.4 and 3.5, respectively. The following conclusions can be drawn:

Table 3.4 Error (%) in individual measurements with parameters variations for Pueblo sand.

		q				p				e				ε_z				u	
		NC-CID	NC-CIU	OC-CID	OC-CIU	NC-CID	NC-CIU	OC-CID	OC-CIU	NC-CID	NC-CIU	OC-CID	OC-CIU	NC-CID	NC-CIU	OC-CID	OC-CIU	NC-CIU	OC-CIU
λ	0.005	40%	25%	3%	0%	3%	25%	0%	0%	1%	0%	3%	0%	**56%**	41%	**94%**	2%	9%	**98%**
	0.0075	32%	15%	2%	0%	2%	15%	0%	0%	1%	1%	3%	0%	**64%**	**64%**	**95%**	5%	6%	**95%**
	0.01	27%	3%	2%	0%	0%	3%	0%	0%	1%	1%	3%	0%	**71%**	**92%**	**95%**	8%	1%	**92%**
	0.014	-	-	-	-	-	-	-	-	-	-	-	-	-	-	-	-	-	-
	0.02	16%	3%	2%	0%	2%	3%	0%	0%	1%	1%	3%	1%	**81%**	**93%**	**95%**	25%	1%	**75%**
	0.025	13%	2%	1%	0%	1%	2%	0%	0%	1%	1%	3%	1%	**84%**	**95%**	**96%**	34%	1%	**65%**
	0.03	**68%**	1%	31%	0%	4%	1%	6%	0%	1%	0%	1%	1%	27%	**97%**	**62%**	**88%**	1%	11%
κ	0.001	**89%**	36%	19%	0%	9%	41%	2%	0%	2%	0%	3%	0%	0%	0%	**75%**	0%	23%	**100%**
	0.0015	**89%**	37%	19%	0%	9%	42%	2%	0%	2%	0%	3%	0%	0%	0%	**75%**	0%	21%	**100%**
	0.002	**89%**	38%	19%	0%	9%	42%	2%	0%	2%	0%	4%	0%	0%	0%	**75%**	0%	20%	**100%**
	0.0024	-	-	-	-	-	-	-	-	-	-	-	-	-	-	-	-	-	-
	0.003	**90%**	38%	16%	0%	9%	43%	0%	0%	2%	0%	3%	0%	0%	0%	**80%**	0%	19%	**100%**
	0.005	**90%**	39%	18%	0%	8%	43%	2%	0%	1%	0%	3%	0%	0%	0%	**77%**	0%	18%	**100%**
	0.008	**91%**	40%	18%	0%	8%	43%	2%	0%	1%	0%	3%	0%	0%	0%	**76%**	0%	17%	**100%**
M	1.0	**88%**	**90%**	**87%**	2%	12%	0%	13%	0%	0%	0%	0%	0%	0%	0%	0%	0%	10%	**98%**
	1.1	**88%**	**90%**	**87%**	2%	12%	0%	13%	0%	0%	0%	0%	0%	0%	0%	0%	0%	10%	**98%**
	1.2	**50%**	1%	**87%**	2%	**50%**	1%	13%	0%	0%	0%	0%	0%	0%	0%	1%	0%	**98%**	**98%**
	1.24	-	-	-	-	-	-	-	-	-	-	-	-	-	-	-	-	-	-
	1.3	**88%**	**90%**	**87%**	2%	2%	0%	13%	0%	0%	0%	0%	0%	0%	0%	0%	0%	10%	**98%**
	1.35	**88%**	**90%**	**87%**	2%	12%	0%	13%	0%	0%	0%	0%	0%	0%	0%	0%	0%	10%	**98%**
	1.4	**88%**	**90%**	**87%**	2%	12%	0%	13%	0%	0%	0%	0%	0%	0%	0%	0%	0%	10%	**98%**
e_0	0.25	0%	0%	0%	0%	0%	0%	0%	0%	**99%**	**98%**	**99%**	**99%**	1%	2%	1%	1%	0%	0%
	0.27	0%	0%	0%	0%	0%	0%	0%	0%	**99%**	**99%**	**99%**	**99%**	1%	1%	1%	1%	0%	0%
	0.3	0%	0%	0%	0%	0%	0%	0%	0%	**98%**	**98%**	**99%**	**99%**	2%	2%	1%	1%	0%	0%
	0.34	-	-	-	-	-	-	-	-	-	-	-	-	-	-	-	-	-	-
	0.4	0%	0%	0%	0%	0%	0%	0%	0%	**99%**	**99%**	**99%**	**99%**	1%	1%	1%	1%	0%	0%
	0.5	0%	0%	0%	0%	0%	0%	0%	0%	**99%**	**99%**	**99%**	**99%**	1%	1%	1%	1%	0%	0%
	0.6	0%	0%	0%	0%	0%	0%	0%	0%	**99%**	**99%**	**99%**	**99%**	1%	1%	1%	1%	0%	0%
G (MPa)	2	**83%**	27%	**79%**	**49%**	8%	27%	10%	4%	0%	0%	0%	0%	9%	2%	11%	4%	44%	43%
	5	**88%**	28%	**86%**	44%	6%	21%	9%	4%	0%	0%	0%	0%	6%	1%	5%	1%	**51%**	**51%**
	10	35%	15%	**90%**	37%	35%	15%	8%	3%	0%	0%	0%	0%	29%	0%	3%	1%	**69%**	**59%**
	20	-	-	-	-	-	-	-	-	-	-	-	-	-	-	-	-	-	-
	40	**92%**	14%	**93%**	**64%**	5%	13%	6%	3%	0%	0%	0%	0%	4%	0%	1%	0%	**72%**	33%
	60	**92%**	13%	**93%**	**70%**	5%	13%	6%	5%	0%	0%	0%	0%	4%	1%	1%	1%	**73%**	25%
	100	**92%**	13%	**93%**	**71%**	5%	14%	6%	7%	0%	0%	0%	0%	4%	1%	2%	1%	**73%**	21%

Notation: Deviatoric stress q, mean effective stress p', void ratio e, axial strain ε_z, pore pressure u, normally-consolidated NC, over consolidated OC, isotropically consolidated drained CD, and isotropically consolidated undrained CIU. Over consolidation ratio = 2.0

- The parameter λ is the major contributor to the error in axial strain ε_z. For OC Pueblo sand in CIU test, the parameter λ has an impact on pore pressure u.
- The parameter κ has a prime effect on the deviator stress q in NC-CID simulation and on the axial strain ε_z in OC-CID simulation.

- The strength parameter M and the shear modulus G dominate the error in the deviator stress q.
- The error in void ratio e is always attributed to the error in the initial void ratio, e_0. The contribution of other material parameters to the error in void ratio is very small
- The contribution of each parameter to individual and total errors must take into consideration the different loading phases (e.g. isotropic loading vs. deviatoric loading).

Table 3.5 Error (%) in individual measurements with parameters variations for Weald clay.

		q				p'				e				ε_z				u	
		NC-CID	NC-CIU	OC-CID	OC-CIU	NC-CID	NC-CIU	OC-CID	OC-CIU	NC-CID	NC-CIU	OC-CID	OC-CIU	NC-CID	NC-CIU	OC-CID	OC-CIU	NC-CIU	OC-CIU
λ	0.04	36%	29%	5%	0%	1%	28%	0%	0%	15%	1%	7%	4%	48%	17%	88%	96%	25%	0%
	0.06	28%	22%	4%	0%	1%	22%	0%	0%	16%	2%	7%	4%	55%	35%	89%	96%	19%	0%
	0.07	26%	19%	4%	0%	1%	19%	0%	0%	16%	2%	7%	4%	57%	43%	90%	96%	17%	0%
	0.088	-	-	-	-	-	-	-	-	-	-	-	-	-	-	-	-	-	-
	0.1	26%	13%	3%	0%	1%	12%	0%	0%	16%	3%	6%	4%	57%	61%	91%	96%	11%	0%
	0.2	13%	4%	2%	0%	1%	3%	0%	0%	12%	4%	5%	3%	74%	86%	93%	97%	3%	0%
	0.4	7%	1%	1%	0%	0%	1%	0%	0%	8%	4%	4%	3%	85%	94%	96%	97%	1%	0%
κ	0.01	83%	28%	6%	0%	4%	33%	0%	0%	13%	0%	7%	9%	0%	0%	86%	91%	39%	0%
	0.015	83%	29%	6%	0%	4%	33%	0%	0%	13%	0%	7%	9%	0%	0%	86%	91%	37%	0%
	0.02	83%	30%	7%	0%	4%	34%	0%	0%	13%	0%	8%	9%	0%	0%	85%	91%	36%	0%
	0.031	-	-	-	-	-	-	-	-	-	-	-	-	-	-	-	-	-	-
	0.04	84%	31%	7%	0%	4%	34%	0%	0%	11%	0%	8%	100%	0%	0%	84%	0%	34%	0%
	0.05	85%	32%	8%	0%	4%	35%	1%	0%	11%	0%	8%	9%	0%	0%	84%	91%	33%	0%
	0.08	89%	34%	12%	0%	4%	34%	1%	0%	8%	0%	8%	9%	0%	0%	79%	91%	31%	0%
M	0.7	94%	90%	93%	50%	6%	0%	7%	0%	0%	0%	0%	0%	0%	0%	0%	0%	10%	50%
	0.75	94%	90%	93%	50%	6%	0%	7%	0%	0%	0%	0%	0%	0%	0%	0%	0%	10%	50%
	0.8	48%	1%	93%	50%	48%	1%	7%	0%	1%	0%	0%	0%	2%	0%	0%	0%	97%	50%
	0.882	-	-	-	-	-	-	-	-	-	-	-	-	-	-	-	-	-	-
	1	93%	90%	93%	50%	1%	0%	1%	0%	0%	0%	0%	0%	0%	0%	0%	0%	10%	50%
	1.1	93%	90%	93%	50%	6%	0%	7%	0%	0%	0%	0%	0%	0%	0%	0%	0%	10%	50%
	1.2	93%	90%	93%	50%	6%	0%	7%	0%	0%	0%	0%	0%	0%	0%	0%	0%	9%	50%
e_0	0.3	0%	0%	0%	0%	0%	0%	0%	0%	97%	97%	97%	97%	3%	3%	3%	3%	0%	0%
	0.4	0%	0%	0%	0%	0%	0%	0%	0%	97%	97%	97%	97%	2%	3%	3%	3%	0%	0%
	0.5	0%	0%	0%	0%	0%	0%	0%	0%	98%	97%	97%	97%	2%	2%	3%	3%	0%	0%
	0.628	-	-	-	-	-	-	-	-	-	-	-	-	-	-	-	-	-	-
	0.7	0%	0%	0%	0%	0%	0%	0%	0%	98%	98%	98%	98%	2%	2%	2%	2%	0%	0%
	0.8	0%	0%	0%	0%	0%	0%	0%	0%	98%	98%	98%	98%	2%	2%	2%	2%	0%	0%
	0.9	0%	0%	0%	0%	0%	0%	0%	0%	98%	98%	98%	98%	1%	2%	2%	2%	0%	0%
G (MPa)	0.3	83%	31%	80%	47%	5%	15%	5%	0%	1%	0%	0%	0%	12%	5%	15%	6%	48%	47%
	0.6	82%	32%	87%	49%	4%	13%	4%	0%	1%	0%	0%	0%	13%	2%	8%	3%	52%	49%
	1	18%	12%	91%	49%	18%	12%	4%	0%	3%	0%	0%	0%	60%	2%	5%	2%	73%	49%
	3	-	-	-	-	-	-	-	-	-	-	-	-	-	-	-	-	-	-
	5	94%	26%	98%	50%	0%	2%	0%	0%	0%	0%	0%	0%	4%	0%	1%	0%	72%	50%
	15	95%	20%	98%	50%	1%	1%	2%	0%	0%	0%	0%	0%	3%	0%	1%	0%	79%	50%
	30	96%	19%	97%	50%	1%	1%	2%	0%	0%	0%	0%	0%	3%	0%	1%	0%	80%	50%

Notation: Deviatoric stress q, mean effective stress p', void ratio e, axial strain ε_z, pore pressure u, normally-consolidated NC, over consolidated OC, isotropically consolidated drained CD, and isotropically consolidated undrained CIU. Over consolidation ratio = 2.5

3.5.4 Detailed Error Study: Normally Consolidated - Drained

The previous section provides a basic understanding of error planes and general trends. However, there is still a need for in-depth understanding of the effect of material parameters on measurements during each phase of the triaxial test. For this purpose, consolidated-drained triaxial (CID) test data are simulated for normally consolidated Weald clay. Figures 3.6 through 3.9 depict a parametric study of G, M, λ, and κ on the 4D triaxial space. The reference case corresponds to the selected case. Each figure shows the effect of changing one parameter at the time. (Note: the initial void ratio e_0 has an important effect only on void ratio values e; therefore, it was not considered in this study - see results in Tables 3.4 and 3.5). Based on the trends shown on Figures 3.6 through 3.9, the following conclusions can be made:

- The effect of the shear modulus G and the strength parameter M is substantial in the ε_z-q projection.
- There is no effect of G on p`-q or p`-e.
- The strength parameter M has a large impact on the deviatoric stress q (Figure 3.7); however, the initial portion of ε_z-q curve is not influenced by the M parameter. The value of M has a limited role in p`-e and ε_z -e plots.
- The parameter λ has a significant impact on deformability and while approaching critical state. It affects all stages of loading: isotropic, deviatoric, and unloading (Figure 3.8). Large values of λ result in lower deformability and critical state is reached at smaller strains (ε_z-q plane).
- The value of κ has the least effect on all deformation data (Figure 3.9).

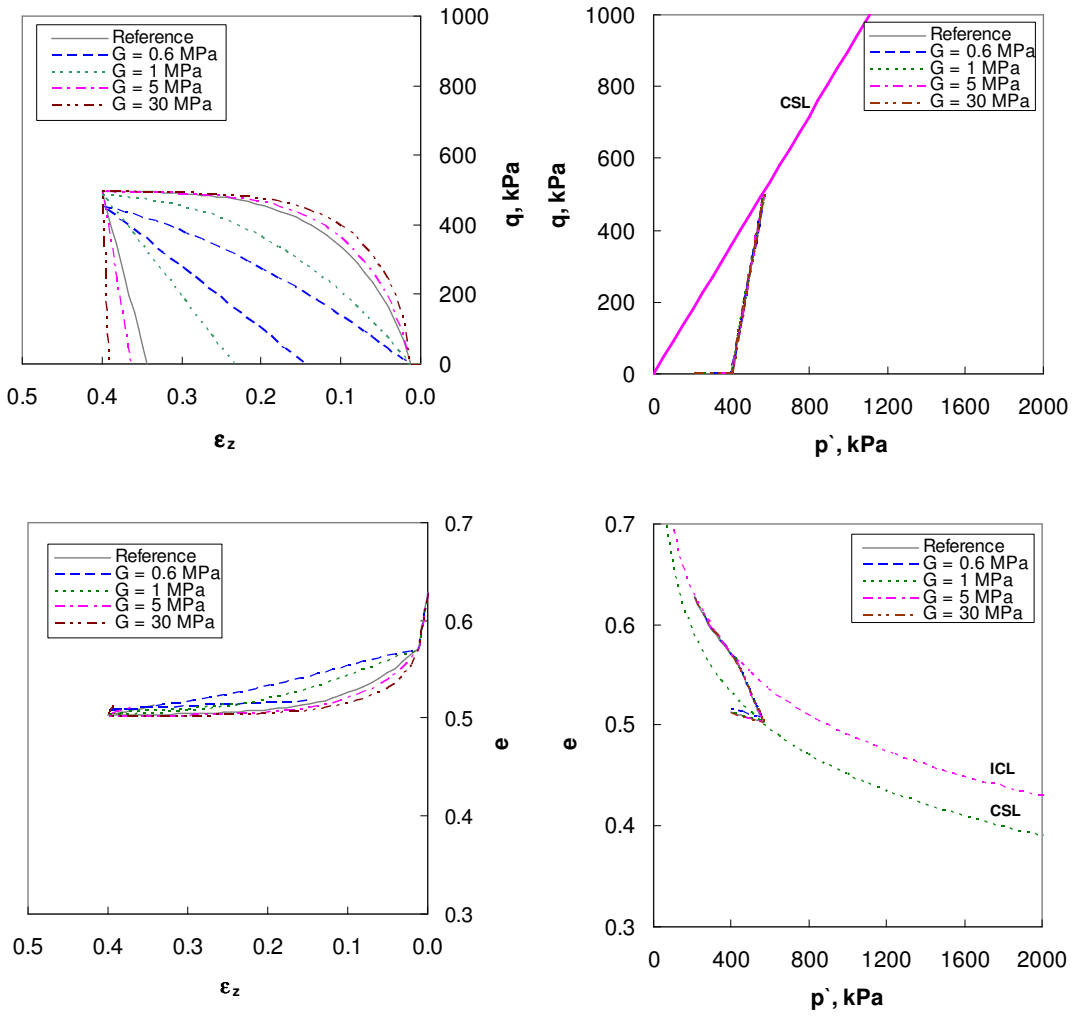

Figure 3.6 Effect of G on measurements of CID triaxial test for Weald clay. Notation: Shear modulus G, mean effective stress p`, deviatoric stress q, void ratio e, axial strain ε_z, isotropic consolidation line ICL, and critical state line CSL. Limit ε_z = 40%.

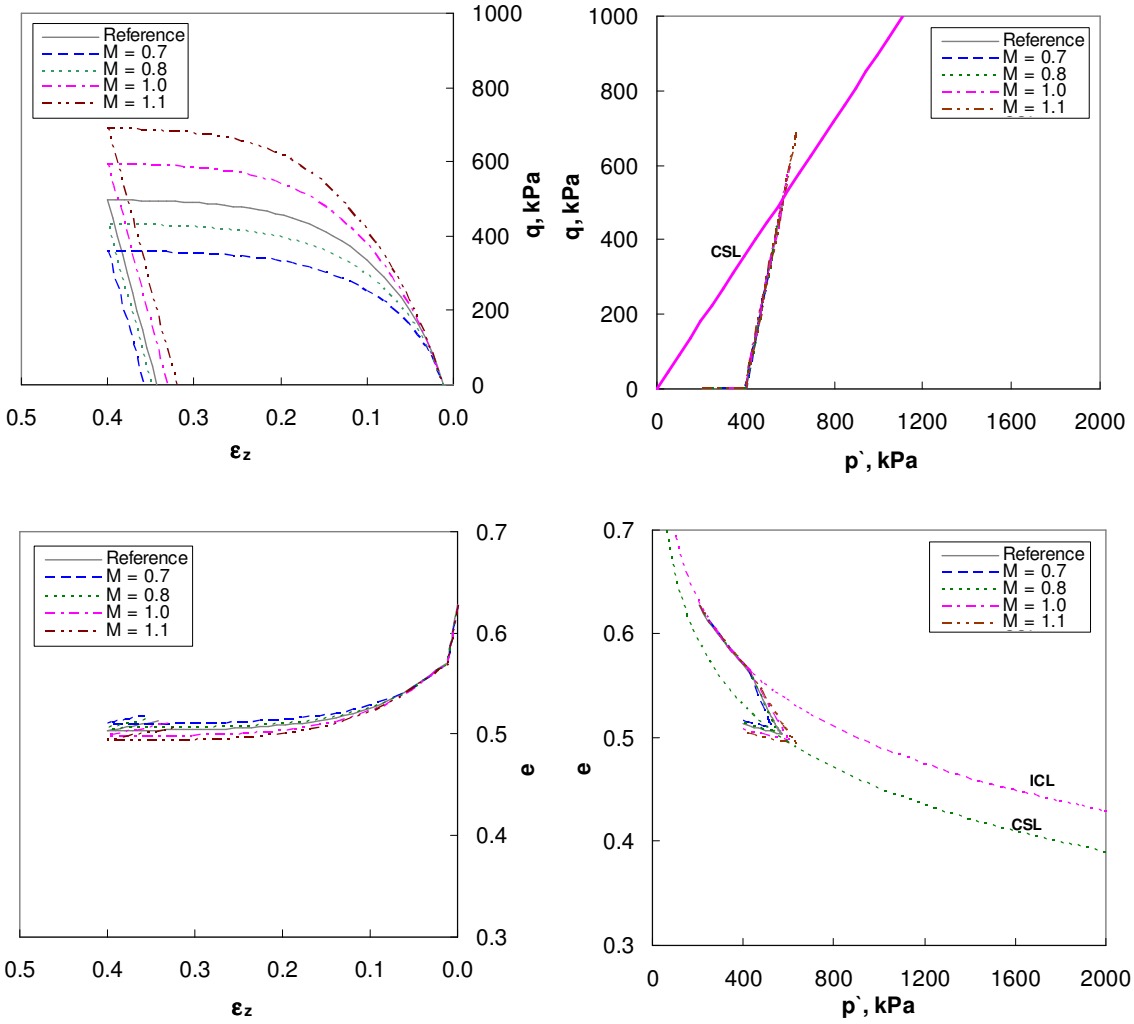

Figure 3.7 Effect of M on measurements of CID triaxial test for Weald clay. Notation: Shear modulus G, mean effective stress p`, deviatoric stress q, void ratio e, axial strain ε_z, isotropic consolidation line ICL, and critical state line CSL. Note: Limit $\varepsilon_z = 40\%$.

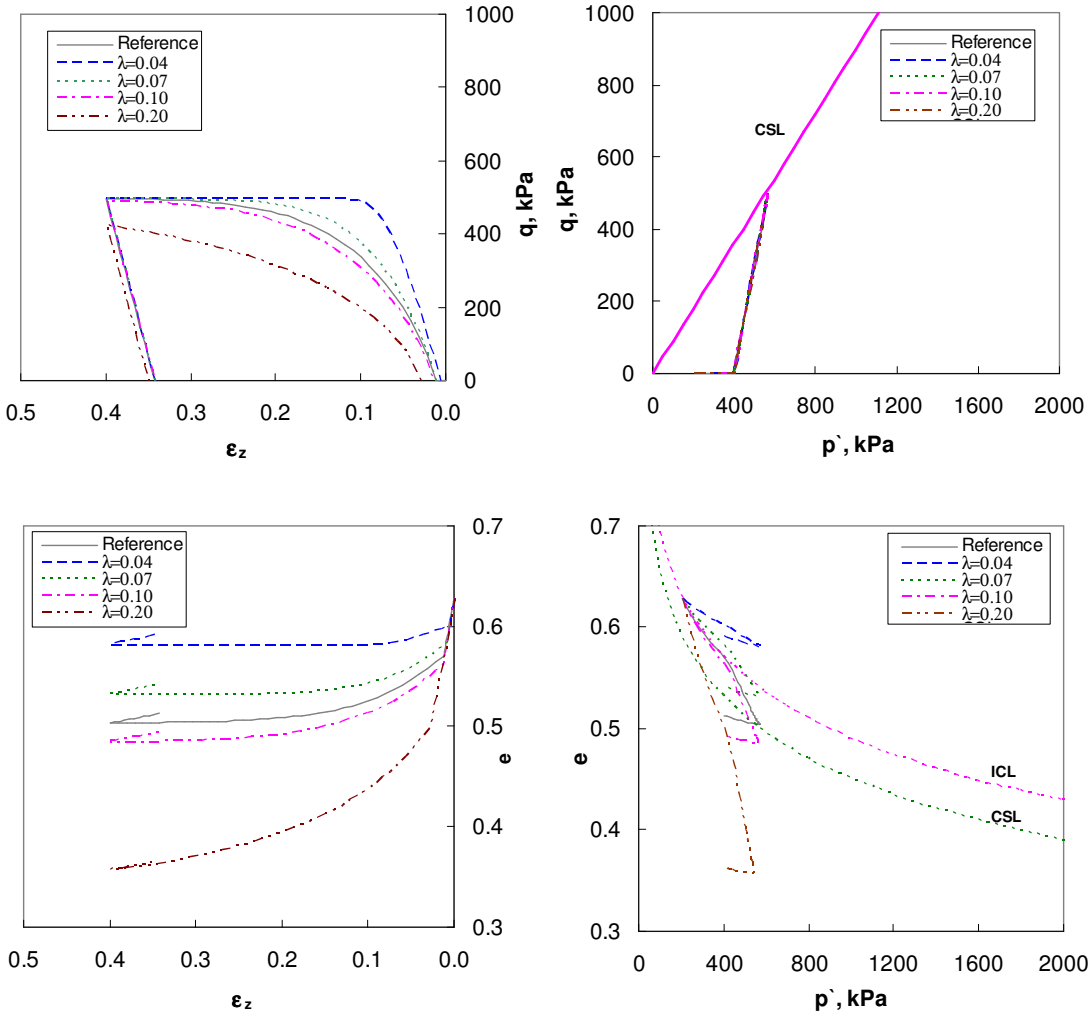

Figure 3.8 Effect of λ on measurements of CID triaxial test for Weald clay. Notation: Shear modulus G, mean effective stress p`, deviatoric stress q, void ratio e, axial strain ε_z, isotropic consolidation line ICL, and critical state line CSL. Note: Limit $\varepsilon_z = 40\%$.

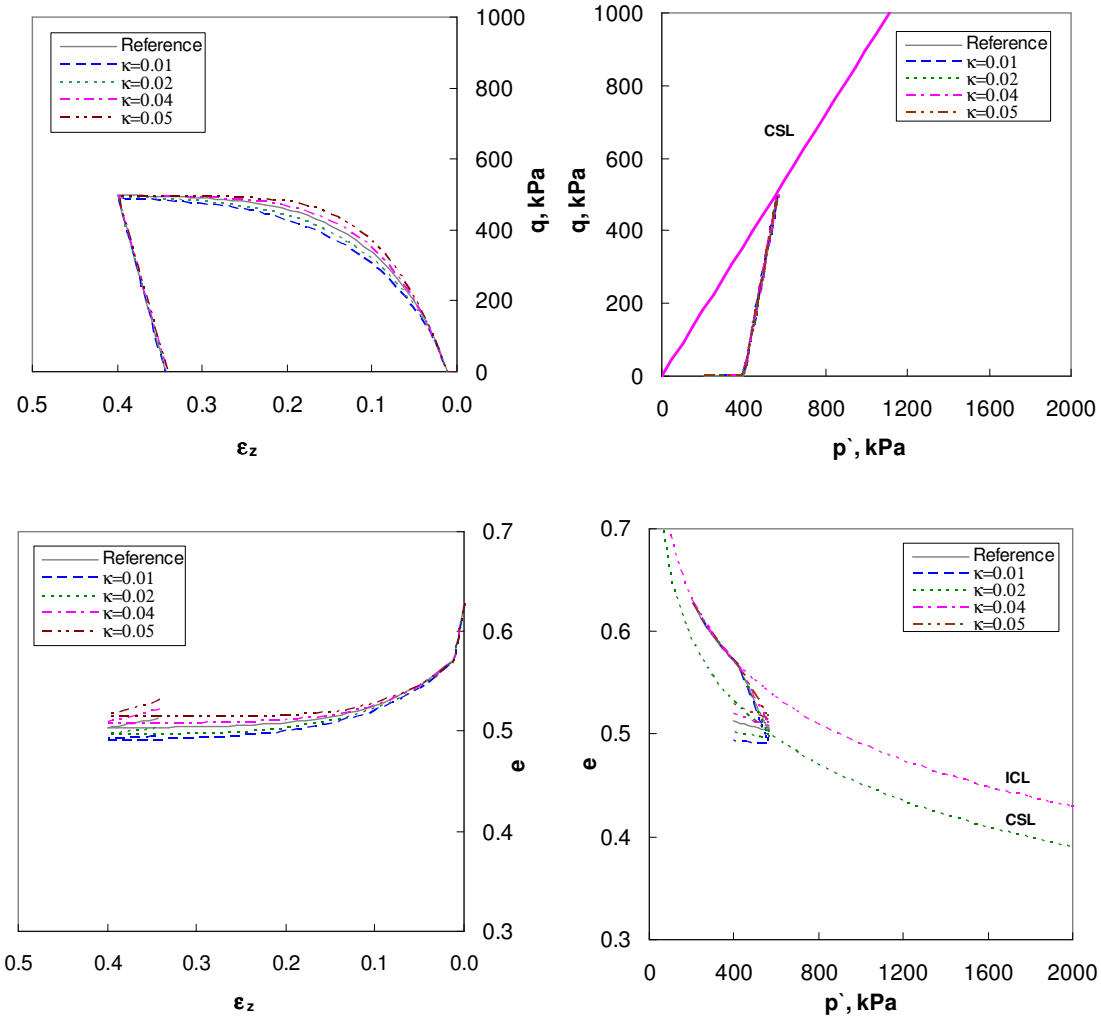

Figure 3.9 Effect of κ on measurements of CID triaxial test for Weald clay. Notation: Shear modulus G, mean effective stress p`, deviatoric stress q, void ratio e, axial strain ε_z, isotropic consolidation line ICL, and critical state line CSL. Note: Limit $\varepsilon_z = 40\%$.

The sensitivity study in the 4D space projections provides clear evidence about the effect of Cam-Clay parameters on measurements (p', q, e, and ε_z). In particular, it shows that model parameters can be extracted from specific measurements (or loading phase) rather than by simultaneously taking into consideration all measurements and all loading phases. The study of error surface components (Equation 3.9) for single measurements (p', q, e, and ε_z) is summarized in Figures 3.10 through 3.14. This detailed study is conducted for isotropically-consolidated drained triaxial (CID) test on normally consolidated Weald clay.

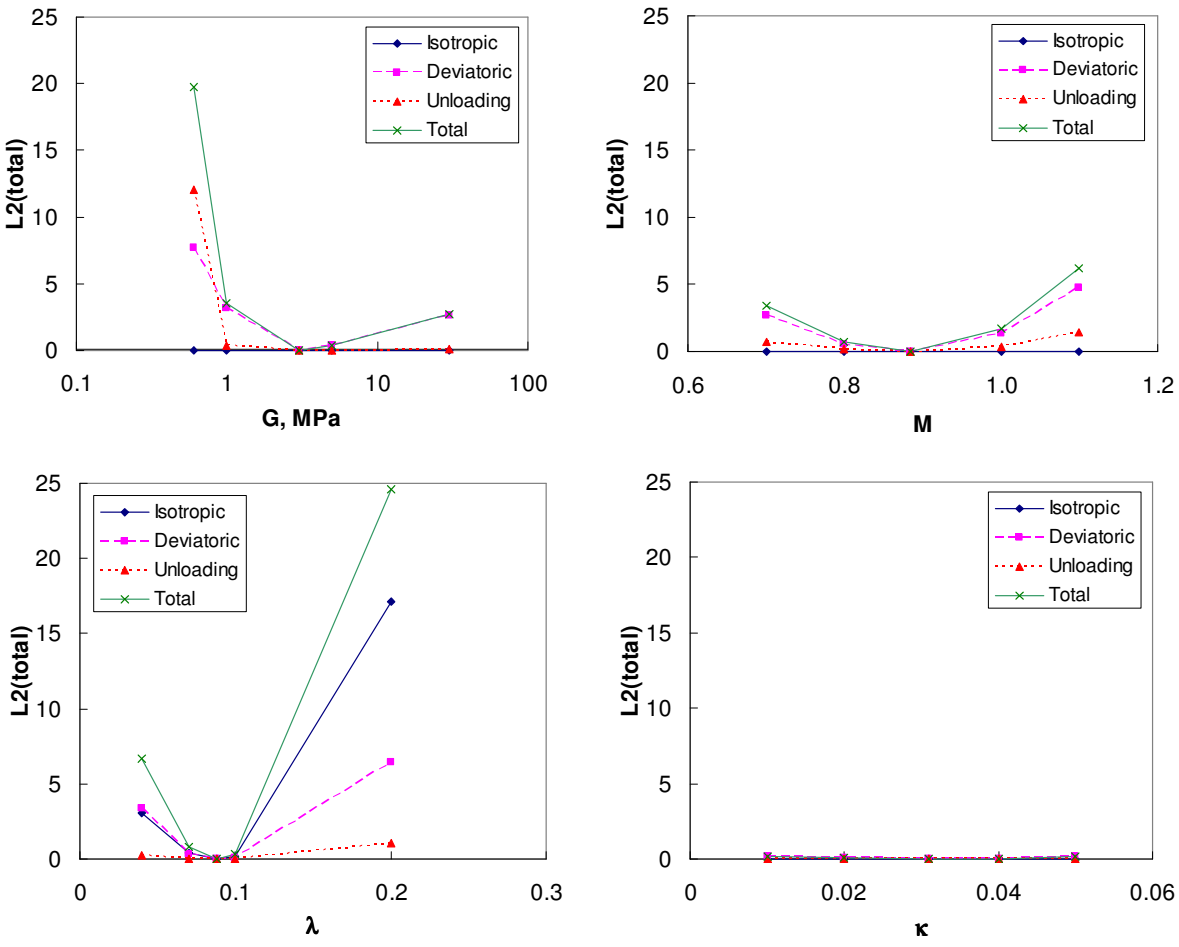

Figure 3.10 Total L2-norm - NC Weald clay - CID triaxial test.

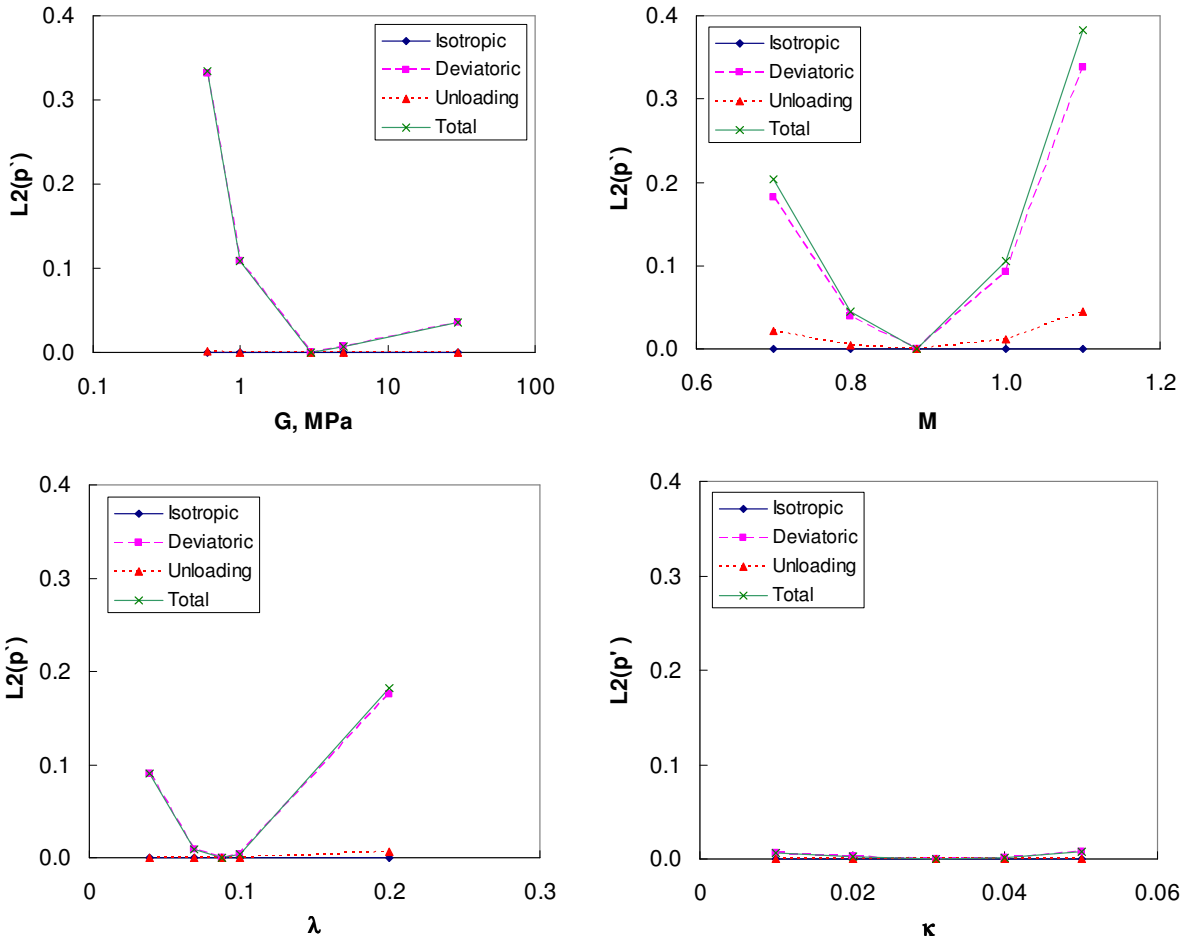

Figure 3.11 L2-norm of the mean effective stress p`- NC Weald clay - CID triaxial test.

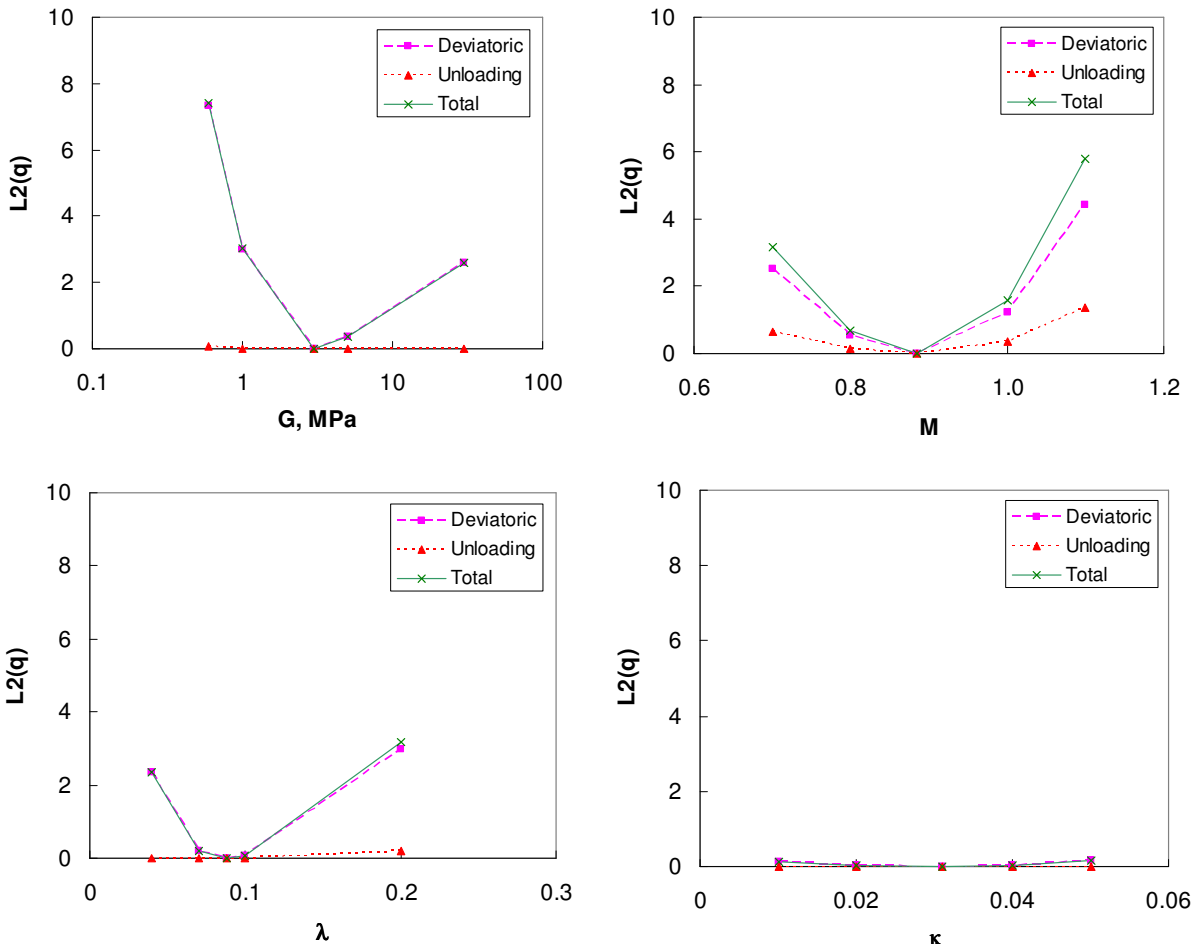

Figure 3.12 L2-norm of the deviatoric stress q - NC Weald clay - CID triaxial test.

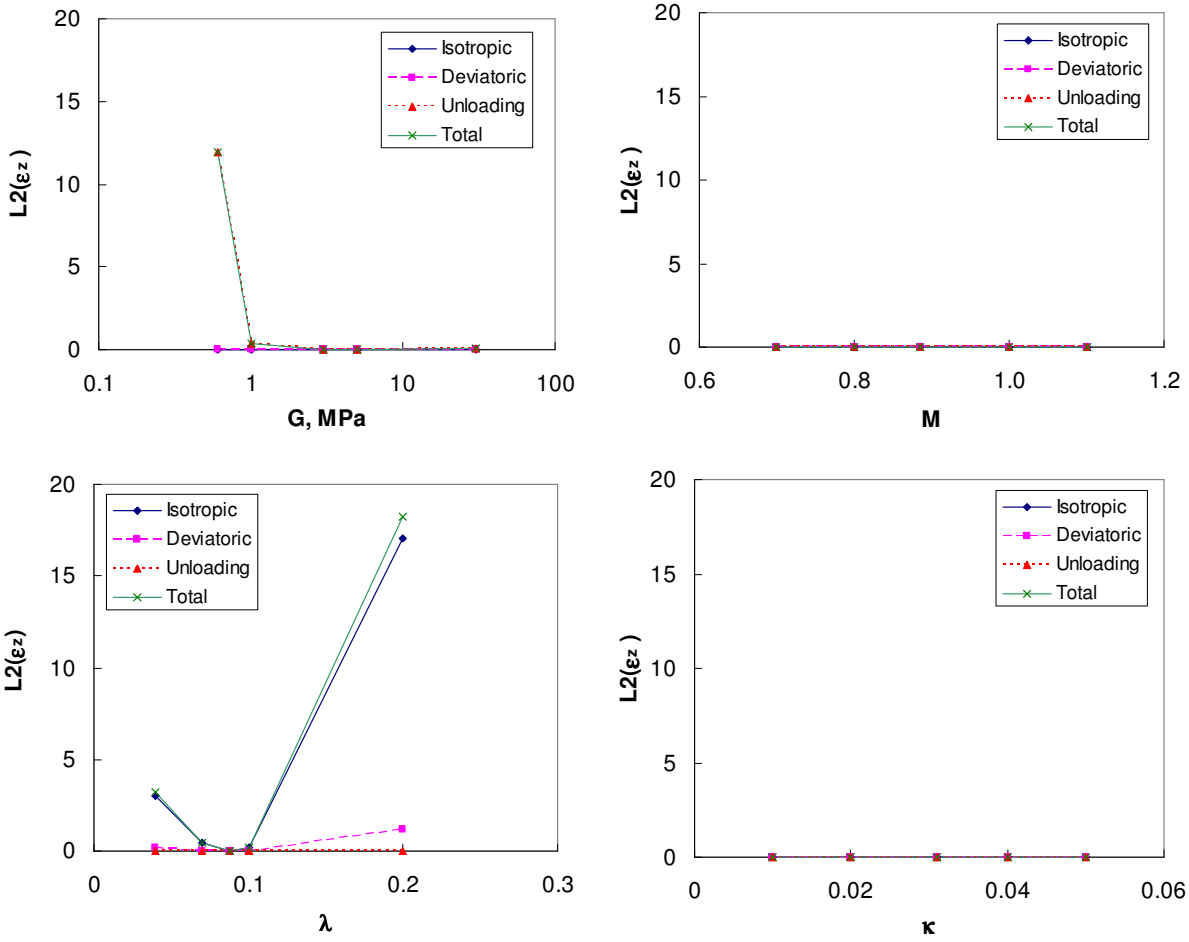

Figure 3.13 L2-norm of the axial normal strain ε_z - NC Weald clay - CID triaxial test.

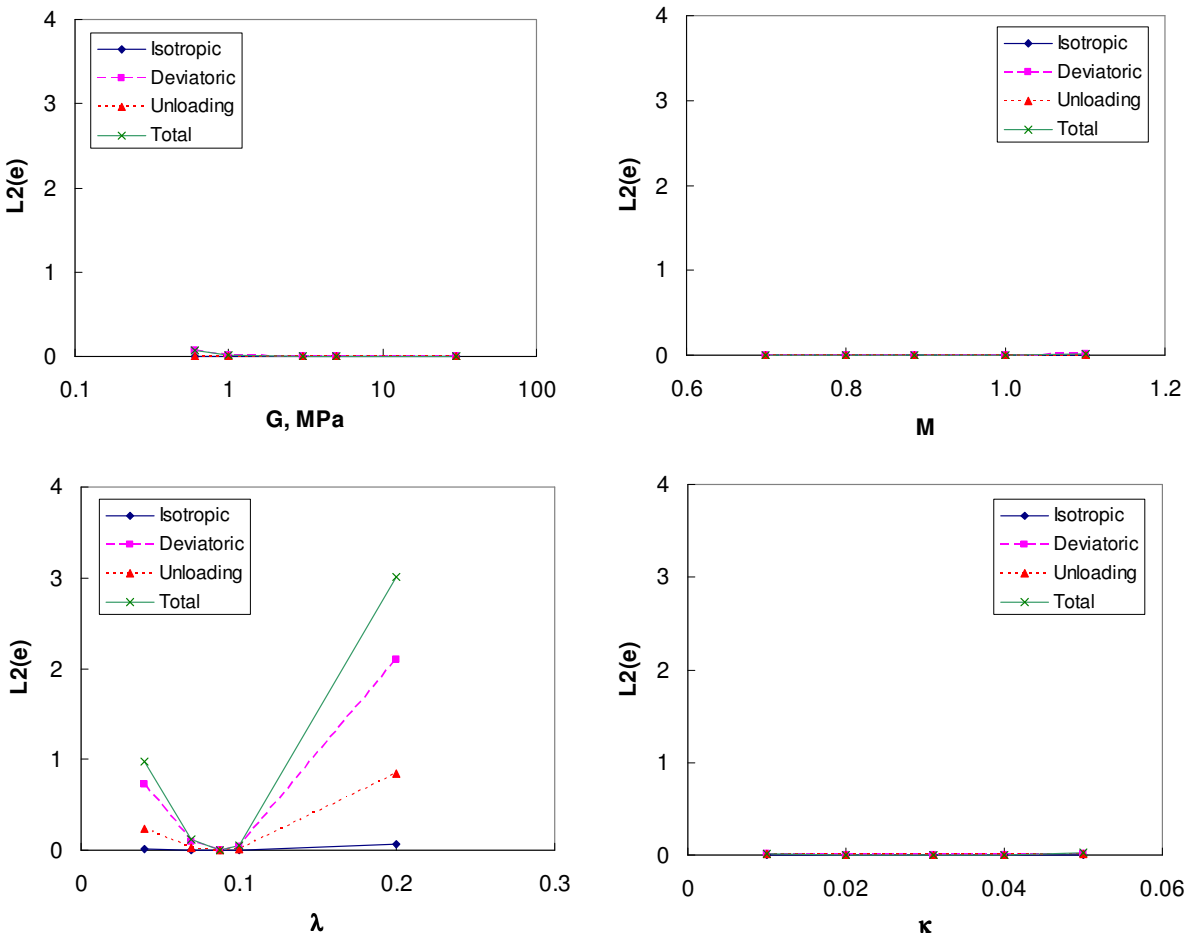

Figure 3.14 L2-norm of the void ratio e - NC Weald clay - CID triaxial test.

Figure 3.10 shows that the total error is concave for all loading phases. Such realization further supports the concavity of total error presented in the previous section (Figures 3.4 and 3.5). Therefore, the possibility of a unique solution of this inverse problem is further confirmed. Figure 3.10 shows that the λ, G, M are the major contributors to the total error for all loading phases, while κ has a very limited effect. This realization facilitates effective guiding of the search for the optimum parameters that minimize the error.

The concavity of individual error components, L2(p`), L2(q), L2(ε_z) and L2(e), is also observed in Figures 3.11 through 3.14. Once again, κ has an insignificant effect on all the measurements. The contributions of the parameters to the individual error components for each loading phase are summarized in Table 3.6. The study on individual error components confirms observations made in the 4D space: the parameter λ plays a major role for all measurements, yet quantitatively most of the effect is in p`-e and ε_z-e planes. The parameters M and G only affect p' and q.

Table 3.6 Contribution of Cam-Clay parameters to individual errors.

		G	M	λ	κ
p'	Isotropic	-	-	-	-
	Deviatoric	√	√	√	√ (small)
	Unloading	-	√	-	-
q	Isotropic	-	-	-	-
	Deviatoric	√	√	√	√ (small)
	Unloading	-	√	-	-
ε_z	Isotropic	-	-	√ (largest)	-
	Deviatoric	-	-	√	-
	Unloading	√ (only for very small G)	-	-	-
e	Isotropic	-	-	√ (small)	-
	Deviatoric	√ (only for very small G)	-	√	-
	Unloading	-	-	√	-

3.6 SUMMARY AND CONCLUSIONS

This chapter addresses the concept of error between data and predictions and the main inversion methods. Then, the error surface associated with idealized triaxial compression tests was studied in detail, taking into consideration drainage condition, over consolidation, and loading phases (isotropic, deviatoric, and unloading). Total and individual L2-norms were evaluated. Based on this study the following conclusions can be drawn:

- The total error is not satisfactory to guide the inversion of constitutive model parameters.
- Certain parameters exert the most control on given global measurements. For example, the parameter M in the ε_z-q plane.
- It is possible to decouple convergence by defining error in 2-dimensional variable spaces and optimizing the controlling constitutive parameter in that space.
- Certain constitutive model parameters are best inverted during different loading conditions. For example, λ can be extracted from isotropic loading, while M can be extracted from deviatoric loading.

CHAPTER IV

MEASUREMENTS AND MODELLING ERRORS - IMPLICATIONS

The new experimental approach proposed in this thesis combines information-rich experiments with successive forward modeling to invert for the parameters of a pre-selected constitutive model. This approach is affected by measurement errors and modeling errors. In fact, the literature on inverse problem solving highlights the magnification of error and non-uniqueness in inverse solutions.

The impact of measurement and model errors in constitutive model calibration is assessed in this chapter using simulated data. The cases consist of triaxial compression loading for normally consolidated and over consolidated soils under either drained or undrained conditions. Finite element simulation results are captured at different stages during the loading phase as summarized in Table 4.1.

Table 4.1 Loading phases. Number of increments.

	Isotropic	Isotropic over consolidation	Deviatoric	Unloading
Normally consolidated	10	-	40	10
Over consolidated	5	5	40	10

4.1 MEASUREMENT ERRORS

Noise (thermal, mechanical, electromagnetic, etc.) and human error affect experimental measurements (Dally et al., 1993). The objective of this section is to study the effect of noisy measurements on the invertability of constitutive parameters.

To achieve this goal, noise is intentionally added to the simulated triaxial test measurements and then the inversion process is conducted to determine the constitutive parameters. The Modified Cam-Clay model MCCM is used for this purpose. This study is parallel to the study of inversion with noiseless data presented in Chapter 3. The effect of noise on constitutive parameters is studied for ideal frictionless boundaries in the triaxial compression test.

Noise is included as 5% random noise added to the measurements (not to the input or constitutive parameters). This level of random noise is selected as an upper bound of typical measurement errors in the laboratory. Noiseless and noisy measurements simulated for a consolidated-drained triaxial test of Weald clay are shown in Figure 4.1 for the MCCM parameters in Table 2.2. The specimen is isotropically consolidated to a mean effective stress p` = 400 kPa and then sheared under strain-controlled vertical loading. A series of forward simulations is then conducted to curve fit the randomized data by minimizing the L2 norm (Chapter 3). The algorithm is summarized in Figure 4.2.

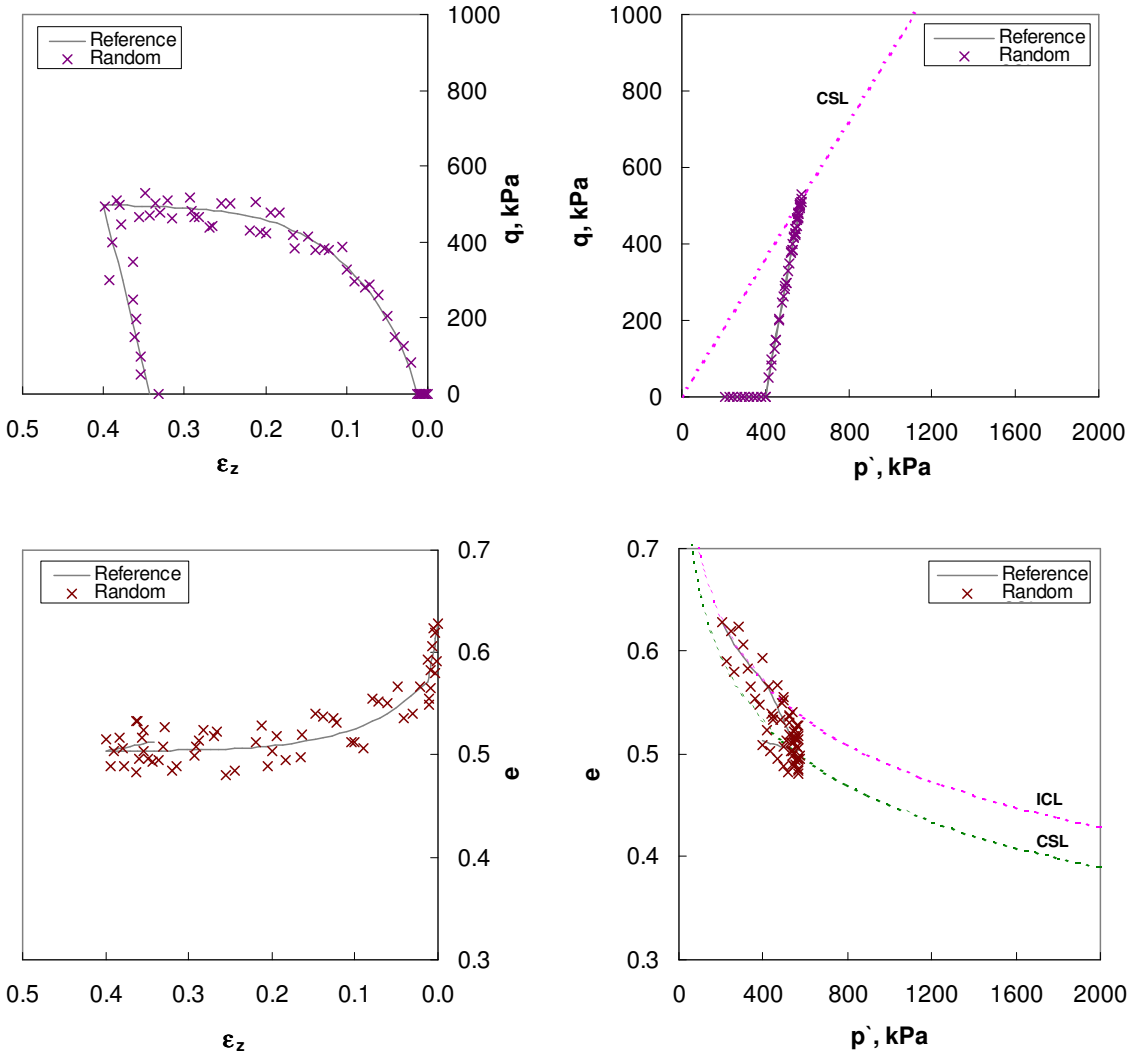

Figure 4.1 Original data and simulated data with 5% noise. Idealized CID triaxial simulations of Weald clay. Parameters in Table 2.2. Notation: Mean effective stress p`, deviatoric stress q, void ratio e, axial strain ε_z, isotropic consolidation line ICL, and critical state line CSL.

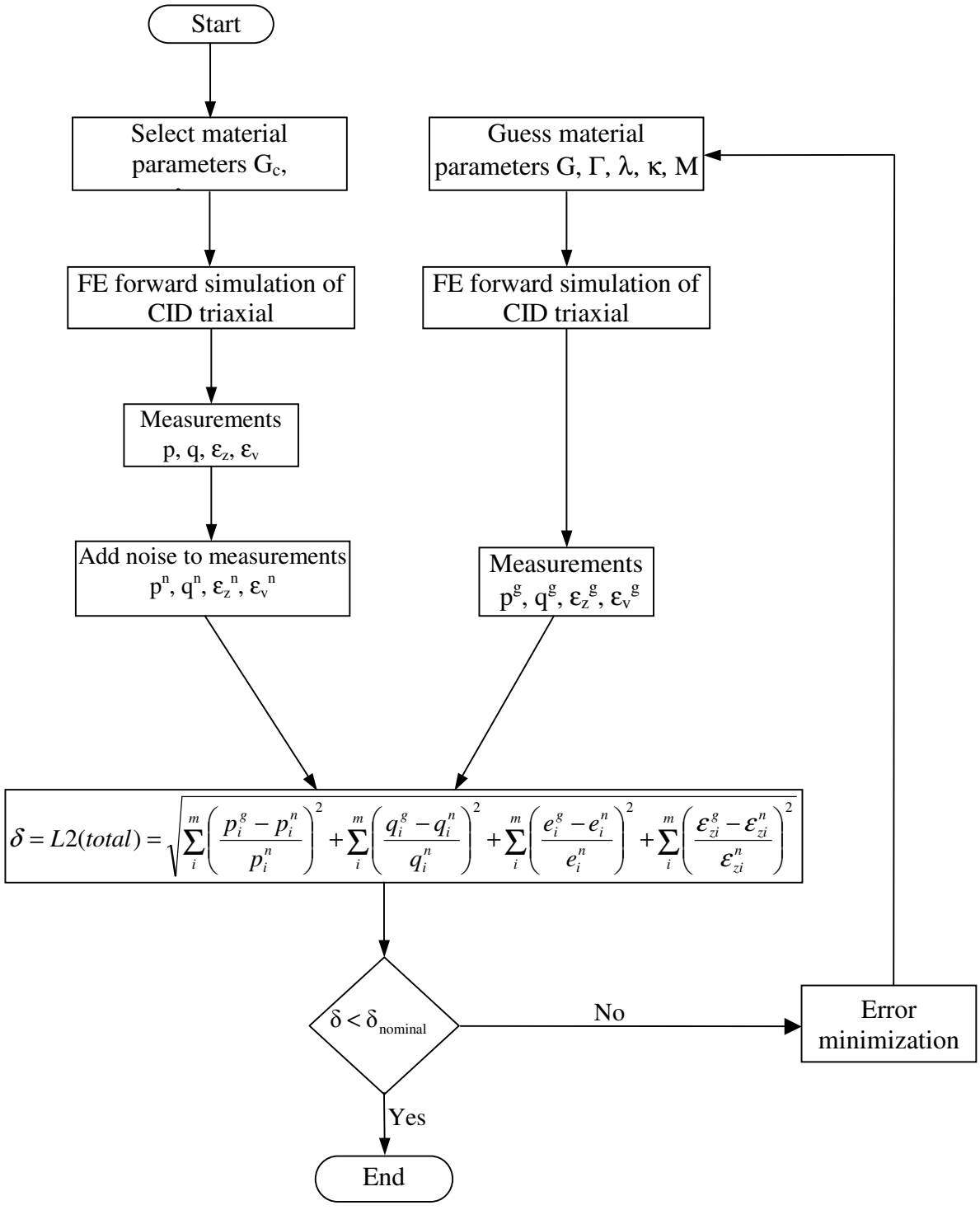

Figure 4.2 Inversion by successive forward simulation for CID triaxial test - Algorithm.

4.1.1 Sensitivity Study

Given the generated noisy data, a sensitivity study is attempted by changing one model parameter at the time while other parameters are kept at their original values. The results are plotted in the 4D triaxial space e-p`-q-ε_z in Figures 4.3 through 4.6.

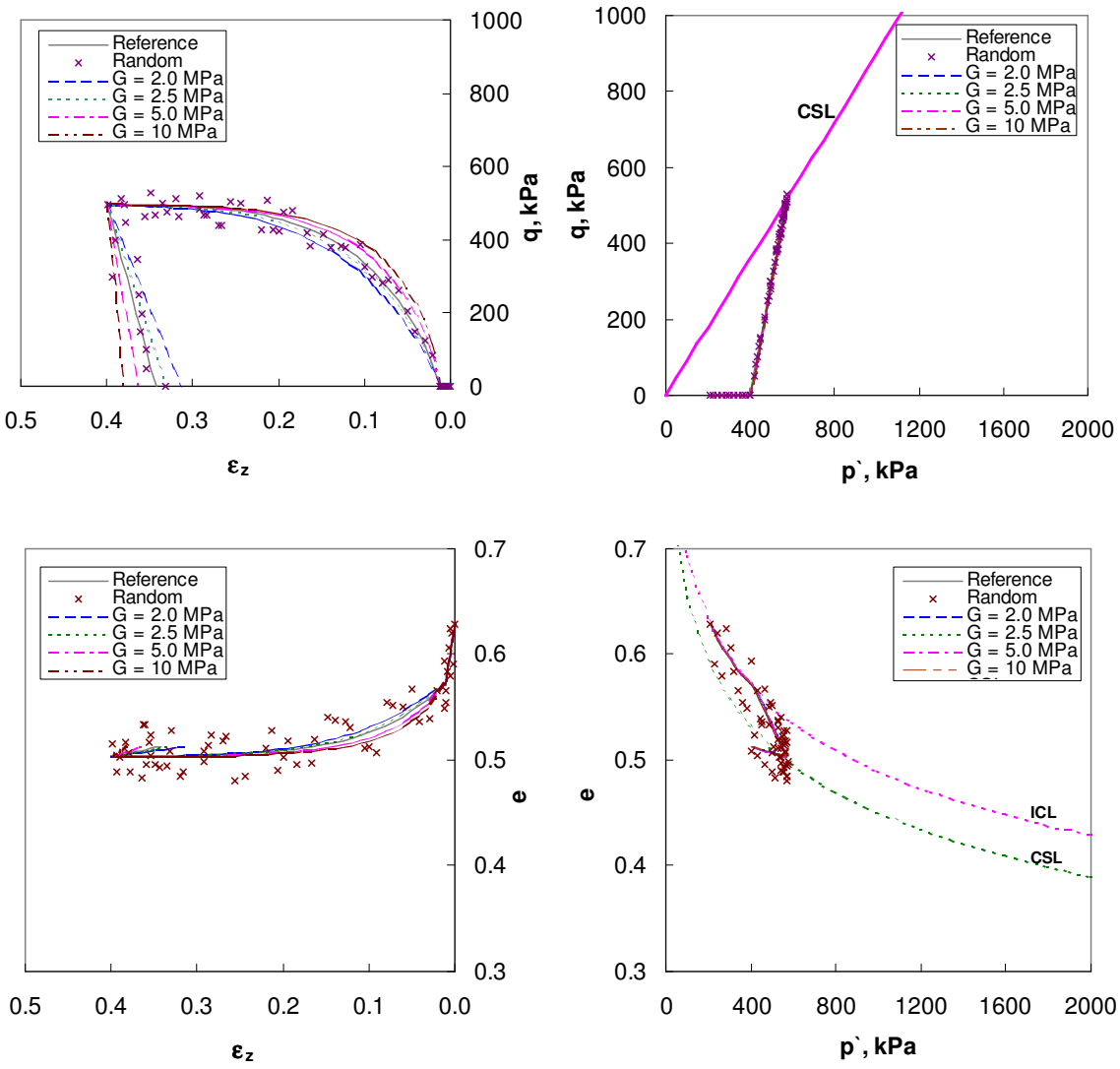

Figure 4.3 Matching trials using G only for CID triaxial test on Weald clay. Notation: Shear modulus G, mean effective stress p`, deviatoric stress q, void ratio e, axial strain ε_z, isotropic consolidation line ICL, and critical state line CSL.

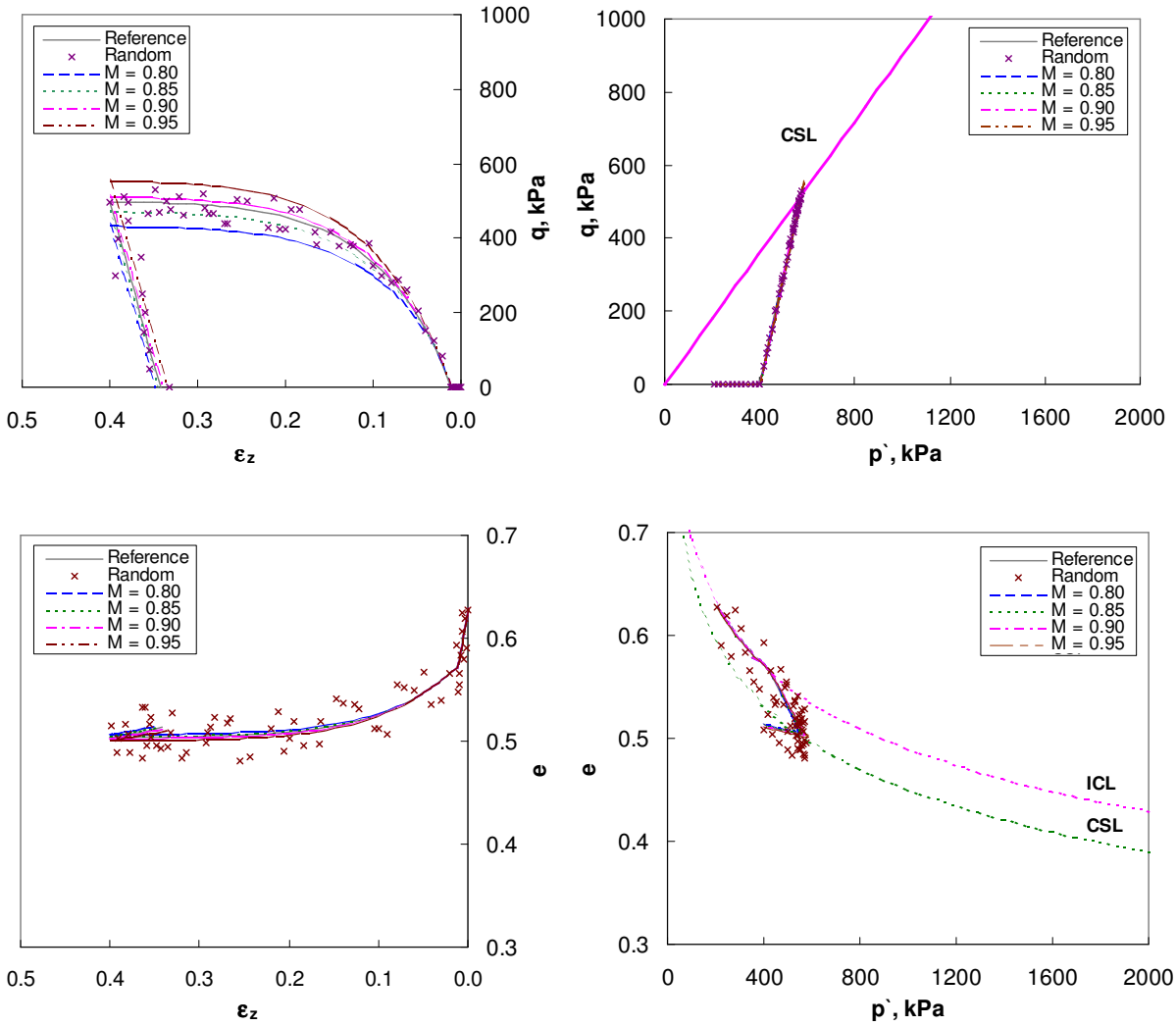

Figure 4.4 Matching trials using M only for CID triaxial test on Weald clay. Notation: Stress ratio M, mean effective stress p`, deviatoric stress q, void ratio e, axial strain ε_z, isotropic consolidation line ICL, and critical state line CSL.

Furthermore, it appears that the identification of the optimum set of constitutive model parameters might be dependent on the number of data points, discretization and sampling of each loading phase in the error function being optimized. Note that figures facilitate the selection of initial values of constitutive parameters during the inversion phase. In general, conclusions made on the similar study in Chapter 3 apply

here as well. In addition, the figures show that the selection of a unique constitutive parameter becomes increasingly more difficult when data are noisy.

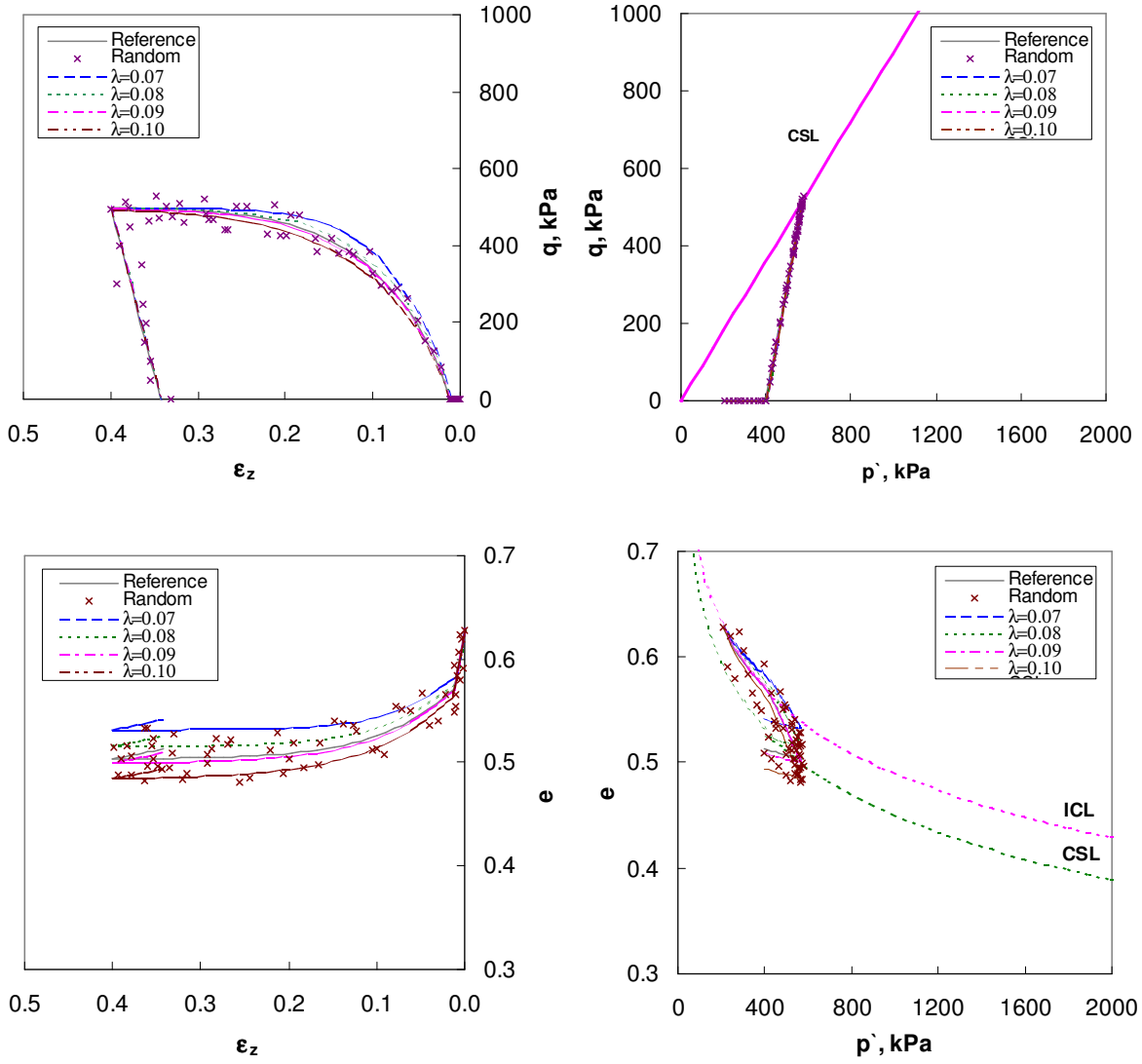

Figure 4.5 Matching trials using λ only for CID triaxial test on Weald clay. Notation: Slope of CSL λ, mean effective stress p`, deviatoric stress q, void ratio e, axial strain ε_z, isotropic consolidation line ICL, and critical state line CSL.

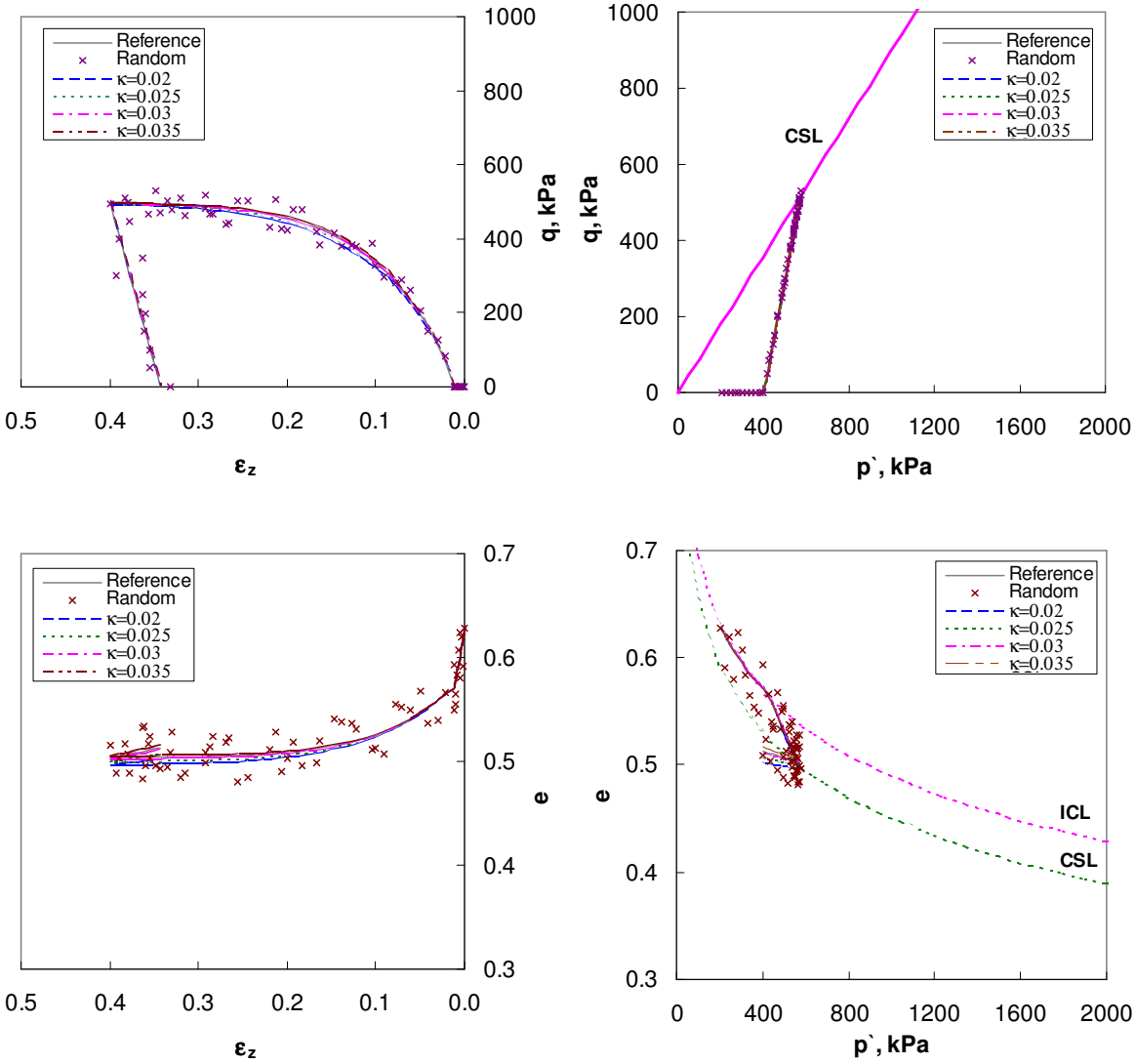

Figure 4.6 Matching trials using κ only for CID triaxial test on Weald clay. Notation: Slope URL κ, mean effective stress p`, deviatoric stress q, void ratio e, axial strain ε_z, isotropic consolidation line ICL, critical state line CSL, and unloading reloading line URL.

4.1.2 Error Surfaces

The individual errors and total error (L2-norms) are shown in Figures 4.7 through 4.11. The following observations can be extracted:

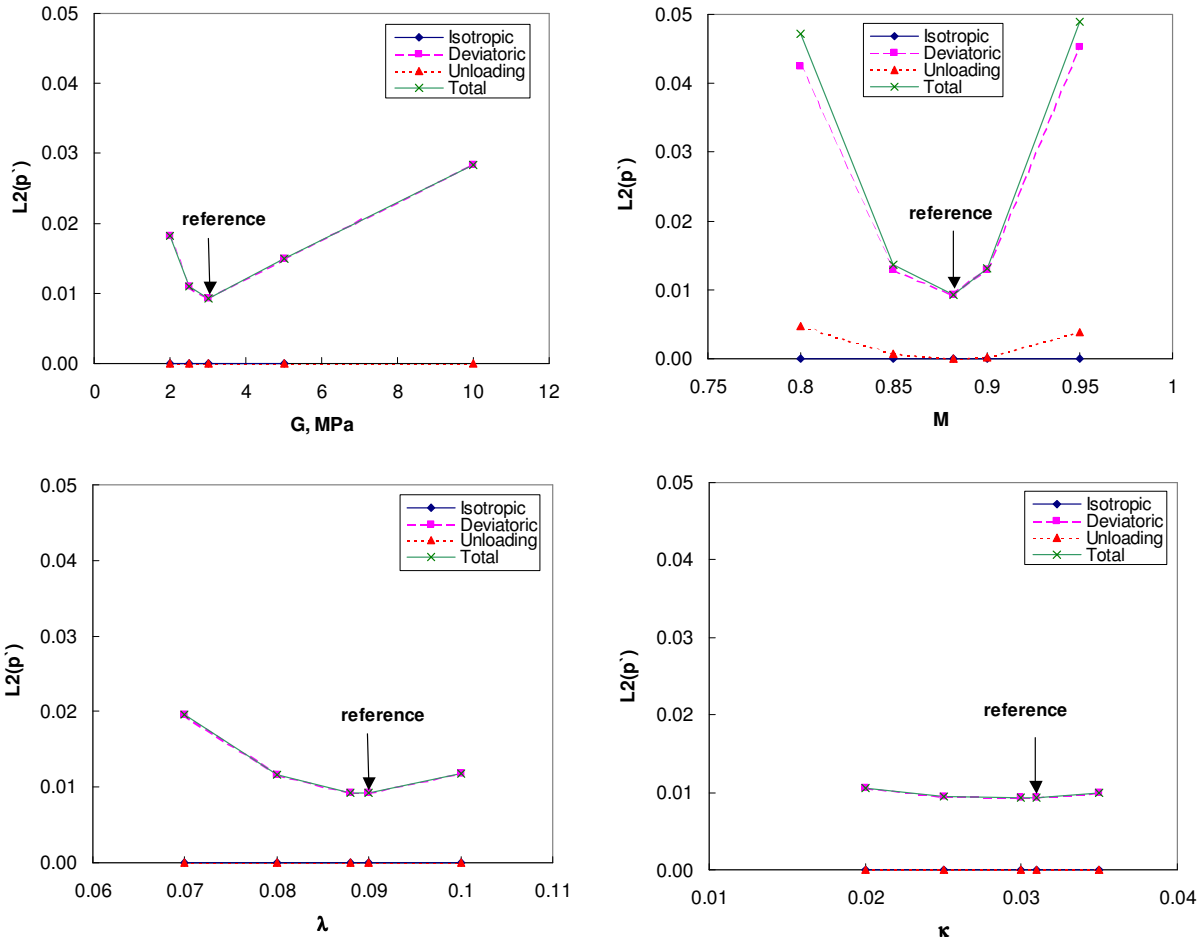

Figure 4.7 L2-norm of the mean effective stress p` - CID triaxial test on Weald clay.

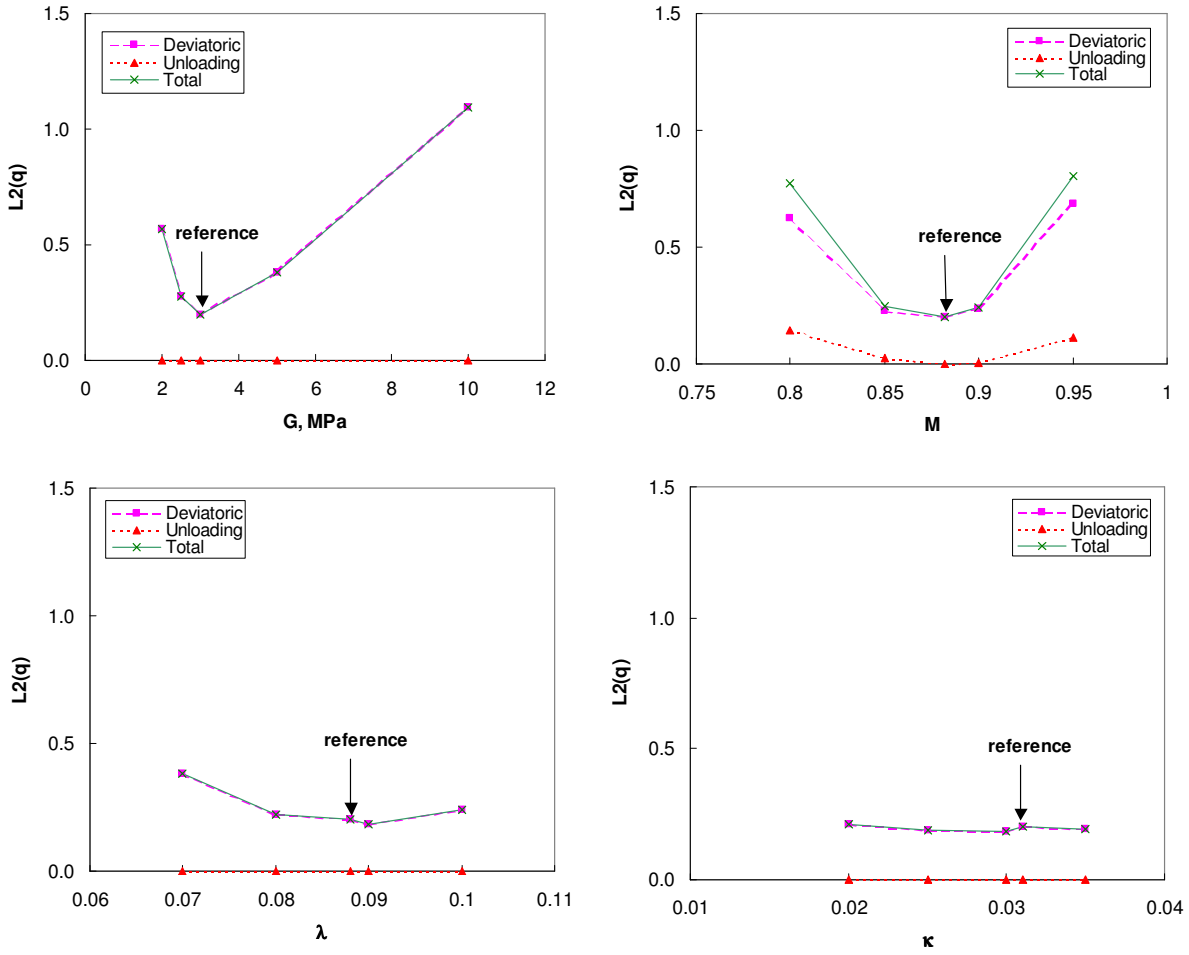

Figure 4.8 L2-norm of the deviatoric stress q - CID triaxial test on Weald clay.

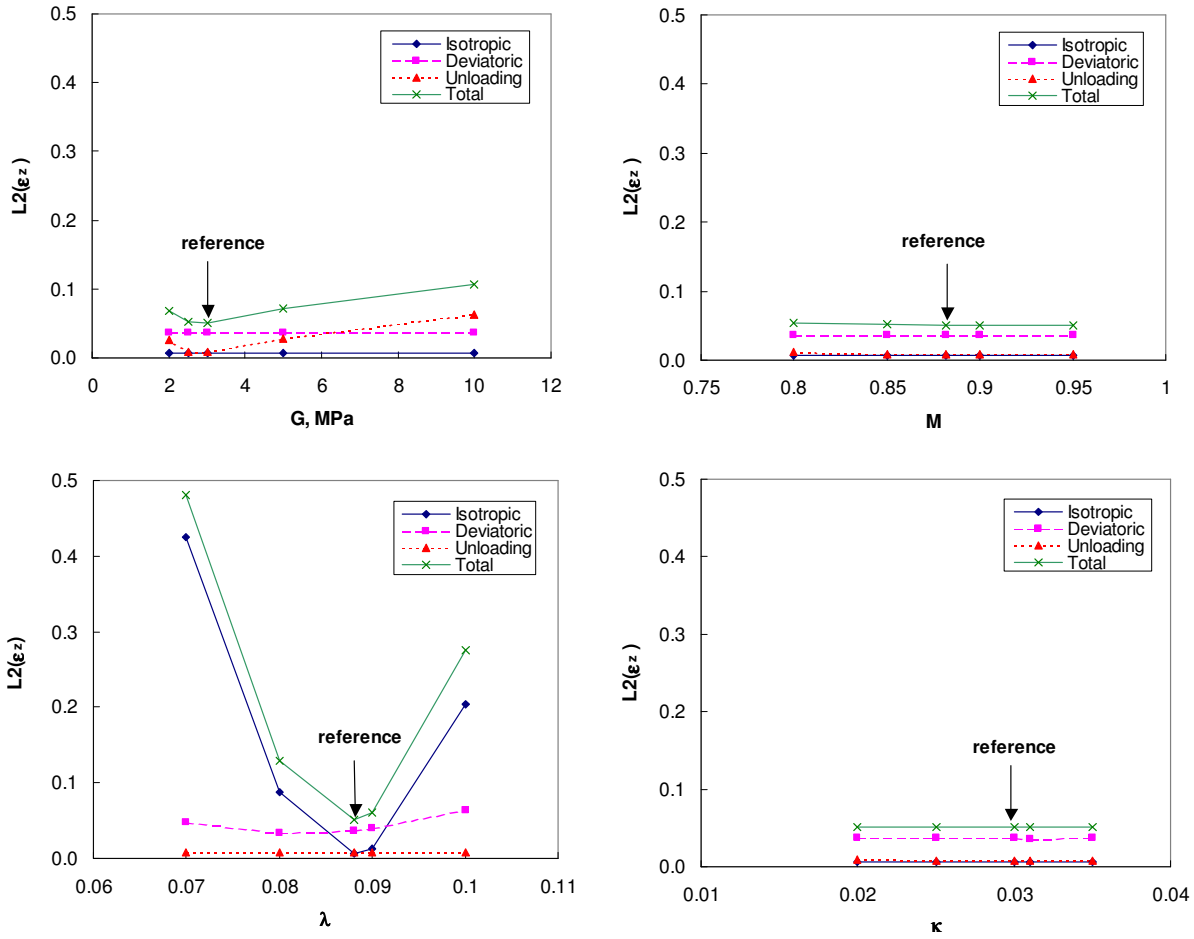

Figure 4.9 L2-norm of the axial normal strain ε_z - CID triaxial test on Weald clay.

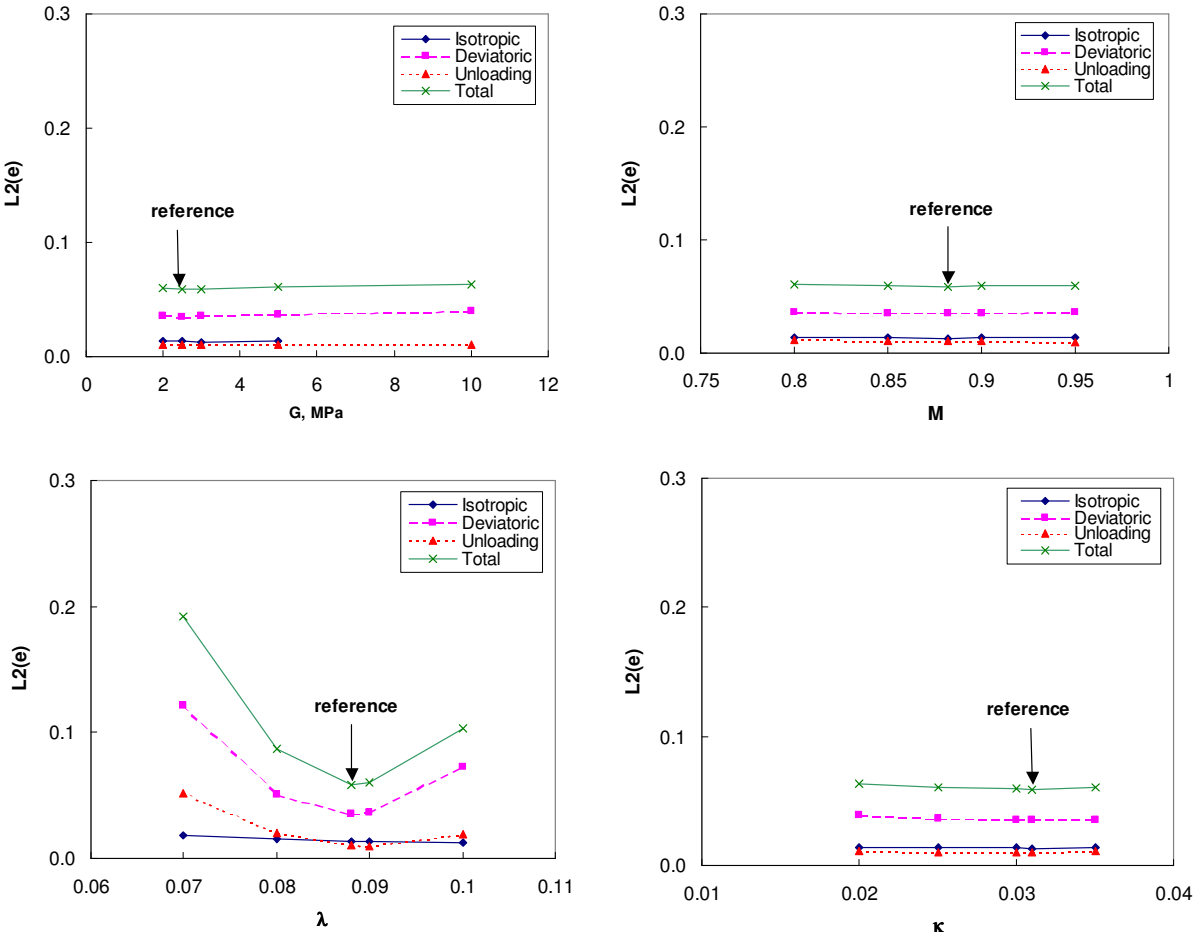

Figure 4.10 L2-norm of the void ratio e - CID triaxial test on Weald clay.

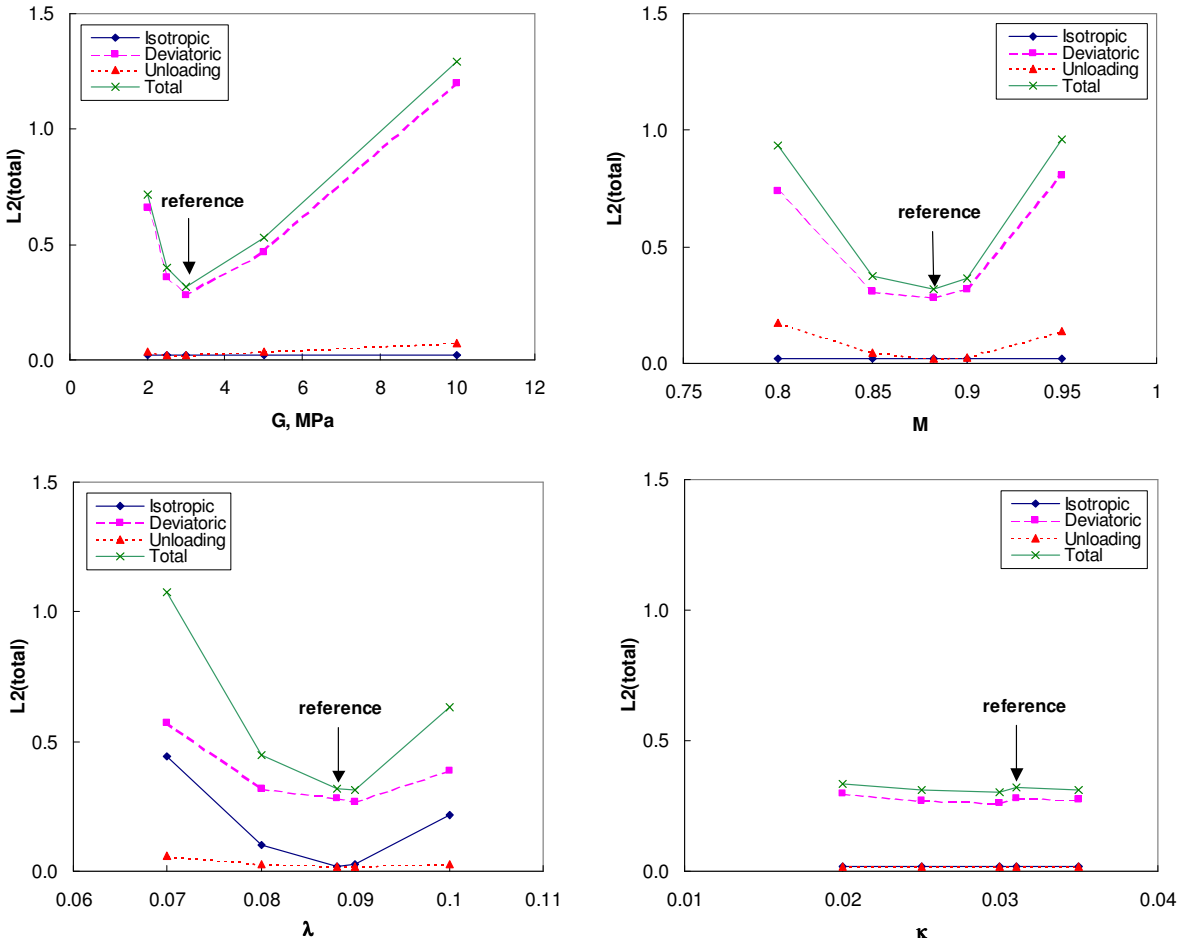

Figure 4.11 Total L2-norm - CID triaxial test on Weald clay.

- An optimum set of constitutive parameters with zero residual error does not exist when noisy data are available.
- Individual error functions generally remain concave. However: M-L2(ε_z) and κ-L2(ε_z) are almost flat (Figure 4.9), while G-L2(e), M-L2(e), and κ-L2(e) have a very light slope with no minimum observed in the studied range of parameters (Figure 4.10).
- The relatively flat curves of individual L2-norms have generally small contribution to that total L2-norm. For example, for the considered κ range the L2(e) is less than 6% of the total L2 while the total error

associated with κ is approximately 30%. Therefore, flat or no-minimum individual error curves have limited effect on the total error, which remains concave.

- The role of constitutive parameters is test phase-dependent. For example λ-L2(ε_z) curve is flat for unloading, yet has a well-defined minimum zone for isotropic loading (Figure 4.9). However, this is not always the case.
- Randomness in data may mask or alter the apparent role of some constitutive parameters. For example, κ is expected to have a major impact on L2(e) during the unloading phases not in the deviatoric loading (Figures 4.7 though 4.11).

4.1.3 Search for Optimum Set of Parameters

A limited search for the optimum set of constitutive model parameters is manually performed to gain insight into the N+1 dimensional error surface. The search for the optimum set starts with the original set of parameters used to generate the noiseless case as the initial guess. Table 4.2 shows the values of the considered parameters and the associated errors (L2-norms). Each constitutive parameter is varied four times (shown in bold face in Table 4.2) while other parameters are kept fixed. The L2-norms of measured variables p`, q, e, ε_z are summed for isotropic loading, deviatoric loading, and unloading (Table 4.2). The total L2-norm is calculated as well. Errors are shown in tabulated form because the very small differences between errors are not suitable for graphical representation and comparisons.

Table 4.2 Single parameter study. Sets of parameter and errors (L2-Norm).

	κ	**λ**	**M**	**e**	**G** (MPa)	**L2-Iso**	**L2-Dev**	**L2-Unl**	**L2 -Total**
REF	0.031	0.088	0.882	0.628	3	0.0154	0.2591	0.0162	0.2907
set-1	0.031	0.0880	**0.870**	0.628	3	**0.0064**	0.2609	0.0266	0.2940
set-2	0.031	0.0880	**0.850**	0.628	3	**0.0064**	0.3137	0.0481	0.3681
set-3	0.031	0.0880	**0.890**	0.628	3	**0.0064**	0.2808	0.0241	0.3114
set-4	0.031	0.0880	**0.860**	0.628	3	**0.0064**	0.2784	0.0350	0.3198
set-5	0.031	**0.0900**	0.870	0.628	3	0.0130	0.2662	0.0264	0.3056
set-6	0.031	**0.0800**	0.870	0.628	3	0.0882	0.3123	0.0361	0.4366
set-7	0.031	**0.0850**	0.870	0.628	3	0.0169	0.2661	0.0286	0.3115
set-8	0.031	**0.0870**	0.870	0.628	3	0.0072	0.2609	0.0271	0.2953
set-9	0.031	0.0880	0.882	0.628	**2.5**	**0.0064**	0.3636	0.0241	0.3941
set-10	0.031	0.0880	0.882	0.628	**2.8**	**0.0064**	0.2879	0.0224	0.3167
set-11	0.031	0.0880	0.882	0.628	**3.2**	**0.0064**	**0.2552**	0.0239	**0.2855**
set-12	0.031	0.0880	0.882	0.628	**3.3**	**0.0064**	0.2553	0.0247	0.2864
set-13	**0.025**	0.0880	0.882	0.628	3	**0.0064**	0.2656	0.0225	0.2945
set-14	**0.028**	0.0880	0.882	0.628	3	**0.0064**	0.2616	**0.0224**	0.2904
set-15	**0.032**	0.0880	0.882	0.628	3	**0.0064**	0.2663	0.0230	0.2957
set-16	**0.033**	0.0880	0.882	0.628	3	**0.0064**	0.2694	0.0233	0.2991

Notation: Isotropic compression Iso, deviatoric loading Dev, unloading Unl. Note: Change in parameter value and minimum errors are in boldface.

An efficient manual search is pursued by varying the parameters in a narrower range and in the direction that minimizes the total error. The results of few trials are graphically plotted in the 4-D space (Figure 4.12) and their total and single stage errors are shown in Table 4.3. The following can be concluded:

- Although L2-total of the single-variable search are all larger than L2-total of the progressive search sets, L2-Iso of many of the single-variable sets are smaller.
- The study proves that the total error does not automatically guarantee an optimum solution. For example, although the total error associated with set-18 is the minimum, the L2-Iso and L2-Unl are not minimum. Indeed this study highlights the importance of considering the phase of loading while searching for the optimum set of constitutive model parameters.
- Set-18 (out of 32) yielded the minimum total and deviatoric error. Constitutive parameters of set-18 are different from those of the reference case. This difference is approximately 12% for the shear modulus G and 10% for the parameter κ. The M and λ parameters are less than 1 % smaller than those of the reference case.
- The isotropic L2-norm is the least sensitive in the search.
- Different sets of parameters may yield the same error. This implies that noisy data may lead to non-unique solutions especially if the total error is used. For example, set-28 and set-30 have the same total error but different phase errors which compensate to yield the same L2-total.

- There is no full decoupling of constitutive parameters: some parameters affect all phases to a lesser or higher degree (Chapter 3).

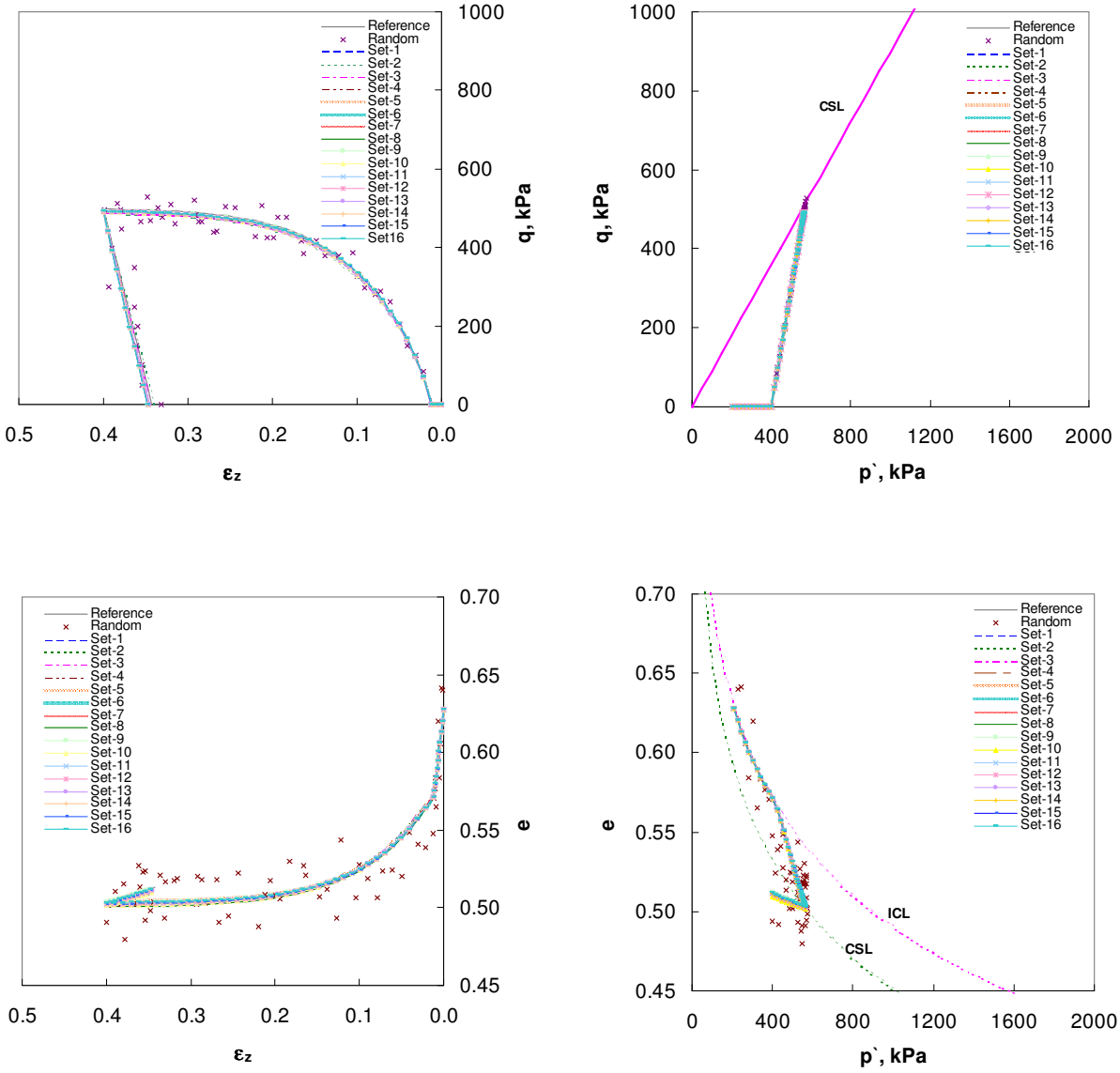

Figure 4.12 Matching trials using combinations of Cam-Clay parameters - CID triaxial test - Weald clay. Notation: Slope URL κ, mean effective stress p`, deviatoric stress q, void ratio e, axial strain ε_z, isotropic consolidation line ICL, critical state line CSL, and unloading reloading line URL.

Table 4.3 Progressive search: sets of parameters and associated errors (L2-Norm).

	κ	λ	M	e	G (MPa)	L2-Iso	L2-Dev	L2-Unl	L2 -Total
REF	0.031	0.088	0.882	0.628	3	0.0154	0.2591	0.0162	0.2907
Set-1	**0.028**	**0.0870**	**0.870**	0.628	**3.2**	0.0164	0.2391	0.0214	0.2769
Set-2	0.028	0.0870	0.870	0.628	**2.8**	0.0164	0.2961	0.0195	0.3321
Set-3	0.028	0.0870	0.870	0.628	**3**	0.0164	0.2598	0.0201	0.2964
Set-4	0.028	0.0870	**0.875**	0.628	**3.2**	0.0164	0.2385	0.0189	0.2737
Set-5	0.028	**0.0865**	0.875	0.628	3.2	0.0179	0.2379	0.0191	0.2749
Set-6	0.028	**0.0875**	0.875	0.628	3.2	0.0156	0.2394	0.0187	0.2738
Set-7	0.028	**0.0880**	0.875	0.628	3.2	**0.0154**	0.2408	0.0186	0.2748
Set-8	0.028	**0.0890**	0.875	0.628	3.2	0.0173	0.2449	0.0184	0.2807
Set-9	**0.03**	0.0880	0.875	0.628	3.2	**0.0154**	0.2393	0.0187	0.2735
Set-10	**0.027**	0.0880	0.875	0.628	3.2	**0.0154**	0.2426	0.0186	0.2767
Set-11	**0.029**	0.0880	0.875	0.628	3.2	**0.0154**	0.2397	0.0186	0.2737
Set-12	**0.0285**	0.0880	0.875	0.628	3.2	**0.0154**	0.2401	0.0186	0.2741
Set-13	0.0285	0.0880	0.875	0.628	**3.1**	**0.0154**	0.2480	**0.0179**	0.2813
Set-14	0.0285	0.0880	0.875	0.628	**3.25**	**0.0154**	0.2374	0.0190	0.2718
Set-15	0.0285	0.0880	0.875	0.628	**3.3**	**0.0154**	0.2353	0.0194	0.2701
Set-16	0.0285	**0.0875**	0.875	0.628	3.3	0.0156	0.2347	0.0195	0.2699
Set-17	0.0285	0.0875	0.875	0.628	**3.35**	0.0156	0.2337	0.0200	0.2692
Set-18	**0.028**	0.0875	0.875	0.628	**3.35**	0.0156	**0.2332**	0.0200	**0.2688**
Set-19	**0.0285**	**0.0870**	0.875	0.628	**3.35**	0.0164	0.2339	0.0202	0.2704
Set-20	**0.028**	0.0870	0.875	0.628	**3.35**	0.0164	**0.2332**	0.0201	0.2697
Set-21	**0.0285**	**0.0875**	**0.870**	0.628	**3.35**	0.0156	0.2366	0.0217	0.2739
Set-22	0.0285	0.0875	0.875	0.628	**3.25**	0.0156	0.2366	0.0191	0.2713
Set-23	**0.028**	0.0875	0.875	0.628	3.25	0.0156	0.2367	0.0191	0.2714
Set-24	**0.0285**	**0.0870**	0.875	0.628	3.25	0.0164	0.2362	0.0193	0.2719
Set-25	**0.028**	0.0870	0.875	0.628	3.25	0.0164	0.2360	0.0193	0.2717
Set-26	**0.0285**	**0.0875**	**0.870**	0.628	3.25	0.0156	0.2366	0.0217	0.2739
Set-27	0.0285	**0.0872**	0.875	0.628	**3.3**	0.0160	0.2347	0.0196	0.2704
Set-28	0.0285	**0.0875**	**0.872**	0.628	3.3	0.0156	0.2337	0.0209	0.2703
Set-29	0.0285	0.0875	**0.874**	0.628	3.3	0.0156	0.2343	0.0200	0.2698
Set-30	0.0285	0.0875	**0.876**	0.628	3.3	0.0156	0.2355	0.0191	0.2703
Set-31	0.0285	0.0875	**0.878**	0.628	3.3	0.0156	0.2375	0.0185	0.2717
Set-32	0.0285	**0.0870**	0.878	0.628	3.3	0.0164	0.2379	0.0187	0.2731

Notation: Isotropic compression Iso, deviatoric loading Dev, unloading Unl. Note: Change in parameter value and minimum errors are in boldface

4.2 MODELING ERRORS

The forward simulation implemented during the inversion of constitutive model parameters (right-hand side - Figure 4.2) brings two important sources of error to the inversion process: (1) experimental and boundary conditions, and (2) selected constitutive model. The effects of these two error components are analyzed next.

4.2.1 Test Boundary Conditions

The inhomogeneity created by triaxial end restraints is not a true material behavior; therefore, test boundary conditions need to be considered for proper calibration of constitutive models (Sheng et al., 1997). This section includes simulations of drained and undrained conventional triaxial compression test to study the effect of frictional versus non-frictional boundaries on test measurements and inverted parameters. Many researchers have studied the end restraint exerted by cap and base in conventional compression triaxial test. The effect of test boundary conditions has been studied using either experimental results (Rowe and Barden, 1964; Bishop and Green, 1965; Duncan and Dunlop, 1968; Lee, 1978) or numerical realizations (Sheng et al., 1997; Liyanapathirana et al., 2005). The combined effects of boundary conditions, slenderness ratio and drainage conditions have been studied including manifestations such as strain localization and shear banding (Peters et al, 1988; Lade et al., 1996; Yamamuro and Lade, 2005; Wang and Lade, 2001; Lade, 2002; Alshibli, 2003). Surprisingly, these studies vary drastically in their conclusions on the severity and nature of the effects of end restraint on the results of triaxial tests.

There are agreed effects. End restraints and partial drainage in conventional triaxial testing are likely the main cause of specimen bulging around its mid height (Sheng et al., 1997 and Liyanapathirana et al., 2005). The frictional cap and base in triaxial tests creates non-uniform volumetric strains in drained tests and moisture migration in undrained tests (Duncan and Dunlop, 1968). The adverse effect of triaxial end restraints on strength is typically minimized by increasing the specimen height-to-width ratio up to 2 or 2.5 beyond which there is no further decrease in strength or by providing a mechanism at the specimen ends that allows free lateral end deformations, typically end lubrication (Duncan and Dunlop, 1968). Since shear strength, stress-strain relations, and friction angle are typically the main concern in triaxial testing, less attention may be given to non-uniformity in volumetric strain and moisture migration (Duncan and Dunlop, 1968). The effect of cap and base on internal friction angle is limited for specimens with height-to-diameter ratios of 2 or larger (Bishop and Green, 1965). End lubrication assists in reducing the overestimated shear strength for specimens with a height-to-diameter ratio of 1.0 (Bishop and Green, 1965). Lubricated platens lead to a more uniform strain field throughout the specimen in triaxial compression (Lade et al., 1996). The effects caused by the frictional triaxial boundaries are insignificant during de-structuring but cause very non-uniform strains and stresses even in the mid-region of a 2:1 height-to-diameter ratio specimen during hardening (Liyanapathirana et al., 2005).

Increasing the specimen slenderness ratio and adding end lubrication do not eliminate the development of inhomogeneity in stress and strain fields. In particular,

shear bands tend to develop in granular materials that exhibit post-peak strain softening behavior (Lade et al., 1996; Lade, 2002; and Peters et al., 1988). The stress-strain response associated with the formation of shear banding is dependent on test configuration (Peters et al., 1988, Lade, 2002, and Alshibli et al., 2003). Both peak and post-peak behaviors are influenced by localization (Peters et al., 1988).

The stress and strain fields created in a triaxial compression test with frictional boundaries are non-homogeneous. However, the data are analyzed assuming the response at a point, i.e., a homogenous response.

Simulations Using Finite Element Method

Triaxial compression tests are simulated for two boundary conditions. The non-frictional condition allows lateral displacements. The frictional condition is modeled in the extreme case of bonding, that is, the top nodes of the soil are laterally restrained. The boundary conditions and loading for the right top quarter of an axi-symmetric soil strip are shown in Figure 4.13. Soil is represented by 8-noded quadrilateral axi-symmetric solid element CAX8R (ABAQUS, 2005). The axi-symmetric slice is represented by 192 elements and 633 nodes. The constitutive model is the Modified Cam-Clay with parameters given in Table 2.2. The confining stress is known at all loading increments. The data needed for complete reporting of the results of a drained and undrained triaxial test in the 4D space are:

- Vertical displacement of the top nodes at all increments (δz_i)
- Nodal forces of the top nodes at all increments (Fz_i)

- Orthogonal/Cartesian normal strain components of all elements at all increments ($\varepsilon 11_i$, $\varepsilon 22_i$, $\varepsilon 33_i$)
- Pore pressure at all increments (u_i)

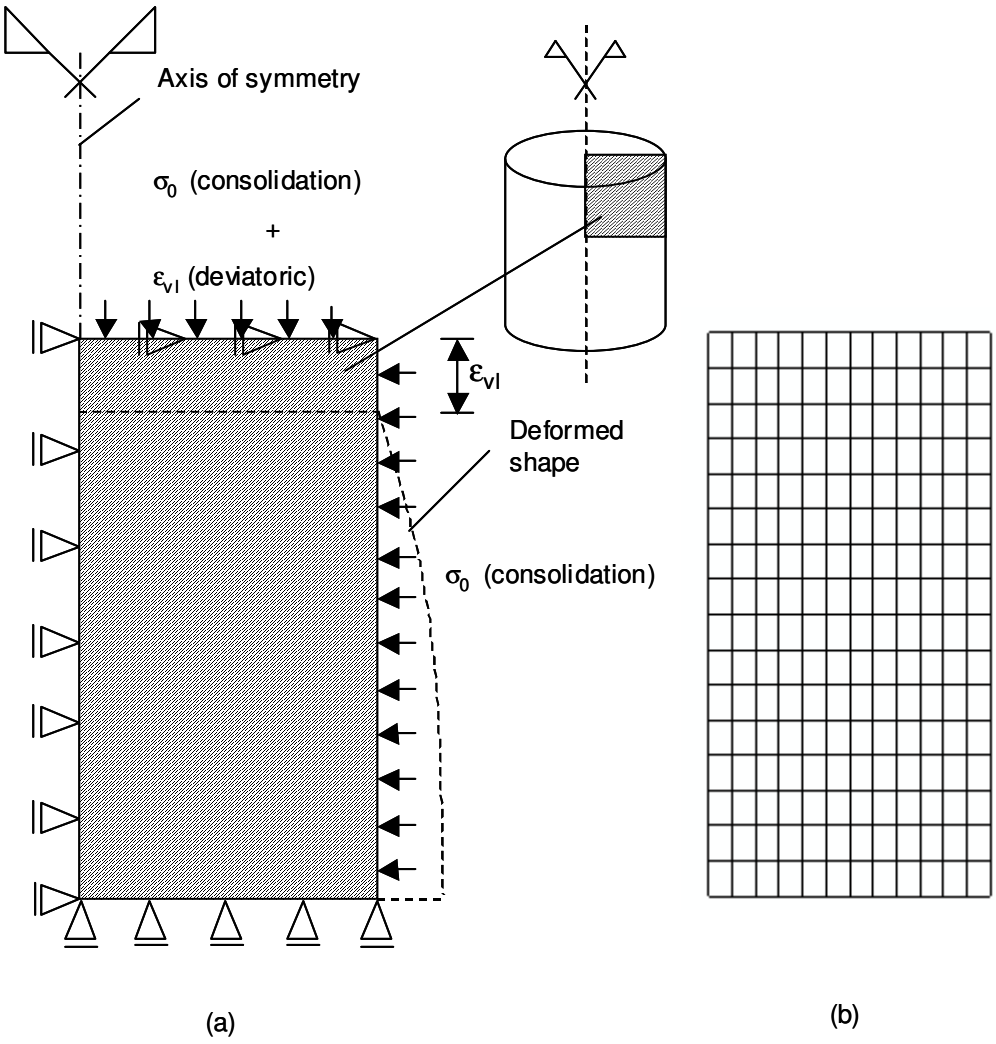

Figure 4.13 Triaxial test simulation for frictional boundaries (a) Geometry, boundary conditions, and loading. (b) Finite element mesh. Notation: Confining stress p_0, and applied vertical displacement δ_{vl}.

The results of the numerical simulations are reported as gathered through experiments, i.e., global measurements, as summarized in Table 4.4.

Table 4.4 Numerically reported triaxial measurements at each *i*-th increment.

Measurement	Equation	Test	Notes
External vertical strain	$\varepsilon_{z_i} = \frac{\sum_{n=1}^{Nt} \delta z_i^n}{Nt \times L_0}$	Drained & undrained	δz = vertical displacement Nt = number of top nodes L_0 = original specimen height
Corrected cross-sectional area	$A_{c_i} = \frac{A_0}{1-\varepsilon_{z_i}}$	Drained & undrained	A_0 = original area (Head, 1994)
Pore pressure	u_i	Undrained	
External vertical effective stress	$\sigma'_{z_i} = \frac{\sum_{m=1}^{Mt} Fz_i^m}{A_{c_i}} - u_i$	Drained & undrained	Fz = nodal force Mt = number of top elements
External mean effective stress	$p_i = \frac{\sigma'_{z_i} + 2(\sigma_0 - u_i)}{3}$	Drained & undrained	σ_0 = cell pressure
External deviatoric stress	$q_i = \sigma'_{z_i} - (\sigma_0 - u_i)$	Drained & undrained	σ_0 = cell pressure
Global volumetric strain	$\varepsilon_{vol_i} = \frac{\sum_{m=1}^{M} (\varepsilon_{11} + \varepsilon_{22} + \varepsilon_{33})_i^m}{M}$	Drained	$\varepsilon_{11}, \varepsilon_{22}, \varepsilon_{33}$ are the cartesian normal strains M = total number of elements
Global void ratio	$e_i = e_o + (1+e_0)\varepsilon_{vol_i}$	Drained	e_0 = initial void ratio

Figures 4.14 through 4.17 show the results of the same four triaxial simulations: normally consolidated-isotropically consolidated drained (NC-CID), over consolidated isotropically consolidated drained (OC-CID), normally consolidated isotropically consolidated undrained (NC-CIU), and over consolidated isotropically consolidated undrained (OC-CIU). Isotropic consolidation line (ICL) and critical state line (CSL) are plotted using Equations 2.6 and 2.8, respectively.

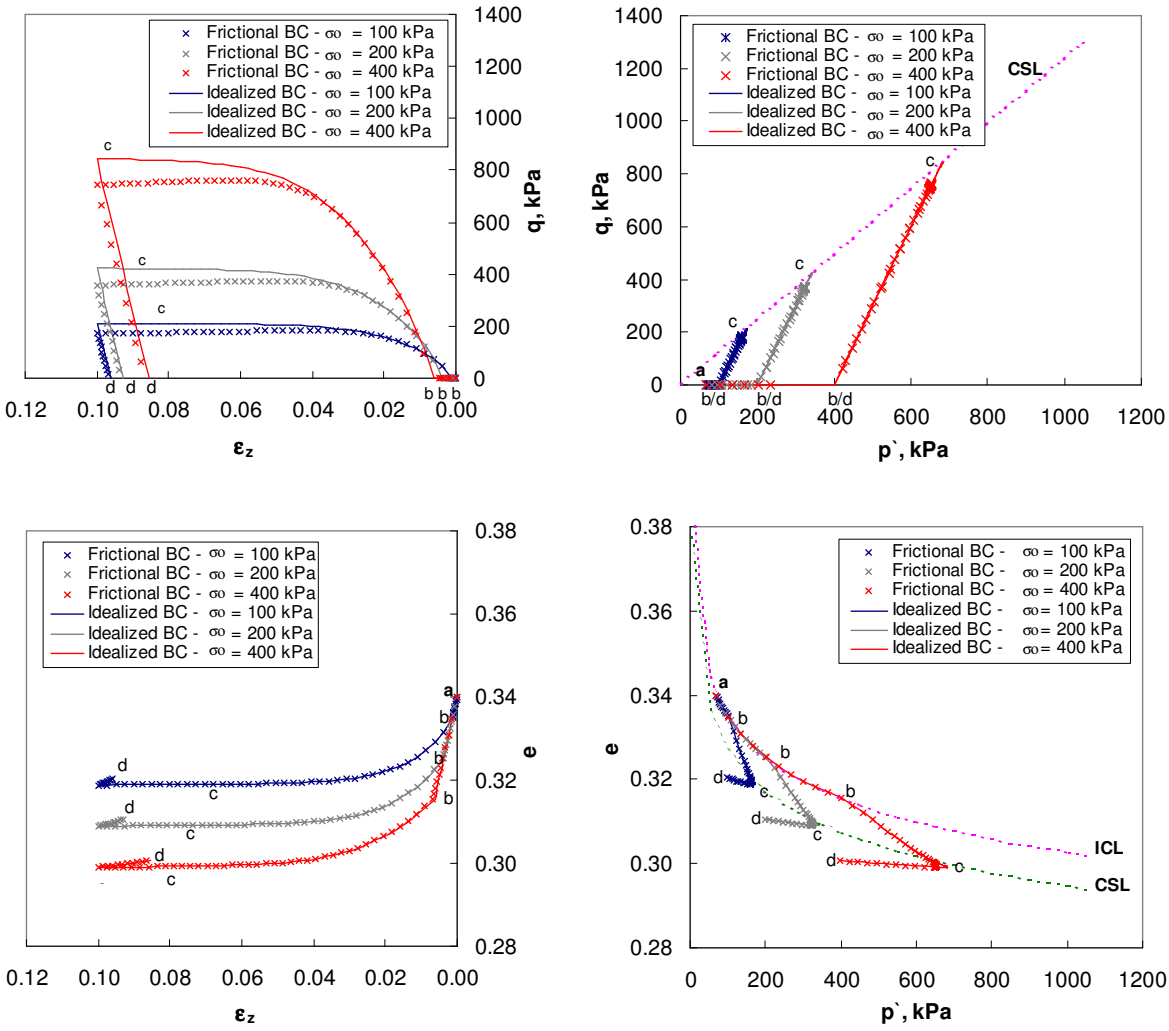

Figure 4.14 Consolidated-drained test (CID) - normally consolidated Pueblo sand. Notation: Mean effective stress p`, deviatoric stress q, void ratio e, axial strain ε_z, isotropic consolidation line ICL, and critical state line CSL.

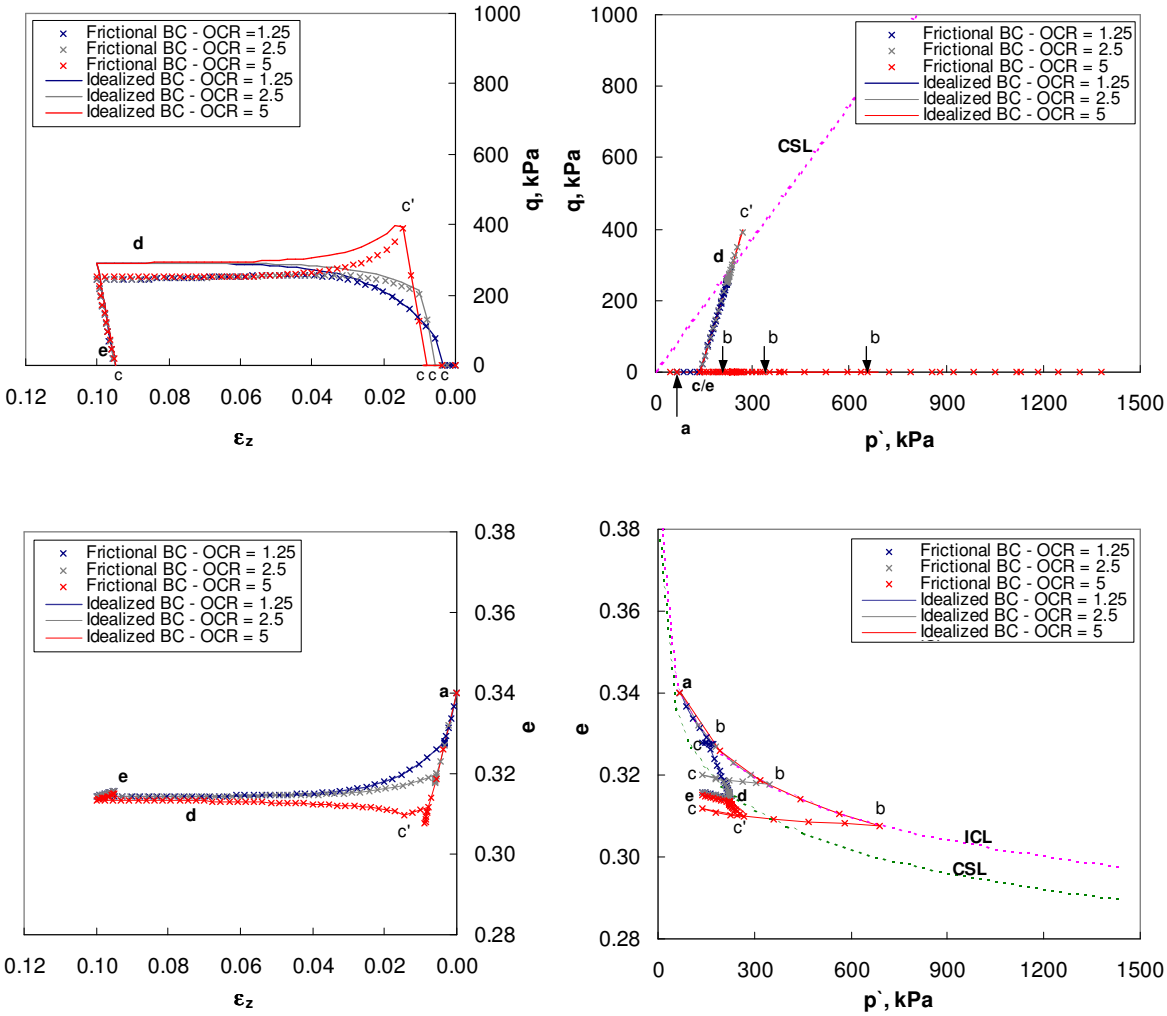

Figure 4.15 Consolidated-drained test (CID) - over consolidated Pueblo sand. Notation: Mean effective stress p`, deviatoric stress q, void ratio e, axial strain ε_z, isotropic consolidation line ICL, and critical state line CSL.

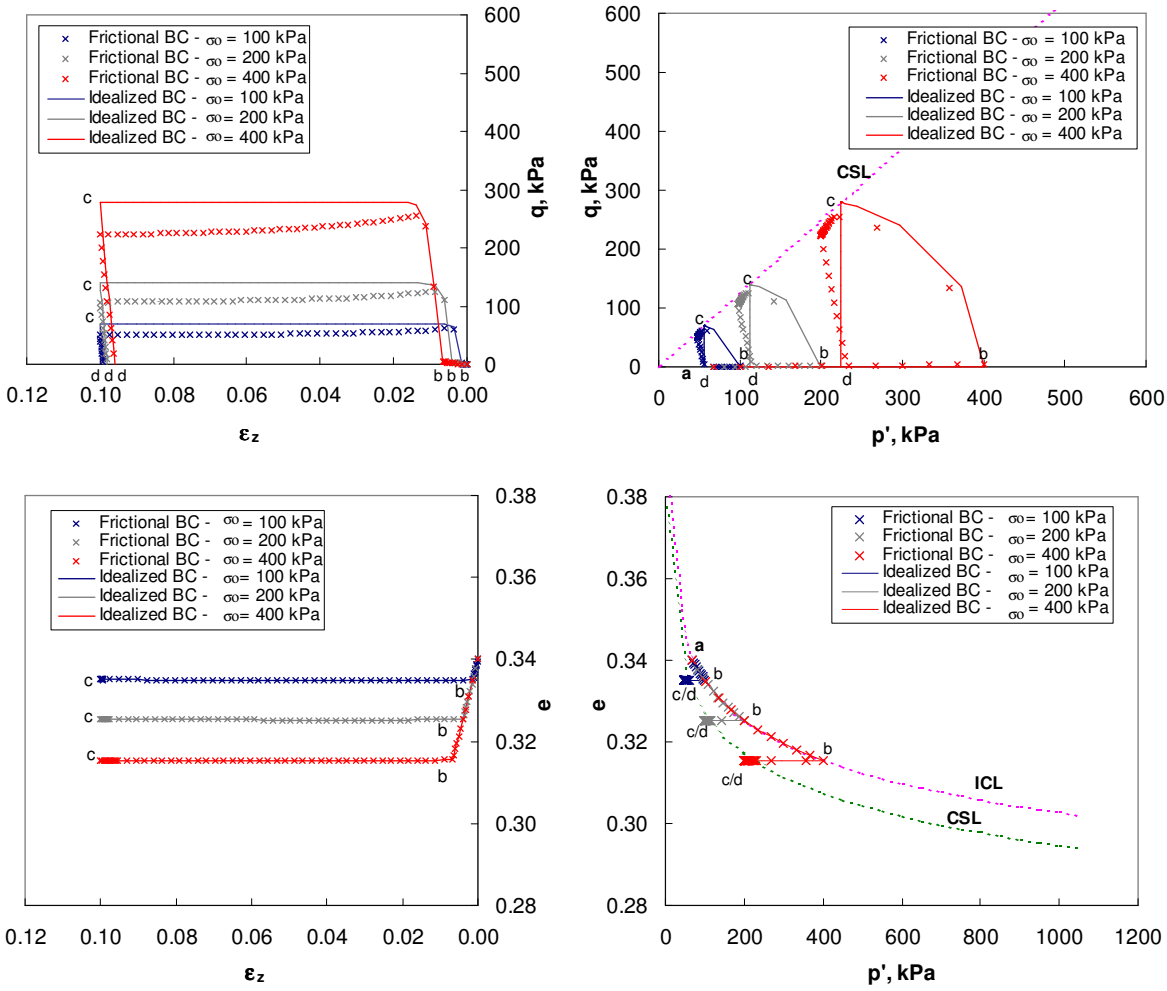

Figure 4.16 Consolidated-undrained test (CIU) - normally consolidated Pueblo sand. Notation: Mean effective stress p`, deviatoric stress q, void ratio e, axial strain ε_z, isotropic consolidation line ICL, and critical state line CSL.

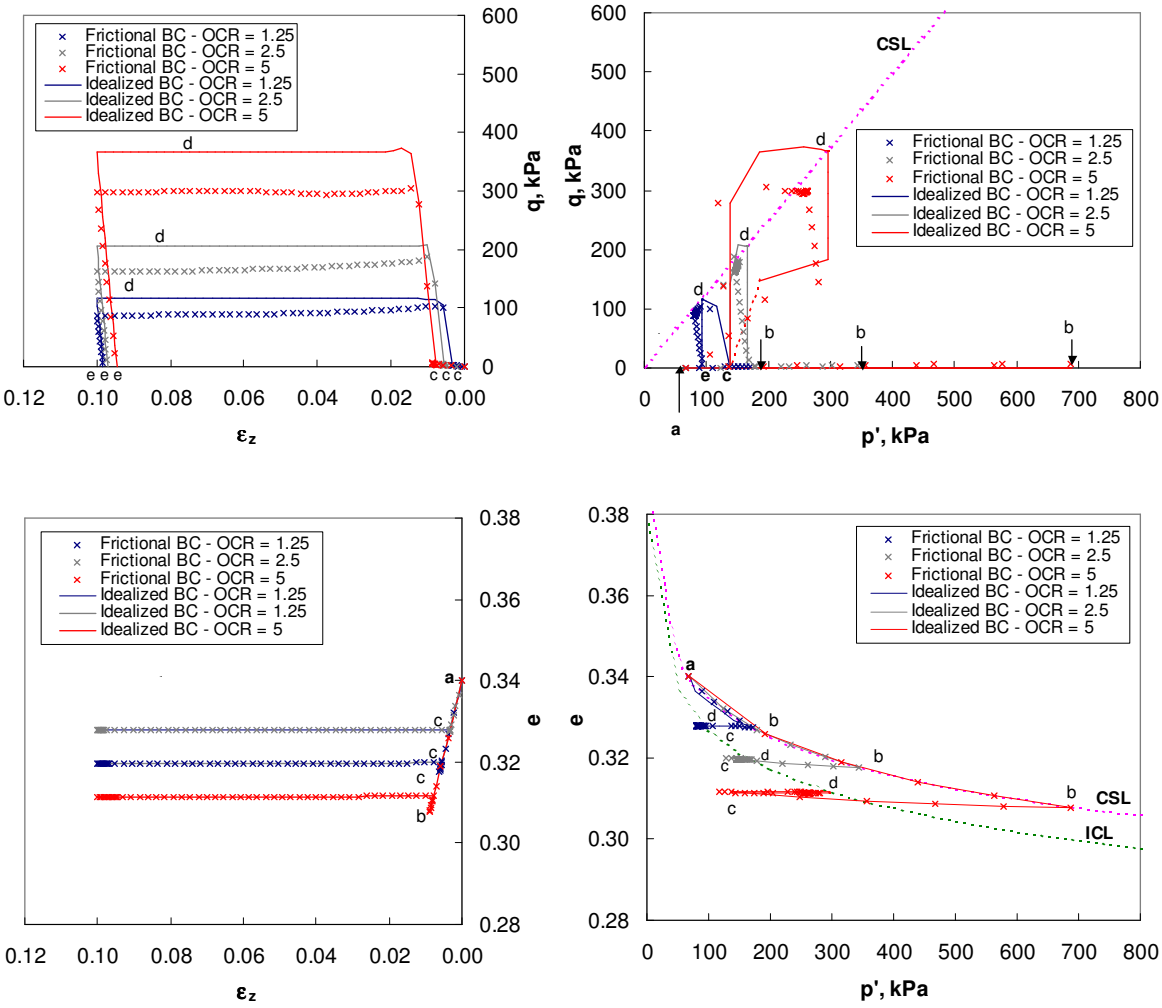

Figure 4.17 Consolidated-undrained test (CIU) - over consolidated Pueblo sand. Notation: Mean effective stress p`, deviatoric stress q, void ratio e, axial strain ε_z, isotropic consolidation line ICL, and critical state line CSL.

The trends on the 4D space are quite similar for both boundary conditions. The ε_z-e plot is identical to that of the frictionless case. The mean effective stress p' is slightly different from the idealized (frictionless) case which is reflected on the p`-e plot. The most affected measurements are the deviatoric stress q and, to a lesser degree, the mean effective stress p'. In all simulations q and p` with frictional boundaries are smaller than those measured with frictionless boundaries.

Deviation from Representative Measurements

While global measurements exhibit relatively small differences, vertical and horizontal strains vary extensively within the specimen as do stresses. Figure 4.18 shows the contours of radial, hoop, and axial stresses and strains in a compression triaxial test on Pueblo sand at the end of deviatoric loading (strain controlled tests, terminal ε_z = 10%). The cell pressure (isotropic stress) is kept at 100 kPa during shearing. While the axial strains are compressive in the entire specimen, the radial and hoop strains are in extension. The axial strain gradually increases towards the center of the specimen. This is expected because the applied displacement in deviatoric loading squeezes the specimen vertically; consequently, the specimen shortening is associated with compressive axial strain while the specimen bulging is associated with tensile radial and hoop strains. The lateral restraint at the boundary of the specimen in conventional triaxial tests is not only responsible for the barrel shape but also alters the normal stress distribution (Scholey et al., 1995). The axial stress near the end of the specimen is approximately 25 to 50% smaller than that at the mid-height (Figure 4.18.f). At the specimen end, the hoop and radial stresses range from 100 kPa to 200 kPa, while the cell pressure is kept at 100 kPa. In fact, lateral restraint at the specimen ends is responsible for the increase in hoop and lateral stresses and the redistribution of stresses and strains in the entire specimen. Hoop and radial stresses are larger than the cell pressure almost everywhere in the specimen with frictional boundaries. These observations explain why the deviatoric stress in Figures 4-14 through 4-17 is always smaller for the frictional boundary case.

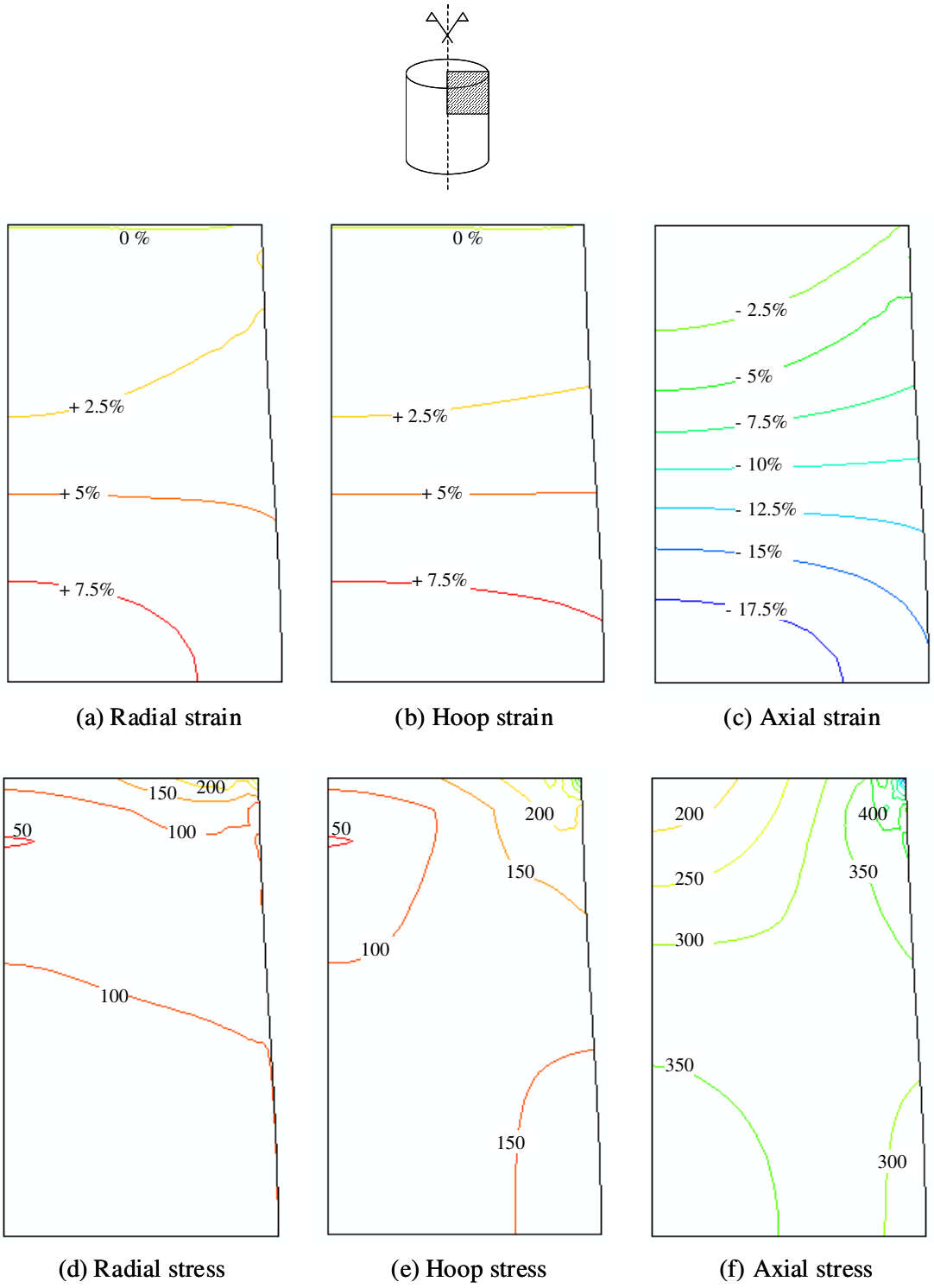

Figure 4.18 Normal stresses and strains for CIU test on normally consolidated Pueblo sand at the end of the deviatoric loading (ε_z = 10%, confining stress = 100 kPa). Note: Stresses in kPa; tensile strain (+); compressive strain (-).

4.2.2 Constitutive Model

Models are an abstraction of reality. For example, the continuum mechanics approach inherently ignores fine-scale structure and most classical constitutive models in geomechanics assume that internal energy is dissipated solely by friction (Oreskes et al., 1994, Murthy et al., 1988 and Murthy et al., 1991). Furthermore, model parameters are generally determined at a much smaller scale than the simulations or applications that utilize the model (Oreskes et al., 1994). In general, all simplifying assumptions cause model uncertainty.

The success of a constitutive model is tied to its ability to qualitatively and quantitatively reproduce the measurements. Figure 4.19 shows experimental q-ε_z data gathered for an over consolidated soil. Three models are fitted: MCCM (5 unknowns), elasto-plastic (3 unknowns), and hyperbolic (2 unknowns). The following observations can be made:

- Models with a larger number of unknowns can fit data better but may fail to predict new data well.
- Familiarity with expected behavior and recognition of the constitutive model limitations help in fitting experimental data.

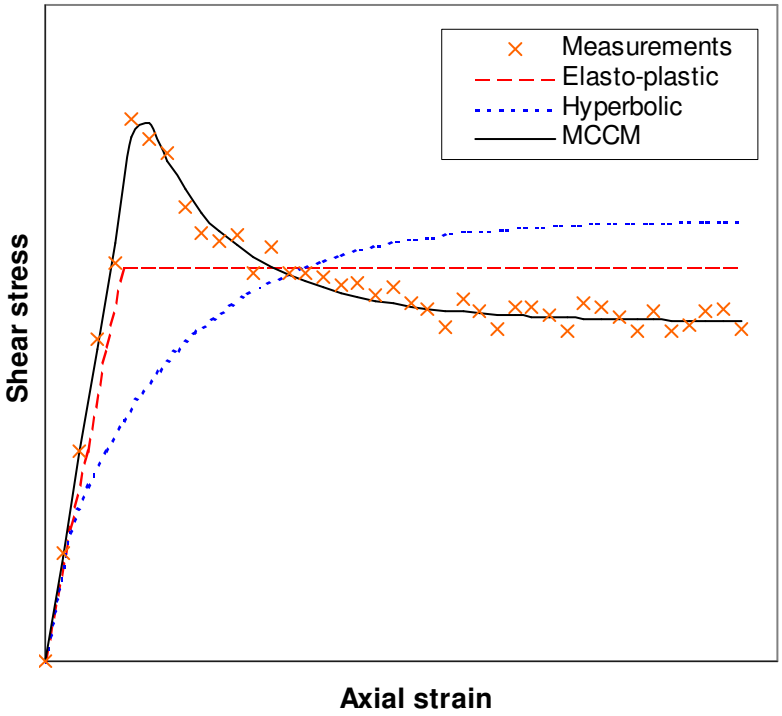

Figure 4.19 Examples of fitting test data with different constitutive models.

4.3 SUMMARY AND CONCLUSIONS

Measurement errors and forward simulation errors (boundary conditions and model selection) affect the adequacy of material characterization through inversion. In particular, numerical results show:

- Partial L2 norms (e.g. κ-L2(q) and λ-L2(q) in Figure 4.8) are not always concave when noisy data are involved; however, the total error curves appear to remain concave.
- The optimum set of parameters obtained from total error inversion may not be the optimum set for individual test measurements.

- Prediction of soil response from estimated constitutive parameters based on noisy test measurements is always accompanied by a residual error.
- While the search for optimum constitutive parameters that minimizes a selected error function is computationally simple, the choice of the error function remains critical.
- The optimum set of constitutive parameters is best obtained when the objective function guiding the inversion is well defined.
- The set of parameters that minimizes the total error could be thought of as an average optimum set, but it does not necessarily yield a minimum error for all loading phases. The solution set depends on the number of points representing the test phase (discretization and data sampling).
- Some of the constitutive parameters estimated for a 5% random error in test measurements deviate from a reference set of constitutive parameters (for non-noisy data) by up to approximately 12%.
- The error function (total or individual) and test phase of interest could govern the search for the optimum set of constitutive parameters.
- Fitting parameters to noisy test data may not lead to a unique solution set.
- Boundary conditions in triaxial testing have a significant effect on the stress and strain distribution within the specimen.
- The current routine in reporting conventional triaxial test data gathered with frictional boundary underpredicts soil strength.

- Using an improper constitutive model hinders the understanding of the expected soil behavior and increases the distance between model and data.

CHAPTER V

A NEW GEOTECHNICAL TEST - DESIGN

The previous chapters considered constitutive model calibration as an inverse problem, analyzed error functions, and the potential effects of measurement and model errors. This chapter centers on the development of a new information-rich test.

The goal is to design a versatile, informative test that can support the calibration of all parameters of the adopted constitutive model at once. The test must accommodate all required measurements, be repeatable and involve a relatively simple device. From the inversion point of view, the test must provide independent information rather than correlated massive data. Therefore diversity of measurements enables robust and unique inverse solutions. Preliminary designs are experimentally tested to explore the suitability of the loading pattern and the richness of the gathered data. Then, the candidate test is numerically simulated to assess invertability.

5.1 LESSONS FROM CONVENTIONAL TESTS

A wide range of conventional laboratory geotechnical tests, including direct shear, ring shear, triaxial, true triaxial, oedometer, and unconfined compression, have been used solely or in combination to obtain constitutive model parameters. Typically, the larger the number of the model parameters, the larger the number of test runs or the type of tests and boundary conditions that are needed (Chapter 4). Most

conventional tests are designed to provide uniform stress and strain fields to facilitate interpretation.

Axial strain measurements in conventional triaxial tests suffer from seating errors, alignment errors, bedding errors, and compliance errors (Jardine et at., 1984; Scholey et al., 1995; Baldi at al., 1996).

Bedding errors and compliance of the loading system cause considerable errors in externally measured deformations (Hird and Yung, 1989). Therefore, local strain measurements have proven to be superior to external measurements (Goto et al., 1991; Cuccovillo and Coop, 1997; Jardine et al., 1984; Hird and Yung, 1989; and Scholey et al., 1995).

5.2 PRELIMINARY TESTING - EXPERIMENTAL

Preliminary tests are conducted to investigate the general displacement pattern associated with various test configurations and possible difficulties that could be experienced during testing. Ottawa 20-30 sand is used in the preliminary tests. A cylindrical, latex-wrapped specimen is prepared for this purpose (Figure 5.1). Confining stress is applied by vacuum through the bottom platen. Vacuum pressure is varied from 10 kPa to 80 kPa. Photographs of some tests are shown in Figure 5.2. Table 5.1 shows the main characteristics of each test setup.

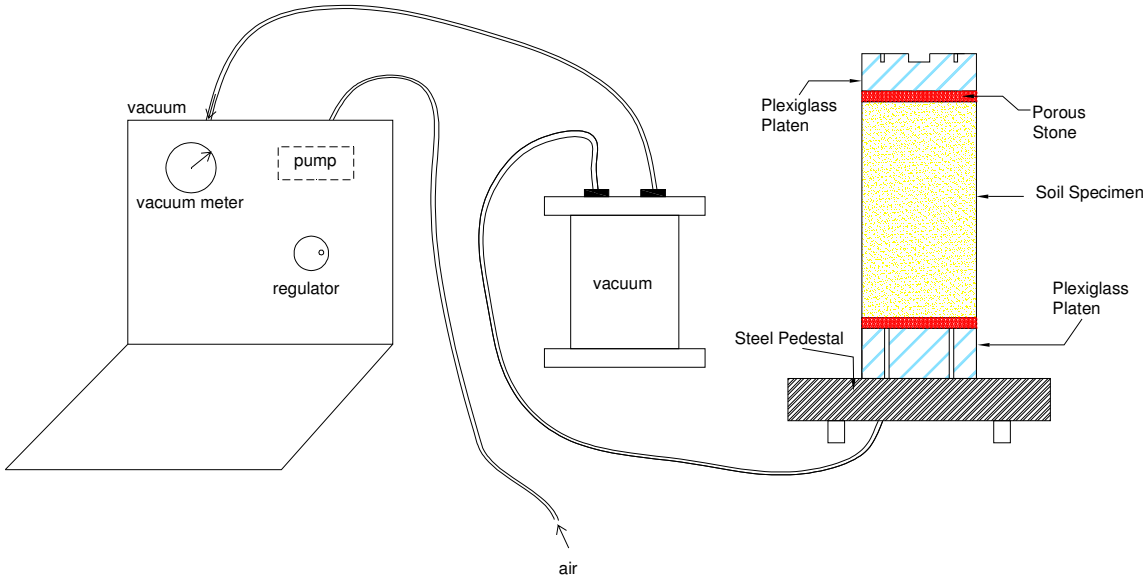

Figure 5.1 Preliminary study - setup for specimen preparation and boundary conditions.

Eccentric deviatoric load. The top cap is pushed down with an eccentric vertical force. At small confinement, shear failure occurs shortly after loading with appreciable bending and bulging. At large confining stress, the specimen bends at early stage of loading and shear failure is less defined. The membrane affects resistance at large flexural deformation.

Torsion and deviatoric load. Torque and vertical compression are applied to the top cap. Generally, the specimen bulges without a clear shear failure plane. When vertical load is applied at later stages of loading, the specimen fails by forming two distinct blocks that slide along the shear band. Slippage may take place between the soil and the caps. The latex membrane contributes to the resistance at large twisting angles.

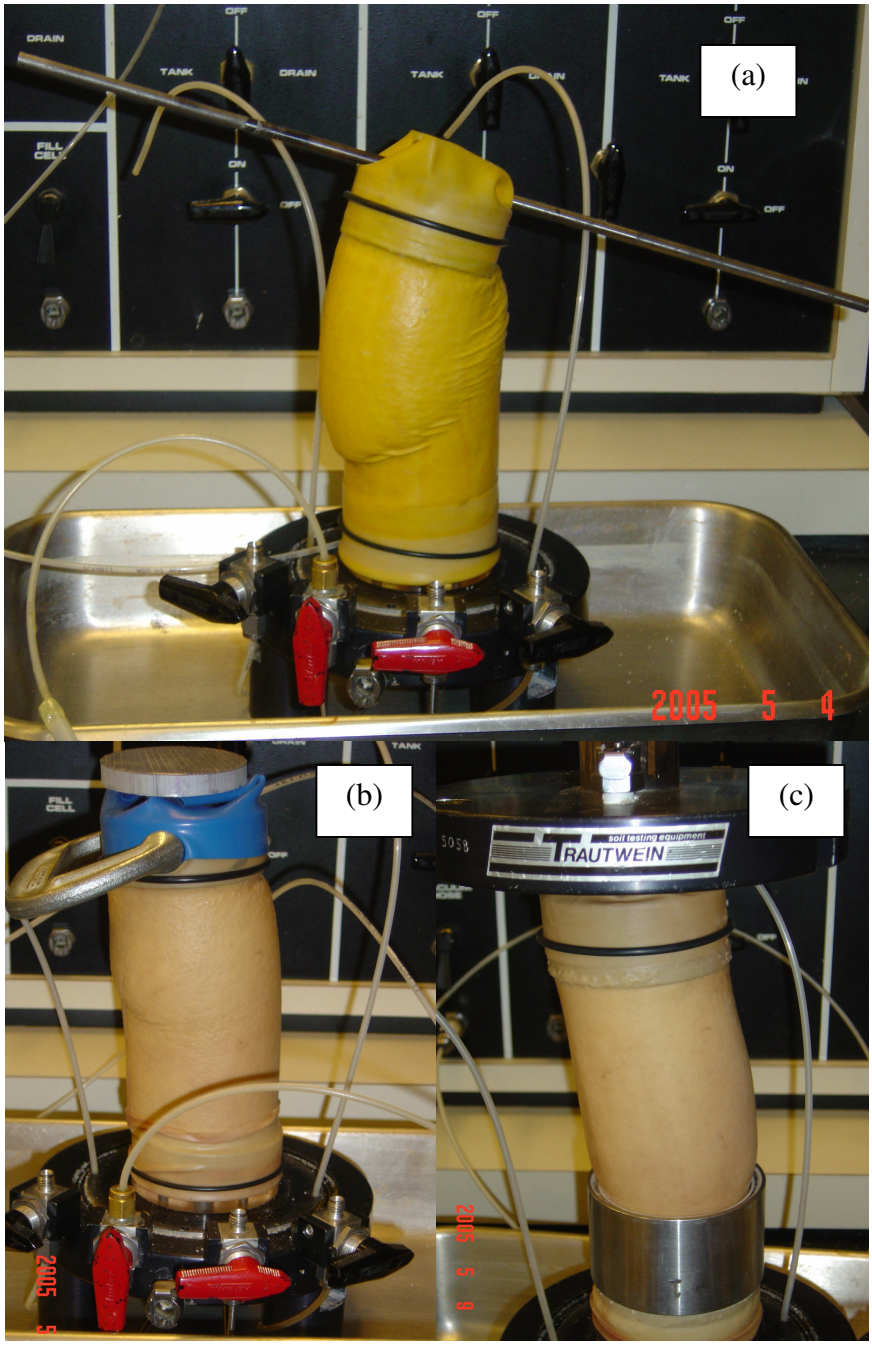

Figure 5.2 Preliminary tests. (a) Flexure. (b) Torsion. (c) Shear.

Table 5.1 Preliminary loading patterns.

Test	Loading	Observed deformation field	Comments
Flexure	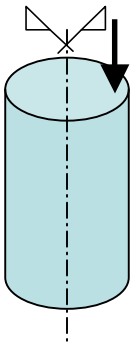	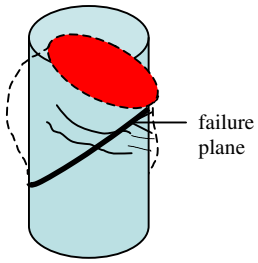	Failure plane at very large load
Torsion	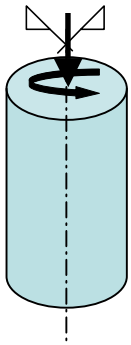	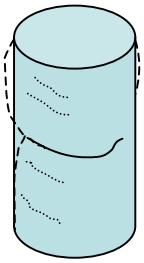	Membrane resistance to twisting
Shear	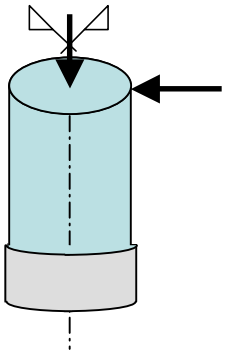	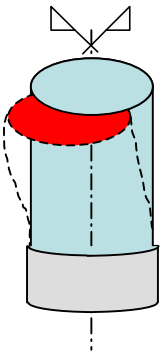	Inclined shear failure plane is formed for small

Shear and deviatoric load. A shear and a normal force are simultaneously applied on top of the specimen. Shearing deformation causes a second moment by the vertical load. The specimen is prone to shear banding under this configuration.

Other Observations - Comparison. Flexural loading produces a non-uniform deformation field, which can be readily measured with external sensors. Furthermore, flexural loading is easy to apply and can be readily implemented in available triaxial cells.

5.3 THREE DIMENSIONAL SIMULATION OF FLEXURAL TEST

The numerical simulation of a cylindrical soil specimen subjected to flexural loading is implemented in this section to gain insight into soil response under these conditions. The finite element program ABAQUS is used for this purpose. The 3D finite element mesh involves 4500 elements (5226 nodes) for the soil specimen and 828 elements (1248 nodes) for the top steel cap. Specimen dimensions, test setup, and boundary conditions are shown in Figure 5.3. The specimen is fully constrained at the bottom, and the steel platen is bonded to the top of the specimen (i.e., no slippage). The specimen undergoes two stages: isotropic compression σ_0 to 100 kPa and concentric vertical load of F = 800 N ($F = F_R + F_L = 400 + 400 = 800$ N) followed by drained flexural loading via an eccentric vertical force (ΔF). The vertical eccentric load is applied onto the steel platen (Figure 5.3). The eccentricity is load-controlled by increasing the vertical load at one end of the loading arm. Eccentricity is calculated as follows:

$$e = \frac{T}{\sigma_0 \cdot \pi r^2 + F_R + F_L + \Delta F} = \frac{\Delta F \cdot L/2}{\sigma_0 \cdot \pi r^2 + F_R + F_L + \Delta F} \tag{5.1}$$

where T is the applied bending moment, ΔF is the additional vertical load, σ_0 is the confining (isotropic) stress, and F_R, F_L, r, and L are defined in Figure 5.3.

The mean effective stress p`, various stress and strain components, and the deformed shape are monitored during loading.

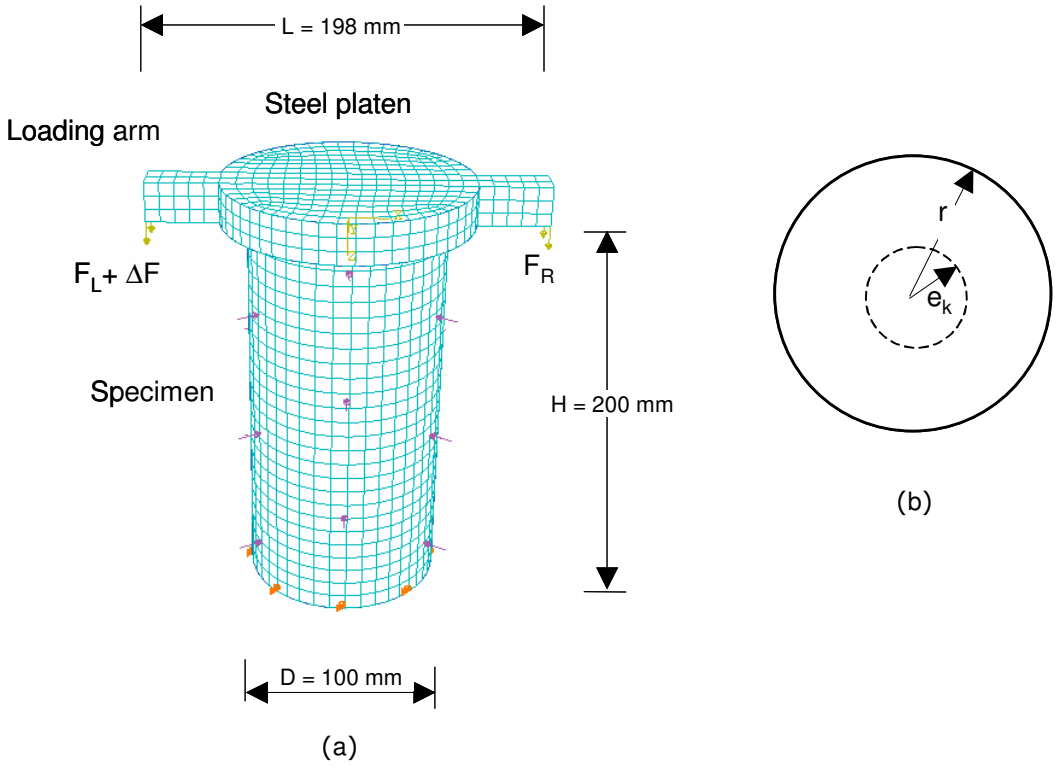

Figure 5.3 Flexural test. (a) Geometry, mesh, boundary conditions, and loading. (b) Circular cross section. Notation: Specimen radius r, Kernel (no-tension zone) radius e_k.

5.3.1 Elastic Specimen

The elastic media representing the soil specimen and the steel platen are assigned isotropic elastic moduli of E = 10 MPa and E = 200 GPa, respectively. Strains in the steel platen are negligible. Eccentricity e is varied between e/r = 0.1 and e/r = 0.26, where r is the specimen radius. Table 5.2 shows the axial normal stress contour and deformed shape at various eccentricities e/r. Tensile stresses occur at an eccentricity e/r ≅ 0.252 (circled in Table 5.2). Radial and hoop normal stresses (not shown) are compressive at all eccentricities. The deformed shape is controlled by the material stiffness (modulus of elasticity). This result is in agreement with closed-form solutions for isotropic elastic solid cylinders (Miller and Doeringsfield, 1960; Richards, 1961). The wide range in stresses and rich displacement field shown in Table 5.2, particularly for high eccentricity, provide further support for the selection of this test configuration. The test can be numerically continued for elastic media regardless of the presence of tensile stresses. Therefore, the suitability of this test for soils must take into consideration soil plasticity.

Table 5.2 Kernel (no-tension zone) check of flexural test - elastic

e/r	0.1	0.2	0.25	0.255	Notes
Vertical normal stress	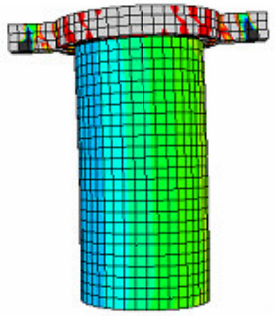	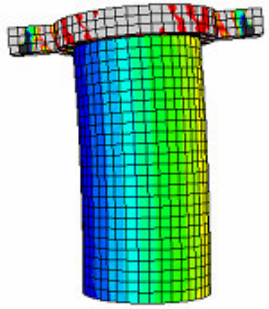	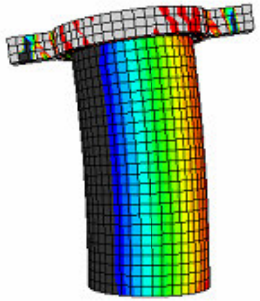	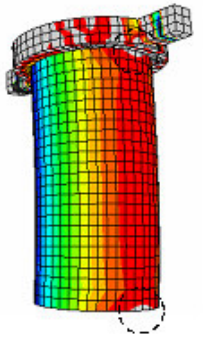	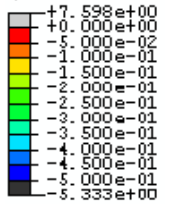 Stresses in N/mm^2 Tensile stresses are circled
Deformed shape	Δx = 1.7 Δy = 3.2 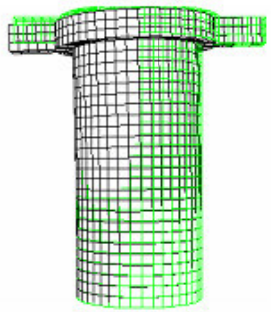	Δx = 2.7 Δy = 4.2 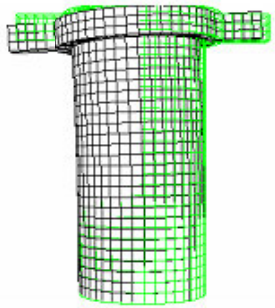	Δx = 4.6 Δy = 6.3 Δy 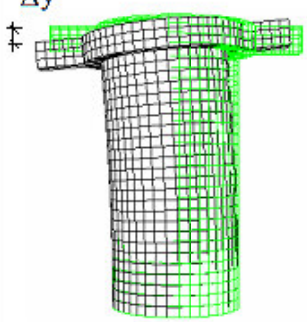	Δx = 4.8 Δy = 6.5 Δx 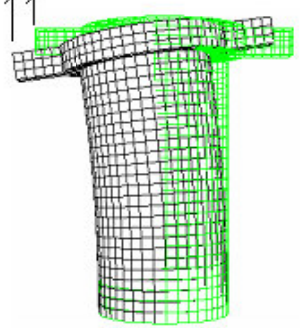	Deformation in mm

Notation: eccentricity e, and radius of specimen r

5.3.2 Modified Cam-Clay Soil Specimen

The same study is repeated for a material that satisfies the Modified Cam-Clay model (MCCM) subjected to drained loading. The goal is to examine the effect of soil plasticity on the stress and deformation field and to investigate the limiting eccentricity beyond which additional flexural moment cannot be applied. A Weald clay cylindrical specimen subjected to flexure is simulated in Figure 5.3 with MCCM parameters defined in Table 5.3.

Table 5.3 Cam-Clay parameters for Weald Clay (Wood, 1990).

λ	0.088
κ	0.031
M	0.882
e_0	0.628[#]
G (MPa)	3.0

[#] initial void ratio at a confining stress of 207 kPa

Table 5.4 shows contours of the axial normal stress and the deformed shape at various eccentricities e/r. For comparison purposes, an eccentricity e/r = 0.25 is used. Mesh refinement, reduction of load increment, and automated incrementation fail to overcome the numerical problems at e/r ≅ 0.22, which appears to be the limiting eccentricity with load-controlled simulation. Normal stress contours stop changing at an eccentricity of e/r ≅ 0.2 and excessive deformations are observed with additional flexural moment (see progress of displacements in Table 5.4). These observations are indicative of failure. The mean effective stress p' and the three normal strain components ε_{11}, ε_{22}, and ε_{33} are depicted in Figure 5.4. The mean effective stress p' (like the axial normal stress in Table 5.4) is maximum on the compression side and minimum on the extension side (Figure 5.4-a). All normal stress components (vertical,

radial, and hoop) are compressive at all eccentricities. The axial strain is compressive at e/r = 0.2 on the compression side and tensile on the extension side (Figure 5.4-b). On the other hand, the hoop and radial strains are compressive on the tension side and tensile on the compression side (Figure 5.4-c and 5.4-d).

From Figure 5.4, maximum and minimum normal stresses and normal strains occur approximately at the mid-height of the specimen. Thus, the stress path for four selected elements at the mid-height of the specimen are monitored (Figure 5.5-a). For the same elements the evolution of stress ratio $\eta = q/p'$ versus eccentricity e/r is shown in Figure 5.5-b. At e/r = 0.207, element number 4 reaches its maximum stress ratio $\eta = 0.882$ in compression associated with excessive material deformations. This is the strength parameter of Weald clay (M = 0.882 in Table 5.3). At e/r = 0.216, element number 1 reaches its maximum stress ratio $\eta = M = 0.91$ in extension. The numerical model fails to proceed with reasonable accuracy beyond this point because the material fails in both compression and extension and the second moment effect dominates the displacement field (flow occurs). From this observation it can be concluded that this simulation can be trusted up to e/r = 0.207. There are parts of the specimen at stress states between triaxial compression and triaxial extension (elements 2 and 3, Figure 5.4).

The limiting eccentricity for the MCCM-modeled specimen, unlike the elastic medium, is governed by the constitutive model parameters (e.g. strength parameter M

Table 5.4 Flexural test simulation - MCCM

e/r	0.1	0.2	0.207	Notes
Vertical normal stress	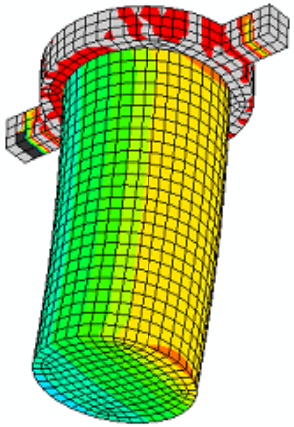	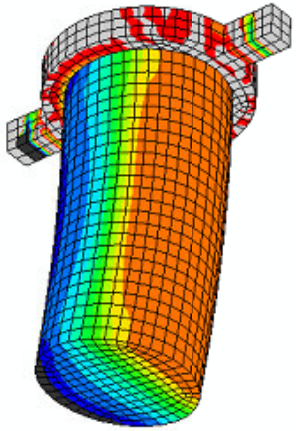	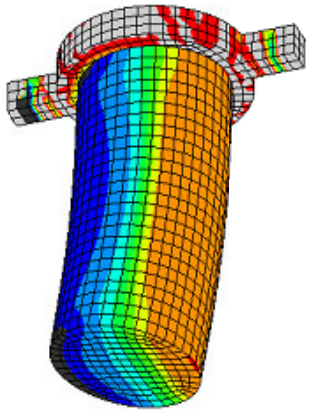	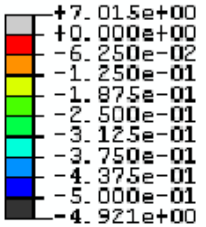 Stresses in N/mm²
Deformed shape	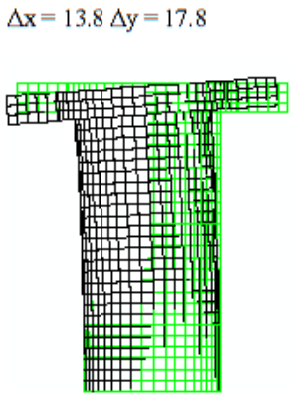	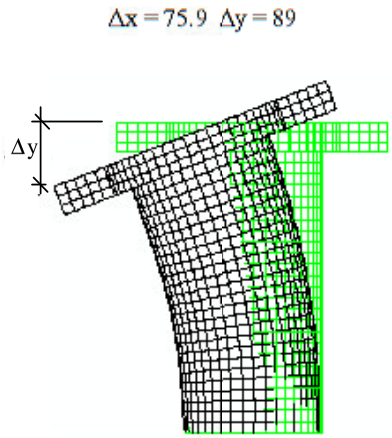	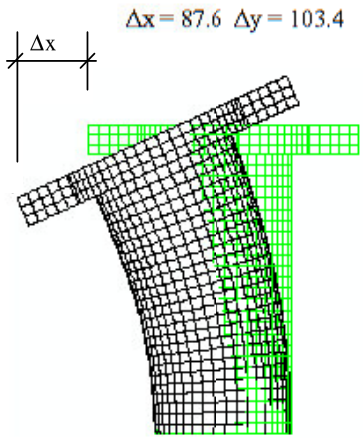	Deformation in mm

Notation: eccentricity e, and radius of specimen r

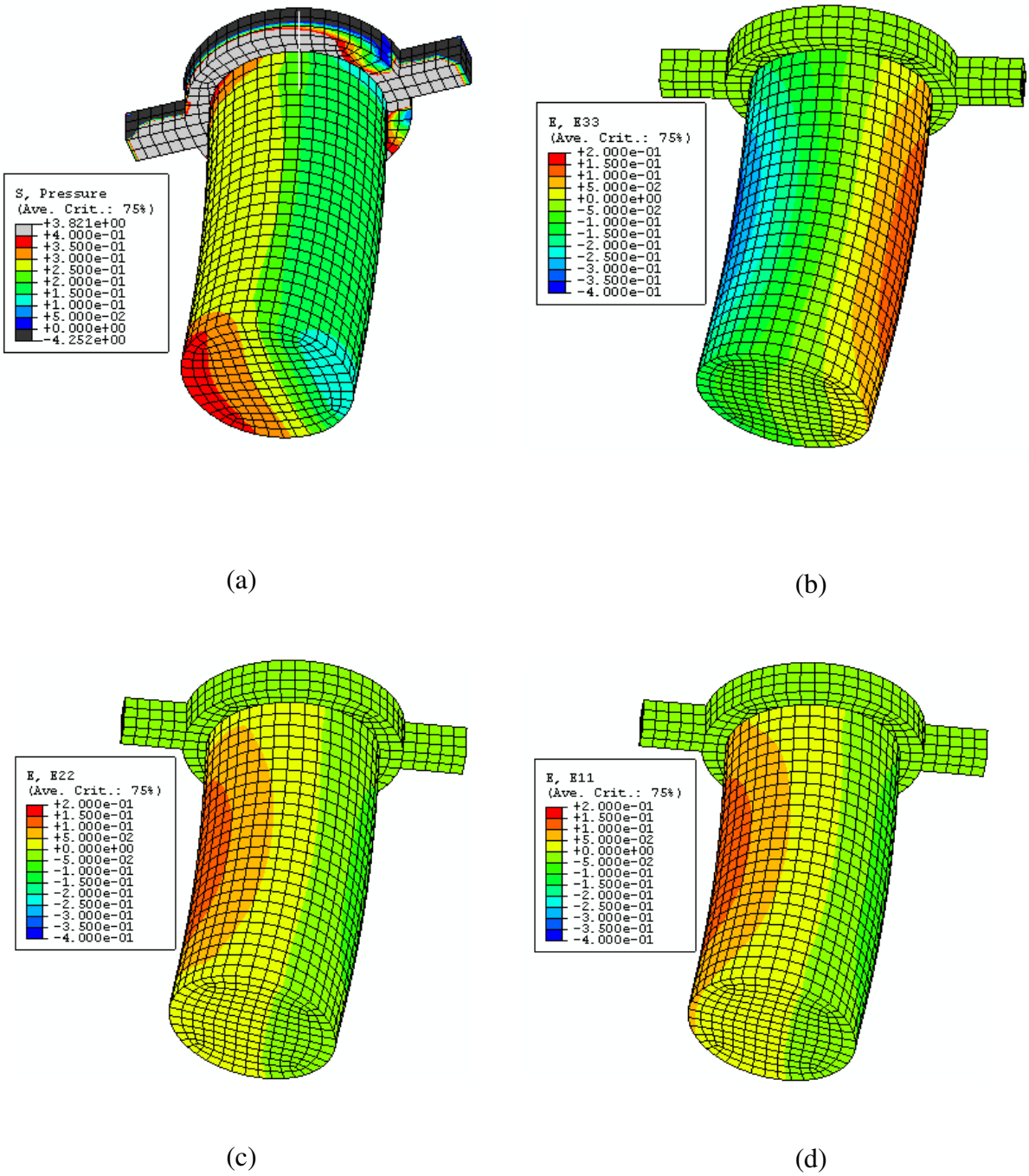

Figure 5.4 Flexural test - MCCM - eccentricity $e_k = 0.2$. (a) Mean effective stress p'. (b) Axial strain. (c) Radial strain. (d) Hoop strain. Note: positive mean effective stress is compressive, stresses are in N/mm^2. Negative strains are compressive and positive strains are tensile.

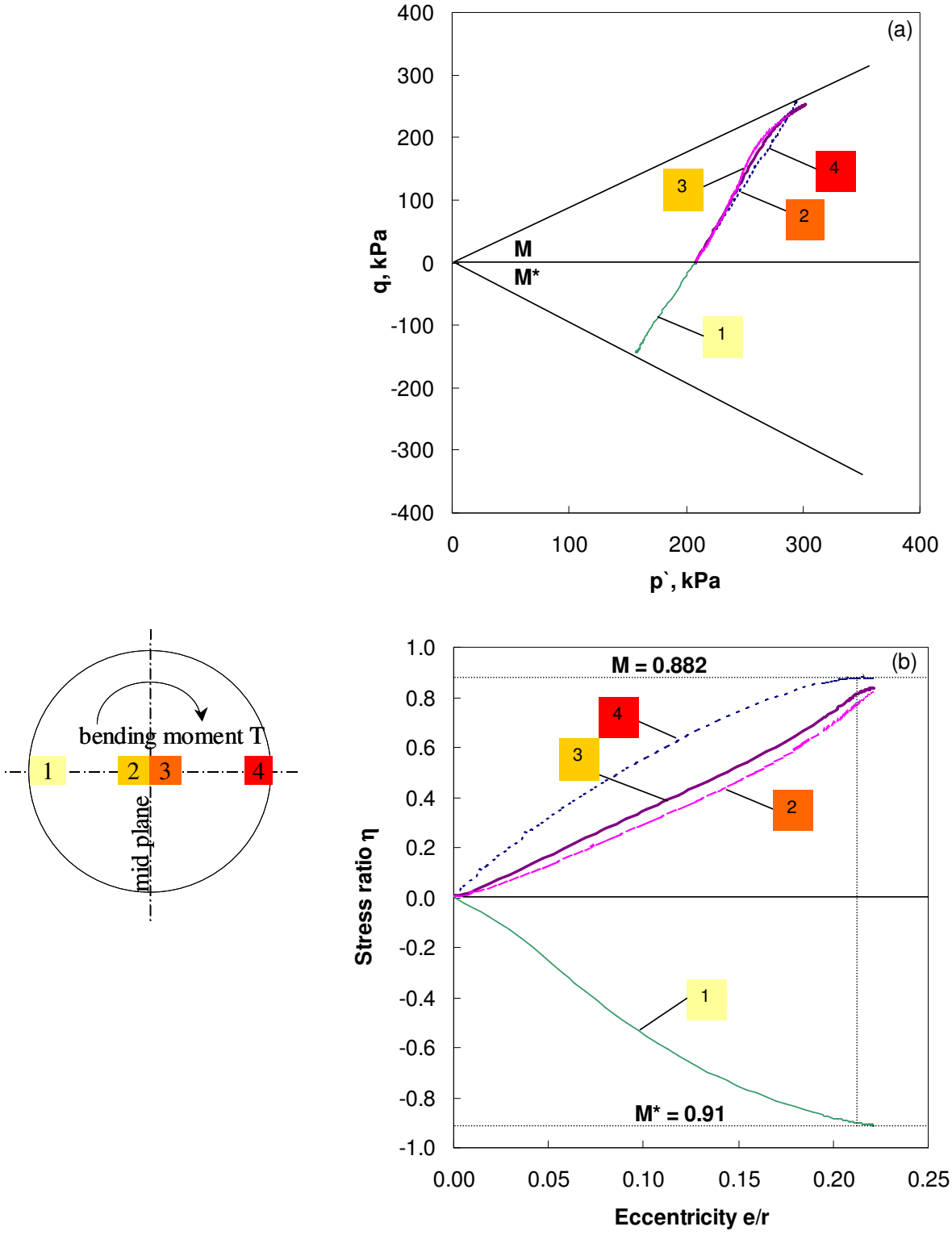

Figure 5.5 Flexural test - Specimen mid-height. (a) Stress path in p'-q plane. (b) Stress ratio $\eta = q/p'$ vs. eccentricity e/r. Notation: Mean effective stress p', deviatoric stress q, stress ratio at failure M (compression), stress ratio at failure M* (extension), specimen radius r.

in MCCM). Numerically, the flexural test experiences no modeling or stability difficulties until failure is approached. Results show rich and diverse stress and strain fields (Figure 5.4).

5.4 CLOSING OBSERVATIONS

Preliminary tests and detailed numerical simulations show the suitability of the flexural test to provide an information-rich displacement field; some parts of the specimen reach failure while other locations remain within the elastic limit. It is proposed that the displacement field will be captured using a digital camera and processed using image-processing techniques. Unlike the ideal triaxial test, the displacement field created in flexural loading is not homogeneous. Such fields are information-rich and very desirable from the inversion standpoint. Application of flexural loading is simple and it can be implemented in modified triaxial cells. The membrane effect in bending needs further analysis.

CHAPTER VI

MODEL CALIBRATION BASED ON AN INFORMATION-RICH TEST

The flexural test in Chapter 5 is selected for its high potential as an information-rich test. This chapter presents the implementation of this test and results obtained using Ottawa 20-30 sand. Emphasis is placed on the inversion of constitutive parameters from successive forward numerical simulations of the test.

6.1 DEVICES AND PROCEDURES

Lateral Deformation-Controlled Flexural Test. The lateral deformation-controlled flexural test is performed by applying a constant concentric vertical load on the top cap (Figure 6.1) followed by a controlled horizontal displacement (Figure 6.2). A conical tip load cell is attached between the horizontal driver and the top cap to facilitate measuring the horizontal load applied to the specimen. The load cell calibration curve is shown in Figure 6.3. Non-slippage between the sand specimen and the top and bottom caps is enforced by gluing sand to the end caps (Figure 6.4).

The specimen is subjected to three loading stages:

1. Isotropic loading: vacuum provides the confining stress.
2. Deviatoric loading: a concentric dead-weight axial load provides the static deviatoric stress.
3. Flexural loading: the horizontal load applied to the top cap.

This displacement-controlled test condition prevents the sudden catastrophic failure of the specimen (observed in eccentrically loaded specimens).

Evaluation of the influence of stress ratio on the results is made possible by considering three principal stress ratios R = σ_1/σ_3 = 1, 1.5, and 2 where σ_1 is the major (vertical) normal stress and σ_3 is the minor (lateral/confining) normal stress.

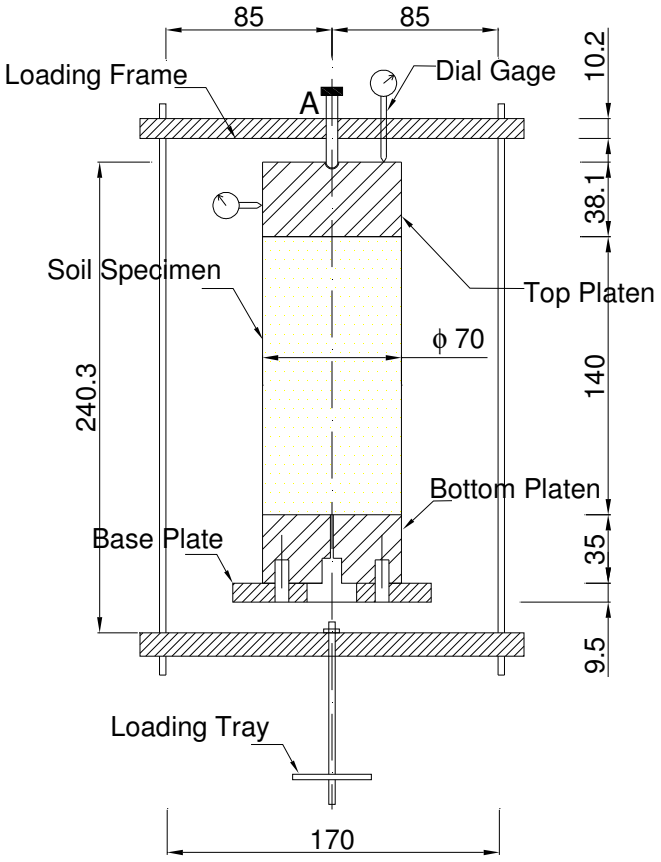

Figure 6.1 Lateral-deformation controlled flexural test - Front view.
Note: Dimensions in mm.

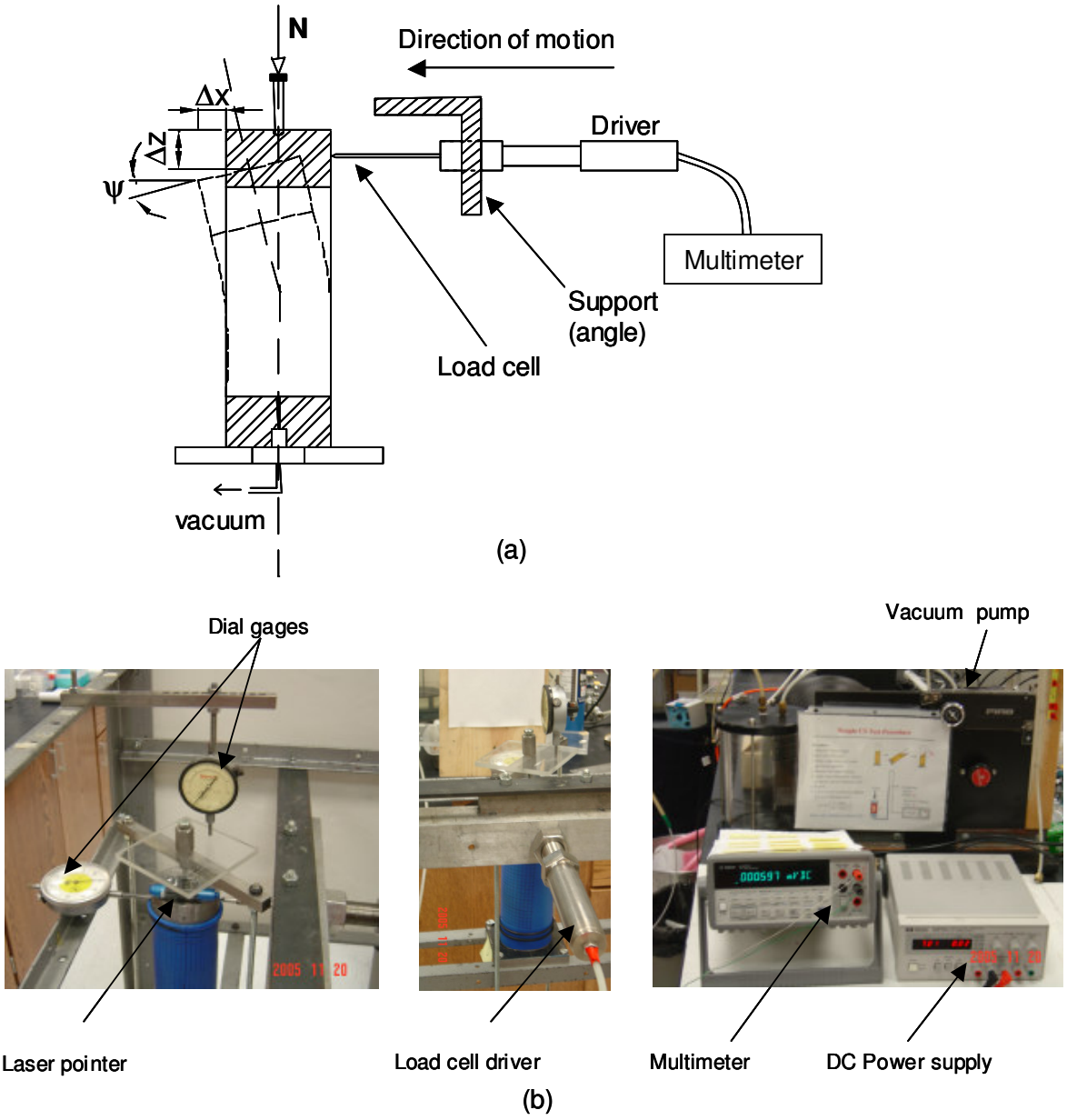

Figure 6.2 Lateral-deformation controlled flexural test - Side view. (a) Procedure schematic. (b) Peripherals. Notation: Normal force N, global horizontal displacement Δx, global vertical displacement Δz, and global tilt angle ψ

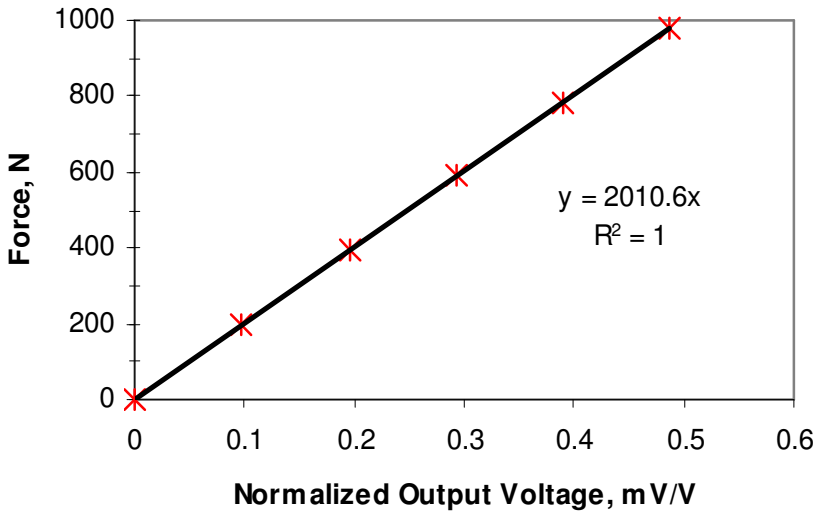

Figure 6.3 Load cell calibration curve (Yun, T., 2005).

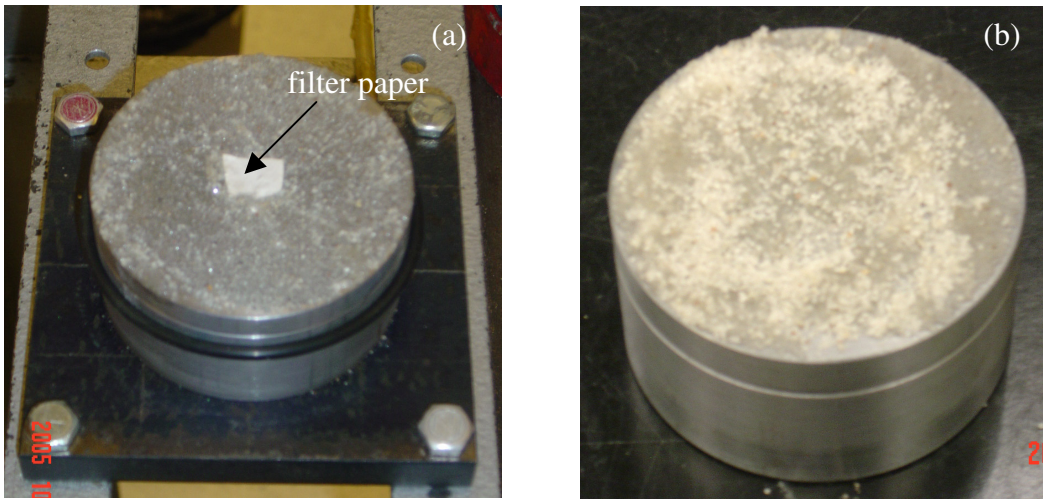

Figure 6.4 End caps: a thin layer of sand is glued. (a) Bottom cap: vacuum hose protected by filter paper at the center of the bottom cap. (b) Top cap.

Local displacement measurements are obtained by post-processing successive digital images of the specimen. Two digital still cameras are used for this purpose; the in-plane side view image has a pixel size 0.2mm; the out-of plane image has a pixel

size 0.55 mm (for comparison, the grain size is D_{50}= 0.7 mm) . Dial gages are used to measure global horizontal and vertical deformations (Figure 6.1). A laser pointer is mounted on the top cap to monitor the angle between the projections of the pointer on a white board before and after the application of the flexural load (Figure 6.2b); this is the tilt angle ψ at the top of the specimen.

6.2 MATERIAL AND SPECIMEN PREPARATION

Ottawa 20-30 sand is used throughout the experimental study conducted as part of this investigation. An aluminum split mold is used to stretch the 0.33 mm thick latex membrane in order to prepare a nominal 70 mm-diameter and 140 mm-height specimen. Vacuum is used to keep the membrane stretched onto the split mold. Table 6.1 summarizes the properties of Ottawa 20-30 sand. The test is performed on air-dry Ottawa sand. The specimen is prepared by air pluviation. Dense and loose specimens are prepared. Loose specimens are prepared by continuous funneling with light tapping of the split mold for leveling, while dense specimens are prepared by compacting each layer (5 layers total) 25 times with a round-ended steel rod.

Table 6.1 Properties of Ottawa 20-30 sand (from Cho, 2001).

e_{max}	e_{min}	D_{50} (mm)	D_{10} (mm)	C_u	C_c	G_s	M (ϕ_{cs} °)	λ	Γ
0.742	0.502	0.72	0.65	1.15	1.02	2.65	1.07 (27°)	0.047	0.802

Coefficient of uniformity $C_u = D_{60}/D_{10}$, Coefficient of curvature $C_c = D_{30}^2/D_{10}D_{60}$, Specific gravity G_s, Strength parameter $M = 6\sin\phi_{cs}/(3- \sin \phi_{cs})$, Critical state friction angle ϕ_{cs}, Slope of CSL on e-log p` $\lambda$, and intercept of CSL at p` = 1 kPa on e-log p` Γ.

Once the top cap is placed and the membrane held to it, the specimen is supported by applying vacuum through the bottom cap (Figure 6.1). A small piece of

filter paper is placed on the vacuum hole (bottom cap) to prevent blockage of the vacuum line (Figure 6.4b). The specimen mass density is determined by carefully measuring the specimen geometry immediately after the application of vacuum. Measurements of the diameter are corrected for the thickness of the membrane. The average diameter is used also in the calculation of the average cross sectional area A_{av} for the vertical normal stress and normalized horizontal force $F_{HN} = F_H/(p_{vac} \times A_{av})$ where F_H is the applied horizontal force, and p_{vac} is the corresponding vacuum pressure. All tests are consolidated-drained.

6.3 MEASUREMENTS

A total of six tests were run: loose and dense specimens and three initial stress ratios. Global measurements include confining pressure, vertical load, vertical and horizontal displacement, tilt of the top cap, and the horizontal force applied to the top cap. The global measurements of the six tests are plotted in Figures 6.5 through 6.10 and compared in Figure 6.11.

Local measurements are the horizontal and vertical displacements of selected points on the specimen surface gathered from the digital images. An orthogonal grid is plotted on the rubber membrane for this purpose. Still images are captured:

1. just before applying vacuum,

2. immediately after applying vacuum,

3. after applying the concentric normal load, and

4. every 0.5 mm of imposed horizontal displacement.

The displacement vector for each point is determined as the spatial difference (Δx, Δz) between the reference image and the image under consideration. The reference image is the one obtained immediately after the application of the concentric normal load. A measurement error of 0.02 mm is expected. The displacement field of the mid line is shown in Figures 6.12 through 6.17.

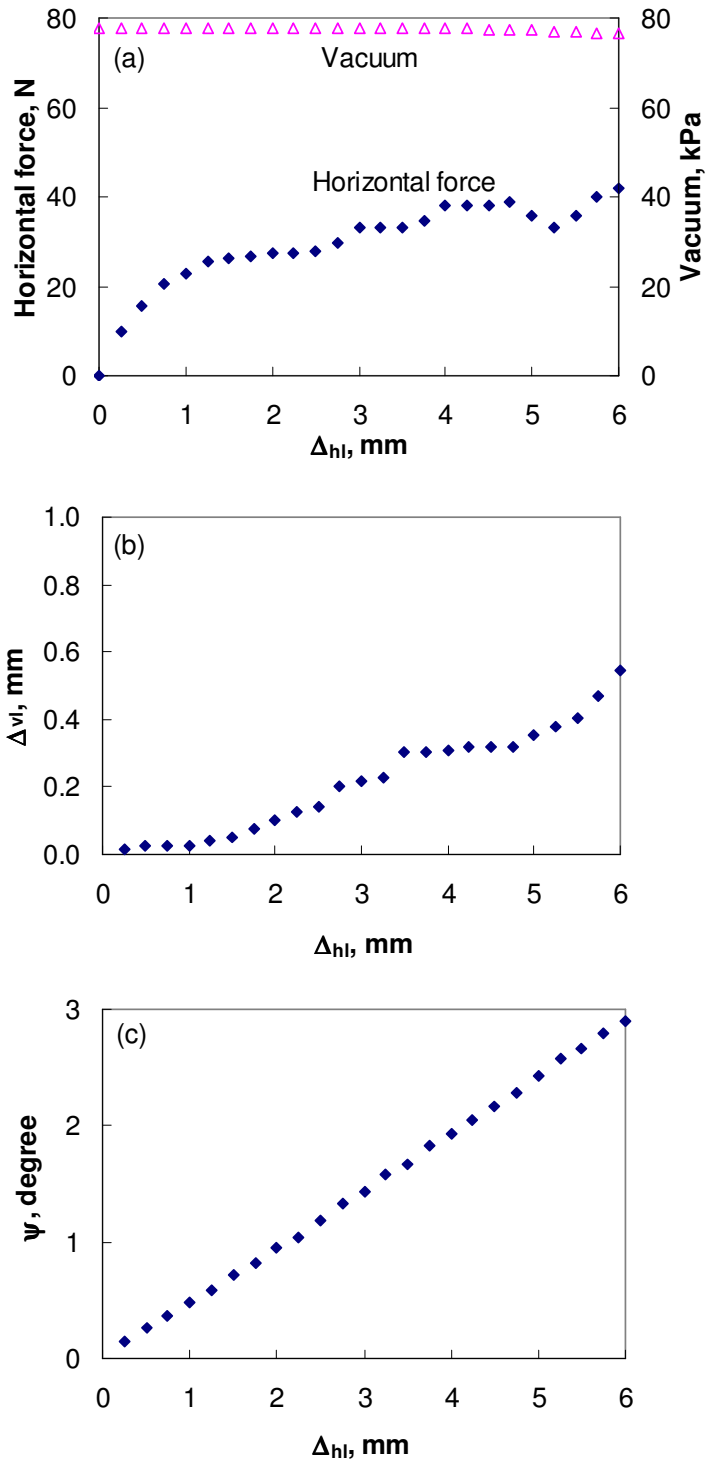

Figure 6.5 Flexural test measurements D_r = 69 and R = 1.1. (a) Horizontal force and vacuum. (b) Global vertical displacement Δ_{hl}. (c) Tilt angle ψ. Notation: Relative density D_r, stress ratio R, applied horizontal displacement Δ_{hl}.

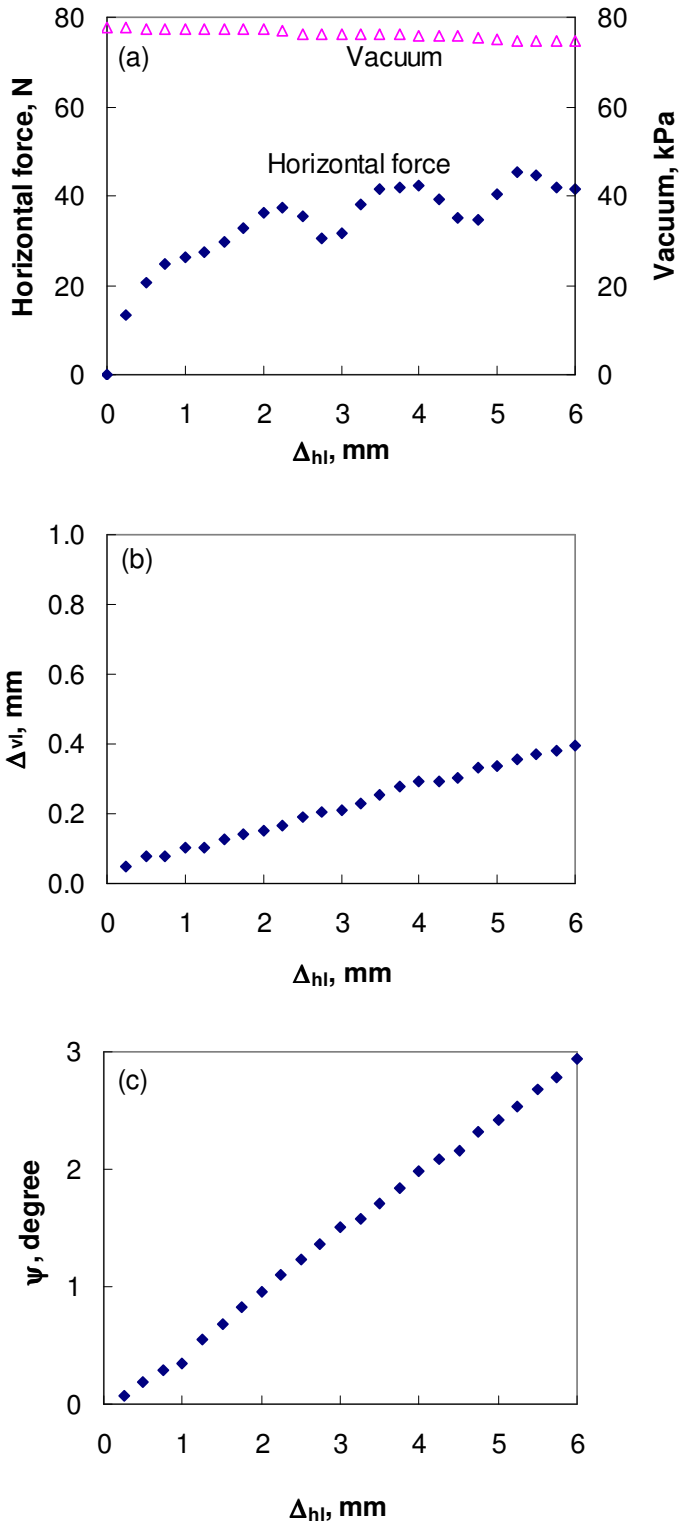

Figure 6.6 Flexural test measurements D_r = 66 and R = 1.5. (a) Horizontal force and vacuum. (b) Global vertical displacement Δ_{hl}. (c) Tilt angle ψ. Notation: Relative density D_r, stress ratio R, applied horizontal displacement Δ_{hl}.

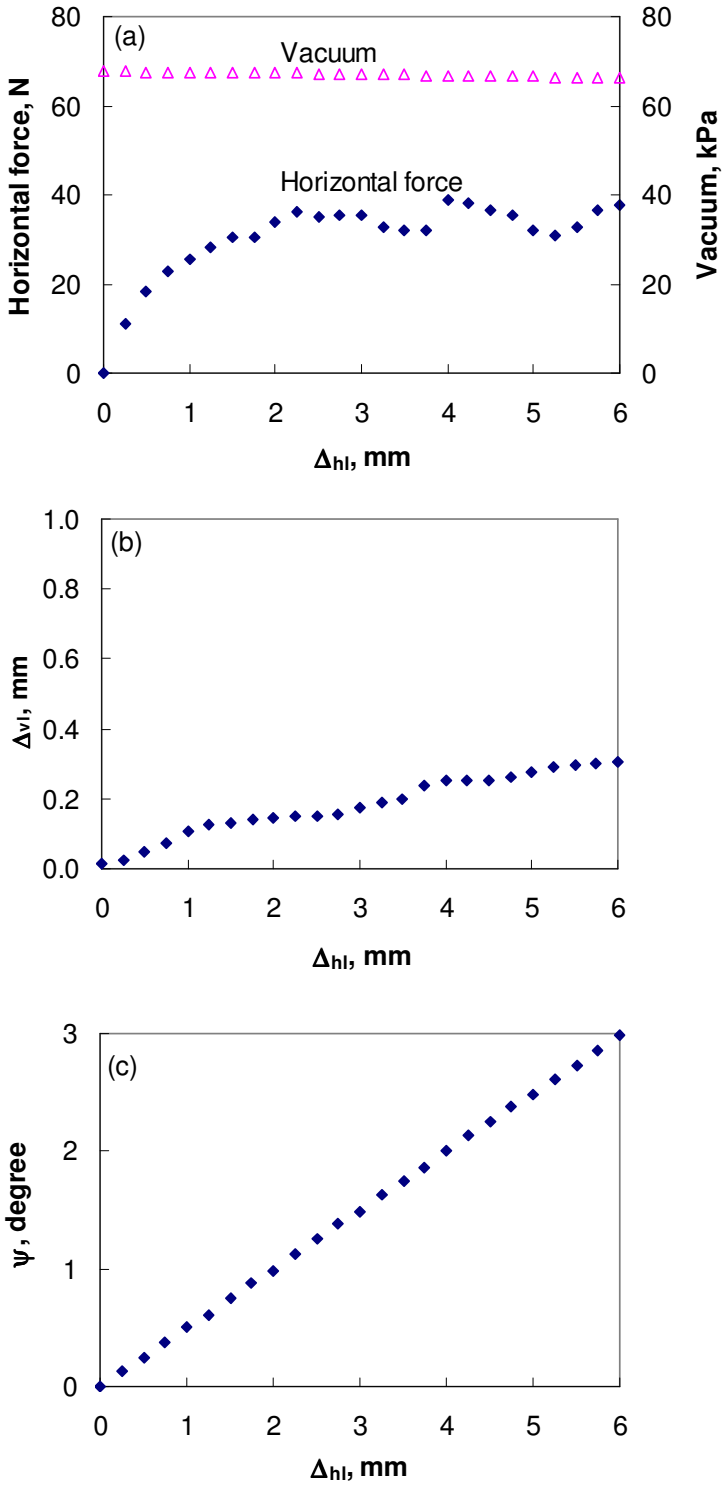

Figure 6.7 Flexural test measurements D_r = 64 and R = 2. (a) Horizontal force and vacuum. (b) Global vertical displacement Δ_{hl}. (c) Tilt angle ψ. Notation: Relative density D_r, stress ratio R, applied horizontal displacement Δ_{hl}.

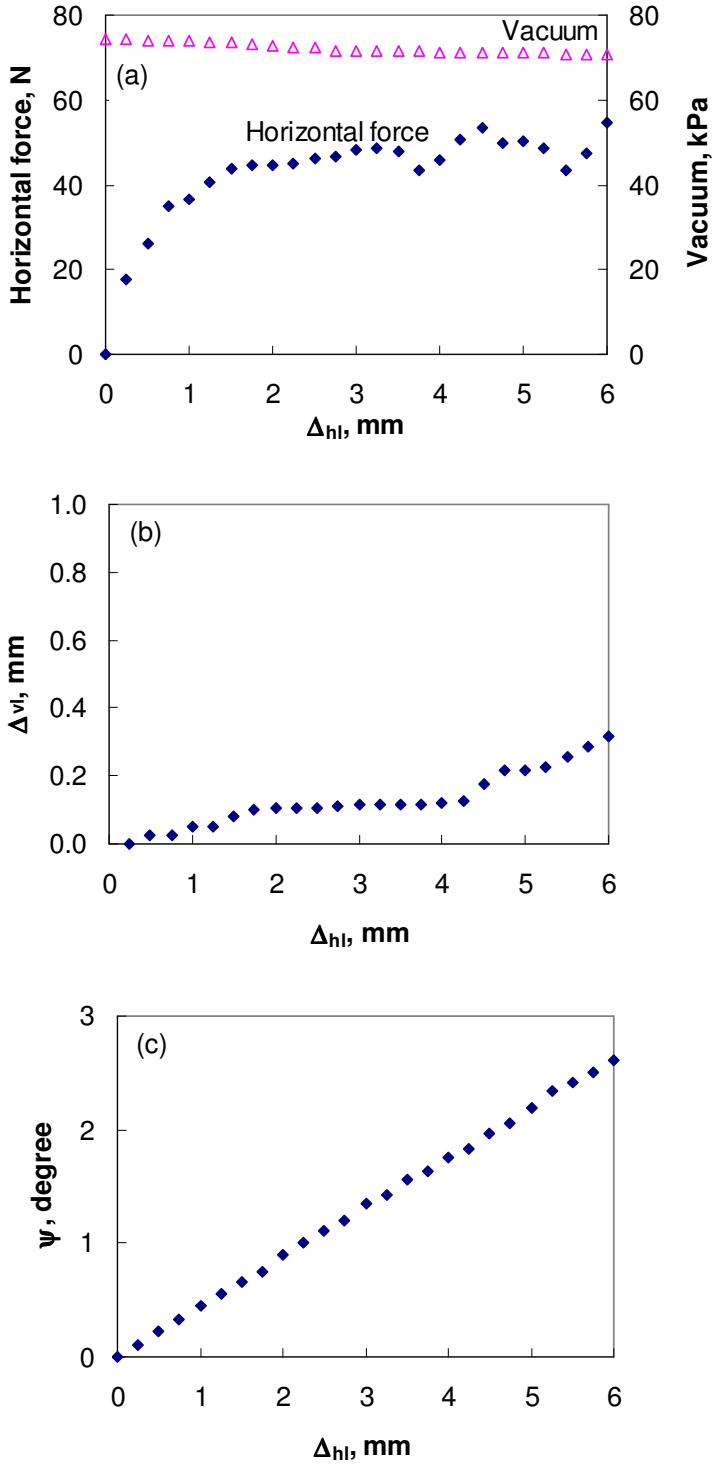

Figure 6.8 Flexural test measurements D_r = 93 and R = 1.1. (a) Horizontal force and vacuum. (b) Global vertical displacement Δ_{hl}. (c) Tilt angle ψ. Notation: Relative density D_r, stress ratio R, applied horizontal displacement Δ_{hl}.

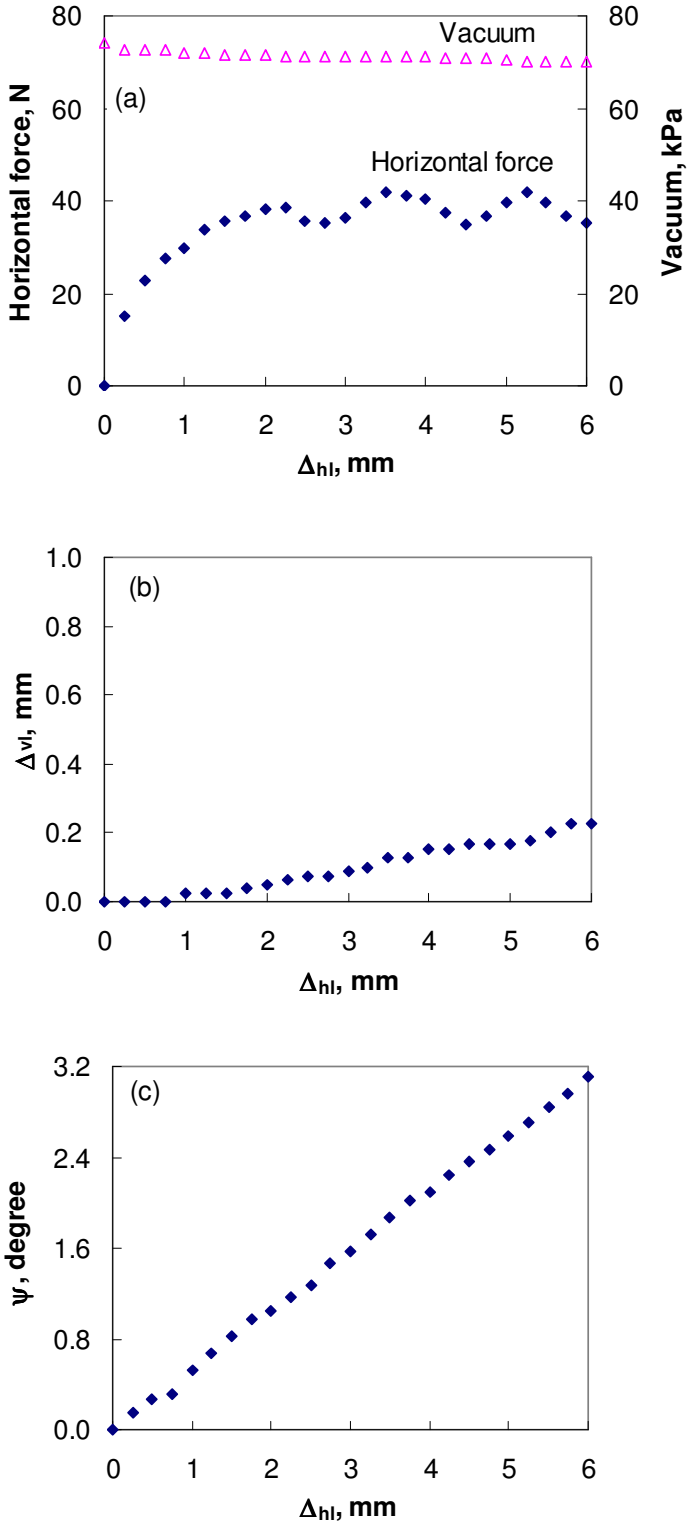

Figure 6.9 Flexural test measurements - D_r = 90 and R = 1.5. (a) Horizontal force and vacuum. (b) Global vertical displacement Δ_{hl}. (c) Tilt angle ψ. Notation: Relative density D_r, stress ratio R, applied horizontal displacement Δ_{hl}.

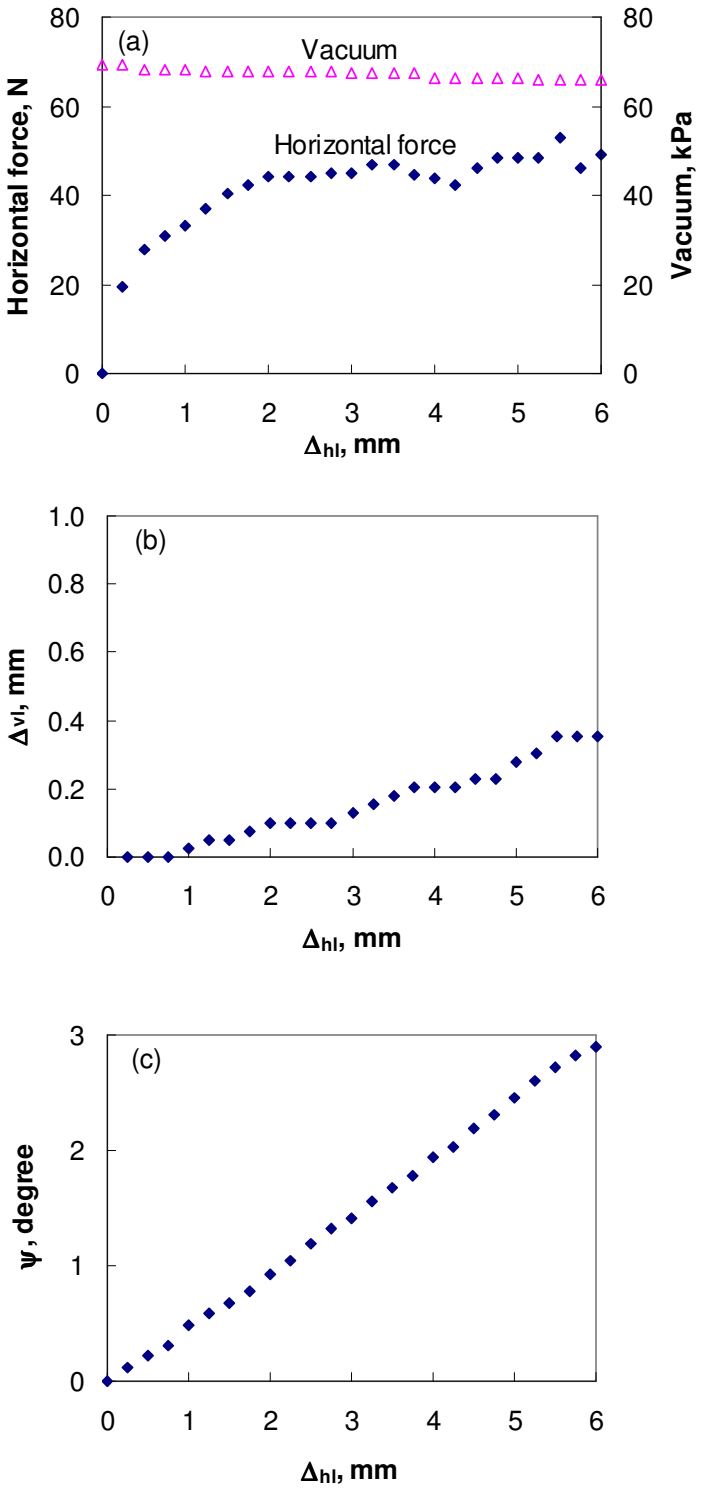

Figure 6.10 Flexural test measurements - D_r = 86 and R = 1.9. (a) Horizontal force and vacuum. (b) Global vertical displacement Δ_{hl}. (c) Tilt angle ψ. Notation: Relative density D_r, stress ratio R, applied horizontal displacement Δ_{hl}.

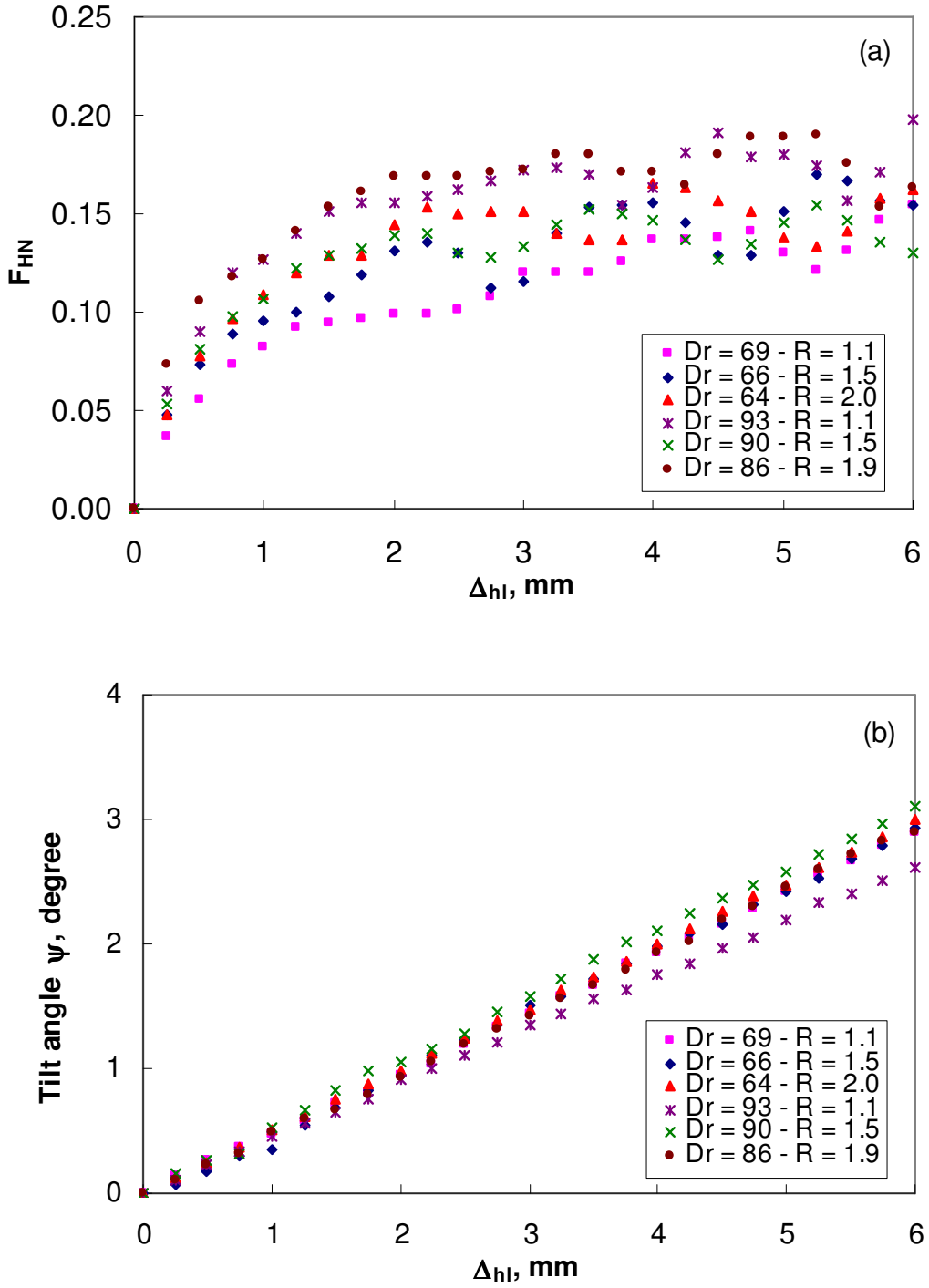

Figure 6.11 Global measurements of flexural test. (a) Applied normalized horizontal force. (b) Global tilt angle. Notation: Relative density D_r, stress ratio $R = \sigma_1/\sigma_3$, and applied horizontal displacement Δ_{hl}.

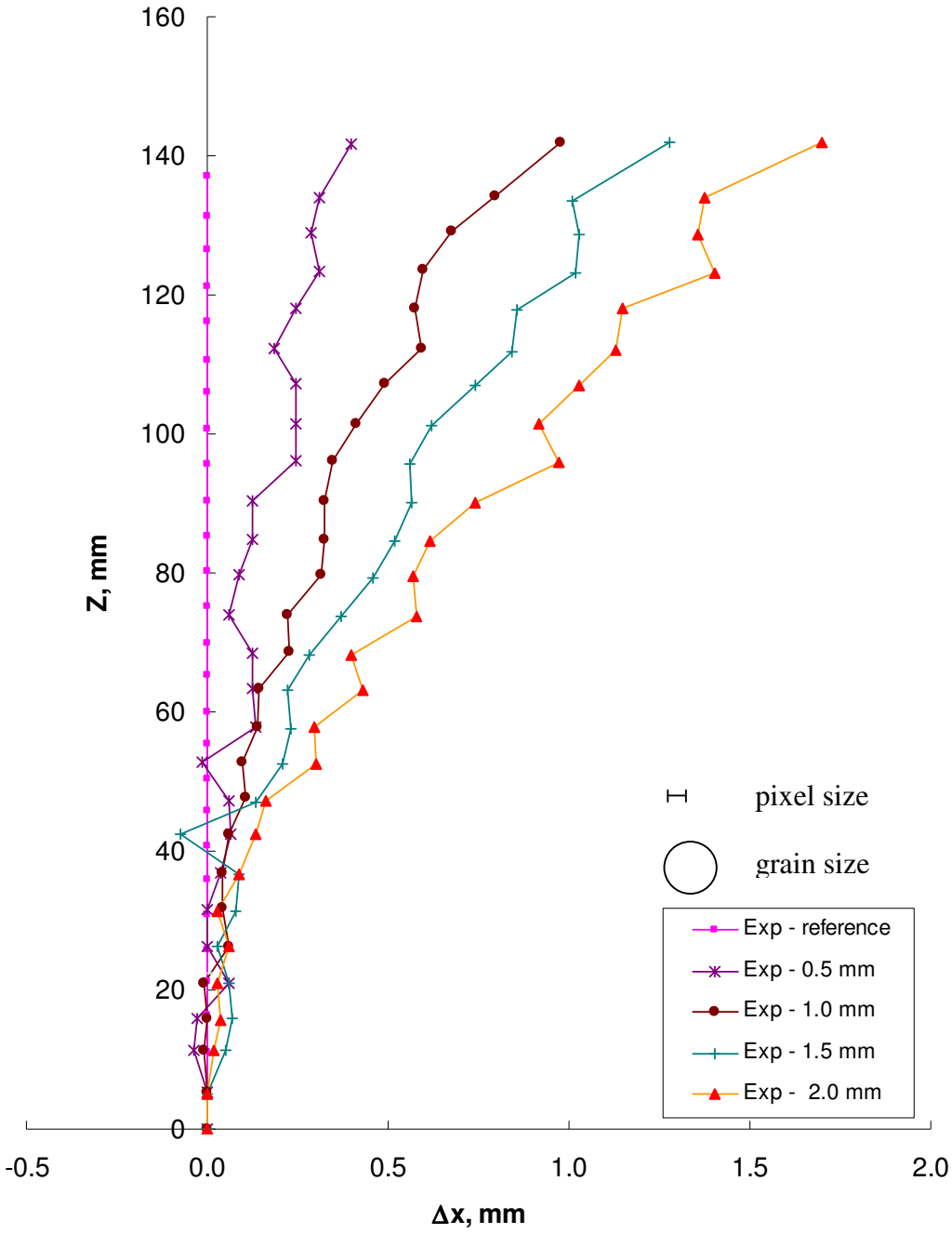

Figure 6.12 Measured horizontal displacement for the midline. Ottawa 20-30 sand at D_r = 69 and stress ratio R = 1.1.

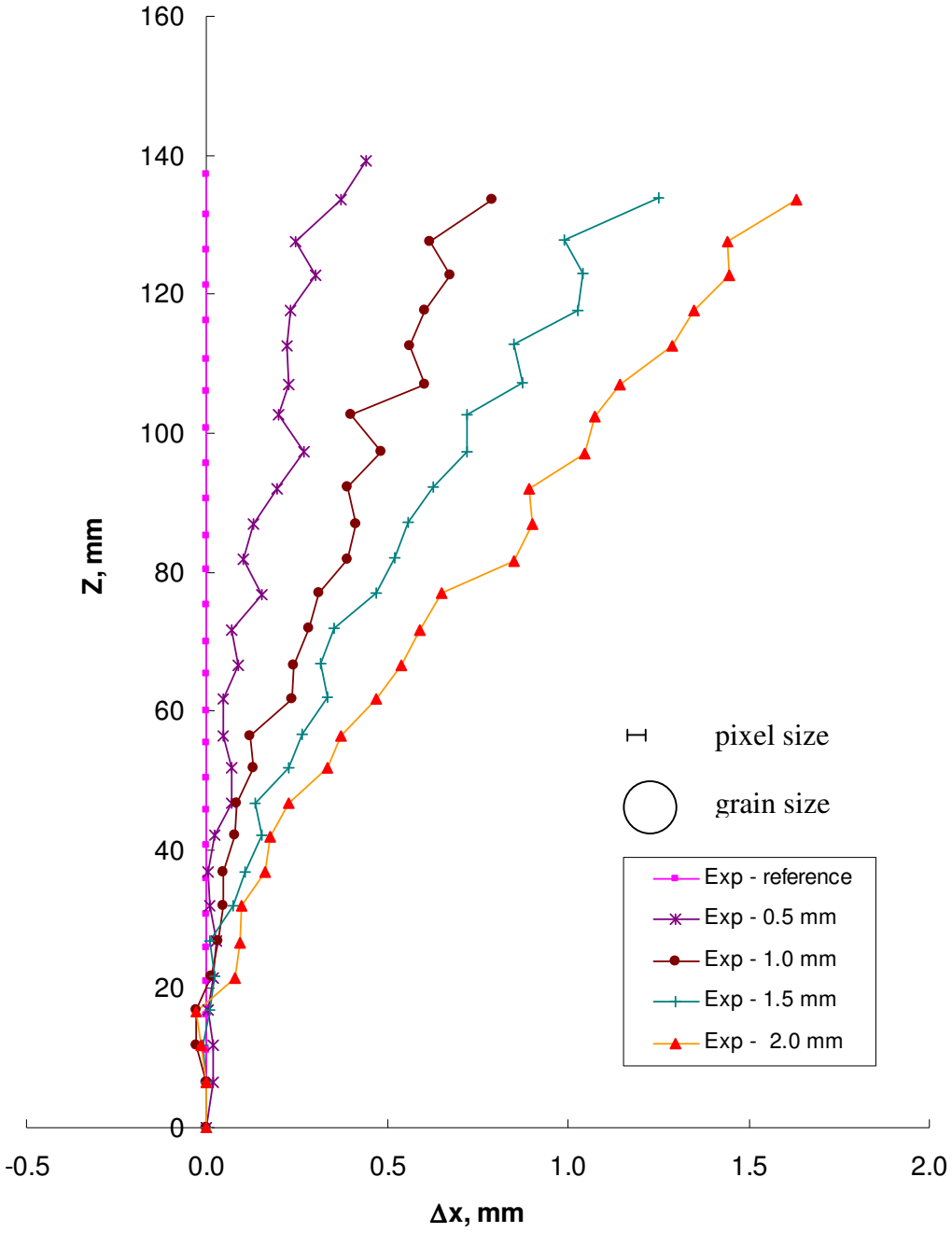

Figure 6.13 Measured horizontal displacement for the midline. Ottawa 20-30 sand at D_r = 66 and stress ratio R = 1.5.

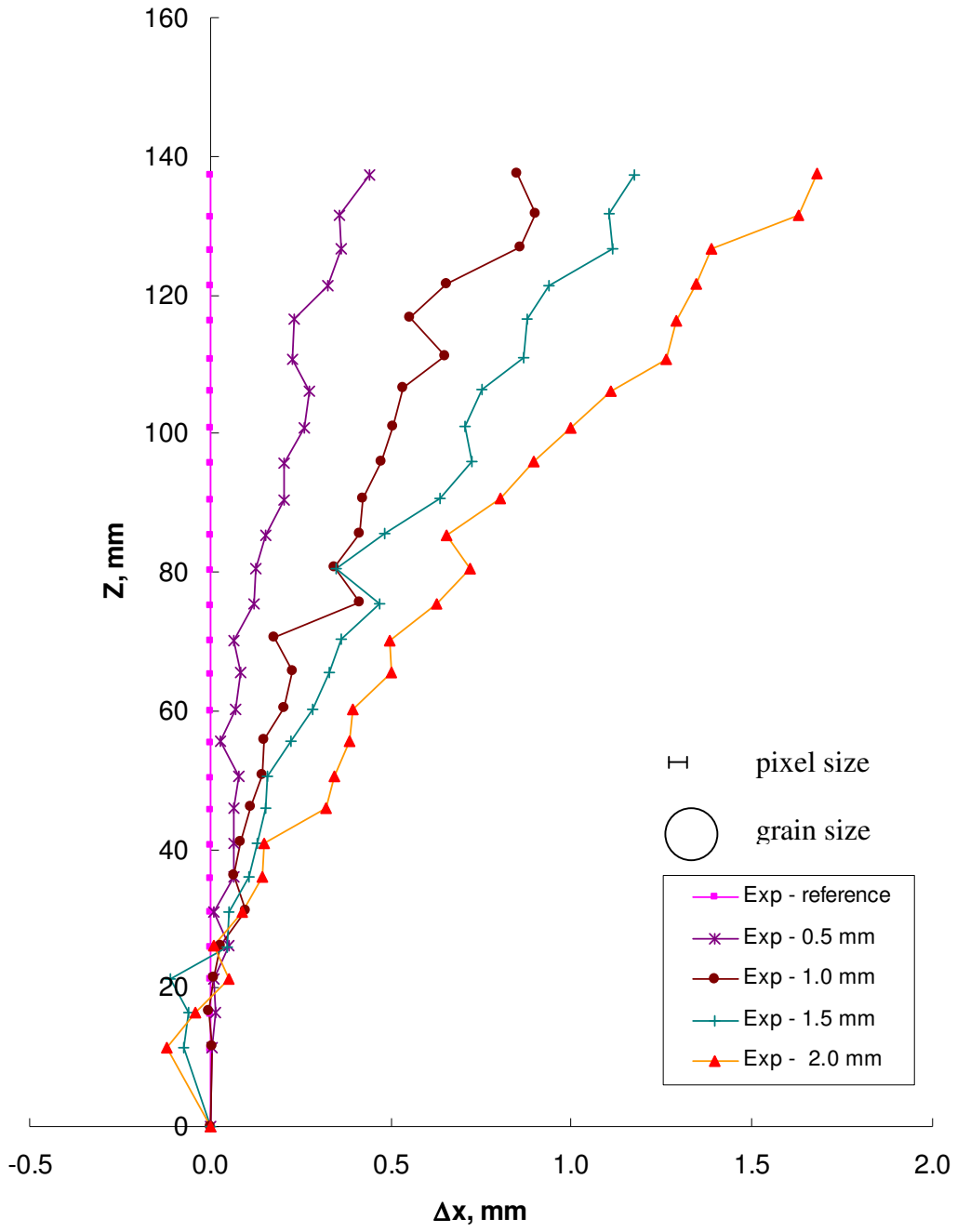

Figure 6.14 Measured horizontal displacement for the midline. Ottawa 20-30 sand at $D_r = 64$ and stress ratio R = 2.

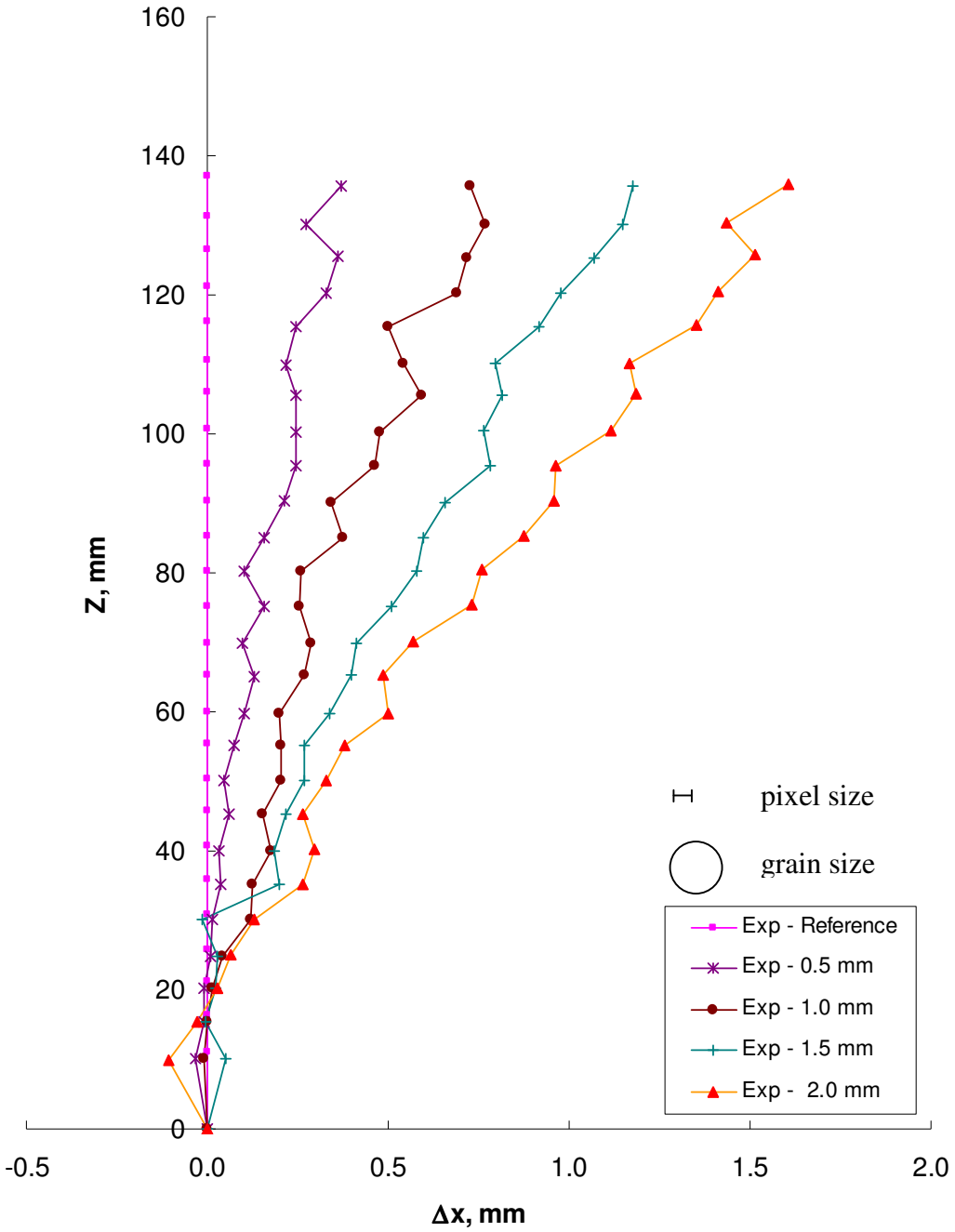

Figure 6.15 Measured horizontal displacement for the midline. Ottawa 20-30 sand at D_r = 93 and stress ratio R = 1.1.

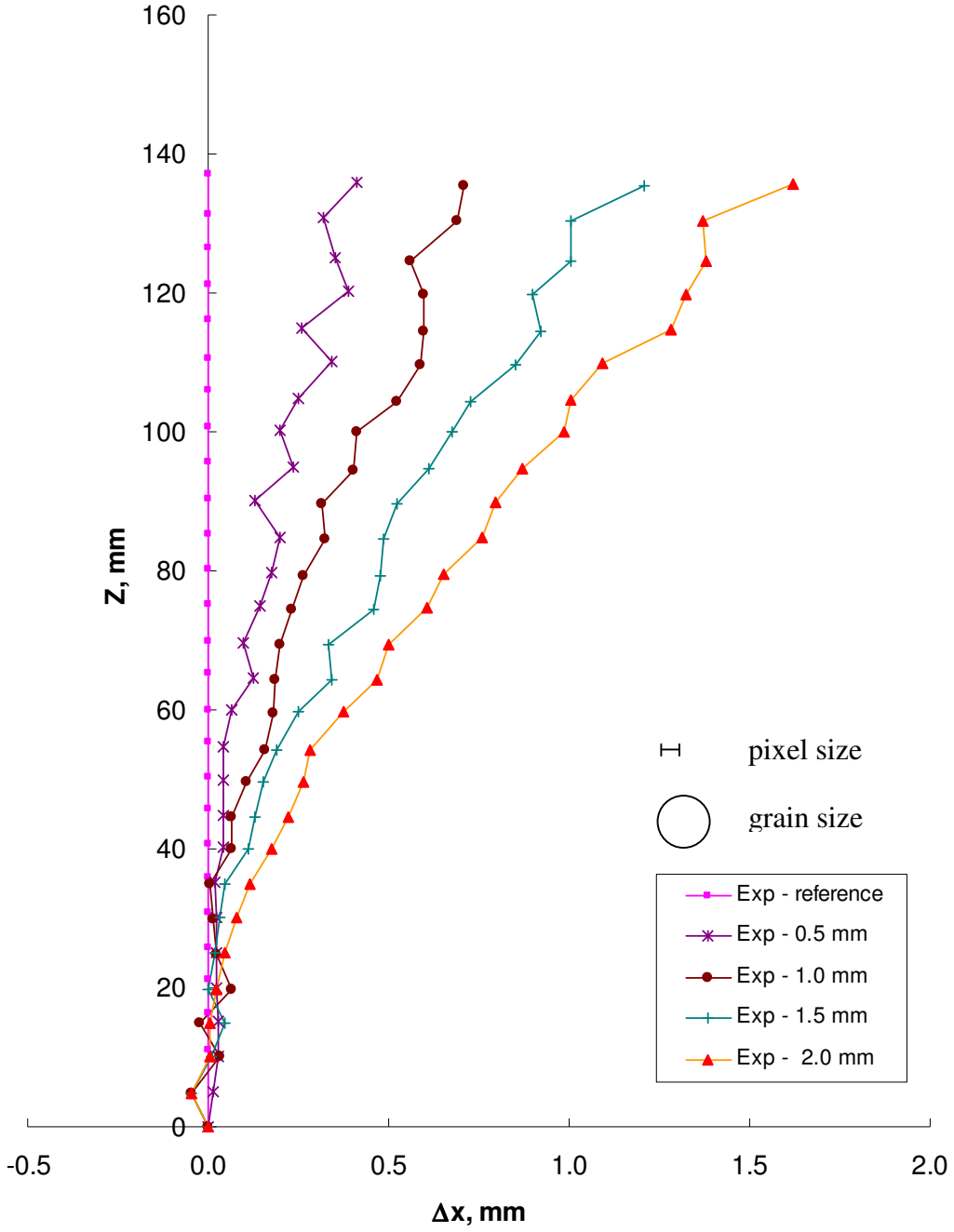

Figure 6.16 Measured horizontal displacement for the midline. Ottawa 20-30 sand at D_r = 90 and stress ratio R = 1.5.

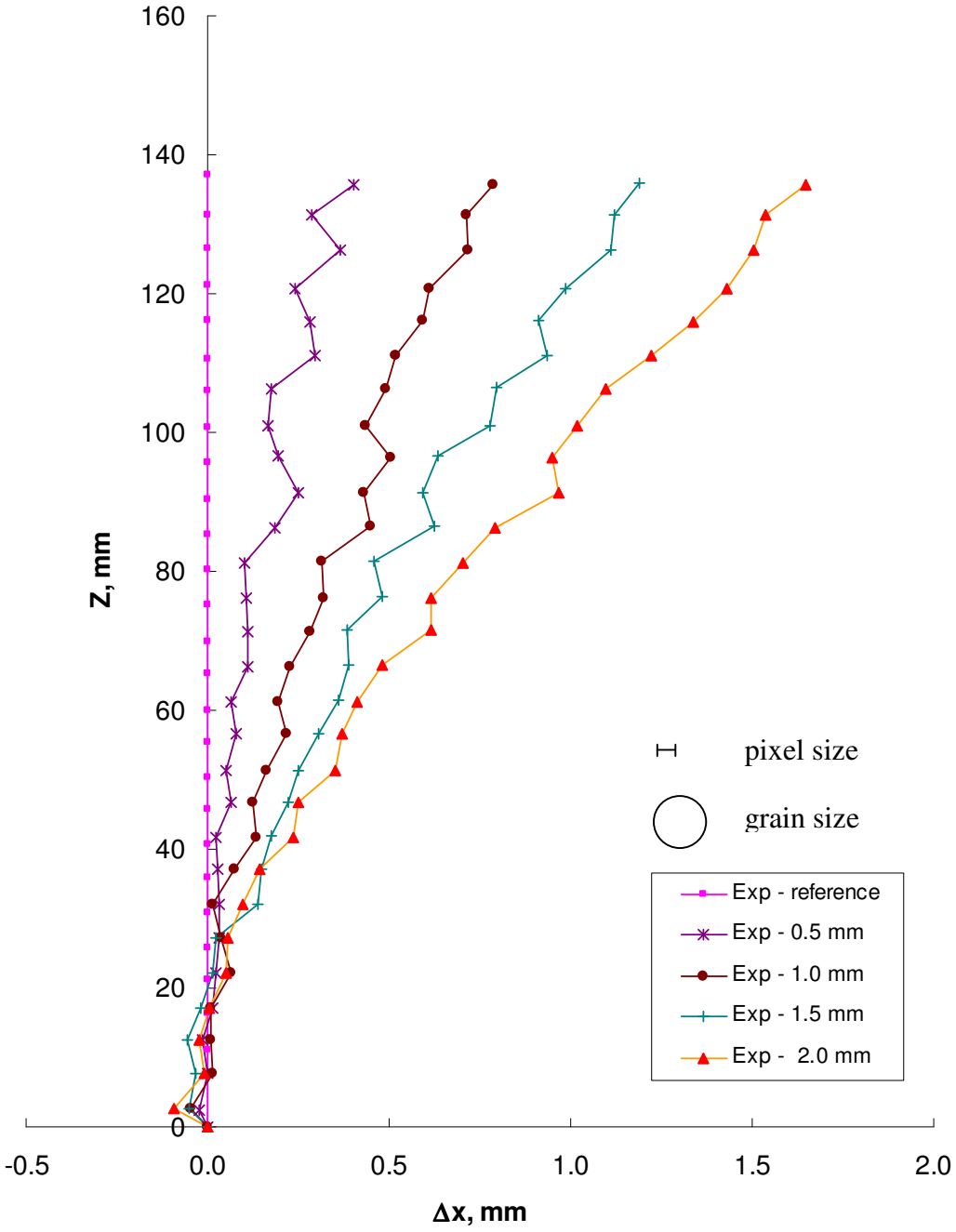

Figure 6.17 Measured horizontal displacement for the midline. Ottawa 20-30 sand at D_r = 86 and stress ratio R = 1.9.

6.4 NUMERICAL MODELING OF THE FLEXURAL TEST

A three-dimensional finite element model is constructed in ABAQUS to simulate the flexural test. Geometry, mesh, boundary conditions, and loading are shown in Figure 6.18. The diameters of dense and loose specimens vary slightly. Therefore, two 3-D models are needed. The 3-D finite element mesh involves 3425 elements (4108 nodes) for soil specimen and 1288 elements (1640 nodes) for the top steel cap. The simulation considers the three phases of loading:

1. confinement provided by all around pressure,
2. deviatoric loading by applying a point load on the center of the top cap, and
3. flexural loading by applying a horizontal displacement on the top cap. The elevation of the point of application is the distance between the top surface of the bottom cap and the point of contact between the load cell tip and the top cap.

The bottom boundary of the specimen is non-slip; therefore, the bottom nodes of the specimen are fixed in the three Cartesian directions (X, Y, Z). The non-slip interface between the top cap and the specimen is simulated by tying the top nodes of the specimen to the bottom nodes of the top cap. These boundary conditions properly match the specimen, as corroborated by digital images. The Modified Cam-Clay model is used to model the soil behavior (refer to Chapter 2).

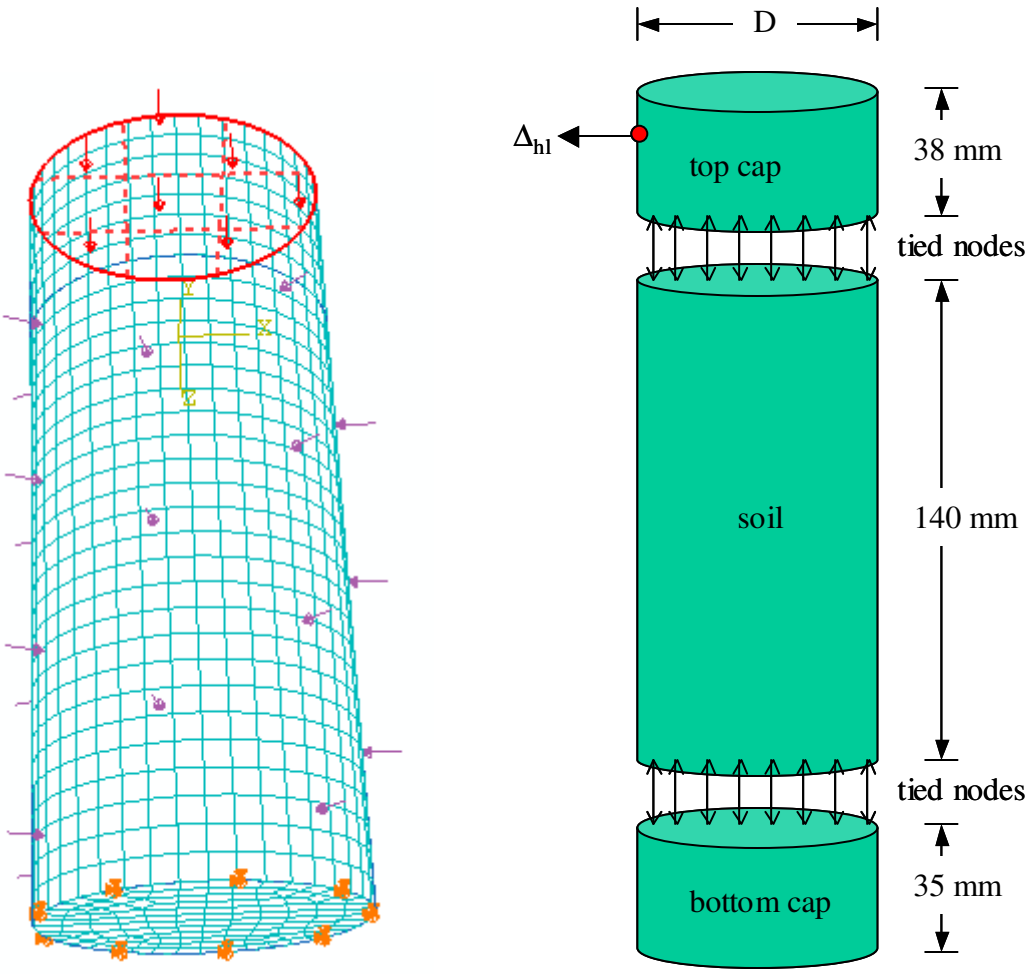

Figure 6.18 Flexural test: model dimensions, mesh, loading, and constraints and boundary conditions. Notation: Sample diameter D, applied horizontal displacement Δ_{hl}.

6.5 STUDIES IN INVERSION

Inversion starts by matching the global measurements; then the predictions of local measurements are verified against the data. The search for optimum constitutive model parameters is performed as shown in Figure 6.19.

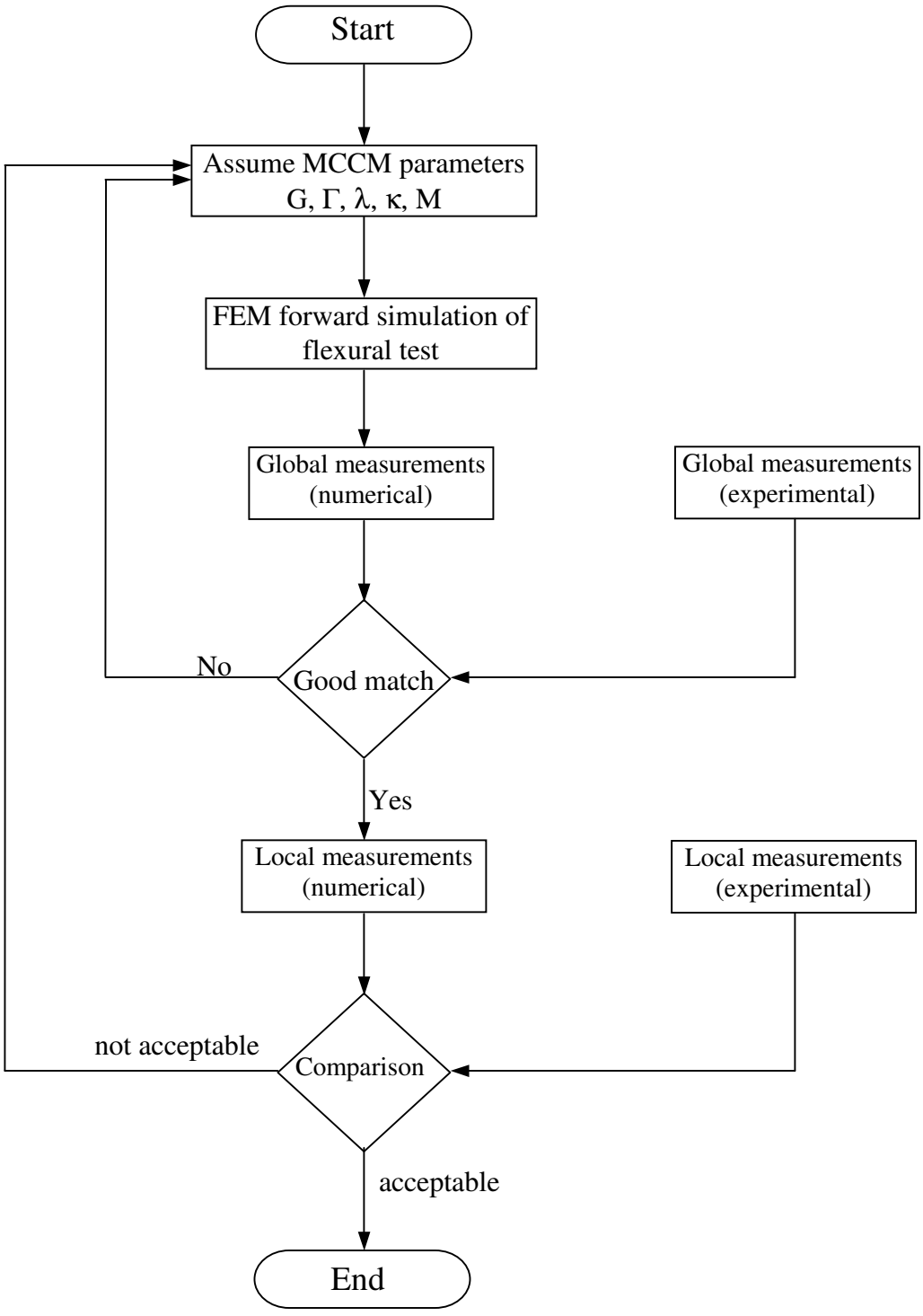

Figure 6.19 Back-calculation of constitutive model parameters – Algorithm.

6.5.1 Matching Global Measurements

The search for the optimum set of parameters is manually performed to gain insight into the nature of the problem. The initial void ratio and loading is known; therefore, only four critical state parameters are varied: κ, λ, M, and G.

1. *Horizontal Force F_{HN}.* The force-displacement is generally hyperbolic during the early stage of the test. However, when the horizontal displacement exceeds 2 to 2.5 mm, the force fluctuates suggesting the development of localizations (Figure 6.20). Therefore, the F_{HN}-Δ_{hl} is fitted up to a nominal horizontal displacement of 2.5 mm. A set of FEM matching trials for Ottawa 20-30 sand at D_r = 90 and stress ratio R = 1.5 are shown in Figure 6.21. Similar matching is performed for all six tests. The best fit for each test is shown in Figure 6.22. The following observations may be drawn from fitting the F_{HN}-Δ_{hl} trends:

- The key constitutive model parameters that control the fitting are the shear stiffness G and the strength parameter M. The value of G helps fit the initial slope of the F_{HN}-Δ_{hl} curve, while M controls the asymptote.
- The parameter λ has a small effect; a smaller value of λ leads to smaller horizontal displacement at the same normalized horizontal force.
- The sensitivity of the trend to the parameter κ is insignificant.
- There is some compensation among parameters. For example, increasing G and decreasing λ as opposed to decreasing G and increasing λ lead to a similar fit.

- The strength parameter M, the shear modulus G, and the parameter λ are larger for dense specimen and large stress ratios.
- Localizations in dense specimens, $D_r \cong 90$ appear to initiate between 0.5 mm and 1 mm horizontal displacement. A lower M value would be obtained if fitting is extended into the localized regime.
- The coexistence of both triaxial compression and triaxial extension zones in the specimen leads to a wide range of stress histories. Thus, the fitting parameters capture the global average behavior of an isotropic soil.

2. *Global Tilt Angle* ψ. Tilt angle is calculated from the numerical simulations from the maximum differential vertical displacement δ of the top cap in the tilting direction and the cap diameter D_{cap}:

$$\psi = \frac{\delta}{D_{cap}}$$

The numerically computed tilt angle using constitutive model parameters inverted from the F_{HN}-Δ_{hl} trends is plotted against the measured tilt angle in Figure 6.23. There is good agreement between the measured and the predicted tilts up to Δ_{hl} = 0.75 to 1 mm. Thereafter, the measured tilt angles experience a noticeable change, while the numerical tilt angle remains almost linear.

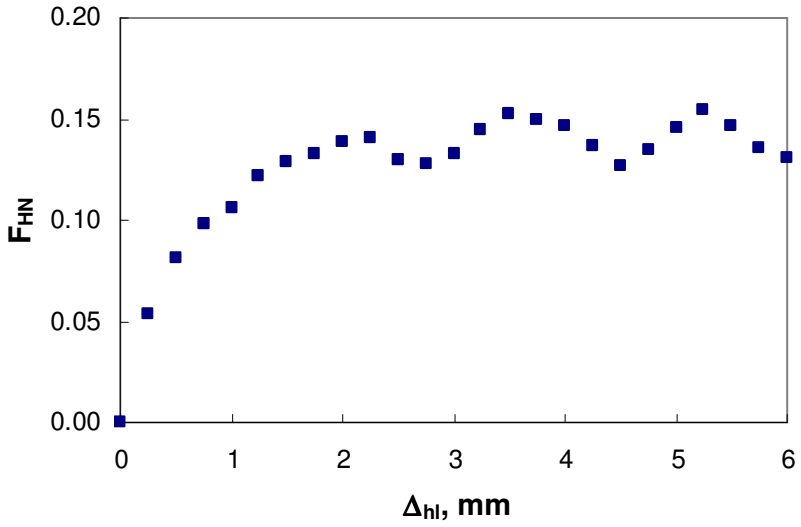

Figure 6.20 Localization manifesting itself in the oscillation of normalized horizontal force. Ottawa 20-30 sand at D_r = 90 and stress ratio R = 1.5. Notation: Normalized horizontal force F_{HN}, applied horizontal displacement Δ_{hl}.

	G (MPa)	λ	M	κ
FEM-1	90	0.0065	1.07	0.0055
FEM-2	100	0.0060	1.1	0.0035
FEM-3	90	0.0065	1.1	0.005
FEM-4	90	0.0065	1	0.005
FEM-5	90	0.0065	1.05	0.005
FEM-6	120	0.0065	1.05	0.005
FEM-7	90	0.0060	1.05	0.005
FEM-8	120	0.0060	1.05	0.005
FEM-9	120	0.0070	1.05	0.005
FEM-10	120	0.0060	1.03	0.005
FEM-11	90	0.0060	1.03	0.005
FEM-12	120	0.0065	1.10	0.004
FEM-13	120	0.0062	1.06	0.004
FEM-14	120	0.0065	1.08	0.004
FEM-15	120	0.0065	1.08	0.005
FEM-16	120	0.0060	1.07	0.004
FEM-17	120	0.0068	1.09	0.005
FEM-18	120	0.006	1.06	0.003
FEM-19	120	0.0067	1.04	0.0045
FEM-20	120	0.057	1.07	0.0035

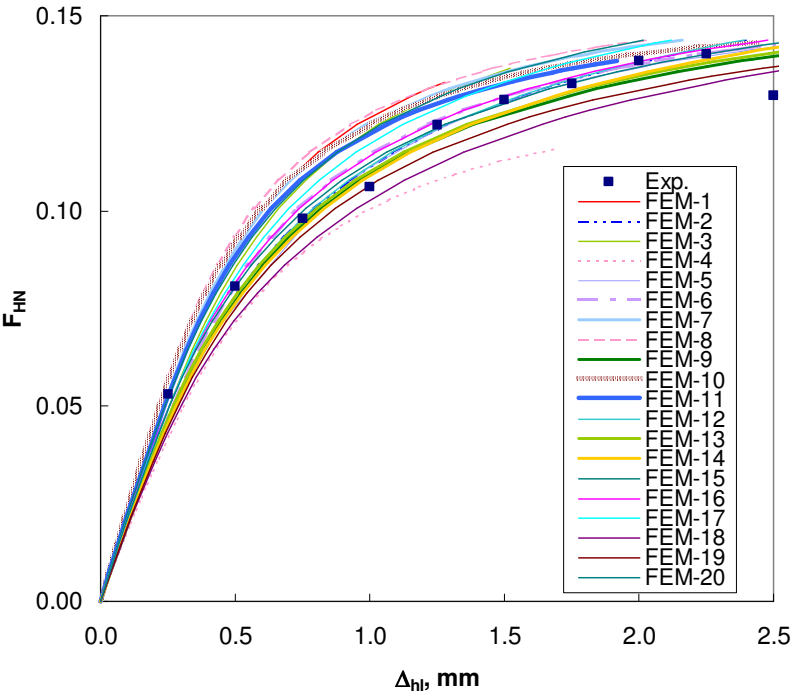

Figure 6.21 Finite element trials to fit the normalized horizontal load for Ottawa 20-30 sand, at D_r = 90 and stress ratio R = 1.5. Notation: Normalized horizontal force F_{HN}, applied horizontal displacement Δ_{hl}, experimental Exp., Numerical FEM.

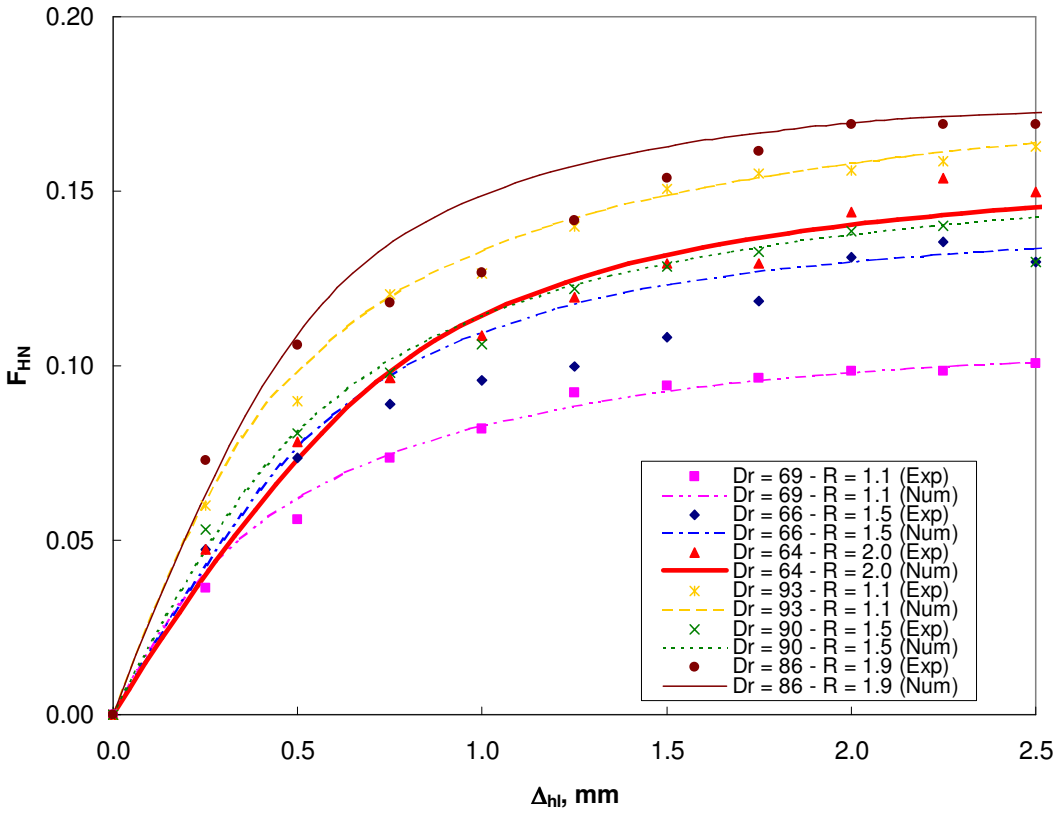

Dr	**69**	**66**	**64**	**93**	**90**	**86**
R	**1.1**	**1.5**	**2.0**	**1.1**	**1.5**	**1.9**
κ	0.005	0.005	0.005	0.005	0.005	0.005
λ	0.0065	0.0065	0.0062	0.0065	0.0065	0.0057
M	0.85	0.95	1.10	1.6	1.05	1.16
G (MPa)	40	50	60	90	120	120

Figure 6.22 Finite element fit to normalized horizontal force. Notation: Normalized horizontal force F_{HN}, Applied horizontal displacement Δ_{hl}, relative density D_r, stress ratio $R = \sigma_1/\sigma_3$, experimental Exp, numerical Num.

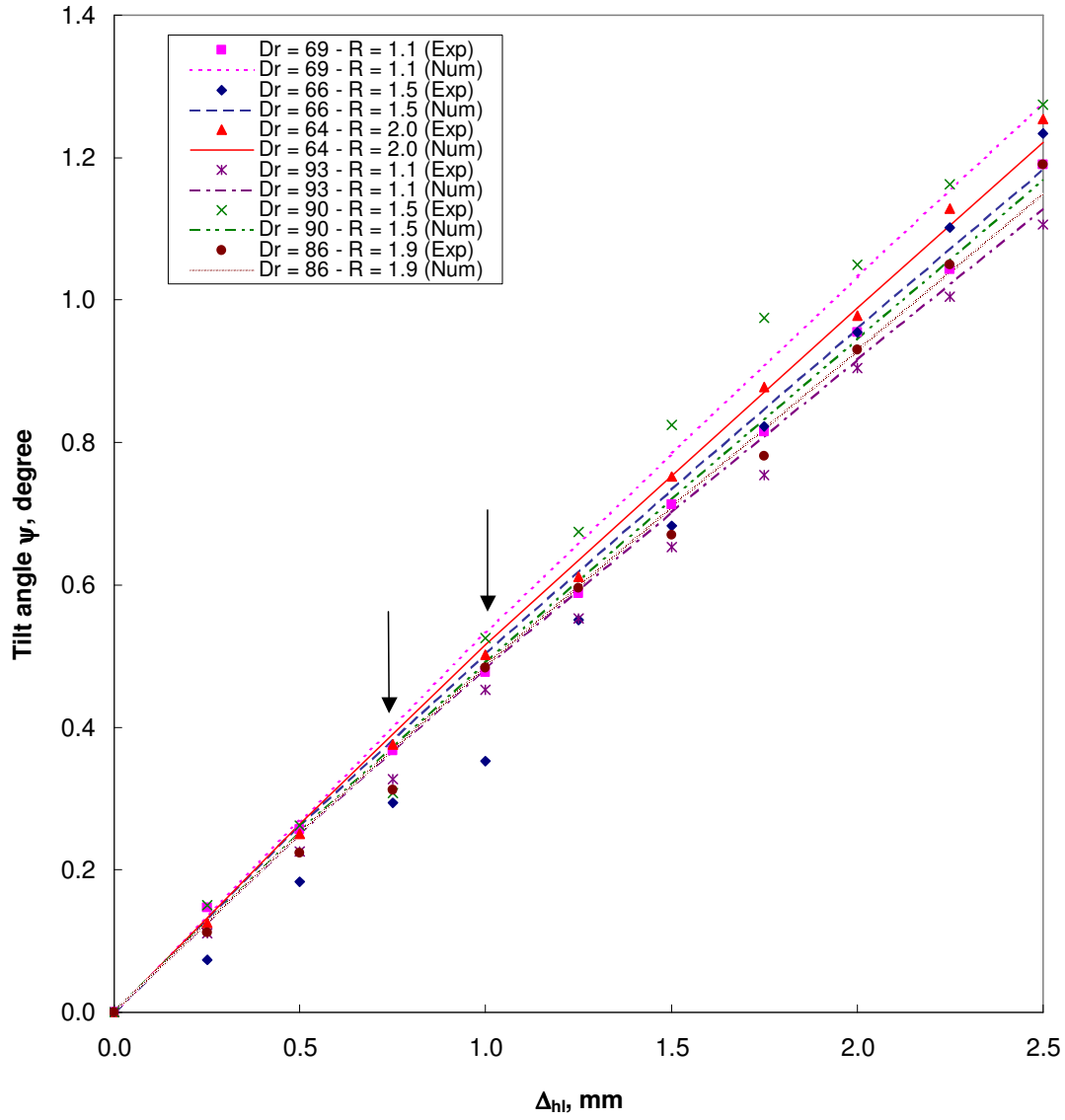

Dr	69	66	64	93	90	86
R	**1.1**	**1.5**	**2.0**	**1.1**	**1.5**	**1.9**
κ	0.005	0.005	0.005	0.005	0.005	0.005
λ	0.0065	0.0065	0.0062	0.0065	0.0065	0.0057
M	0.85	0.95	1.10	1.6	1.05	1.16
G (MPa)	40	50	60	90	120	120

Figure 6.23 Global tilt angle: finite element prediction vs. experimental measurements. Notation: Global tilt angle ψ, applied horizontal displacement Δ_{hl}, experimental Exp, numerical Num.

6.5.2 Matching Displacement Field

For the sake of visualizing the complete displacement field both in-plane and out-of-plane displacements (one case) are checked for matching. The in-plane displacements of the midline are considered. The profile of the specimen perpendicular to the direction of the applied displacement is used for determining transverse displacements. All displacements are post-processed from the images and compared with the corresponding displacements.

1. *Midline Displacement Field.* Image frames of the midline of the mesh are tracked up to 2 mm applied horizontal displacement for each test. Drafting software (AutoCAD) is used for this purpose. Every image (frame) is inserted in AutoCAD file and scaled. Point markers are located on the midline for each frame including the reference frame (image before the application of the horizontal displacement). The coordinates of point markers (x, z) are then exported as an ASCII file. For each frame, the displacement field (Δx and Δz) of the midline is computed as the difference between the coordinates of the current and reference frames. The displacement field is plotted in terms of horizontal displacement Δx versus vertical position z, where z is the new vertical coordinate (position) after applying the global displacement. For each test, numerical simulations with the selected parameters from normalized horizontal force fitting are furnished to predict the displacement field of the midline of the grid (Figures 6.24 though 6.29). The following observations can be made:

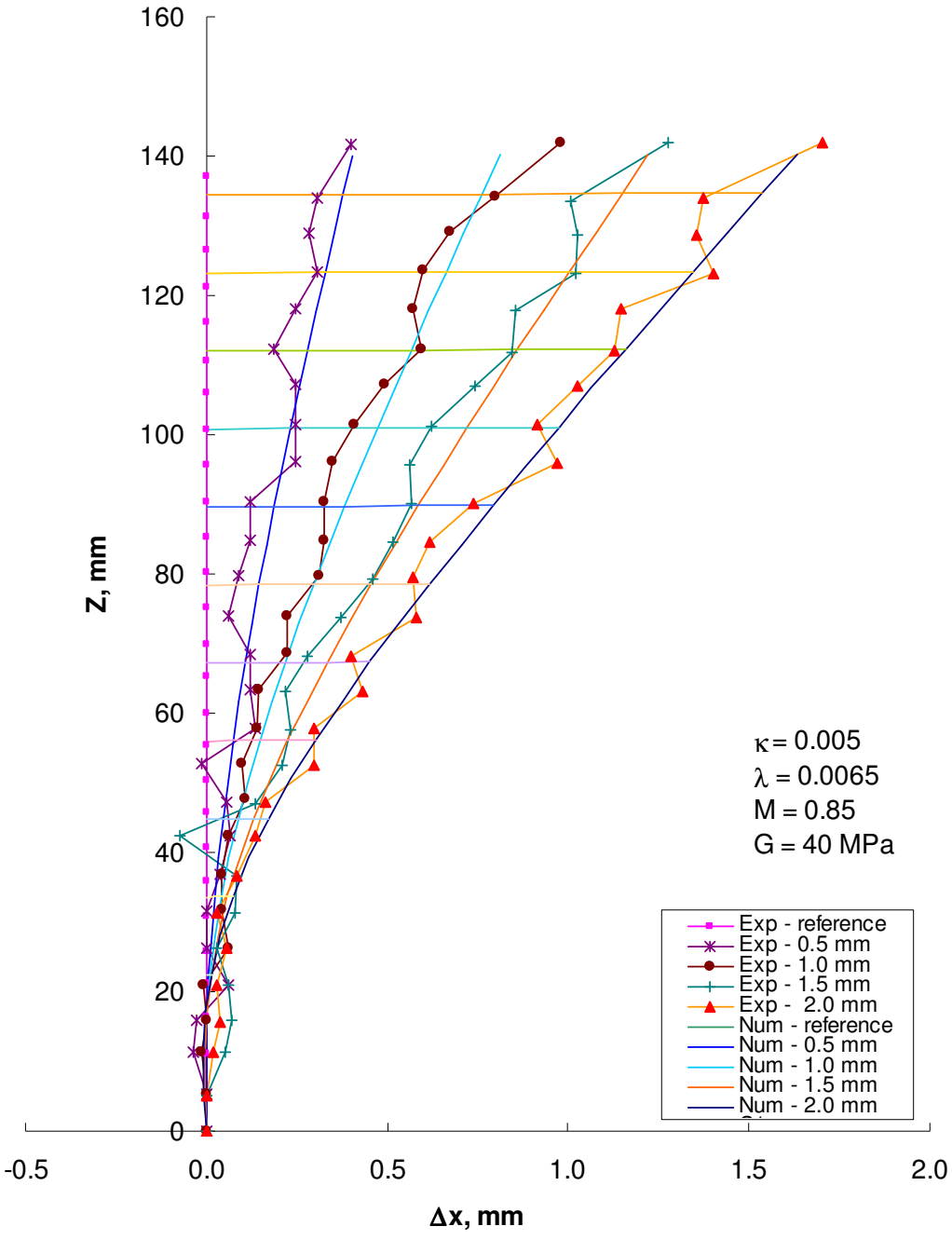

Figure 6.24 Midline horizontal displacement for Ottawa 20-30 sand at D_r = 69 and stress ratio R = 1.1.

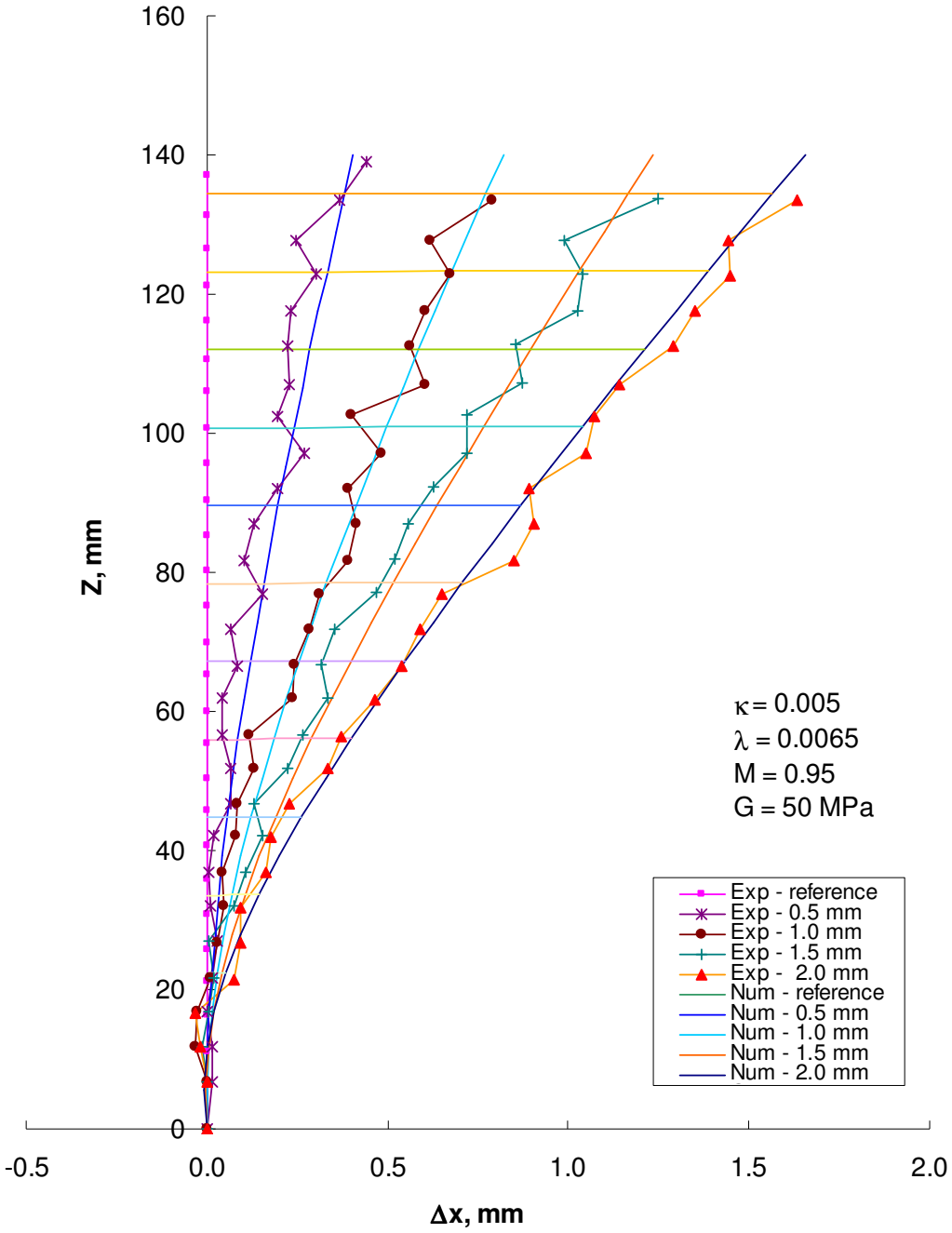

Figure 6.25 Midline horizontal displacement for Ottawa 20-30 sand at D_r = 66 and stress ratio R = 1.5.

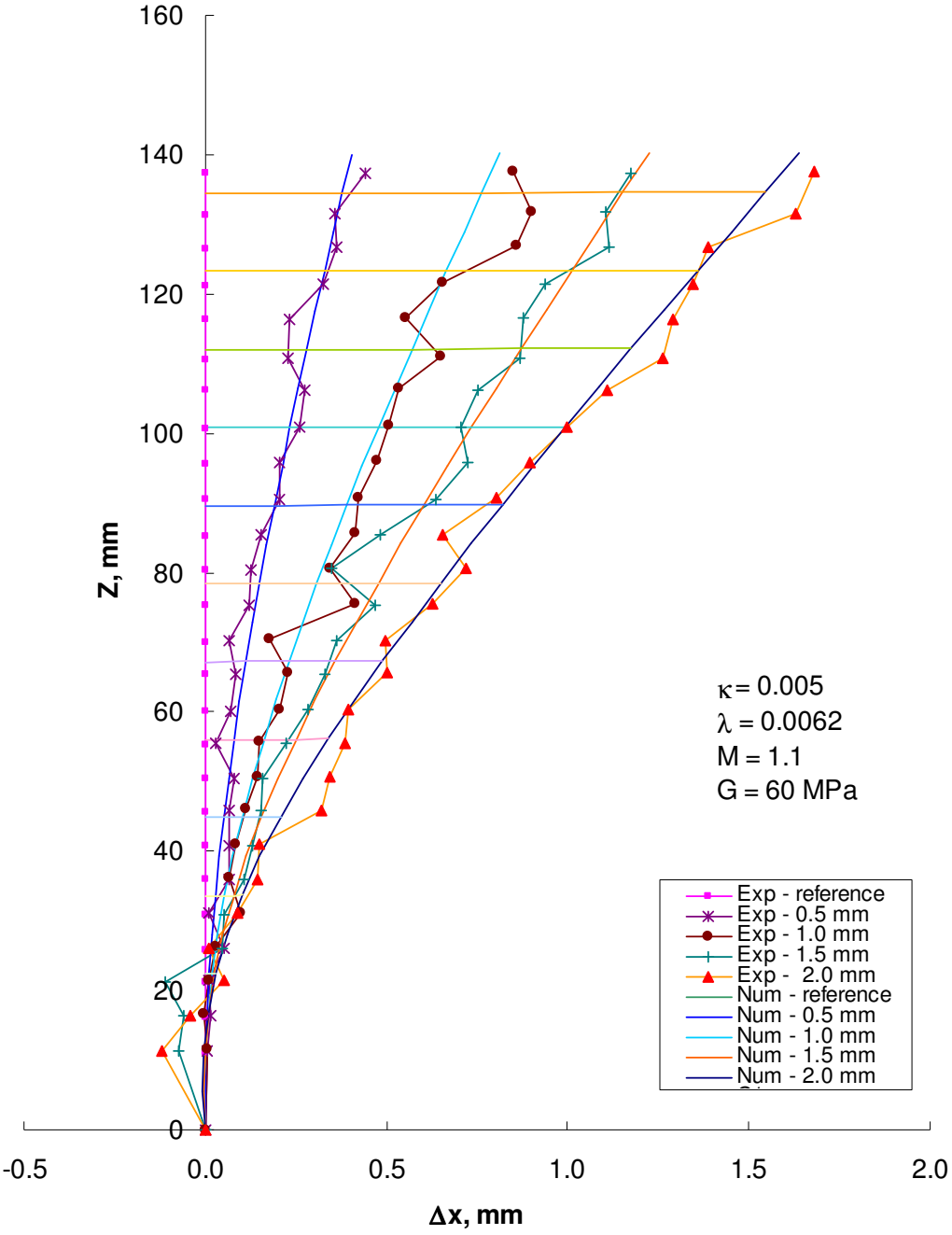

Figure 6.26 Midline horizontal displacement for Ottawa 20-30 sand at D_r = 64 and stress ratio R = 2.0.

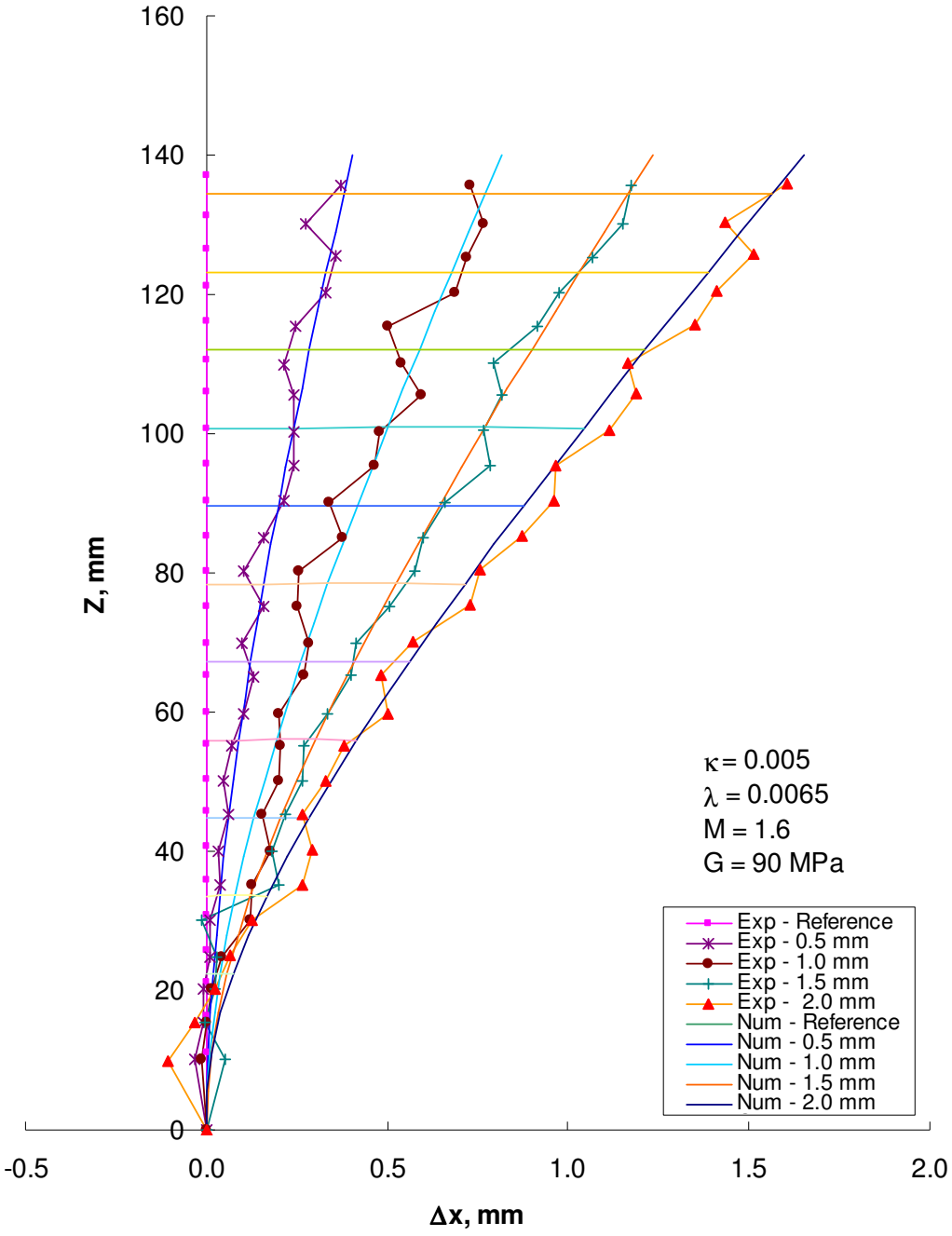

Figure 6.27 Midline horizontal displacement for Ottawa 20-30 sand at D_r = 93 and stress ratio R = 1.1.

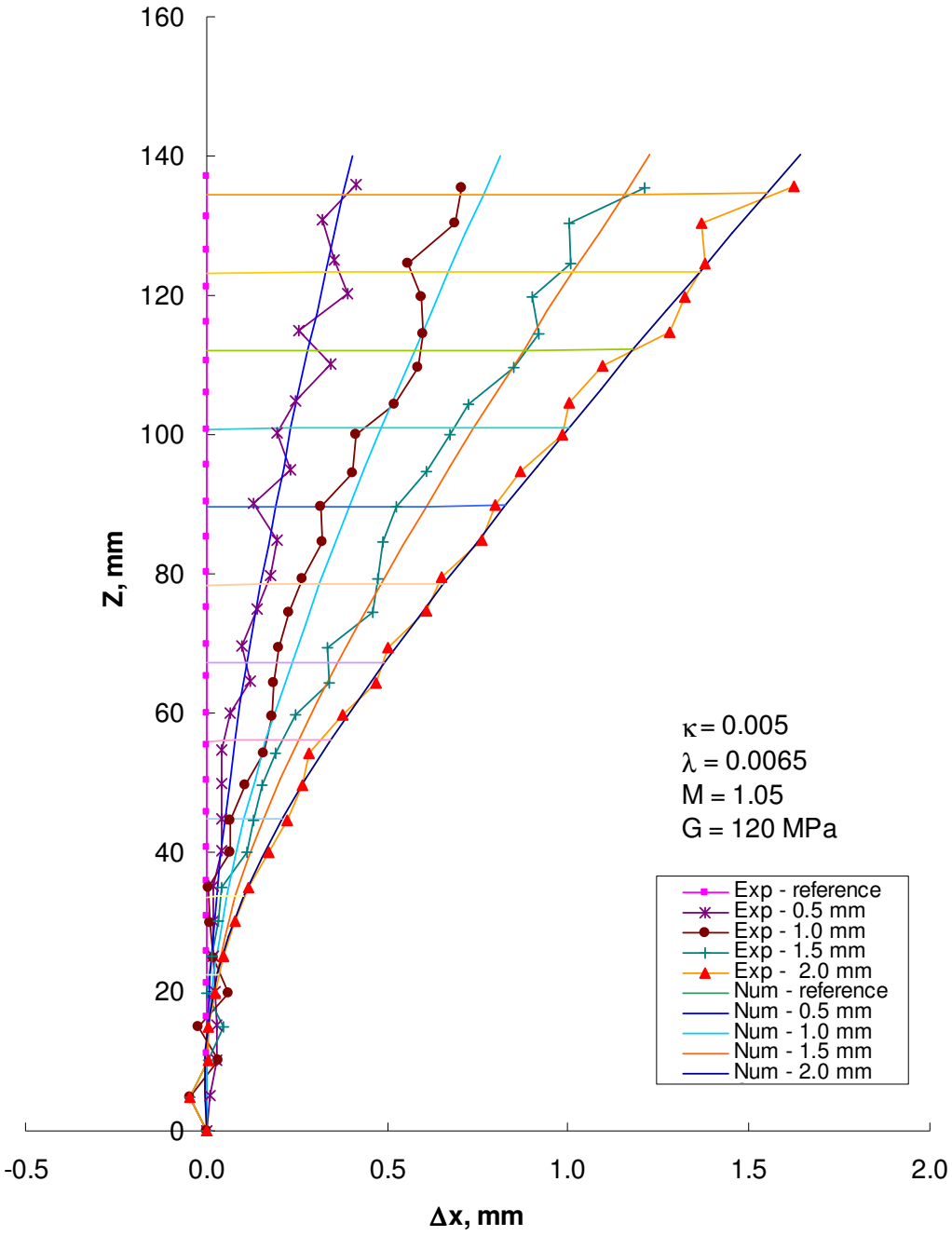

Figure 6.28 Midline horizontal displacement for Ottawa 20-30 sand at D_r = 90 and stress ratio R = 1.5.

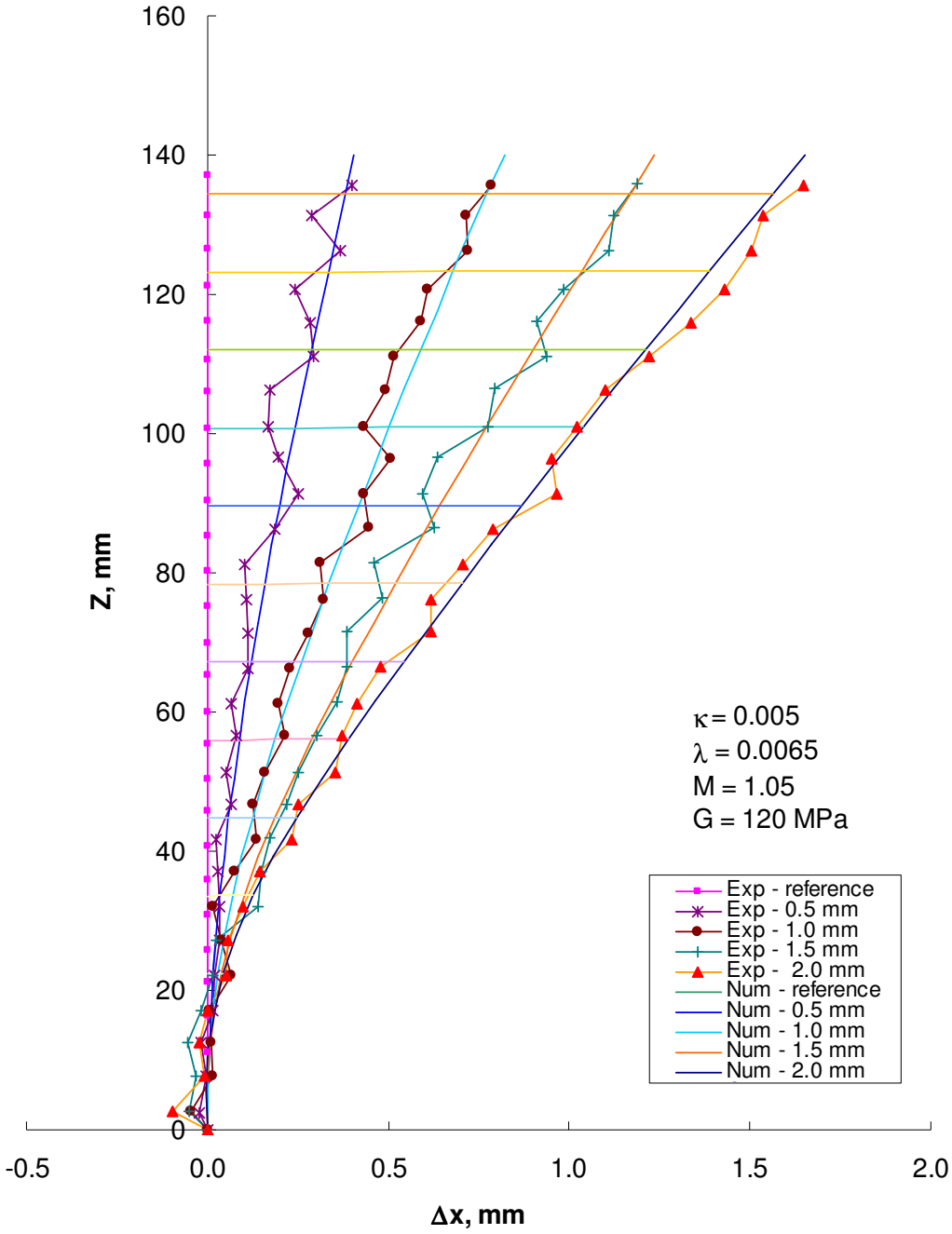

Figure 6.29 Midline horizontal displacement for Ottawa 20-30 sand at D_r = 86 and stress ratio R = 1.9.

- There is fair agreement between numerical and experimental trends. Several numerical simulations (not shown) are conducted with sets of parameters different from the fitting set gathered with F_{HN}-Δ_{hl}. This is attributed to the fashion in which the test is performed. The applied displacement at the free end of the specimen (top cap) results in cantilever-type deformations.
- Experimental and numerical data show a bulge in the midline near the bottom of the specimen. The numerical bulge is very small. The interpretation of this observation requires careful analyses of stress paths at the bottom of the specimen.

2. *Vertical Displacement of Midline right below Top Cap* δ_{vl}. The vertical displacement of a marker glued to the specimen at the top end of the midline (right below the top cap) is monitored in detail through digital images. Measured and numerical results are plotted against the applied horizontal displacement up to 2.5 mm (Figure 6.30). The fitting set of parameters (Table 6.2) is used in the simulations. The following observations can be drawn:

- The vertical displacement from numerical simulations is always downward (negative); while measured vertical displacements oscillate. The constitutive model appears to be incapable of capturing the measured trend.
- The measured displacements are downwards (except for D_r = 90 and R =1.5) during the first Δ_{hl} = 0.5 mm horizontal displacement. Between Δ_{hl} = 0.5 mm and 1 mm a considerable upward vertical displacement is observed. This observation is in agreement with the observed change in the measured global tilt angle between

Δ_{hl} = 0.5 mm and 1 mm (Figure 6.12). It appears that the sudden decrease in the measured tilt angle ψ between Δ_{hl} =0.5 mm and 1 mm can be justified by the sudden upward vertical displacement at the top of the specimen.

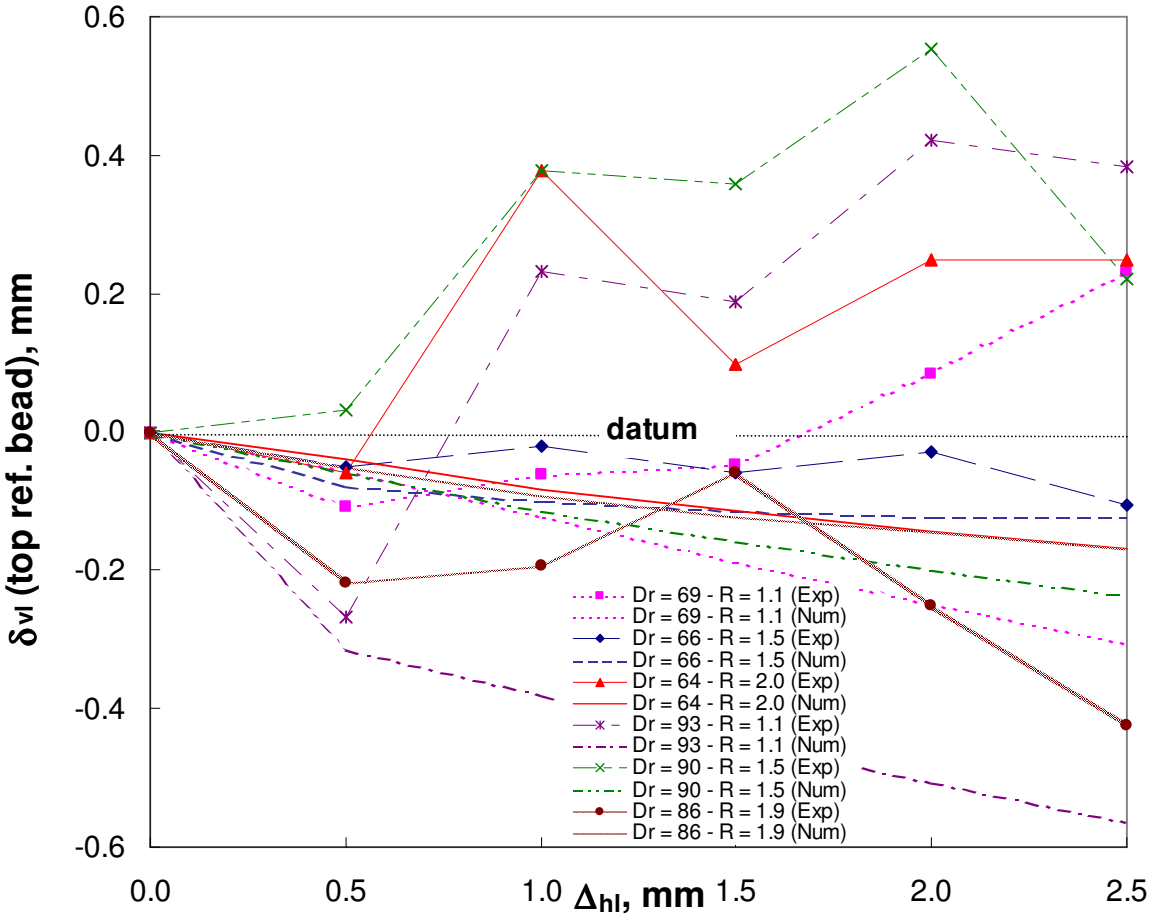

Dr	69	66	64	93	90	86
R	1.1	1.5	2.0	1.1	1.5	1.9
κ	0.005	0.005	0.005	0.005	0.005	0.005
λ	0.0065	0.0065	0.0062	0.0065	0.0065	0.0057
M	0.85	0.95	1.10	1.6	1.05	1.16
G (MPa)	40	50	60	90	120	120

Figure 6.30. Vertical displacement of soil right below top cap δ_{vl}. Finite element prediction vs. experimental measurements. Notation: Applied horizontal displacement Δ_{hl}.

Table 6.2 Inverted critical state parameters from flexural tests on Ottawa 20-30 sand.

D_r	69	66	64	93	90	86
R	**1.1**	**1.5**	**2.0**	**1.1**	**1.5**	**1.9**
κ	0.005	0.005	0.005	0.005	0.005	0.005
λ	0.0065	0.0065	0.0062	0.0065	0.0065	0.0057
M	0.85	0.95	1.10	1.6	1.05	1.16
G (MPa)	40	50	60	90	120	120

Notation: Relative density D_r, stress ratio $R = \sigma_1/\sigma_3$, slope of URL on e-log p` κ, slope of CSL on e-log p` λ, strength parameter M, shear modulus G.

3. *Transverse Profile.* The plane perpendicular to the application of horizontal displacement shows the evolution of out-of-plane displacements during flexure. The transverse profile at 2.5 mm horizontal displacement for the $D_r = 64$ and stress ratio $R = 2$ is plotted in Figure 6.31. The following observations can be made:

- Numerical profiles show that out-of-plane (transverse) displacements are fairly small, yet they could be very informative. Maximum transverse displacements shift upward as the applied horizontal displacement increases.

- The largest out-of-plane displacements occur within the bottom third of the specimen.

- Transverse profiles from experimental measurements agree qualitatively with the numerical profile; however, the degree of accuracy does not allow quantitative comparisons.

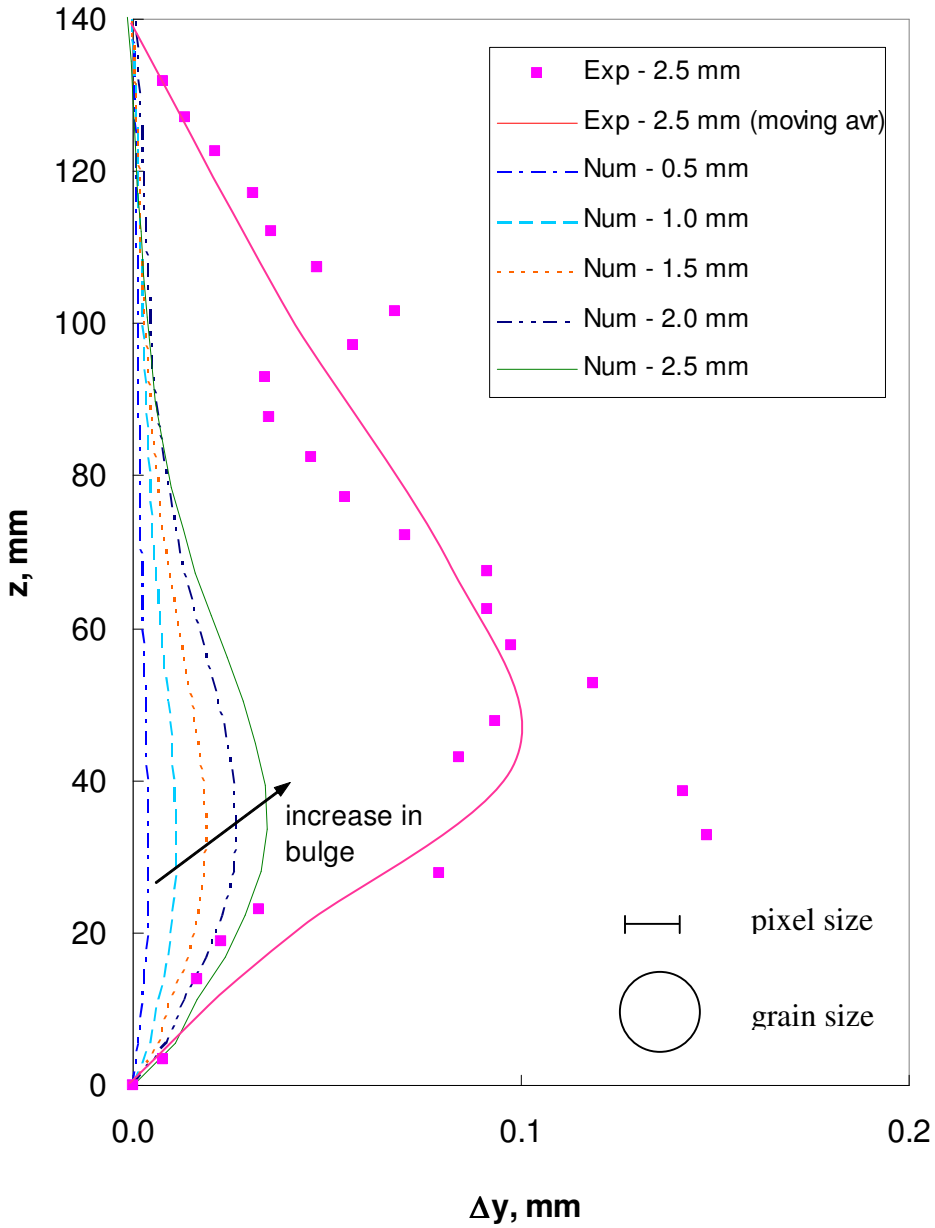

Figure 6.31. Out-of-plane displacement field - transverse profile. Ottawa 20-30 sand at D_r = 64 and stress ratio R = 2.0. Notations: Vertical position z, out-of-plane displacement, experimental Exp, numerical Num.

6.6 TEST MECHANISM AND STRESS FIELD

Flexural tests conducted in this study create a rich stress field that is captured numerically. The stress field for the flexural test undergoes two districts phases. First, a uniform stress field before the application of horizontal displacement; this phase is very similar to isotropic or deviatoric phases in conventional geotechnical tests. Second, a non-uniform stress field during flexural loading. Unlike the non-uniform field created unintentionally by the frictional boundaries in conventional triaxial tests, the non-uniform stress field in this study is intended.

The vertical stress distribution predicted for the Ottawa 20-30 sand specimen at $D_r = 69$ at an initial stress ratio $R = 1.1$ is shown in Figure 6.32. The horizontal load applied to the top cap creates a bending moment that increases towards the bottom of the specimen. It is worth noting that all stresses are compressive. Furthermore:

- The disturbance in vertical stress distribution varies from negligible at the top of the specimen to moderate at the mid-height to extreme at the bottom of the specimen. This reflects the bending moment.

- At the mid-height of the specimen, the bending moment increases the normal stress on the compression side and to a similar extent decreases the normal stress on the extension side and the neutral axis remains in the center of the circular cross section.

- At the bottom of the specimen, the stress distribution is antisymmetric at small horizontal displacement Δ_{hl} = 0.5 mm. However, the stresses on the compressive side are larger than those on the extension side at larger displacements. Therefore, there is a gradual shift in the neutral axis towards the compression side. While stresses increase gradually on the compression side, stresses on the extension side reach a plateau. This is a sign that the extension side at the bottom of the specimen has reached failure before the compression side.

The numerically predicted stress paths at various points within Ottawa sand specimens at D_r = 69 at an initial stress ratio R = 1.1, and D_r = 64 at an initial stress ratio R = 2.0 are shown in Figures 6.33 and 6.34, respectively. Results indicate that:

- The top and mid-height of the specimen are not at failure, while the bottom of the specimen reaches failure (in compression and extension).

- The asymmetry of vertical stress distribution observed in Figure 6.32 at mid-height is also shown in the stress path (Figure 6.33b).

- For the bottom section, the shift in loading mechanism from triaxial compression to triaxial extension is observed (Figure 6.33c). The plateau in vertical stress on the extension side in Figure 6.32c is reached while the compression side is not at failure (Figure 6.33c). Points at the bottom specimen fail in extension much faster those under compression. Note that the M* value equals the M value in this simulation: M = 0.85.

Similar conclusions can be drawn from Figures 6.34, 6.35 and 6.36. The following additional observations can be drawn:

- At the bottom of the specimen, vertical stress fluctuates beyond 0.5 mm horizontal displacement (Δ_{hl}) (Figure 6.34c). This is indicative of numerical instability created by local stress redistribution on the extension side.

- Compression failure is reached at mid-height. The bending moment at the mid-height is theoretically half of that at the bottom; therefore, compressive vertical stresses, created by the large axial load, dominate the stress path at mid-height (Figure 6.35b).

- Elements in the transition zone between triaxial compression and triaxial extension are shifted towards the compression side because of the presence of the large axial load (stress ratio R = 2.0).

- Stress paths of elements 1 and 2 at the bottom of the specimen (Figure 6.35c) apparently intersect with the critical state line on the extension side at point k. Triaxial extension failure is reached at M*=1.1 for a horizontal applied displacement $\Delta_{hl} \cong 0.4$ mm while triaxial compression failure is reached at M = 1.1 for $\Delta_{hl} \cong 2.5$ mm. This appears to result from the imposed non-slip boundary condition which affects the equilibrium conditions in the lowest layer of elements.

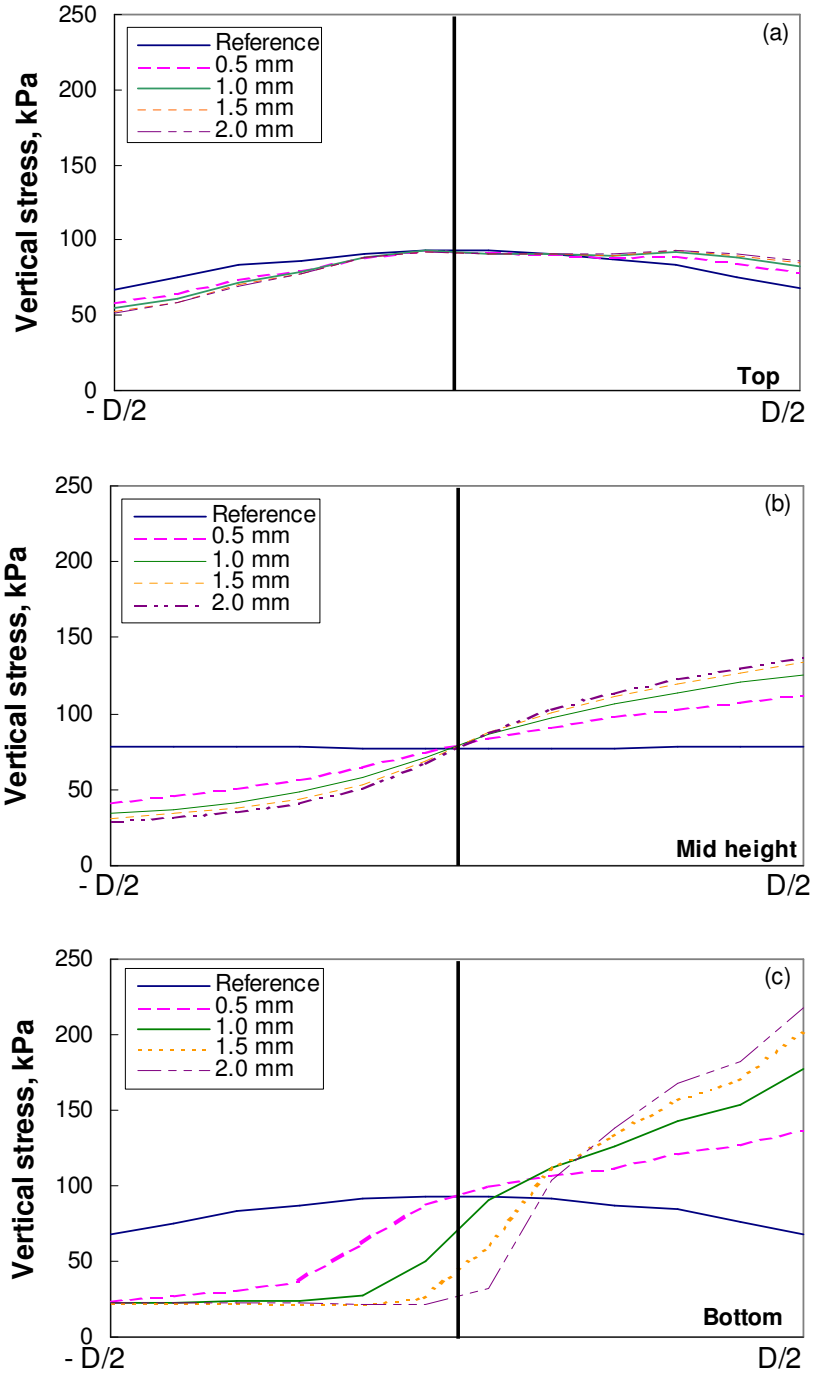

Figure 6.32. Numerical prediction of normal vertical stress distribution for Ottawa 20-30 sand (D_r = 69, stress ratio R = 1.1). (a) Top of the specimen right below top cap. (b) Mid height. (c) Bottom of the specimen right above the bottom cap. Notation: Specimen diameter D. Compressive vertical stress is positive.

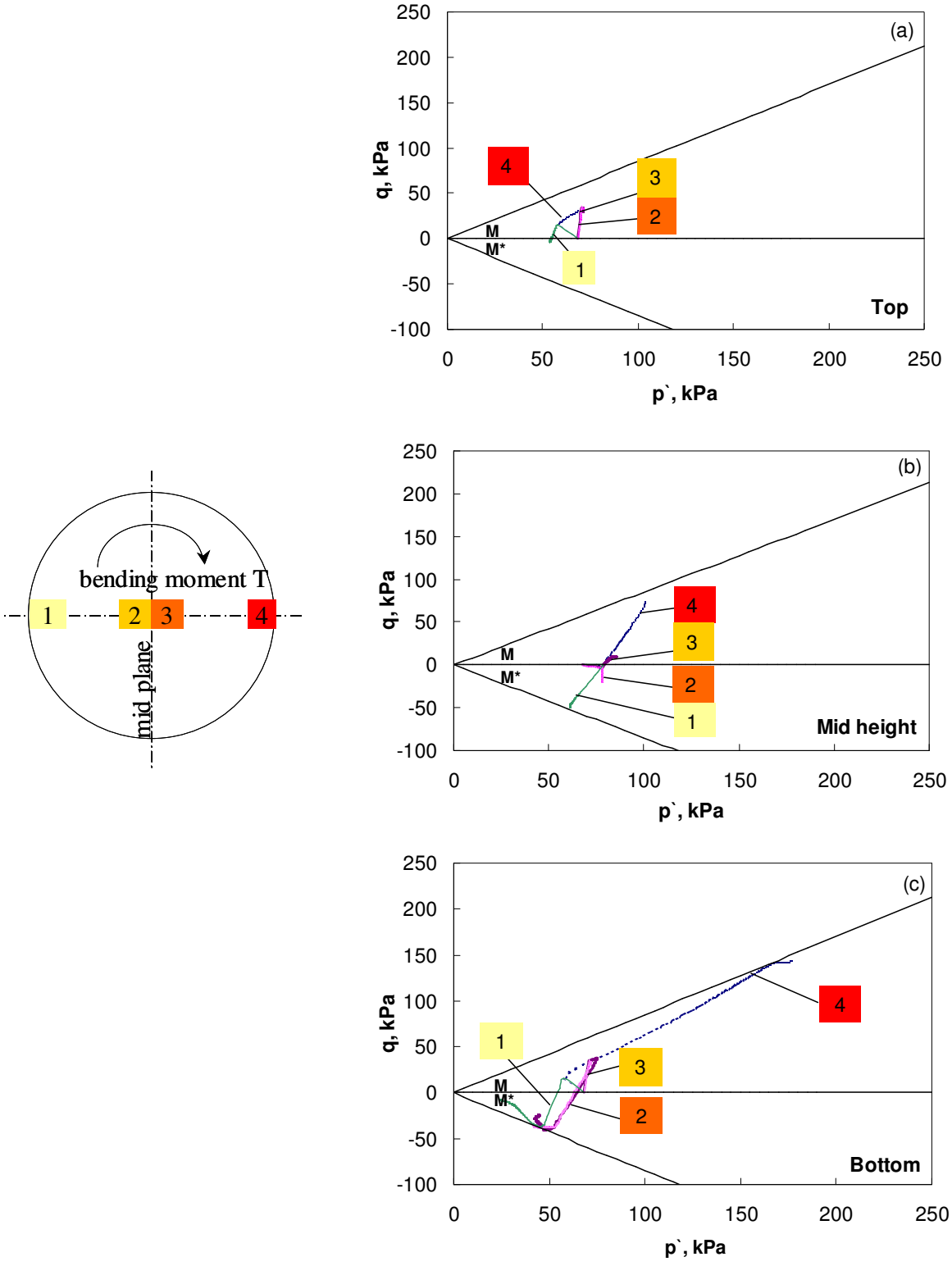

Figure 6.33. Stress paths for Ottawa 20-30 sand (D_r = 69; stress ratio R = 1.1). (a) Top of the specimen. (b) Mid height. (c) Bottom of the specimen. Notation: Mean effective stress p`, deviatoric stress q, strength parameter in compression M, strength parameter in extension M*. Note: Displacement-controlled flexure; limit Δ_{hl} = 15 mm.

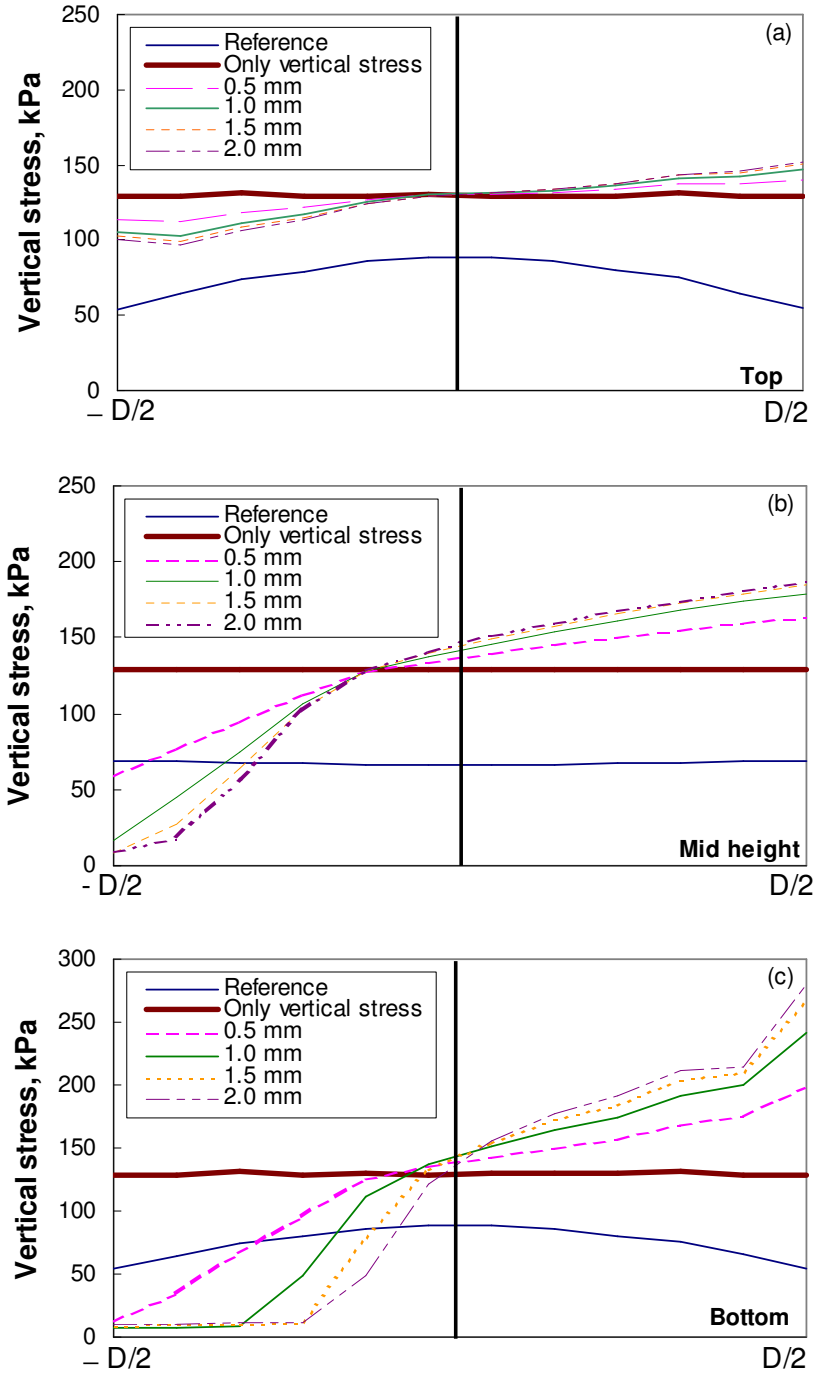

Figure 6.34. Numerical prediction of normal vertical stress distribution for Ottawa 20-30 sand (D_r = 64, stress ratio R = 2). (a) Top of the specimen right below top cap. (b) Mid height. (c) Bottom of the specimen right above the bottom cap. Notation: Specimen diameter D. Compressive vertical stress is positive.

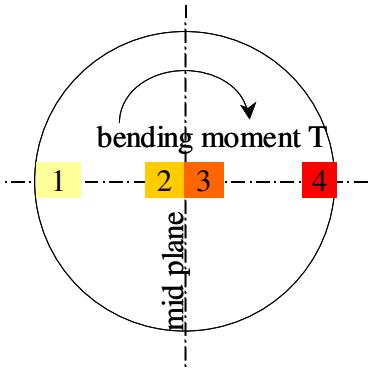

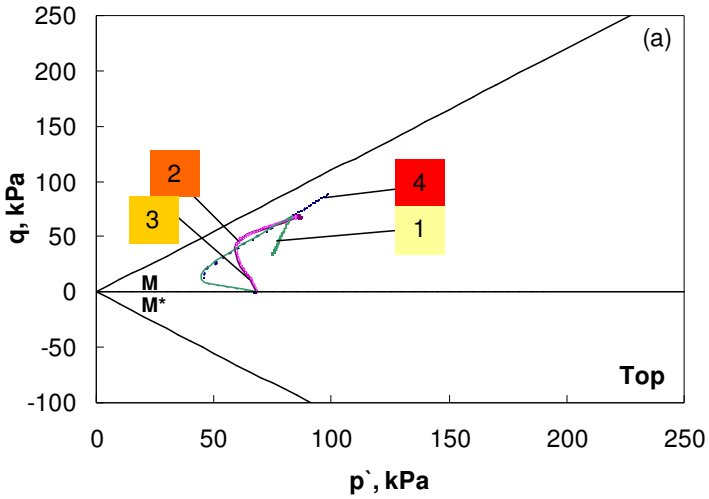

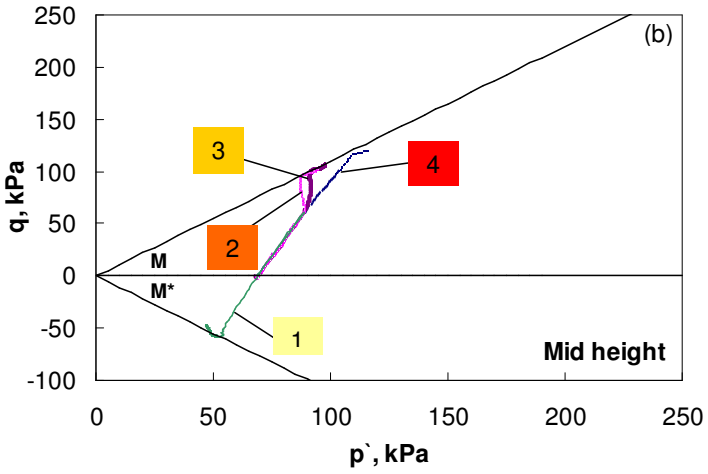

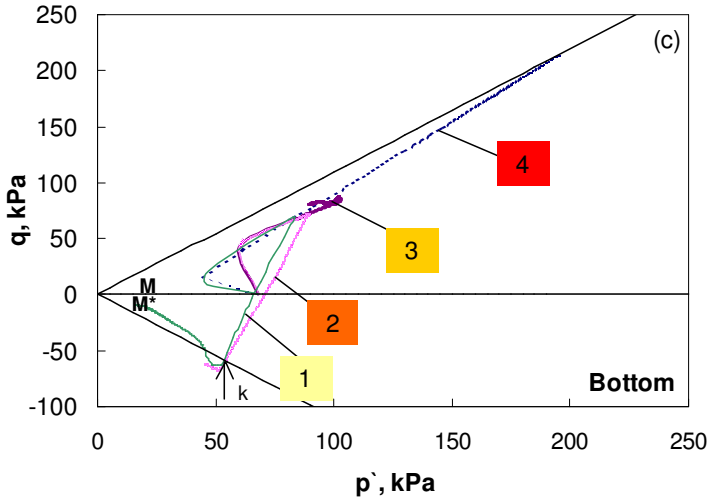

Figure 6.35. Stress path for Ottawa 20-30 sand (D_r = 64; stress ratio R = 2.0). (a) Top of the specimen. (b) Mid height. (c) Bottom of the specimen. Notation: Mean effective stress p`, deviatoric stress q, strength parameter in compression M, strength parameter in extension M*. Note: Displacement-controlled flexure; limit $\square_{hl}$ = 15 mm.

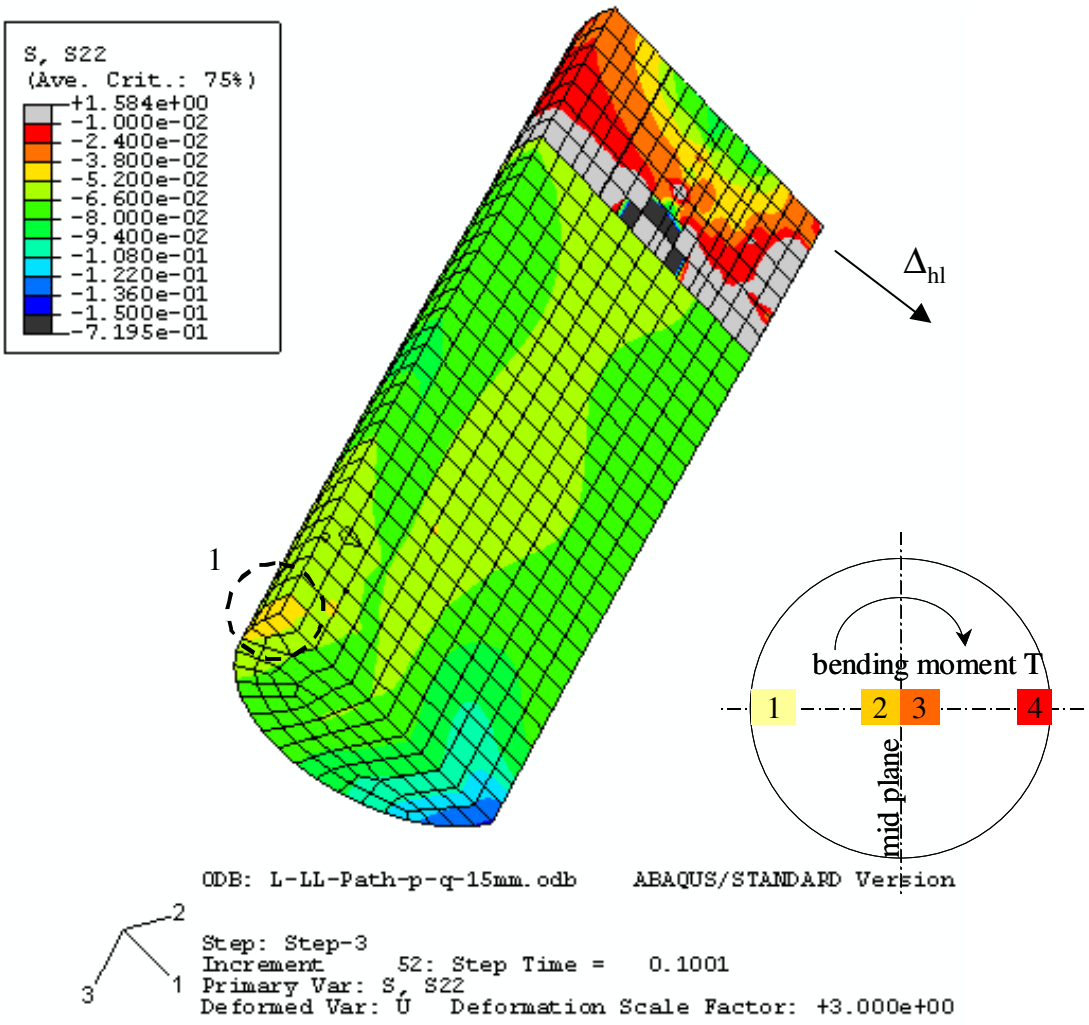

Figure 6.36. Hoop stress contour for Ottawa 20-30 sand (D_r = 64; stress ratio R = 2.0) at applied horizontal stress Δ_{hl} = 0.4 mm. Note: smaller hoop stresses (localized) are circled; stresses are in N/mm^2; compressive stresses are negative.

6.7 DISCUSSION AND CONCLUSIONS

The flexural test is information-rich. Still, there are limitations in extracting a unique set of constitutive model parameters from a single test. Related observations follow.

- The in-plane displacement is fairly insensitive to constitutive model parameters.

- The out-of-plane transverse displacement pattern is informative; however, the digital imaging technique used in this study is rather crude. More accurate imaging or displacement measurement techniques could make use of the entire displacement field, especially the out-of-plane profile.

- In this study, the back-calculation of constitutive model parameters is initiated using the normalized horizontal force vs. horizontal displacement F_{HN}-Δ_{hl}. In other words, global data are used to generate an acceptable "initial guess". Automated routines may explore alternative conversion paths.

- The test causes both triaxial compression and triaxial extension at the same time, and a wide range of strain levels.

- The localized failure at the bottom of the specimen may bias results if specimens are heterogeneous.

CHAPTER VII

CONCLUSIONS AND RECOMMENDATIONS

This research considered constitutive model calibration as an inverse problem and explored the invertability of constitutive model parameters in the presence of measurement and modeling errors. Early results prompted the development of an information-rich test that can be used to enhance the inversion of constitutive model parameters. The main conclusions from this study follow:

- The design of an information-rich test must be guided by establishing an apriori connection between the nature of gathered data and their usefulness in the inversion of model parameters in the adopted constitutive model.

- The Modified Cam-Clay Model is a simple yet robust constitutive model that captures many key characteristics of soil behavior. These are desirable from the inversion standpoint.

- Inversion results, i.e., the optimum set of constitutive parameters are intimately dependent on the selected error function. The definition of error and of a single error norm is mathematically and philosophically challenging.

- The set of parameters that minimizes the total error (L2-total) does not necessarily yield a minimum error for all loading phases. The solution set depends on the number of points representing the test phase (discretization and data sampling).

- Error surfaces are concave for all Cam-Clay parameters in the absence of noise. However, the optimum parameter set may not be unique when data are noisy.

- In this study, concavity of the suggested total error (L2-total) does not guarantee concavity of single measurements and does not ensure uniqueness of inversion.

- The decoupling of constitutive model parameters facilitates inversion. However, there is no full decoupling of constitutive parameters even in the simple Cam-Clay model: parameters affect all phases to a lesser or higher degree.

- The prediction of soil response from estimated constitutive parameters based on noisy test measurements is always accompanied by a residual error.

- The Cam-Clay parameters with greatest convergence are the strength parameter M and the shear modulus G.

- Boundary conditions in triaxial tests have a significant effect on the stress and strain distribution within the specimen. Triaxial test data gathered with frictional boundaries underpredicts soil strength.

- Using an improper constitutive model hinders the understanding of the expected soil behavior and increases the distance between model and data.

- The displacement and stress fields in flexural loading are highly non-homogenous, and the specimen experiences both triaxial compression and triaxial extension.

- Full utilization of global measurements (e.g., external forces and boundary displacements) and local measurements (displacement field) would enable a more robust inversion of constitutive parameters.

- Accurate measurements are needed. In particular, the simple approach to capture displacements in this study is insufficient.

- The integration of automatic test controllers and effective inversion algorithms can lead to a paradigm shift in laboratory testing and constitutive model calibration.

The following developments can be recommended for further research:

- More “interesting” information-rich displacement fields need to be created, for example, a penetrometer pushing into the soil specimen from the top cap. The slenderness ratio H/D of the specimen should be optimized.

- Additional measurements can enhance inversion, such as: total volume change, base stresses, acoustic emission, and thermal field. Furthermore, monitoring acoustic emission or infrared imagery can explicitly show the development of yield or localization zones in the specimen.

APPENDIX A

ONE-ELEMENT SIMULATION USING CONSTITUTIVE EQUATIONS OF MCCM

Four triaxial simulations are conducted using constitutive equations of the modified Cam-Clay model (MCCM). In all simulations Pueblo sand is used.

A.1 Normally Isotropically-Consolidated Drained

Material Constants

$e0 := 0.34$ $M := 1.24$ $\lambda := 0.014$ $\kappa := 0.0024$ $\nu := 0.28$ $GSC := 20000$

@ p_0 = 69 kPa

Initialize

$m := 4000$ $\Delta q := 3.0$ $\Delta p := 1$ $n := 100$ $i0 := 69$ $i := i0..m$ $l := 1..400$

$dp_i := if(i \le n, \Delta p, \Delta p)$ $d\eta_i := 0$

$dq_i := if(i > n, \Delta q, 0.0)$ $d\varepsilon q_i := 0$

$de_i := 0$ $d\varepsilon p_i := 0$

$e_i := e0 + de_i$ $\eta f := M$

$q_i := 0$

Definitions

$p_i := p_i + dp_i$

$q_i := q_i + dq_i$

$\beta_i = \frac{\left[M^2 + (\eta_i)^2\right]}{(\lambda - \kappa)}$ common factor

$\eta_i := \frac{q_i}{p_i}$ $d\eta_i := \frac{dq_i - \eta_i \cdot dp_i}{p_i}$ $GS_i = 1.5 \cdot \frac{p_i \cdot (1 + e0) \cdot (1 - 2 \cdot \nu)}{\kappa \cdot (1 + \nu)}$ shear modulus (if variable)

Elastic Strains

$$\begin{pmatrix} d\varepsilon pe_i \\ d\varepsilon qe_i \end{pmatrix} = \begin{bmatrix} \frac{\kappa}{(1 + e_i) p_i} & 0 \\ 0 & \frac{1}{3GSC} \end{bmatrix} \cdot \begin{pmatrix} dp_i \\ dq_i \end{pmatrix}$$

Total Strains

$$\begin{pmatrix} d\varepsilon p_i \\ d\varepsilon q_i \end{pmatrix} = \frac{1}{(1 + e_i) \cdot \beta_i \cdot p_i} \cdot \begin{bmatrix} \left[M^2 - (\eta_i)^2\right] + \kappa \cdot \beta_i & 2 \cdot \eta_i \\ 2 \cdot \eta_i & \left[\frac{4 \cdot (\eta_i)^2}{M^2 - (\eta_i)^2}\right] + \frac{\left[(1 + e_i) \cdot \beta_i \cdot p_i\right]}{3 \cdot GSC} \end{bmatrix} \cdot \begin{pmatrix} dp_i \\ dq_i \end{pmatrix}$$

Initial Conditions and Incrementation

$i := 69..m \qquad p_i := 0 \qquad p0 := 69$

$dp_i := if(i \le n, \Delta p, \Delta p)$

$dq_i := if(i > n, \Delta q, 0.0)$

Update

$p_i := if(i \cdot \Delta p \ge p0, i \cdot dp_i, p0) \qquad q_i := if[i > n, (i - n) \cdot dq_i, 0.0]$

$ep_i := ep_i + dep_i \qquad eq_i := eq_i + deq_i$

$GS_i := 1.5 \cdot \frac{p_i \cdot (1 + e0) \cdot (1 - 2 \cdot \nu)}{\kappa \cdot (1 + \nu)} \qquad \eta_i := \frac{q_i}{p_i} \qquad e_i = e_i + de_i$

$de_i := if\left(i \ge i0, -\lambda \cdot \frac{dp_i}{p_i}, -\kappa \cdot \frac{dp_i}{p_i}\right)$

$e_i := if(i > i0, e_{i-1} + de_i, e0)$

$\beta_i := \frac{\left[M^2 + (\eta_i)^2\right]}{(\lambda - \kappa)}$ common factor

Limiting stress incrementation at η=M (critical State)

$dp_i := if(\eta_i < M, dp_i, 0)$

$dq_i := if(\eta_i < M, dq_i, 0)$

$cs_i := if\left[\frac{q_i}{p_i} \le M, n + (i - n) \cdot dp_i, 0\right] \qquad cs := max(cs) \qquad cs = 170$

Elastic Strains

$depe_i := if\left[\left(p_i \le p0\right), \frac{\kappa}{(1 + e_i) p_i} \cdot dp_i, 0\right]$

$deqe_i := if\left[\left(p_i \le p0\right), \frac{1}{3GSC} \cdot dq_i, 0\right]$

Total Strains

$$\begin{pmatrix} dep_i \\ deq_i \end{pmatrix} := \frac{1}{(1 + e_i) \cdot \beta_i \cdot p_i} \cdot \begin{bmatrix} \left[M^2 - (\eta_i)^2\right] + \kappa \cdot \beta_i & 2 \cdot \eta_i \\ 2 \cdot \eta_i & \left[\frac{4 \cdot (\eta_i)^2}{M^2 - (\eta_i)^2}\right] + \frac{\left[(1 + e_i) \cdot \beta_i \cdot p_i\right]}{3 \cdot GSC} \end{bmatrix} \cdot \begin{pmatrix} dp_i \\ dq_i \end{pmatrix}$$

Limiting loading and control volumetric and shear strains at η=M (critical State)

$p_i := \text{if}(\eta_i < M, p_i, p_{i-1})$

$q_i := \text{if}(\eta_i < M, q_i, q_{i-1})$

$\varepsilon p_i := \text{if}(i \geq i0, \varepsilon p_{i-1} + d\varepsilon p_i, d\varepsilon p_i)$ to limit volumetric strain at Critical State

$\varepsilon q_i := \text{if}(i \geq i0 \wedge \eta_i < M, \varepsilon q_{i-1} + d\varepsilon q_i, \varepsilon q_{i-1} + 0.00001)$ to allow infinite shear strain after Critical State (flow)

$e_i := \text{if}[i \geq i0, [e0 - (1 + e0) \cdot \varepsilon p_i], e0]$

$\eta_i := \text{if}(\eta_i < M, \eta_i, M)$

Axial and Radial Strains

$\varepsilon z_i := \frac{\varepsilon p_i}{3} + \varepsilon q_i$

$\varepsilon r_i := \frac{\varepsilon p_i}{3} - \frac{\varepsilon q_i}{2}$

Check Stress Path and Milestones

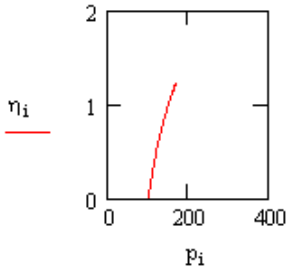

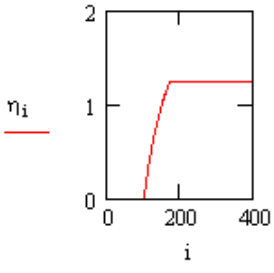

Initial condition: $p_{i0} = 69$ $q_{i0} = 0$

Isotropic loading: $p_n = 100$ $q_n = 0$

Critical state: $p_{cs} = 170$ $q_{cs} = 210$ $\eta_{cs} = 1.235$ $e_{cs} = 0.319$

Flow: $p_m = 170$ $q_m = 210$ $\eta_m = 1.24$ $e_m = 0.319$

Isotropic Consolidation and Critical State Lines

$q_{CSL_1} := M \cdot [(1) \cdot \Delta p]$

$e0_{icl} := e0 + \lambda \cdot (\ln(p0) - 1)$

$e0_{icl} = 0.385$

$e0_{csl} := e0 - (\lambda - \kappa) \cdot \ln(2)$

$e0_{csl} = 0.332$

$e_{CSL_1} := [e0_{icl} - \lambda \cdot (\ln(1) - 1) - (\lambda - \kappa) \cdot \ln(2)]$

$e_{ICL_1} := [e0_{icl} - \lambda \cdot (\ln(1) - 1)]$

Critical State Space

Pueblo Sand NC - CD Test - stress controlled - constant G

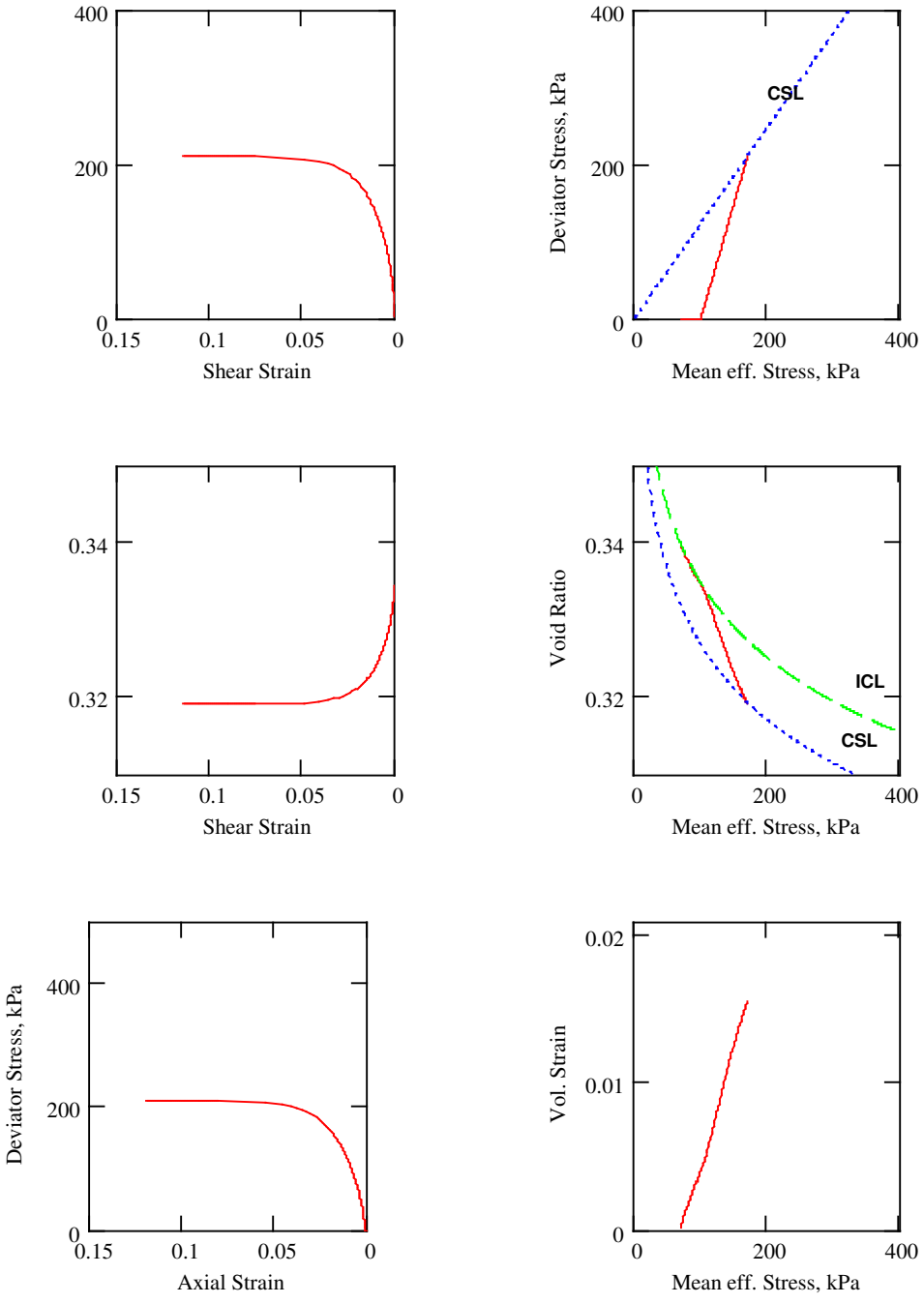

A.2 Normally Isotropically-Consolidated Undrained

Pueblo Sand

Normally Consolidated - Consolidated Undrained - Stress Controlled - Constant Shear Modulus

Material Constants

$e0 := 0.34$ $M := 1.24$ $\lambda := 0.014$ $\kappa := 0.0024$ $\nu := 0.28$ $GSC := 20000$

@ p_0 = 69 kPa

Initialize

$m := 4000$ $n := 100$ $i0 := 69$ $i := i0..m$ $l := 1..400$

$de_i := 0$ $d\eta_i := 0$

$e_i := e0 + de_i$ $d\varepsilon q_i := 0$

$q_i := 0$ $d\varepsilon p_i := 0$

$\eta f := M$ $\Lambda := \frac{\lambda - \kappa}{\lambda}$

Definitions

$p_i = p_i + dp_i$ $q_i = q_i + dq_i$

$\eta_i = \frac{q_i}{p_i}$ $d\eta_i = \frac{dq_i - \eta_i \cdot dp_i}{p_i}$ $GS_i = 1.5 \cdot \frac{p_i \cdot (1 + e0) \cdot (1 - 2 \cdot \nu)}{\kappa \cdot (1 + \nu)}$ shear modulus (if variable)

$a = \frac{2 \cdot (\lambda - \kappa)}{\lambda \cdot \left(M^2 + \eta^2\right) - 2(\lambda - \kappa) \cdot \eta^2}$ pore pressure parameter

$\beta_i = \frac{\left[M^2 + (\eta_i)^2\right]}{(\lambda - \kappa)}$ common factor

Elastic Strains

$$\begin{pmatrix} d\varepsilon pe_i \\ d\varepsilon qe_i \end{pmatrix} = \begin{bmatrix} \frac{\kappa}{(1 + e_i) p_i} & 0 \\ 0 & \frac{1}{3GSC} \end{bmatrix} \cdot \begin{pmatrix} dp_i \\ dq_i \end{pmatrix}$$

Total Strains

$$\begin{pmatrix} d\varepsilon p_i \\ d\varepsilon q_i \end{pmatrix} = \frac{1}{(1 + e_i) \cdot \beta_i \cdot p_i} \cdot \begin{bmatrix} \left[M^2 - (\eta_i)^2\right] + \kappa \cdot \beta_i & 2 \cdot \eta_i \\ 2 \cdot \eta_i & \left[\frac{4 \cdot (\eta_i)^2}{M^2 - (\eta_i)^2}\right] + \frac{\left[(1 + e_i) \cdot \beta_i \cdot p_i\right]}{3 \cdot GSC} \end{bmatrix} \cdot \begin{pmatrix} dp_i \\ dq_i \end{pmatrix}$$

Initial Conditions and Incrementation for Isotropic Loading

$i := 69..m \qquad p_i := 0 \qquad p0 := 69 \qquad pc := 100 \qquad \Delta q := 3.00 \qquad \Delta p := 1$

$dp_i := if(i \le n, \Delta p, \Delta p)$

$dq_i := if(i > n, \Delta q, 0.0)$

Update

$p_{i-1} := p0$

$p_i := if\left[n \ge i > i0, p_0 + (i)\,dp_i, p0\right] \qquad q_i := if\left[n \ge i \ge i0, 0, (i-n)\cdot dq_i\right]$

$\varepsilon p_i := \varepsilon p_i + d\varepsilon p_i \qquad \varepsilon q_i := \varepsilon q_i + d\varepsilon q_i$

$\eta_i := \frac{q_i}{p_i}$

$de_i := if\left(pc \ge i \ge i0, -\lambda\cdot\frac{dp_i}{p_i}, de_{i-1}\right)$

$e_i := if\left(i > i0, e_{i-1} + de_i, e0\right)$

$\beta_i := \frac{\left[M^2 + (\eta_i)^2\right]}{(\lambda - \kappa)}$ common factor

Elastic Strains

$d\varepsilon pe_i := if\left[\left(p_i \le p0\right), \frac{\kappa}{(1+e_i)p_i}\cdot dp_i, 0\right] \qquad d\varepsilon qe_i := if\left[\left(p_i \le p0\right), \frac{1}{3GSC}\cdot dq_i, 0\right]$

Total Strains

$$\begin{pmatrix} d\varepsilon p_i \\ d\varepsilon q_i \end{pmatrix} := \frac{1}{(1+e_i)\cdot\beta_i\cdot p_i}\cdot\begin{bmatrix} \left[M^2 - (\eta_i)^2\right] + \kappa\cdot\beta_i & 2\cdot\eta_i \\ 2\cdot\eta_i & \left[\frac{4\cdot(\eta_i)^2}{M^2 - (\eta_i)^2}\right] + \frac{\left[(1+e_i)\cdot\beta_i\cdot p_i\right]}{3\cdot GSC} \end{bmatrix}\cdot\begin{pmatrix} dp_i \\ dq_i \end{pmatrix}$$

Imposing zero total volumeteric strain during deviatoric loading

$pnew := 100 \qquad j := 1..m$

$f(pnew, j) := 0 \quad \text{on error root}\left[(2\cdot\Lambda - 1)\cdot\ln(pnew) - \Lambda\cdot\ln\left[M^2\cdot(pnew)^2 + [(j)\cdot 0.5]^2\right] + \Lambda\cdot\ln\left(M^2\right) + \ln(pc), pnew\right]$

$F_j := \text{if}(\text{Im}(f(pnew, j)) \neq 0, 0, f(pnew, j))$ Excluding imaginary solutions

$\eta_j := \text{if}\left[F_j \neq 0 \wedge \left(\frac{j\cdot 0.5}{F_j}\right) < M, \frac{j\cdot 0.5}{F_j}, M\right]$ Limiting η

$\max(\eta) = 1.24$

trapping critical mean effective stress

$MM := M$

$dd(\eta, MM) := \begin{| } j \leftarrow 1 \\ \text{while } \eta_j < MM \\ \quad j \leftarrow j + 1 \\ j - 1 \end{| }$

$trap := dd(\eta, MM)$

$trap = 139$

$\eta_{trap} = 1.205$

$pp := (trap + 1)\cdot\frac{0.5}{M}$

$qq := (trap + 1)\cdot 0.5$

Adjusting Stress Path (Isotropic, Deviatoric to critical) and Discontinue loading at η=M

$p(j) := \begin{| } p_j \text{ if } j \leq pc \\ F_{j-pc+1} \text{ if } pc < j \leq trap + pc \\ pp \text{ if } trap + pc < j \end{| }$

$q(i) := \begin{| } 0 \text{ if } i0 \leq i \leq pc \\ (i - pc)\cdot 0.5 \text{ if } pc < i \leq trap + pc \\ qq \text{ if } trap + pc < i \end{| }$

$p_j := p(j)$

$q_i := q(i)$

$\eta_i := \text{if}\left[p_i \neq 0 \wedge \left(\frac{q_i}{p_i}\right) < M, \frac{q_i}{p_i}, M\right]$ Update η for new index $\qquad a := \max(\eta) \qquad a = 1.24$

$d\eta_i := \eta_i - \eta_{i-1}$

$\beta_i := \frac{\left[M^2 + (\eta_i)^2\right]}{(\lambda - \kappa)}$

$dp_j := \begin{| } \left(p_j - p_{j-1}\right) \text{ if } j \leq pc + trap \\ 0 \text{ otherwise} \end{| }$

$dq_j := \begin{| } \left(q_j - q_{j-1}\right) \text{ if } j \leq pc + trap \\ 0 \text{ otherwise} \end{| }$

Calculation of Strains

a) Elastic strains

$$depe_i := if\left[pc < i \le trap + pc, \frac{\kappa}{(1 + e_i)\cdot p_i}\cdot dp_i, 0\right]$$

$$deqe_i := if\left(pc < i \le trap + pc, \frac{1}{3GSC}\cdot dq_i, 0\right)$$

$$epe_i := if\left(pc < i \le trap + pc, \sum_{i = pc+1}^{i} depe_i, 0\right)$$

$$eqe_i := if\left(pc < i \le trap + pc, eqe_{i-1} + deqe_i, eqe_{i-1}\right)$$

b) Plastic strains

$$\begin{pmatrix} depp_i \\ deqp_i \end{pmatrix} = \frac{1}{(1 + e_i)\cdot\beta_i\cdot p_i}\cdot\begin{bmatrix} \left[M^2 - (\eta_i)^2\right] & 2\cdot\eta_i \\ 2\cdot\eta_i & \left[\frac{4\cdot(\eta_i)^2}{M^2 - (\eta_i)^2}\right] \end{bmatrix}\cdot\begin{pmatrix} dp_i \\ dq_i \end{pmatrix}$$

1- Volumetric

$$depp_i := \begin{cases} 0 \text{ if } i < i0 & \\ \left[\frac{(\lambda - \kappa)\cdot dp_i}{(1 + e_i)\cdot p_i}\right] \text{ if } i0 < i \le pc & \text{isotropic} \\ \left[\frac{1}{(1 + e_i)\cdot\beta_i\cdot p_i}\right]\left[\left[M^2 - (\eta_i)^2\right]\cdot dp_i + 2\cdot\eta_i\cdot dq_i\right] \text{ if } pc < i \le pc + trap & \text{loading to critical state} \\ 0 \text{ otherwise} & \text{flow} \end{cases}$$

$$epp_i := \begin{cases} 0 \text{ if } i \le i0 & \\ epp_{i-1} + depp_i \text{ if } i0 < i \le pc + trap & \text{loading to critical state} \\ epp_{pc+trap} \text{ otherwise} & \text{flow} \end{cases}$$

Check at the end of deviatoric undrained loading: elastic strain must = plastic strain

$$epp_{pc+trap} - epp_{pc} = 1.07 \times 10^{-3}$$

$$epe_{pc+trap} = -1.073 \times 10^{-3}$$

2- Shear

$$d\varepsilon qp_i := \begin{cases} 0 & \text{if } i < i0 \\ \left[\left[\frac{1}{\left(1+e_i\right)\cdot\beta_i\cdot p_i}\right]\left[2\cdot\eta_i\cdot dp_i + \left[\frac{4\cdot\left(\eta_i\right)^2}{M^2-\left(\eta_i\right)^2}\right]\cdot dq_i\right]\right] & \text{if } i0 \le i \le pc + trap \wedge \eta_i < 1.24 \quad \text{loading to critical state} \\ 0 & \text{otherwise} \end{cases}$$

$$\varepsilon qp_i := \begin{cases} 0 & \text{if } i < i0 \\ \varepsilon qp_{i-1} + d\varepsilon qp_i & \text{if } i0 \le i \le pc + trap \quad \text{loading to critical state} \\ \varepsilon qp_{i-1} + 0.0000001\cdot i & \text{otherwise} \quad \text{flow} \end{cases}$$

c) Total strains

$totalds_i := d\varepsilon pp_i + d\varepsilon pe_i$ total volumetric strain incerement (must be zero)

1- Volumetric

$$\varepsilon p_i := \begin{cases} 0 & \text{if } i \le i0 \\ \varepsilon pp_i & \text{if } i0 < i \le pc \quad \text{isotropic} \\ \varepsilon pe_i + \varepsilon pp_i & \text{if } pc < i \le trap + pc \quad \text{loading to critical state} \\ \varepsilon p_{trap+pc} & \text{otherwise} \quad \text{constant plastic strain during flow} \end{cases}$$

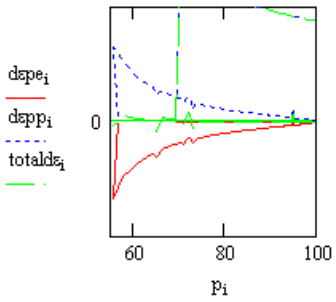

2- Shear

$$\varepsilon q_i := \begin{cases} 0 & \text{if } i \le i0 \\ 0 & \text{if } i0 < i \le pc \quad \text{isotropic} \\ \varepsilon qe_i + \varepsilon qp_i & \text{if } pc < i \le trap + pc \quad \text{loading to critical state} \\ \varepsilon q_{i-1} + i\cdot 0.00000001 & \text{otherwise} \quad \text{flow} \end{cases}$$

d) Axial and Radial Strains

$$\varepsilon z_i := \frac{\varepsilon p_i}{3} + \varepsilon q_i \qquad \varepsilon r_i := \frac{\varepsilon p_i}{3} - \frac{\varepsilon q_i}{2}$$

Void Ratio

$$e_i := \begin{cases} e0 & \text{if } i \le i0 \\ e_i & \text{if } i0 < i \le pc \quad \text{isotropic} \\ e_{pc} + \left(1+e_{i-1}\right)\cdot d\varepsilon p_i & \text{if } pc < i \le pc + trap \quad \text{Calculation of void ratio using incremental total volume strain (e must be constant during undrained deviatoric loading)} \\ e_{pc+trap} & \text{otherwise} \quad \text{flow} \end{cases}$$

Isotropic Consolidation Line (ICL) and Critical State Line (CSL)

$q_{CSL_1} := M \cdot [(1) \cdot \Delta p]$

$e0_{icl} := e0 + \lambda \cdot (\ln(p0) - 1)$

$e0_{icl} = 0.385$

$e0_{csl} := e0 - (\lambda - \kappa) \cdot \ln(2)$

$e0_{csl} = 0.332$

$e_{CSL_1} := \left[e0_{icl} - \lambda \cdot (\ln(1) - 1) - (\lambda - \kappa) \cdot \ln(2) \right]$

$e_{ICL_1} := \left[e0_{icl} - \lambda \cdot (\ln(1) - 1) \right]$

Total Stress Path q : p' = 3 : 1

Assume a total stress path using this incremental q-p relationship

$dptotal_i := \frac{dq_i}{3}$ for undrained deviatoric loading: change in total stress = change in pore pressure. i.e. effective stress path is always the same

Total Mean Stress

$$ptotal_i := \begin{cases} p_i & \text{if } i0 \le i \le pc \\ \left[pc + (i - pc) \cdot dptotal_i \right] & \text{if } (pc < i \le pc + trap) \\ ptotal_{pc+trap} & \text{otherwise} \end{cases}$$

isotropic

loading critical state

flow

Check Stress Path (η) and Milestones

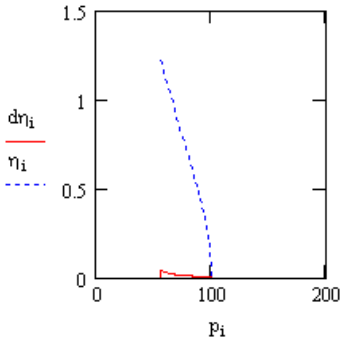

Initial condition: $p_{i0} = 69$ $q_{i0} = 0$

Isotropic loading: $p_n = 100$ $q_n = 0$

Critical state: $p_{pc+trap} = 55.617$ $q_{pc+trap} = 69.5$ $\eta_{pc+trap} = 1.24$ $e_{pc+trap} = 0.335$

Flow: $p_m = 56.452$ $q_m = 70$ $\eta_m = 1.24$ $e_m = 0.335$

Critical State Space

Pueblo Sand NC - CU Test - stress controlled - constant G

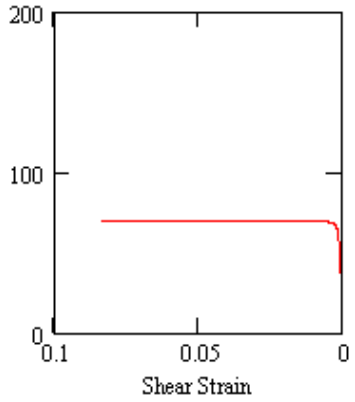

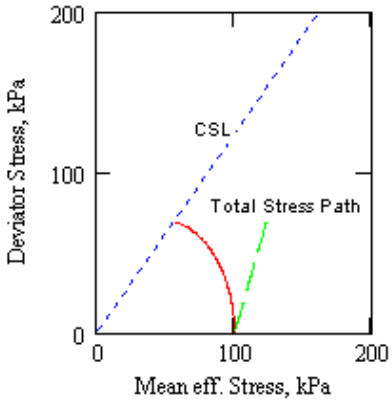

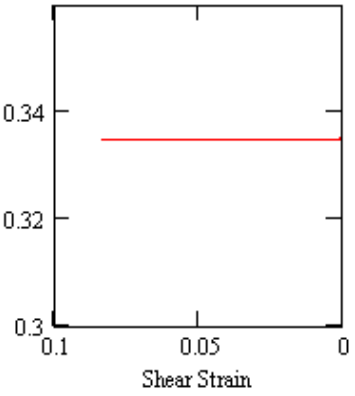

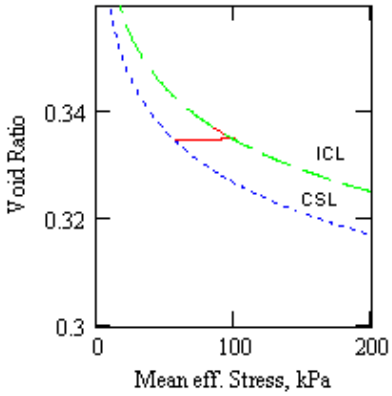

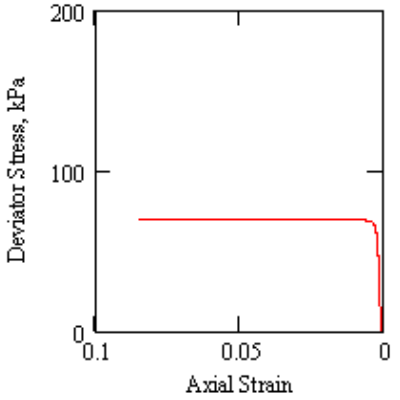

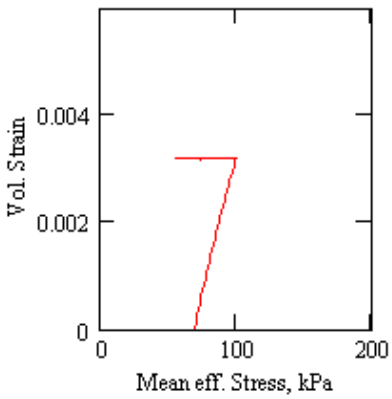

A.3 Isotropically-Over Consolidated Drained

Pueblo Sand

Highly Over Consolidated - Consolidated Drained - Stress Controlled - Constant Shear Modulus

Material Constants

$e0 := 0.34$ $M := 1.24$ $\lambda := 0.014$ $\kappa := 0.0024$ $\nu := 0.28$ $GSC := 20000$

@ $p_0 = 69$ kPa

Initialize

$ipc := 1242$ $g := 1800$ $\Delta p := 1$ $\Delta q := 3$ $n := 100$ $i0 := 69$ $i := i0 .. g$ $1 := 1 .. 1000$

$dp_i := if(i \le n, \Delta p, \Delta p)$ $d\eta_i := 0$

$dq_i := if(i > n, \Delta q, 0.0)$ $d\varepsilon q_i := 0$ $IR := \frac{\Delta q}{\Delta p}$ $\varepsilon pe_i := 0$

$de_i := 0$ $d\varepsilon p_i := 0$ $u := 1$ unloading factor

$e_i := e0 + de_i$ $\eta f := M$

$q_i := 0$ $\eta_i := 0$

Definitions

$p_i := p_i + dp_i$

$q_i := q_i + dq_i$

$\eta_i := \frac{q_i}{p_i}$

$\beta_i = \frac{\left[M^2 + (\eta_i)^2\right]}{(\lambda - \kappa)}$ common factor

$GS_i = 1.5 \cdot \frac{p_i \cdot (1 + e0) \cdot (1 - 2 \cdot \nu)}{\kappa \cdot (1 + \nu)}$ shear modulus (if variable)

Elastic Strains

$$\begin{pmatrix} d\varepsilon pe_i \\ d\varepsilon qe_i \end{pmatrix} = \begin{bmatrix} \frac{\kappa}{(1 + e_i) p_i} & 0 \\ 0 & \frac{1}{3 \cdot GSC} \end{bmatrix} \cdot \begin{pmatrix} dp_i \\ dq_i \end{pmatrix}$$

Total Strains

$$\begin{pmatrix} d\varepsilon p_i \\ d\varepsilon q_i \end{pmatrix} = \frac{1}{(1 + e_i) \cdot \beta_i \cdot p_i} \cdot \begin{bmatrix} \left[M^2 - (\eta_i)^2\right] + \kappa \cdot \beta_i & 2 \cdot \eta_i \\ 2 \cdot \eta_i & \left[\frac{4 \cdot (\eta_i)^2}{M^2 - (\eta_i)^2}\right] + \frac{\left[(1 + e_i) \cdot \beta_i \cdot p_i\right]}{3 \cdot GSC} \end{bmatrix} \cdot \begin{pmatrix} dp_i \\ dq_i \end{pmatrix}$$

Initial Conditions and Incrementation for Isotropic loading and Unloading

$i := 69 .. g \qquad p_i := 0 \qquad p0 := 69 \qquad pc := 690 \qquad ic := 690 \qquad ipc := 1242$

$dp_i := if(ic < i \le ipc, -\Delta p, \Delta p)$

$dq_i := if(i > ipc, 3\, dp_i, 0.0)$

Update

$p_i := if[i0 \le i \le ic, p0 + (i - i0)\cdot\Delta p, if[ic < i \le ipc, p0 + (2ic - i0 - i)\cdot\Delta p, p0 + (i - 2\cdot ipc + 2\cdot ic - i0)\cdot\Delta p]]$

$q_i := if[i \ge ipc, (i - ipc)\cdot dq_i, 0]$

$\varepsilon p_i := \varepsilon p_i + d\varepsilon p_i \qquad \varepsilon q_i := \varepsilon q_i + d\varepsilon q_i$

$GS_i := 1.5\cdot\frac{p_i\cdot(1 + e0)\cdot(1 - 2\cdot\nu)}{\kappa\cdot(1 + \nu)} \qquad \eta_i := \frac{q_i}{p_i}$

$de_i := if\left[(ipc \ge i > ic), -\kappa\cdot\frac{dp_i}{p_i}, if\left[(m \ge i > ipc), -\kappa\cdot\frac{dp_i}{p_i}, -\lambda\cdot\frac{dp_i}{p_i}\right]\right]$

$e_i := if(i > i0, e_{i-1} + de_i, e0)$

Elastic Strains

$d\varepsilon pe_i := if\left[ic < i \le m, \frac{\kappa}{(1 + e_i)p_i}\cdot dp_i, 0\right] \qquad d\varepsilon qe_i := if\left[(p_i \le p0), \frac{1}{3GSC}\cdot dq_i, 0\right]$

$\varepsilon pe_i = if(ic < i \le m, \varepsilon pe_{i-1} + d\varepsilon pe_i, d\varepsilon pe_i)$

$\beta_i := \frac{\left[M^2 + (\eta_i)^2\right]}{(\lambda - \kappa)}$ common factor

Plastic Strains

$$\begin{pmatrix} d\varepsilon pp_i \\ d\varepsilon qp_i \end{pmatrix} := \frac{1}{(1 + e_i)\cdot\beta_i\cdot p_i}\cdot\begin{bmatrix} \left[M^2 - (\eta_i)^2\right] & 2\cdot\eta_i \\ 2\cdot\eta_i & \left[\frac{4\cdot(\eta_i)^2}{M^2 - (\eta_i)^2}\right] \end{bmatrix}\cdot\begin{pmatrix} dp_i \\ dq_i \end{pmatrix}$$

Total Strains

$$\begin{pmatrix} d\varepsilon p_i \\ d\varepsilon q_i \end{pmatrix} := \frac{1}{(1+e_i)\cdot\beta_i\cdot p_i}\cdot\begin{bmatrix} \left[M^2-(\eta_i)^2\right]+\kappa\cdot\beta_i & 2\cdot\eta_i \\ 2\cdot\eta_i & \left[\frac{4\cdot(\eta_i)^2}{M^2-(\eta_i)^2}\right]+\frac{\left[(1+e_i)\cdot\beta_i\cdot p_i\right]}{3\cdot GSC} \end{bmatrix}\cdot\begin{pmatrix} dp_i \\ dq_i \end{pmatrix}$$

$$d\varepsilon p_i := \frac{\left[M^2-(\eta_i)^2+\kappa\cdot\beta_i\right]}{\left[(1+e_i)\cdot\beta_i\cdot p_i\right]}\cdot dp_i + \frac{2\cdot\eta_i}{(1+e_i)\cdot\beta_i\cdot p_i}\cdot dq_i$$

$$d\varepsilon q_i := \frac{2\cdot\eta_i}{\left[(1+e_i)\cdot\beta_i\cdot p_i\right]}\cdot dp_i + \left[\frac{\frac{4\cdot(\eta_i)^2}{M^2-(\eta_i)^2}}{(1+e_i)\cdot\beta_i\cdot p_i}+\frac{1}{3\cdot GSC}\right]\cdot dq_i$$

$$\varepsilon p_i := if\left(ic < i \le ipc, \varepsilon p_{i-1} + d\varepsilon p_i, d\varepsilon p_i\right)$$

$$\varepsilon q_i := if\left(i \ge i0, \varepsilon q_{i-1} + d\varepsilon q_i, \varepsilon q_{i-1} + d\varepsilon q_i\right)$$

finding the intesection of the re-loading stress path with the yield locus

$pc = 690$ $p_{ipc} = 138$ $IR = 3$ Guess root: $pr := 250$ stress path: $q = 3p$

$$a := root\left[\left(IR^2+M^2\right)\cdot pr^2-\left(2\cdot IR^2\cdot p_{ipc}+M^2\cdot pc\right)\cdot pr+IR^2\left(p_{ipc}\right)^2, pr\right]$$ substituting stress path into yield locus

$a = 277.875$

$pr := a$

$$qr := \sqrt{M^2\cdot pr\cdot(pc-pr)}$$

$pr = 277.875$ $qr = 419.625$ corresponding q

$pr := ceil(pr)$

$ir := pr - p_{ipc} + ipc$

$ir = 1.382\times10^3$

Determination of Critical State:

m and coressponding p and q

Guess root $m := 1500$

$$m := \text{root}\left[q_{ir} - u\cdot\Delta q\cdot(m - ir) - M\cdot\left[p_{ir} - u\cdot\Delta p\cdot(m - ir)\right], m\right]$$

$$m := \text{ceil}(m)$$

$$m = 1.425 \times 10^{3}$$

Check at critical state: p and q

$$p_m := p_{ir} - (m - ir)\cdot\Delta p \qquad p_m = 235$$

$$q_m := q_{ir} - (m - ir)\cdot\Delta q \qquad q_m = 291$$

Adjustment of p and q incrementation:

$$dp_i := \begin{cases} \Delta p & \text{if } i0 \le i \le ic \\ -\Delta p & \text{if } ic < i \le ipc \\ \Delta p & \text{if } ipc < i \le ir \\ -\Delta p & \text{if } ir < i \le m \\ 0 & \text{otherwise} \end{cases}$$

isotropic loading

unloading

reloading inside yield locus (failure)

critical state

flow

$$p_i := \begin{cases} p0 & \text{if } i \le i0 \\ \left(p_{i-1} + dp_i\right) & \text{if } i0 < i \le m \\ p_m & \text{otherwise} \end{cases}$$

critical state & flow

$$dq_i := \text{if}\left(i > ipc, 3\,dp_i, 0\right)$$

$$q_i := \begin{cases} 0 & \text{if } i0 \le i \le ipc \\ \left(q_{i-1} + dq_i\right) & \text{if } ipc < i \le m \\ q_m & \text{otherwise} \end{cases}$$

critical state & flow

$$\eta_i := \frac{q_i}{p_i} \qquad \beta_i := \frac{\left[M^2 + (\eta_i)^2\right]}{(\lambda - \kappa)}$$

Calculation of Strains

a) Elastic strains

$$d\varepsilon pe_i := if\left[ic < i \le ir, \frac{\kappa}{(1 + e0)p_i} \cdot dp_i, 0 \right]$$

$$d\varepsilon qe_i := if\left(ic < i \le ir, \frac{1}{3GSC} \cdot dq_i, 0 \right)$$

$$\varepsilon pe_i := if\left(ic < i \le ir, \sum_{i=ic}^{i} d\varepsilon pe_i, 0 \right)$$

$$\varepsilon qe_i := if\left(ipc < i \le ir, \varepsilon qe_{i-1} + d\varepsilon qe_i, \varepsilon qe_i\right)$$

b) Plastic strains

$$\begin{pmatrix} d\varepsilon pp_i \\ d\varepsilon qp_i \end{pmatrix} := \frac{1}{\left(1 + e_i\right) \cdot \beta_i \cdot p_i} \cdot \begin{bmatrix} \left[M^2 - (\eta_i)^2\right] & 2 \cdot \eta_i \\ 2 \cdot \eta_i & \left[\frac{4 \cdot (\eta_i)^2}{M^2 - (\eta_i)^2}\right] \end{bmatrix} \cdot \begin{pmatrix} dp_i \\ dq_i \end{pmatrix}$$

1- Volumetric

$$\varepsilon pp_i := \varepsilon pp_{i-1} + d\varepsilon pp_i$$

2- Shear

$$\varepsilon qp_i := \begin{cases} 0 & \text{if } i0 \le i \le ir \\ \varepsilon qp_{i-1} + d\varepsilon qp_i & \text{if } ir < i \le m \\ 0 & \text{otherwise} \end{cases}$$

reloading to failure

critical state

c) Total strains

1- Volumetric

$$\varepsilon p_i := \text{if}\left(ic \geq i \geq i0, \varepsilon pp_i, \text{if}\left(ic < i \leq ipc, \varepsilon pp_{ic} + \varepsilon pe_i, \text{if}\left(ipc < i \leq ir, \varepsilon p_{i-1} + d\varepsilon pe_i, \varepsilon p_{ir}\right)\right)\right)$$

2- Shear

$$\varepsilon q_i := \begin{cases} 0 \text{ if } i0 \leq i \leq ipc & \text{isotropic} \\ \left(\varepsilon qe_{i-1} + d\varepsilon qe_i\right) \text{ if } ipc < i \leq ir & \text{unloading} \\ \left(\varepsilon qe_{ir} + \varepsilon qp_i\right) \text{ if } ir < i < m & \text{reloading to failure} \\ \varepsilon q_m + i \cdot 0.00002 \text{ otherwise} & \text{critical state \& flow} \end{cases}$$

d) Axial and Radial Strains

$$\varepsilon z_i := \frac{\varepsilon p_i}{3} + \varepsilon q_i$$

$$\varepsilon r_i := \frac{\varepsilon p_i}{3} - \frac{\varepsilon q_i}{2}$$

Void Ratio

$\upsilon_{i-1} := 1 + e_{i-1}$ specific volume at previous incerement

$$e_i := \begin{cases} \left[e0 + \left(\sum_{i=i0}^{i} -\lambda \cdot \frac{dp_i}{p_i}\right)\right] \text{ if } i0 \leq i \leq ic & \text{isotropic} \\ \left(e_{ic} - \upsilon_{i-1} \cdot \varepsilon pe_i\right) \text{ if } ic < i \leq ipc & \text{unloading} \\ \left(e_{i-1} - \upsilon_{i-1} \cdot d\varepsilon pe_i\right) \text{ if } ipc < i \leq ir & \text{reloading to failure} \\ \left(e_{ir} - \sum_{i=ir+1}^{i} \upsilon_{i-1} \cdot d\varepsilon pp_i\right) \text{ if } ir < i \leq m & \text{critical state} \\ e_m \text{ otherwise} & \text{flow} \end{cases}$$

Check Stress Path (η) and Milestones

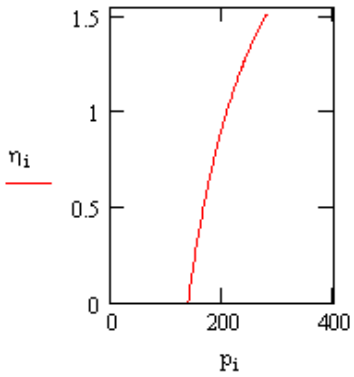

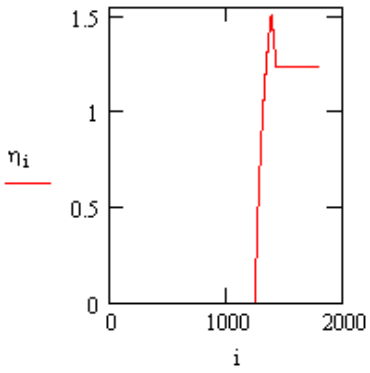

Initial condition:	$p_{i0} = 69$	$q_{i0} = 0$	
Isotropic loading:	$p_{ic} = 690$	$q_{ic} = 0$	
Unloading:	$p_{ipc} = 138$	$q_{ipc} = 0$	
Reloading inside yield locus (failure):	$p_{ir} = 278$	$q_{ir} = 420$	$\eta_{ir} = 1.511$
Critical state:	$p_m = 235$	$q_m = 291$	$\eta_m = 1.238$
	$e_m = 0.315$		
Flow:	$p_g = 235$	$q_g = 291$	$\eta_g = 1.238$
	$e_g = 0.315$		

Isotropic Consolidation and Critical State Lines

$q_{CSL_1} := M \cdot [(1) \cdot \Delta p]$

$e0_{icl} := e0 + \lambda \cdot (\ln(p0) - 1)$

$e0_{icl} = 0.385$

$e0_{csl} := e0 - (\lambda - \kappa) \cdot \ln(2)$

$e0_{csl} = 0.332$

$e_{CSL_1} := \left[e0_{icl} - \lambda \cdot (\ln(1) - 1) - (\lambda - \kappa) \cdot \ln(2) \right]$

$e_{ICL_1} := \left[e0_{icl} - \lambda \cdot (\ln(1) - 1) \right]$

$\eta f := \max(\eta)$

$\eta f = 1.511$ stress ratio at failure (maximum)

Critical State Space

Pueblo Sand OC - CD Test - stress controlled - constant G

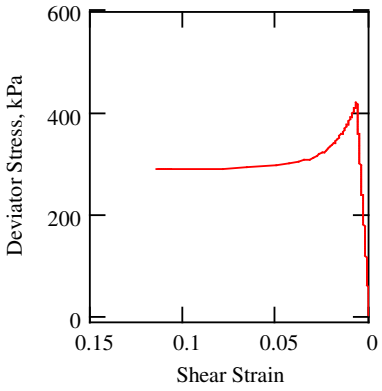

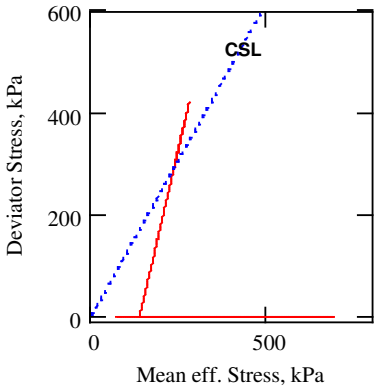

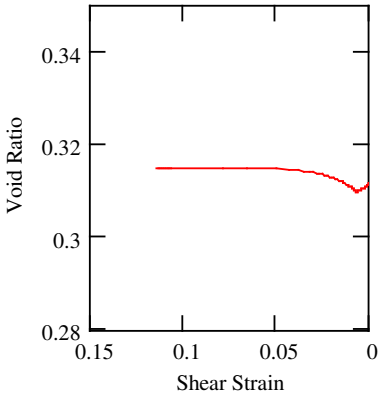

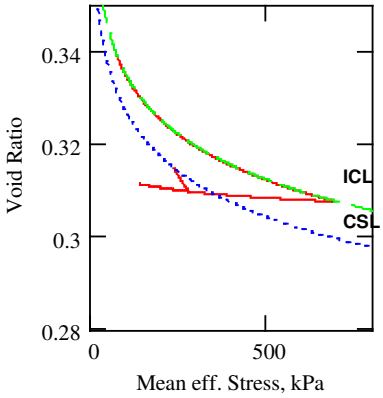

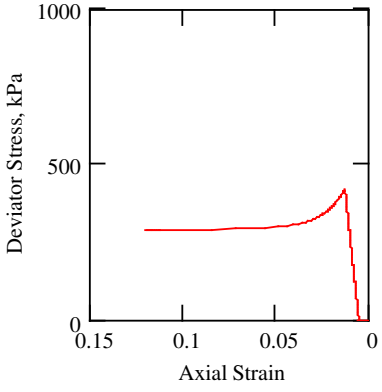

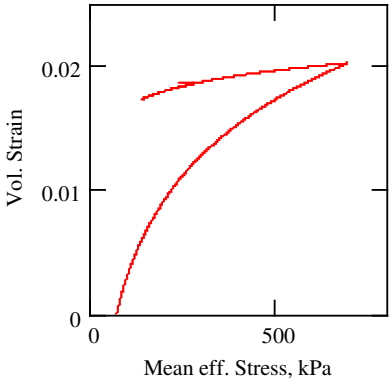

A.4 Isotropically-Over Consolidated Undrained

Pueblo Sand

Highly Over Consolidated - Consolidated Undrained - Stress Controlled - Constant Shear Modulus

Material Constants

$e0 := 0.34$ $M := 1.24$ $\lambda := 0.014$ $\kappa := 0.0024$ $\nu := 0.28$ $GSC := 20000$

@ p_0 = 69 kPa

Initialize

$ipc := 1242$ $m := 2000$ $i0 := 69$ $i := i0..m$ $l := 1..1000$

$de_i := 0$ $d\eta_i := 0$ $p0 := 69$ $pc := 690$ $p_{ipc} := 138$

$e_i := e0 + de_i$ $d\varepsilon q_i := 0$

$q_i := 0$ $d\varepsilon p_i := 0$ $\Delta p := 1$

$\eta_i := 0$ $\varepsilon pe_i := 0$ $\Delta q := 3$

p and q increments for isotropic loading and reloading within initial yield locus

Definitions

$p_i = p_i + dp_i$

$q_i = q_i + dq_i$

$GS_i = 1.5 \cdot \frac{p_i \cdot (1 + e0) \cdot (1 - 2 \cdot \nu)}{\kappa \cdot (1 + \nu)}$ shear modulus (if variable)

$\eta_i = \frac{q_i}{p_i}$ $d\eta_i = \frac{dq_i - \eta_i \cdot dp_i}{p_i}$ $\beta_i = \frac{\left[M^2 + (\eta_i)^2\right]}{(\lambda - \kappa)}$ common factor

Elastic Strains

$$\begin{pmatrix} d\varepsilon pe_i \\ d\varepsilon qe_i \end{pmatrix} = \begin{bmatrix} \frac{\kappa}{(1 + e_i) p_i} & 0 \\ 0 & \frac{1}{3 \cdot GSC} \end{bmatrix} \cdot \begin{pmatrix} dp_i \\ dq_i \end{pmatrix}$$

Total Strains

$$\begin{pmatrix} d\varepsilon p_i \\ d\varepsilon q_i \end{pmatrix} = \frac{1}{(1 + e_i) \cdot \beta_i \cdot p_i} \cdot \begin{bmatrix} \left[M^2 - (\eta_i)^2\right] + \kappa \cdot \beta_i & 2 \cdot \eta_i \\ 2 \cdot \eta_i & \left[\frac{4 \cdot (\eta_i)^2}{M^2 - (\eta_i)^2}\right] + \frac{\left[(1 + e_i) \cdot \beta_i \cdot p_i\right]}{3 \cdot GSC} \end{bmatrix} \cdot \begin{pmatrix} dp_i \\ dq_i \end{pmatrix}$$

Finding the intesection of the re-loading stress path with the yield locus

$pc = 690$ $p_{ipc} = 138$ stress path: p = p_{ipc}

Guess root: $qr := 300$

$qr := root\left[qr^2 - M^2 \cdot \left[p_{ipc} \cdot \left(pc - p_{ipc}\right)\right], qr\right]$ substituting stress path into yield locus

$qr := floor(qr)$ $qr = 342$ at $p_{ipc} = 138$

$irq := ipc + \frac{qr}{\Delta q}$ $irq = 1.356 \times 10^3$

$p_{irq} := p_{ipc}$ $p_{irq} = 138$ $p_{pc} = 0$ $p_{ipc} = 138$

$\eta_{irq} := \frac{qr}{p_{irq}}$ $\eta_{irq} = 2.478$ this is the maximum stress ratio

Isotropic Consolidation and Critical State Lines

$q_{CSL_1} := M \cdot [(1) \cdot \Delta p]$

$e0_{icl} := e0 + \lambda \cdot (\ln(p0) - 1)$

$e0_{icl} = 0.385$

$e0_{csl} := e0 - (\lambda - \kappa) \cdot \ln(2)$

$e0_{csl} = 0.332$

$e_{CSL_1} := \left[e0_{icl} - \lambda \cdot (\ln(1) - 1) - (\lambda - \kappa) \cdot \ln(2)\right]$

$e_{ICL_1} := \left[e0_{icl} - \lambda \cdot (\ln(1) - 1)\right]$

Determination of Critical State:
ics and coressponding p and q

$e_{pc} := e0 - \lambda \cdot (\ln(pc) - \ln(p0))$

$e_{csl} := e_{pc} + \kappa \cdot \left(\ln(pc) - \ln\left(p_{ipc}\right)\right)$ $e_{csl} = 0.312$

using CSL equation only

$\lambda\left(\ln\left(p_{csl}\right) - \ln(p0)\right) = e0_{csl} - ef_{csl}$

Guess root $p_{csl} := 200$

$p_{csl} := \text{root}\left[\lambda \cdot \left(\ln\left(p_{csl}\right) - \ln(p0)\right) - \left(e0_{csl} - e_{csl}\right), p_{csl}\right]$

$\max\left(p_{csl}\right) = 294.849$ $p_{csl} := \text{ceil}\left(p_{csl}\right)$ $p_{csl} = 295$

corresponding q: $q_{csl} := \text{ceil}\left(M \cdot p_{csl}\right)$ $q_{csl} = 366$

$ics := 1500$

$ics := \text{root}\left[p_{csl} - p_{irq} - (ics - irq) \cdot \Delta p, ics\right]$

$ics := \text{floor}(ics)$ $ics = 1.513 \times 10^{3}$ $e_{csl} = 0.312$

@ Critical State : Determine coressponding q increment (Δq) : f(Δp)

Guess root $f := 0.1$

$f := \text{root}\left[M \cdot p_{irq} + M \cdot \Delta p \cdot (ics - irq) - qr - f \cdot \Delta p \cdot (ics - irq), f\right]$ yield surface equation at critical state (flow: η=M)

$f = 0.152$ dq = fraction of dp

Check at critical state: p and q

$p_{ics} := p_{irq} + (ics - irq) \cdot \Delta p$ $p_{ics} = 295$

$q_{ics} := qr - (ics - irq) \cdot f \cdot \Delta p$ $q_{ics} = 318.2$

Initial Conditions and Incrementation

$i := 69.. m$ $p0 := 69$ $pc := 690$ $ic := 690$ $ipc := 1242$

Redifine p, q after reaching the origial yield locus during re-loading

$$dp_i := \begin{cases} \Delta p & \text{if } i0 < i \le ic \quad \text{isotropic} \\ -\Delta p & \text{if } ic < i \le ipc \quad \text{unloading} \\ 0 & \text{if } ipc < i \le irq \vee i \le i0 \quad \text{reloading to failure} \\ \Delta p & \text{if } irq < i \le ics \quad \text{loading to critical state} \\ 0 & \text{otherwise} \quad \text{flow} \end{cases} \qquad dq_i := \begin{cases} 0 & \text{if } i \le i0 \\ 0 & \text{if } i0 < i \le ipc \\ 3\cdot\Delta p & \text{if } ipc < i \le irq \quad \text{reloading to failure} \\ f\cdot\Delta p & \text{if } irq < i \le ics \quad \text{loading to critical state} \\ 0 & \text{otherwise} \quad \text{flow} \end{cases}$$

update p and q

$p_{i-1} := 69$

$p_i := p_{i-1} + dp_i$ $q_i := q_{i-1} + dq_i$

$\eta_i := \frac{q_i}{p_i}$

$\eta_{ics} = 1.24$ $\eta_{irq} = 2.478$ $\max(\eta) = 2.478$

Update

$\varepsilon p_i := \varepsilon p_i + d\varepsilon p_i$ $\varepsilon q_i := \varepsilon q_i + d\varepsilon q_i$

$\eta_i := \frac{q_i}{p_i}$

$de_i := if\left[(ipc \ge i > ic), -\kappa\cdot\frac{dp_i}{p_i}, if\left[(irq \ge i > ipc), -\kappa\cdot\frac{dp_i}{p_i}, 0\right]\right]$

$e_i := if(i > i0, e_{i-1} + de_i, e0)$

Elastic Strains

$d\varepsilon pe_i := if\left[ic < i \le m, \frac{\kappa}{(1 + e_i)p_i}\cdot dp_i, 0\right]$ $d\varepsilon qe_i := if\left(ipc < i \le irq, \frac{1}{3GSC}\cdot dq_i, 0\right)$

$\varepsilon pe_i = if(ic < i \le m, \varepsilon pe_{i-1} + d\varepsilon pe_i, d\varepsilon pe_i)$

Plastic Strains

$$\beta_i := \frac{\left[M^2 + (\eta_i)^2\right]}{(\lambda - \kappa)} \qquad \text{common factor}$$

$$\begin{pmatrix} d\varepsilon pp_i \\ d\varepsilon qp_i \end{pmatrix} := \frac{1}{(1 + e_i)\cdot\beta_i\cdot p_i}\cdot\begin{bmatrix} \left[M^2 - (\eta_i)^2\right] & 2\cdot\eta_i \\ 2\cdot\eta_i & \left[\frac{4\cdot(\eta_i)^2}{M^2 - (\eta_i)^2}\right] \end{bmatrix}\cdot\begin{pmatrix} dp_i \\ dq_i \end{pmatrix}$$

Total Strains

$$\begin{pmatrix} d\varepsilon p_i \\ d\varepsilon q_i \end{pmatrix} := \frac{1}{(1 + e_i)\cdot\beta_i\cdot p_i}\cdot\begin{bmatrix} \left[M^2 - (\eta_i)^2\right] + \kappa\cdot\beta_i & 2\cdot\eta_i \\ 2\cdot\eta_i & \left[\frac{4\cdot(\eta_i)^2}{M^2 - (\eta_i)^2}\right] + \frac{\left[(1 + e_i)\cdot\beta_i\cdot p_i\right]}{3\cdot GSC} \end{bmatrix}\cdot\begin{pmatrix} dp_i \\ dq_i \end{pmatrix}$$

$$d\varepsilon p_i := \frac{\left[M^2 - (\eta_i)^2 + \kappa\cdot\beta_i\right]}{\left[(1 + e_i)\cdot\beta_i\cdot p_i\right]}\cdot dp_i + \frac{2\cdot\eta_i}{(1 + e_i)\cdot\beta_i\cdot p_i}\cdot dq_i$$

$$d\varepsilon q_i := \frac{2\cdot\eta_i}{\left[(1 + e_i)\cdot\beta_i\cdot p_i\right]}\cdot dp_i + \left[\frac{\frac{4\cdot(\eta_i)^2}{M^2 - (\eta_i)^2}}{(1 + e_i)\cdot\beta_i\cdot p_i} + \frac{1}{3\cdot GSC}\right]\cdot dq_i$$

$$\varepsilon p_i := \text{if}\left(ic < i \le ipc, \varepsilon p_{i-1} + d\varepsilon p_i, d\varepsilon p_i\right)$$

$$\varepsilon q_i := \text{if}\left(i \ge i0, \varepsilon q_{i-1} + d\varepsilon q_i, \varepsilon q_{i-1} + d\varepsilon q_i\right)$$

$$\beta_i := \frac{\left[M^2 + (\eta_i)^2\right]}{(\lambda - \kappa)}$$

plastic strains

$$\begin{pmatrix} d\varepsilon pp_i \\ d\varepsilon qp_i \end{pmatrix} := \frac{1}{\left(1 + e_i\right)\cdot\beta_i\cdot p_i}\cdot\begin{bmatrix} \left[M^2 - \left(\eta_i\right)^2\right] & 2\cdot\eta_i \\ 2\cdot\eta_i & \left[\frac{4\cdot\left(\eta_i\right)^2}{M^2 - \left(\eta_i\right)^2}\right] \end{bmatrix}\cdot\begin{pmatrix} dp_i \\ dq_i \end{pmatrix}$$

$$d\varepsilon qp_i := \begin{cases} 0 \text{ if } i0 \le i \le irq \\ \left[\frac{1}{\left(1 + e_i\right)\cdot\beta_i\cdot p_i}\right]\cdot\left[2\cdot\eta_i\cdot dp_i + \left[\frac{4\cdot\left(\eta_i\right)^2}{M^2 - \left(\eta_i\right)^2}\right]\cdot dq_i\right] \text{ if } irq < i < ics \wedge \eta_i > M + 0.1 \\ 0 \text{ otherwise} \end{cases}$$

to avoid singularity and appreaciably large strain increments near critical state

$$\varepsilon pp_i := \varepsilon pp_{i-1} + d\varepsilon pp_i$$

$$\varepsilon qp_i := \varepsilon qp_{i-1} + d\varepsilon qp_i$$

elastic strains

$$d\varepsilon pe_i := \text{if}\left[ic < i \le ics, \frac{\kappa}{(1 + e0)p_i}\cdot dp_i, 0\right]$$

$$d\varepsilon qe_i := \text{if}\left(i0 < i \le ics, \frac{1}{3GSC}\cdot dq_i, 0\right)$$

$$\varepsilon pe_i := \text{if}\left(ic < i \le ics, \sum_{i=ic}^{i} d\varepsilon pe_i, 0\right)$$

$$\varepsilon qe_i := \text{if}\left(i0 < i \le ics, \varepsilon qe_{i-1} + d\varepsilon qe_i, 0\right)$$

total strains

$$\varepsilon p_i := \text{if}\left(ic \ge i \ge i0, \varepsilon pp_i, \text{if}\left(ic < i \le ipc, \varepsilon pp_{ic} + \varepsilon pe_i, \text{if}\left(ipc < i \le irq, \varepsilon p_{i-1} + d\varepsilon pe_i, \varepsilon p_{irq}\right)\right)\right)$$

$$\varepsilon q_i := \begin{cases} \varepsilon qp_i \text{ if } i0 \le i \le ic & \text{isotropic} \\ \varepsilon qp_i \text{ if } ic < i \le ipc & \text{unloading} \\ \left(\varepsilon q_{ipc} + \varepsilon qe_i\right) \text{ if } ipc < i \le irq & \text{reloading to failure} \\ \left(\varepsilon q_{irq} + \varepsilon qp_i\right) \text{ if } irq < i < ics & \text{critical state} \\ \left(\varepsilon q_{ics-1} + i\cdot 0.00008\right) \text{ otherwise} & \text{flow} \end{cases}$$

Void Ratio

$\upsilon_{i-1} := 1 + e_{i-1}$ specific volume at previous incerement

$$e_i := \text{if}\left[(ic \geq i \geq i0), e0 + \left(\sum_{i=i0}^{i} -\lambda \cdot \frac{dp_i}{p_i}\right), \text{if}\left[(ipc \geq i > ic), e_{ic} - \upsilon_{i-1} \cdot \varepsilon pe_i, \text{if}\left(ics \geq i > ipc, e_{i-1} - 0, e_{irq} - 0\right)\right]\right]$$

Axial and Radial Strains

$$\varepsilon z_i := \frac{\varepsilon p_i}{3} + \varepsilon q_i \qquad \varepsilon r_i := \frac{\varepsilon p_i}{3} - \frac{\varepsilon q_i}{2}$$

Stress Ratio

$\eta f := \max(\eta)$

$\eta f = 2.478$ stress ratio at failure (maximum)

$\eta_{ics} = 1.24$ stress ratio at critical state

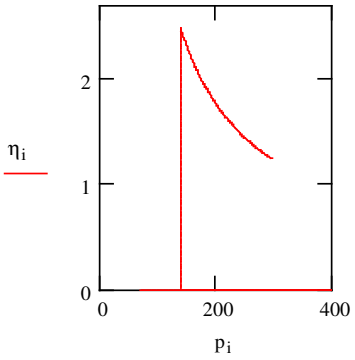

Milestones

Initial condition:	$p_{i0} = 69$	$q_{i0} = 0$		
Isotropic loading:	$p_{ic} = 690$	$q_{ic} = 0$		
Unloading:	$p_{ipc} = 138$	$q_{ipc} = 0$		
Reloading inside yield locus:	$p_{irq} = 138$	$q_{irq} = 342$	$\eta_{irq} = 2.478$	
Critical state:	$p_{ics} = 295$	$q_{ics} = 365.8$	$\eta_{ics} = 1.24$	$e_{ics} = 0.312$
Flow:	$p_m = 295$	$q_m = 365.8$	$\eta_m = 1.24$	$e_m = 0.312$

Critical State Space

Pueblo Sand OC - CU Test - stress controlled (OCR = 5.0) - constant G

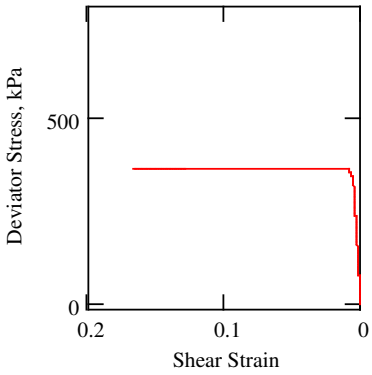

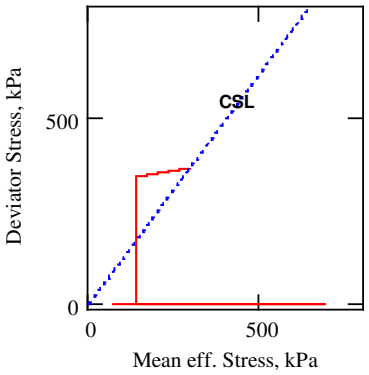

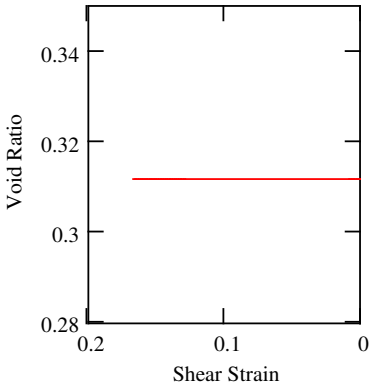

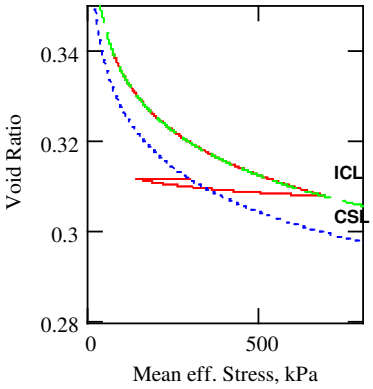

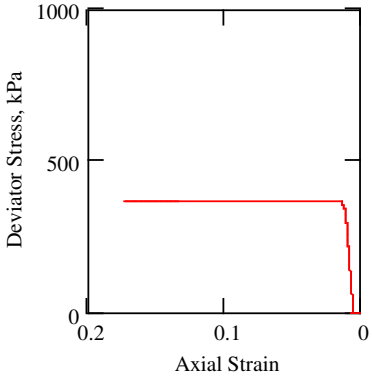

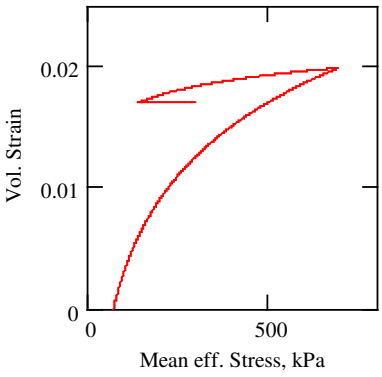

REFERENCES

ABAQUS, Theory Manual, Version 6.5 (2005), Hibbit, Karlson & Sorensen, Inc. Pawtucket, Rhode Island, U.S.A.

Alshibli, K.A., Batiste, S., and Sture, S. (2003), "Strain localization is sand: plane strain versus triaxial compression," Journal of Geotechnical and Geoenvironmental Engineering, ASCE, Vol. 129, No. 6, pp. 483-494.

Atkinson, J. (1993), An Introduction To The Mechanics of Soils And Foundations Through Critical State Soil Mechanics, McGraw-Hill Co.

Baldi, G., Hight, D.W., and Thomas, G.E. (1996), "A Reevaluation of conventional triaxial test methods," Advanced Triaxial Testing of Soil and Rock, ASTM STP No. 977, edited by Donaghe, R.T., Chaney, R.C., and Silver, M., Baltimore, pp. 219-263.

Bates, D.M., and Watts, D.G. (1988), Nonlinear Regression and Its Applications, Wiley, New York: pp. 77-78.

Bishop, A.W., and Green, G.E. (1965), "The influence of end restraint on the compression strength of a cohesionless soil," Geotechnique, Vol. 15, No. 3, pp. 243-266.

Bose, S.K., and Som, N.N. (1998), "Parametric study of a braced cut by finite element method," Computers and Geotechnics, Vol. 22, No. 2, pp. 91-107.

Burland, J.B. (1967), Deformation of soft clay, Dissertation, Cambridge University.

Cho, G.C. (2001), Saturation effects and post-liquefaction shear strength, PhD thesis, School of Civil and Environmental Engineering, Georgia Institute of Technology, Atlanta.

Cho, G.C., Dodds, J., and Santamarina, J. C. (2005), "Particle shape effects on packing density, stiffness and strength - natural and crushed sands," Internal report, Georgia Institute of Technology, p. 34.

Cuccovillo, T., Coop, M.R. (1997), "The measurements of local strains in triaxial tests using LVDTs," Geotechnique, Vol. 47, No. 1, pp. 167-171.

Curtis, A. (2004), "Theory of model-based geophysical survey and experimental design - part 1- linear problems," The Leading Edge, Vol. 23, No. 10, pp. 997-1004.

Goto, S., Tatsuoka, F., Shibuya, S., Kim, Y-S., and Sato, T. (1991), "A Simple gage for local small strain measurements in the laboratory," Soils and Foundations, Vol. 31, No. 1, pp 169-180.

Dally, J.W., Riley, W.F., and McConnell, K. (1993), Instrumentation for Engineering Measurements, 2nd Edition, John Wiley & Sons Inc., New York, p. 584.

Defalias, Y.F., Papadimitrious, A.G., and Manzari, M.T. (2003) "Simple anisotropic plastic model for soft clays," Proc. Int. Workshop on Geotechnics of Soft Clays: Theory and Practice, P.A. Vermeer et al. (eds.), pp. 189-195.

Desai, C.S. (2005), "Constitutive modeling for geologic materials: significance and directions," International. Journal of Geomechanics, ASCE, Vol. 5, No. 2, pp. 81-84.

Desai, C.S., and Siriwardane, H.J. (1984), Constitutive Laws for Engineering Materials with Emphasis on Geologic Materials, Prentice-Hall, Inc., Englewood Cliffs, NJ, p. 468.

Duncan, J.M., and Dunlop, P. (1968), "The significance of cap and base restraint," Journal of Geotechnical Engineering, ASCE, Vol. 94, No. SM1, pp. 271-290.

Feng, X.F., Zhao, H., and Li, S. (2004), "A new displacement back analysis to identify mechanical geo-material parameters based on hybrid intelligent methodology," International Journal for Numerical and Analytical Methods in Geomechanics, Vol. 28, pp. 1141-1165.

Ganendra, D., and Potts, D.M. (1995) Discussion of 'Evaluation of constitutive model for overconsolidated clays,' A.J. Whittle (eds.), Geotechnique, Vol. 45, No. 1, pp. 169-173

Gens, A., and Potts, D.M. (1988), "Critical state models in computational geomechanics," Engineering Computations, Vol. 5, No. 3, pp. 178-197.

Gill, P.R., Murray, W., and Wright, M.H. (1981), "The Levenberg-Marquardt Method," Section 4.7.3 in Practical Optimization, London: Academic Press, pp. 136-137.

Head. K.H. (1994), Manual of Soil Laboratory Testing, Vol. 2, 2nd edition, Bookcraft (Bath) Ltd., UK.

Hird, C.C., and Yung, C.Y. (1989), "The use of proximity transducers for local strain measurements in triaxial tests," Vol. 12, No. 4, pp. 292-296.

Honjo, Y., Wen-Tsung, L., and Guha, S. (1994), "Inverse analysis of an embankment on soft clay by extended bayesian method," International. Journal for Numerical and Analytical Methods in Geomechanics, Vol. 18, No. 10, pp. 709-734.

Jardine, R.J., Symes, M.J., and Burland, J.B. (1984), "The measurements of soil stiffness in the triaxial apparatus," Geotechnique, Vol. 34, No. 3, pp. 323-340.

Jefferies, M.G. (1993), "Nor-Sand: a simple critical state model for sand," Geotechnique, Vol. 43, No. 1, pp. 91-103.

Jefferys W.H., and Berger, J.O. (1992), "Ockham's Razor and Bayesian analysis," American Scientist, Vol. 80, No. 1, pp. 64-72.

Lade, P.V., Yamamuro, J.A., and Skyers, B.D. (1996), "Effects of shear band formation in triaxial extension tests," Geotechnical Testing Journal, Vol. 19, No. 4, pp. 398-410.

Lade, P.V. (2005), "Overview of constitutive models for soils," Geotechnical Special Publications No 139, Calibration of Constitutive Models, Proceedings of Sessions of Geo-Frontiers 2005 Congress, (2005 : Austin, Tex.), From Soil Constitutive Models: Evaluation, Selection, and Calibration (Geotechnical Special Publication No. 128) (2005) (pp. 2493-2526). Edited by Jerry A. Yamamuro, Ph.D., P.E. and Victor N. Kaliakin, Ph.D. Published by ASCE, Reston, VA.

Lade, P.V. (2002), "Instability, shear banding, and failure in granular materials," International Journal of Solids and Structures, Vol. 39, No. 13-14, pp. 3337-3357.

Lambe, T.W., and Whitman, R.V. (1969), Soil Mechanics, John Wiley & Sons, Inc., New York, p. 553.

Ledesma, A., Gens, A., and Alonso, E.E (1996a), "Parameter and variance estimation in geotechnical backanalysis using prior information," International Journal for Numerical and Analytical Methods in Geomechanics, Vol. 20, pp. 119-141.

Ledesma, A., Gens, A., and Alonso, E.E. (1996b), "Estimation of parameters in geotechnical backanalysis-I. maximum likelihood approach," Computers and Geotechnics, Vol. 18, pp. 1-27.

Lee, K.L. (1978), "End restraint effects on undrained static triaxial strength of sand," Journal of Geotechnical Engineering, ASCE, Vol. 104, No. GT6, pp. 687-704.

Levenberg, K. (1944), "A method for the solution of certain problems in least squares," Quarterly of Applied Mathematics, Vol. 2, pp. 164-168.

Liu, M.D., and Carter, J.P. (2002), "A structured Cam Clay Model," Canadian Geotechnical Journal, Vol. 39, No. 6, pp. 1313-1332.

Liyanapathirana, D.S., Carter, J.P., and Airey, D.W. (2005), "Numerical modeling of nonhomogeneous behavior of structured soils during triaxial tests," International Journal of Geomechanics, Vol. 5, No. 1, pp. 10-23.

Marquardt, D. (1963), "An algorithm for least-squares estimation of nonlinear parameters," Journal of the Society for Industrial and Applied. Mathematics, Vol. 11, No. 2, pp. 431-441.

MathSoft (2001), Version 2001i Professional, MathSoft Engineering & Education, Inc. Cambridge, MA, USA.

Miller, F.E., and Doeringsfield, H.A. (1960), Mechanics of Materials, International Textbook Company, Scranton, Pennsylvania, p. 514.

Murthy, B.R.S., Vatsala, A., and Nagaraj, T.S. (1988), "Can Cam-Clay Model be generalized?," Journal of Geotechnical Engineering, ASCE, Vol. 114, No. 5, pp. 601-613.

Murthy, B.R.S., Vatsala, A., and Nagaraj, T.S. (1991), "Revised Cam-Clay Model," Journal of Geotechnical Engineering, ASCE, Vol. 117, No. 6, pp. 851-871.

Oda, M. (1993), "Inherent and induced anisotropy in plasticity theory of granular soils," Mechanics of Materials, Vol. 16, No 1-2, pp. 35-45.

Oreskes, N., Shrade-Frechette, K., and Belitz, K. (1994), "Verification, validation, and confirmation of numerical models in the earth sciences," Science, Vol. 263, No. 5147, pp. 641-646.

Peters, J.F., Lade, P.V., and Bro, A. (1988), "Shear band formation in triaxial and plane strain tests," Advanced Triaxial Testing of Soil and Rock, ASTM STP No. 977, Baltimore, edited by Donaghe, R.T., Chaney, R.C., and Silver, M., pp. 604-627.

Richards, C.W. (1961), Engineering Materials Science, Wadsworth Publishing Company, San Francisco, p.546.

Robinet, J.C., Pakzad, M., Jullien, A., and Plas, F. (1999), "A general modeling of expansive and non-expansive clays," Int. J. for Num. and Analytical. Methods in Geomechanics, Vol. 23, No. 12, pp. 1319-1335.

Roscoe, K. H., and Burland, J.B. (1968), "On the generalised stress-strain behaviour of 'wet' clay," in J. Heyman and F.A. Leckie (eds.), Engineering Plasticity (Cambridge: Cambridge University Press), pp. 535-609.

Rowe, P.W., and Barden, L. (1964), " Importance of free ends in triaxial testing," Journal of Soil Mechanics, ASCE, Vol. 90, No. SM1, pp. 1-27.

Santamarina, J.C., and Fratta, D. (1998), Introduction to Discrete Signals and Inverse Problems in Civil Engineering, ASCE Press. Reston, Virginia, p. 327.

Schofield, A., and Wroth, P. (1968), Critical State Soil Mechanics, McGraw-Hill Publishing Company Limited, Berkshire, England, p. 310.

Scholey, G.K., Frost, J.D., Lo Presti, D.C.F., and Jamiolkowski, M. (1995), "A review of instrumentation for measuring small strains during triaxial testing of soil specimens," Geotechnical Testing Journal, GTJODJ, Vol. 18, No. 2, pp. 137-156.

Sheng, D., Westerberg, B., Mattsson, H. and Axelsson, K. (1997), "Effect of end restraint and strain in triaxial tests," Computers and Geotechnics, Vol. 21, No. 3, pp. 163-182.

Skempton, A.W. and Northey, R.D. (1952), "Sensitivity of clays," Geotechnique, Vol. 3, No.1, pp. 30-53.

Sobol, I.M. (1974), The Monte Carlo Method. Translated from second Russian edition. Editors: Robert Messer, John Stone, and Peter Fortini, Chicago, Illinois: The University of Chicago Press.

Tarantola, A. (1987), Inverse Problem Theory. Elsevier: Amsterdam, p. 613.

Taylor, D.W. (1948), Fundamentals Of Soil Mechanics, John Wiley & Sons, Inc: New York, p. 700.

Wang, Q., and Lade, P.V. (2001), "Analysis of shear banding on true triaxial tests on sand," Journal of Engineering Mechanics, ASCE, Vol. 127, No. 8, pp. 754-761.

Whittle, A.J. (1993) "Evaluation of a constitutive model for overconsolidation clays," Geotechnique, Vol. 43, No. 2, pp. 289-313.

Whittle, A. J., and DeGroot, D. J. (1994), "Model prediction of anisotropic behavior of Boston Blue Clay," Journal of Geotechnical Engineering, ASCE, Vol. 120, No. 1, pp. 199-224.

Wood, D.M. (1990), Soil Behaviour and Critical State Soil Mechanics, Cambridge University Press: New York, Port Chester, Melbourne, Sydney, p. 462.

Wood, D.M., and Graham, J. (1990), "Anisotropic elasticity and yielding of a natural plastic clay," International Journal of Plasticity, Vol. 6, No. 4, pp. 377-388.

Yamamuro, J.A., and Lade, P.V. (1995), "Strain localization in extension tests on granular materials," Journal of Engineering Mechanics, ASCE, Vol. 121, No. 7, pp. 828-836.

Yin, J.H, and Graham, J. (1999),"Elastic viscoplastic modeling of the time-dependent stress-strain behavior of soils," Canadian Geotechnical Journal, Vol. 36, No. 4, pp. 736-745.

Yu, H.S. (1998), "CASM: A unified state parameter model for clay and sand," International Journal for Numerical and Analytical Methods in Geomechanics, Vol. 22, No. 8, pp 621-653.

Yun, T-S (2005), Mechanical and thermal study of hydrate bearing sediments, Ph.D. thesis, School of Civil and Environmental Engineering, Georgia Institute of Technology, Atlanta.

Zytynski, M., Randolph, M.F., Nove, R., and Wroth, C.P. (1978), "Short communications on modelling the unloading-reloading behaviour of soils," Int. J. for Num. and Analytical Methods in Geomechanics, Vol. 2, pp. 87-94.